Experimental and Theoretical Studies of Quasifission

A thesis submitted for the degree of

Doctor of Philosophy

of The Australian National University

Aditya Wakhle

May 6, 2013

Preface

This thesis describes experimental and theoretical work on quasifission in reactions forming heavy and superheavy elements. This project was originally motivated by Prof. D. J. Hinde and Prof. M. Dasgupta. All measurements documented in this work were made with the assistance of the nuclear reaction dynamics group and the technical staff of the Department of Nuclear Physics. All measurements were carried out using the CUBE detector system consisting of two large area position sensitive multi-wire proportional counters. Analysis of the data was carried out by the author, using the customised software `dagui` written by Dr. R. du Rietz, which was based on the existing `C++ ROOT` framework and its libraries. The Time Dependent Hartree Fock (TDHF) calculations were performed by the author under the guidance of Dr. C. Simenel, the developer of the TDHF3D code that was used.

The following publications are directly related to the work in this thesis, and have been or will be published:

1. *Quasifission and Shell Effects in Reactions Forming* ^{266}Sg,
   A. Wakhle, D. J. Hinde, M. Dasgupta, R. du Rietz, C. Simenel, M. Evers, D. H. Luong and R. Rafiei, EPJ Web of Conferences **35**, 05008, 2012.

Furthermore the author has contributed to the following publications, which have been or will be published:

1. *Influence of entrance-channel magicity and isospin on quasi-fission*,

C. Simenel, D. J. Hinde, R. du Rietz, M. Dasgupta, M. Evers, C. J. Lin, D. H. Luong and **A. Wakhle**, Phys. Lett. B, **710**, 607, 2012.

2. *Effects of Nuclear Structure in Heavy Element Formation Dynamics*,
   D. J. Hinde, R. du Rietz, C. Simenel, M. Dasgupta, **A. Wakhle**, M. Evers, and D. H. Luong, 9th Latin American Symposium on Nuclear Physics and Applications, AIP Conference Proceedings, **1423**, 65-72, 2012.

3. *Optimising conditions for production of He-6, Li-8, Be-10 and B-12 radioactive ion beams with the SOLEROO separator*,
   A. J. Horsley, D. J. Hinde, M. Dasgupta, R. Rafiei, **A. Wakhle**, M. Evers, D. H. Luong and R. du Rietz, Nuclear Instruments and Methods **646**, 174, 2011.

4. *Measured g factors and the tidal-wave description of transitional nuclei near A=100*,
   S. K. Chamoli, A. E. Stuchbery, S. Frauendorf, J. Sun, Y. Gu, R. F. Leslie, P. T. Moore, **A. Wakhle**, M. C. East, T. Kibédi, and A. N. Wilson, Phys. Rev. C **83**, 054318, 2011.

5. *Optimising conditions for production of He-6, Li-8, Be-10 and B-12 radioactive ion beams with the SOLEROO separator*,
   R. Rafiei, D.J. Hinde, M. Dasgupta, D.C. Weisser, A.G. Muirhead, A.B. Harding, A.K. Cooper, H.J. Wallace, N.R. Lobanov, **A. Wakhle**, M.L. Brown, C.J. Lin, A.J. Horsley, R. du Rietz, D.H. Luong and M. Evers, Nuclear Instruments and Methods **631**, 12, 2011.

6. *Predominant Time Scales in Fission Processes in Reactions of S, Ti and Ni with W: Zeptosecond versus Attosecond*,
   R. du Rietz, D. J. Hinde, M. Dasgupta, R. G. Thomas, L. R. Gasques, M. Evers, N. Lobanov and **A. Wakhle**, Phys. Rev. Lett. **106**, 052701, 2011.

No part of this thesis has been submitted for a degree at any other university.

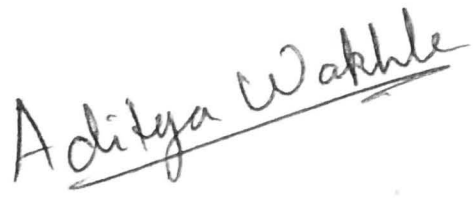

Aditya Wakhle

Canberra, May 2013

Acknowledgments

The largest portion of my gratitude goes to Professor David Hinde for his pivotal role during my candidature. His indefatigable patience, friendliness and ability to strike a balance between providing guidance and encouraging independent thought made him the perfect supervisor. I would also like to thank Professor Nanda Dasgupta for her guidance and no nonsense advice over the last four years. Thank you both for maintaining an "open-door" policy and always being available. Thanks to Doctor Cedric Simenel for his role as a supervisor during work hours, as a cherished friend outside the office and for his hospitality in France. Also for his boundless patience in explaining theoretical concepts to an experimentalist.

I would like to thank my colleagues and friends Doctors Duc Huy Luong, Maurits Evers, Rickard du Rietz, Ramin Rafiei and Matthew Reed for their assistance during experiments, company at conferences and uplifting antics throughout the last four years. Special thanks to Huy for his invaluable expertise on all things "eye-candy" related and real-world IT troubleshooting. Thanks to Rickard for being a valued friend and developer of the analysis program. Thanks to Matthew Reed and Maurits for their company during the final months of thesis writing.

I am very thankful for all the work Doctor Nikolai Lobanov put in towards my experiments and his tireless support during two extremely challenging LINAC runs. Without his expertise and hard work, a crucial part of my project would not have been possible. My thanks also extend to the technical staff that made my experiments possible: Alan Cooper, Justin Heighway, Tom Kitchen, Gareth Crook, Alistair Muirhead, Dimitrios Tsifakis and Angus Gratton. Special thanks to Petra Rickman, for being what can only be described as awesome.

Thanks to Doctor Elizabeth Williams for reading my initial thesis chapters and pro-

viding excellent feedback. Thanks to Doctor Ramachandran for enlightening physics discussions. A big thanks to everyone at the Department of Nuclear Physics for making it a unique, intellectual and inspiring work environment.

Finally, a big thanks to Alex for putting up with me and being incredibly supportive through some very testing times.

This thesis is dedicated to my parents. Their unconditional love, support and sacrifice have sustained me throughout my life.

Abstract

The quest to synthesise superheavy elements is at the frontier of nuclear physics research. These elements can only be formed by the fusion of two heavy nuclei. The repulsive electrostatic energy between such nuclei is extremely large and more often than not, the system re-separates prematurely into two heavy fragments, intermediate in mass compared to the original nuclei. This non-equilibrium process is called quasifission. Only occasionally does fusion occur resulting in the formation of a compound nucleus.

Finding the variables determining the competition between quasifission and fusion is a problem currently challenging experimentalists and theoreticians. The dynamic evolution of the dicnulear system is governed by several degrees of freedom, fluctuations and quantum properties. A self consistent and reliable calculation of the competition between quasifission and fusion is beyond current theoretical capabilities. Prediction of the most favorable reactions to form superheavy elements, thus currently relies on empirical systematics. To aid in the development of a complete, self-consistent, realistic and tractable model, it is important to determine which degrees of freedom are critical in quasifission dynamics and what is the dynamical nature of quasifission.

This thesis addresses this problem by studying reactions forming heavy and superheavy elements using experimental and theoretical methods. In total eight reactions with targets of ^{238}U and ^{232}Th were studied experimentally. Six reactions were studied in pairs forming the same compound nucleus while the two heaviest reactions were between projectiles of ^{40}Ca and targets of ^{238}U and ^{232}Th. For the heaviest reaction (^{40}Ca + ^{238}U) a detailed theoretical study was also conducted.

The experimental part of this thesis presents a detailed analysis of the binary fission events from these reactions. The large angular coverage of the CUBE fission spectrometer was used to obtain wide-ranging mass-angle distributions for each reaction, at energies

spanning the Coulomb barrier. The results point to the role of shell effects around ^{208}Pb in the mass-asymmetric quasifission exit channel, the presence of mass-symmetric quasifission and the evolution of the balance between quasifission and fusion with increasing $Z_P Z_T$.

The theoretical part of this thesis examined the ^{40}Ca + ^{238}U reaction within the Time Dependent Hartree Fock (TDHF) model, using the TDHF3D code. This is the first time that the TDHF approach has been used to extensively study quasifission. The results revealed that the orientation of the heavy deformed prolate nucleus plays a major role in the reaction outcome, in agreement with experiment. It was found that aligned collisions lead to quasifission and short contact times of 5-10 zs, whilst anti-aligned collisions lead to longer contact times ($>$ 23 zs). TDHF accurately predicted the presence of quasifission and the average mass splits in this reaction. The influence of shell effects around ^{208}Pb in the calculated quasifission characteristics was confirmed by an analysis of the neutron and proton numbers of the outgoing fragments.

These findings are a promising step towards the formulation of a consistent theoretical picture of nuclear reaction dynamics of heavy systems.

Contents

Chapter 1

Introduction and Motivation

At the frontier of nuclear physics research is the push to synthesise superheavy elements (SHE), lying at and beyond the limits of the periodic table, with atomic numbers above Z=100. They have only been made artificially and their short half-lives cause them to decay after a time ranging from a few minutes to just a few milliseconds (the longest lived exception being Dubnium, with a half life of over a day). These elements are created in quantities on the atomic scale, atom by atom, and no practical method of mass creation has been found. Their very short half-life makes their physical and chemical properties extremely hard to study. This is further compounded by the fact that they are very difficult to make as a consequence of their minuscule (pico barn to sub-pico barn) formation cross sections.

Superheavy elements can only be created through the bombardment of elements in a particle accelerator, by the fusion of two lighter nuclei. The nuclei are brought into contact by providing them kinetic energy sufficient to overcome their mutual Coulomb repulsion. Interest in the formation of these very heavy elements was sparked by theoretical predictions of an island of elements, on the periodic table, with enhanced stability. This stability resulted from quantum mechanical shell effects, around neutron number N=184 and proton numbers between Z=114 to 126 [1, 2, 3], associated with symmetries of the spherical shape. Experimental efforts aiming to form superheavy nuclei followed this prediction [4, 5].

In recent years there has been a steady stream of experimental evidence for SHE highlighting the topical nature of this field. Evidence of the formation of long-lived isotopes of

elements with Z = 113 [6], 114 [7], 116 [8], 117 [9] and 118 [1] have given further momentum to this quest.

1.1 Quasifission: A competing process to fusion

Producing superheavy elements is an extremely challenging experimental task due to several reasons. Firstly, the formation of an evaporation residue (ER) is heavily suppressed by fission of the equilibrated compound nucleus (CN), via a process known as fusion-fission (FF). Moreover, the non-equilibrium process called quasifission (QF) hinders CN formation by several orders of magnitude [10, 11, 12, 13]. The formation of a true CN is characterised by equilibration of all degrees of freedom and a complete loss of identity of the entrance channel [14]. In the QF process, following the capture of the projectile by the target nuclei, the system re-separates prematurely, not forming a true CN. QF events mark the transition between deep inelastic collisions (DIC) and complete fusion. In DIC the entrance channel mass-asymmetry is preserved, but there can be large dissipation of kinetic energy and angular momentum [15]. QF events exhibit full energy dissipation but incomplete drift towards the energetically favored mass-symmetric configuration [16].

Finding the variables that determine the competition between quasifission and fusion is a problem currently challenging experimentalists and theoreticians.

1.2 The Interplay between Experiment and Theory

The ground state and excited state energies of SHE provide a testing ground for models of nuclear structure and the limits of nuclei. Hence producing new nuclei in this region and studying their nuclear structure and chemical properties is an important goal in nuclear physics. Progress in the field is driven by testing and refining theories using experimental results and the theories in turn making predictions for future experiments.

The outcome of a heavy-ion collision depends essentially on a few properties of the entrance channel: energy, masses, angular momentum, N/Z asymmetry, deformation and orientation of the nuclei, and their internal structure [10, 11, 12, 17, 18]. Microscopic effects such as shell closure and neutron excess are also reported to influence the probability of QF [19, 20]. The experimental problem is to identify the role of each of these variables in CN formation. The theoretical problem is similar, in that we need models that can

account for all of these properties. However, the challenge is to have a self consistent model, with a few input parameters, that can reproduce existing experimental results and also make predictions that guide future experimental efforts. The ultimate goal is to have a theory that can accurately predict optimal reactions to form SHE, thereby eliminating the need to perform expensive experiments that may fail to do so.

In this work, this problem is addressed by measuring the characteristics of QF events and their relationship with FF.

1.3 Thesis Outline

This thesis is an experimental and theoretical study of quasifission and heavy-ion reactions. Measurements were made of the fission fragment mass-angle distributions for reactions of ^{12}C, ^{18}O, ^{24}Mg, ^{28,30}Si, ^{34}S and ^{40}Ca with targets of ^{232}Th and ^{238}U forming composite nuclei ranging from ^{250}Cf to ^{278}Cp, at near-barrier energies. The reaction forming ^{278}Cp was studied further using the Time Dependent Hartree Fock (TDHF) model, a numerical solution to quantum mechanics.

The thesis outline follows:

Chapter 2: Theory This chapter explains the theoretical descriptions of heavy-ion reactions relevant to this work. It discusses capture reactions before a brief review of the current literature. We discuss the first empirical evidence for quasifission and the subsequent work in this field. We then explain how the Liquid Drop Model (LDM) predicts the evolution of the dinuclear system and how Potential Energy Surface (PES) are used, within a classical physics picture, together with Langevin dynamics to describe the evolution of the shape degrees of freedom. We end with the Time-Dependent Hartree-Fock formalism.

Chapter 3: Experimental Methods and Instrumentation A description of how the experiments were conducted and of the supercomputing facilities used in this work. It includes details of heavy-ion beam production using the ANU 14UD accelerator, the targets, the detector system and measurement procedure for the reactions presented in Chapter 5. Also included is a brief description of the MERCURE and NCI computing systems used in the work presented in Chapter 6.

Chapter 4: Mass-Angle Distributions (MADs) A description of Mass Angle Distributions, the kinematic coincidence method and the data analysis procedure.

Chapter 5: Results and Interpretation of MADs This chapter presents the results of the experimental measurements made in this work and a systematic investigation to determine which degrees of freedom are critical in QF dynamics. Results from the eight reactions studied are presented in ascending order of compound nucleus mass. Shells effects in the exit channel are the primary focus. Other observations such as threshold values beyond which fusion starts to be suppressed by QF, thresholds between mass-symmetric and mass-asymmetric quasifission and the effect of target nuclei are also presented.

Chapter 6: Time-Dependent Hartree-Fock Calculations. This chapter presents a theoretical study of the ^{40}Ca + ^{238}U reaction using the Time-Dependent Hartree-Fock (TDHF) systematics. An extensive computational campaign was undertaken to investigate the role of energy, orientation and angular momentum in this reaction. A comparison with experimental results is discussed and suggestions made for future work with this model.

Chapter 7: Conclusion. A summary of the results and discussion presented in Chapter 5 and 6, with a focus on the most significant results.

Chapter 2

Background and Theory

Heavy ion reactions are the cornerstone of nuclear physics research. They provide a means of forming and studying nuclei, including SHE, and nuclear states not seen in nature. An understanding of the dynamics of heavy ion reactions is necessary to predict optimal conditions for SHE production. This thesis presents an experimental study of a range of reactions that form very heavy and super heavy compound nuclei, and a theoretical study of the heaviest reaction measured here.

In this chapter we present a brief history of the knowledge of heavy ion reactions relevant to this work. We begin with an outline of the various possible outcomes of heavy ion reactions, leading in to the discovery and nature of quasifission and the experimental methods of studying it. We then outline the liquid drop model, a macroscopic model used extensively to predict the behaviour of heavy ion reactions. The chapter ends with the Time-Dependent Hartree-Fock (TDHF) formalism.

2.1 Nuclear Reactions

A heavy ion reaction begins with the interacting nuclei approaching each other. During this initial phase, the nuclei interact only through the long range electromagnetic force which has infinite range. As the nuclei are both positively charged, they experience a mutually repulsive force. The attractive nuclear force has a much shorter range (typically a few fm), comparable to the size of a nucleon. As they come together, there are broadly three possible outcomes:

1. Elastic scattering: The nuclei may pass each other without influencing each others internal structure. This outcome occurs if the relative kinetic energy of the nuclei is too low for them to overcome the potential energy barrier (or Coulomb barrier) resulting from the Coulomb interaction. It may also occur if the impact parameter (b), the distance between the centres of the nuclei at closest approach if they were to follow straight lines, is too high, thereby reducing the radial injection energy [16].

2. Inelastic scattering: The nuclei may pass each other, like in elastic scattering, but at least one is excited from its ground state by the electromagnetic force. Energy of relative motion of the nuclei is coupled to the internal states of the nuclei. This energy is eventually lost from the system through the emission of one or more gamma rays.

3. Reactions: The nuclei have enough energy to overcome the Coulomb barrier and can approach close enough to interact through the nuclear force. Kinetic energy is then dissipated through nuclear interactions. This outcome occurs when the surfaces of the nuclei "touch", which is a reasonable approximation if the nuclei are modelled as hard spheres. The interaction via the nuclear force manifests in a wide variety of nuclear reactions, which can involve considerable changes in shape, transfer of nucleons and dissipation of energy. These include capture, where the system is trapped for some time in the potential pocket inside the barrier.

   Following capture, the collective motion of the nuclei is governed by the nuclear and electromagnetic force. This motion is far more complicated than that of the first phase since the shape of the nuclear system can vary as a function of time and the motion is not limited to the single degree of freedom describing the separation of the centres of the nuclei. This phase of the motion is not well understood and several models are used to describe it. Regardless of the description of the motion, three specific outcomes can be identified:

   (a) Deep inelastic scattering (DIS): The nuclei reseparate, never having been joined by more than a neck. While nucleons can pass through this neck to achieve N/Z equilibration and kinetic energy dissipation, little or no net transfer of mass can occur. The fragments that result from this reaction thus have masses very similar to those of the reacting nuclei in the entrance channel.

(b) Quasifission (QF): The nuclei achieve a mono-nuclear state characterised by a wide neck, but still end up reseparating. The kinetic energy of the nuclei is completely dissipated and net mass transfer takes place from the heavy nucleus to the light nucleus. The wide neck of the mono-nuclear state facilitates rapid mass transfer. Thus the masses of the outgoing fragments can fall anywhere between the masses of the initial nuclei and complete symmetry. Although deep inelastic scattering and quasifission both result in the separation of two fragments on short time scales, experimental results [16] provide a very clear distinction between the two. This implies that there is a bifurcation in reaction trajectories, leading to the different outcomes.

(c) Compound Nucleus (CN) formation: The nuclei form a compact shape, known as a compound nucleus and no longer correspond to two nuclei joined by a neck. The probability of reaching this state is denoted P_{CN}. Any information about the initial conditions such as mass asymmetry or particle identity is lost. The formation and decay of the intermediate CN are decoupled and only certain quantities are conserved, namely the total angular momentum, linear momentum and energy. After equilibration the CN may lose energy through neutron evaporation to form an evaporation residue (ER).

Alternately, the CN may reseparate into two fragments via a process known as fusion fission (FF). The excitation energy of the CN has a strong influence on its decay by fission. At high enough excitation energies the CN decays into two symmetric fragments. At lower excitation energies its sensitivity to shell effects around the spherical closed shells N, Z= 20, 28 and 50 [21] and deformed closed shells N = 88 and Z = 53 [22] increases and asymmetric mass splits may be observed. This is much like neutron induced fission of ^{238}U or the spontaneous fission of nuclei in the actinide region, but at higher excitation energy and angular momenta.

2.2 Quasifission

The QF process was discovered over three decades ago [23, 24], when it was first recognized that fission fragments from a heavy-ion induced reactions do not necessarily originate from the fission of a compound nucleus. It was realised that fission fragments could come from

a non-equilibrium process where a CN is not formed.

This conclusion was based on several different observations: Firstly, in the reaction of ^{132}Xe + ^{56}Fe [24] an unusually large fission cross section of 1040 mb was measured. This exceeded the upper bound imposed by the disappearing fission barrier for spins larger than 72 $\hbar$, according to the Rotating Liquid Drop Model [25]. Therefore, the fission-like processes originating from total angular momenta above 72 $\hbar$ was termed "fission without a barrier".

Secondly, it was noticed that the width of the mass distribution increased significantly for the partial waves where the fission barrier vanishes and was wider than expected on the basis of a compound nucleus model [26]. The fission mass distribution in reactions of ^{20}Ne + ^{nat}Re and ^{40}Ar + ^{165}Ho [27] was observed to widen above partial waves for which the fission barrier disappeared. This was confirmed in a subsequent study [28] that examined a larger data set and the term "fast fission" was used for l-values where the fission barrier vanishes. Finally, it was noted that the fission fragment anisotropy in heavy-ion induced fission substantially exceed expectations based on the transition state model (TSM) [29, 30, 31, 32, 33]. Large deviations of angular anisotropies from the predictions of the TSM [106] for compound nucleus fission were shown in Ref. [29, 30] for reactions of projectiles heavier than and including ^{24}Mg with ^{208}Pb targets. These results were interpreted as the presence of QF in these systems.

Subsequent studies of the two-dimensional mass-angle distributions [16, 26, 32, 34, 35, 36, 37, 38, 39, 40] and mass-energy distributions [41, 42, 43, 44] of fission fragments clearly demonstrated that these fragments are the result of a dynamic process, in which the system evolves toward mass symmetry on a time scale similar to the rotational period of the complex. This process is now referred to as quasi-fission although formerly the terms "fission without a barrier" and "fast fission" were also used.

2.2.1 Recent work

Recently, much progress in the theoretical description of this process has been achieved and further precise experiments have been conducted, which provide further constraints on our understanding of these complex processes that also play a critical role in attempts to synthesize heavy and super-heavy nuclei via heavy-ion fusion processes.

Mass-angle distribution measurements reported in Ref. [39], using beams of ^{208}Pb on targets ranging from ^{16}O to ^{64}Ni followed later by those of Ref. [16, 26] using beams of ^{238}U, on targets ranging from ^{16}O to ^{89}Y showed broadened mass distributions and strong mass-angle correlations for targets heavier than ^{27}Al. In these experiments, evidence for QF included the observation of broadened mass distributions for the fission-like fragments and a strong correlation between fragment mass and emission angle. The associated timescale of QF was inferred to be 10^{-20}-10^{-21}s, different from that of FF which is at minimum 10^{-20}-10^{-19}s [45, 46].

In Ref. [47] a direct proportionality was found between the entrance-channel mass-symmetry and the QF flux. Reactions forming ^{243,249}Md showed incomplete relaxation of the mass degree of freedom for more mass-symmetric entrance-channels. The nuclear orientation of the interacting nuclei was found to influence QF in Ref. [36, 37]. Unusually large anisotropies were seen for ^{16}O + ^{238}U at sub-barrier energies, and were interpreted as enhancement of the probability of QF for tip collisions with the prolate deformed ^{238}U nucleus. This work also demonstrated the existence of QF for charge product $Z_P{}^*Z_T$= 736, far less than the threshold value of 1600 set by earlier dynamical models [10]. Similar observations were made by Ref. [48, 49] using light projectiles ranging from ^{7}Li to ^{16}O on actinide targets, confirming the effect of deformation on QF. However, measurements of ER cross sections for the ^{16}O + ^{238}U reaction showed that CN formation is still present at sub-barrier energies [50] showing that these two processes can exist at similar partial waves. However, severe inhibition of ER cross sections for ^{60,64}Ni + ^{154}Sm at sub-barrier energies was reported in Ref. [19, 51], showing the dominance of QF for capture on the tip of a deformed target nucleus, for reactions with heavy projectiles and highlighting the fact that QF hinders ER formation by several orders of magnitude.

While these measurements of QF were focused on heavy composite nuclei, subsequent experimental work on lighter composite nuclei indicated an unexpected shift to lighter systems, in the onset of QF. Evidence for QF was seen for asymmetric reactions, forming systems as light as ^{216}Ra and ^{220}Th. Several reactions forming the same composite system were used, thus varying the entrance channel mass-symmetry. For ^{216}Ra, reduction in the ER cross sections [52] and broadened mass distributions [52, 53] were observed for the more mass-symmetric entrance channels. This entrance channel dependence of QF is also strongly seen in the reactions forming ^{220}Th system. Substantial reductions in ER cross

sections were observed for reactions involving projectiles heavier than and including ^{40}Ar forming ^{220}Th [54]. Incomplete mass relaxation was also observed in the fragment mass distributions for projectile heavier than and including ^{34}S forming ^{220}Th [38]. For each of these relatively light systems it is clear that there exists a critical entrance channel mass-asymmetry and charge product which marks the onset of QF.

Disentangling QF and FF processes experimentally is not always easy since their observable characteristics may overlap considerably. The work in Ref. [32] identified a second, distinct mode of quasifission. For reactions with relatively large entrance channel mass asymmetry it was observed that quasifission can also contribute to mass-symmetric fission. This reaction mechanism has been called deep quasifission (DQF) in the theoretical works of Aritomo [55, 56]. Experimental work in the last decade has shown that the competition between fusion-fission and quasifission is affected by shell driven deformation and orientation as well [32, 36, 37, 57, 58].

In the current work we show that the quasifission process is strongly influenced by shell effects encountered during the evolution of the dinuclear system. Reactions of projectiles ranging from ^{12}C to ^{40}Ca with actinide targets ^{232}Th and ^{238}U are used. We use two unique combinations of nuclei to form the same isotope of heavy elements ranging from ^{250}Cf to ^{278}Cp.

2.3 Nuclear Models

This section briefly describes the Liquid Drop Model and the Shell Model, two core models used to study nuclear reactions.

2.3.1 The Liquid Drop Model

The nucleus is made up of protons and neutrons, which are in turn made up of three quarks. The protons and neutrons interact through the strong and weak nuclear forces and the electromagnetic interaction. However, a quantum chromodynamic (QCD) approach solves for every interaction that takes place between these particles. A QCD approach however, isn't practical for nucleon-nucleon interactions since the problem quickly becomes numerically intractable for even light mass nuclei. Therefore alternative models are required to practise nuclear physics. Broadly speaking, there are two approaches: macroscopic and

microscopic.

Macroscopic approaches parameterise various properties of the nucleus and make analogies with larger systems like fluids. They are used to predict properties such as mass and binding energy as smoothly varying functions of atomic number Z and neutron number N. Microscopic models use a quantum mechanical approach to build up an energy level structure and therefore can account for the discrete values of quantities like energy and angular momentum, and experimentally observed deviations from the smooth behaviour predicted by purely macroscopic approaches.

The liquid drop model (LDM) assumes that the nucleus can be treated as a uniformly charged, incompressible fluid of uniform density. These are reasonable assumptions since, to a first approximation, the nucleus is an incompressible, homogeneous mixture of protons and neutrons. Moreover, due to Coulomb repulsion the protons will be distributed approximately evenly. Based on this, the semi empirical mass formula [59] is used to estimate the binding energy of a nucleus:

$$E_B = a_V A - a_S A^{2/3} - a_C Z(Z-1)A^{-1/3} - a_{symm}\frac{(A-2Z)^2}{A} + \delta(A,Z), \qquad (2.1)$$

where A is the mass number and Z is the atomic number. The terms correspond to the volume, surface, Coulomb, symmetry and pairing effects, respectively. The coefficients are calculated by fitting to experimentally measured masses of nuclei

The volume term ensures that the binding energy increases with increasing nucleon number. Since the strong nucleon-nucleon interaction is a short range force, each nucleon interacts only with its nearest neighbours. Hence an increase in volume causes a linear increase in the binding energy.

The surface term takes into account the fact that nucleons at the surface of a nucleus interact with fewer other nucleons than those in the interior. These nucleons contribute less toward the binding energy. Hence, the surface term is negative and is proportional to the surface area, which in turn is proportional to $A^{2/3}$ for a given spheroidal shape.

The Coulomb term accounts for the repulsive force between protons. It decreases the binding energy as the number of protons increases. As a first approximation, the nucleus can be considered a sphere of uniform charge density. The potential energy of such a

charge distribution is:

$$E = \frac{3}{5}\frac{Z^2e^2}{4\pi\epsilon_0 R}, \tag{2.2}$$

where e is the charge of an electron and R is the radius of the sphere. Since the nuclear radius is proportional to $A^{1/3}$ the Coulomb term is proportional to $A^{-1/3}$. Internal electrostatic repulsion exists only in nuclei with more than one proton. Hence as a refinement to the commonly used Z^2 dependence, following Bohr and Mottelson [61] we take the term proportional to Z(Z - 1).

The symmetry term is introduced to account for the fact that nuclei have nearly equal number of protons and neutrons. It prevents nuclei like a hydrogen atom with 100 neutrons from being energetically favourable. The symmetry term determines the width of the mass "peninsula" and together with the Coulomb term determines the path of the stability line through the N, Z plane. This reflects the fact that as Z increases, the line of stability moves along $N > Z$ and not $N = Z$.

The pairing term accounts for the experimentally observed fact that nuclei with even numbers of protons and neutrons tend to have lower binding energies than those with odd numbers of protons and neutrons.

Nuclear deformation can also be parameterised in the liquid drop model. As the nucleus deforms, the surface energy increases while the Coulomb energy decreases. To incorporate deformation in the LDM the nuclear radius is parameterised using spherical harmonics and a deformation parameter β_2. The spherical surface and Coulomb energies are denoted by E_S^0 and E_C^0 respectively. The Coulomb term is then determined by calculating the Coulomb energy of a homogeneous charge distribution. The surface term is determined by integrating over a surface element dS. The change in energy due to deformation of the liquid drop is then [60]:

$$\Delta E = E_S^0\left(\frac{1}{2\pi}\beta_2^2 - \frac{4}{105}\left(\frac{5}{4\pi}\right)^{\frac{3}{2}}\beta_2^3 + ...\right) - E_C^0\left(\frac{1}{4\pi}\beta_2^2 + \frac{4}{105}\left(\frac{5}{4\pi}\right)^{\frac{3}{2}}\beta_2^3 - ...\right) \tag{2.3}$$

This expression can be used to determine the fission barrier within the LDM. To simplify notation we introduce $a_2 = (5/4\pi)^{1/2}\beta_2$ and the conventional fissility parameter:

$$x = \frac{E_C^0}{2E_S^0} \tag{2.4}$$

The fissility parameter x quantifies the 'readiness' of the nucleus to scission. The following derivation is only valid for small values of $\mid 1 - x \mid$. Equation 2.3 can then be written as:

$$\Delta E = E_S^0 \left(\frac{2}{5} (1 - x) a_2^2 - \frac{4}{105} (1 + 2x) a_2^3 + ... \right) \tag{2.5}$$

For $x < 1$ and $a_2 = 0$ the deformation energy has a positive curvature. For sufficiently large a_2 the deformation energy is negative. The third-order expression in a_2 allows us to calculate a fission barrier. The maxima of the third order polynomial is found by solving:

$$\frac{\partial \Delta E}{\partial a_2} = 0 = E_s^0 \left(\frac{4}{5}(1 - x)a_2 - \frac{4}{35}(1 + 2x)a_2 \right) \tag{2.6}$$

The two roots of this equation are $a_2 = 0$ and $7(1 - x)/(1 + 2x)$. The first corresponds to the spherical minimum and the second to the maximum barrier height:

$$E_{barr} = \frac{98}{15} \frac{(1 - x)^3}{(1 + 2x)^2} E_S^0 \tag{2.7}$$

For $x > 1$ the fission barrier disappears and for $x < 1$ it has a non-zero height. Using the LDM parameters of Myers and Swiatecki [62] we get an expression for the fissility parameter:

$$x = 0.01965 \frac{Z^2}{A} \frac{1}{\left(1 - 1.17826 \frac{(N-Z)}{(N+Z)}\right)} \tag{2.8}$$

The liquid drop model without the pairing term is a purely macroscopic treatment of the nucleus. While it predicts the overall trend in binding energy quite well (figure 2.1), it fails to predict the locally observed deviations from a smooth behaviour. It is also incapable of accounting for the fine structure of nuclear excitations.

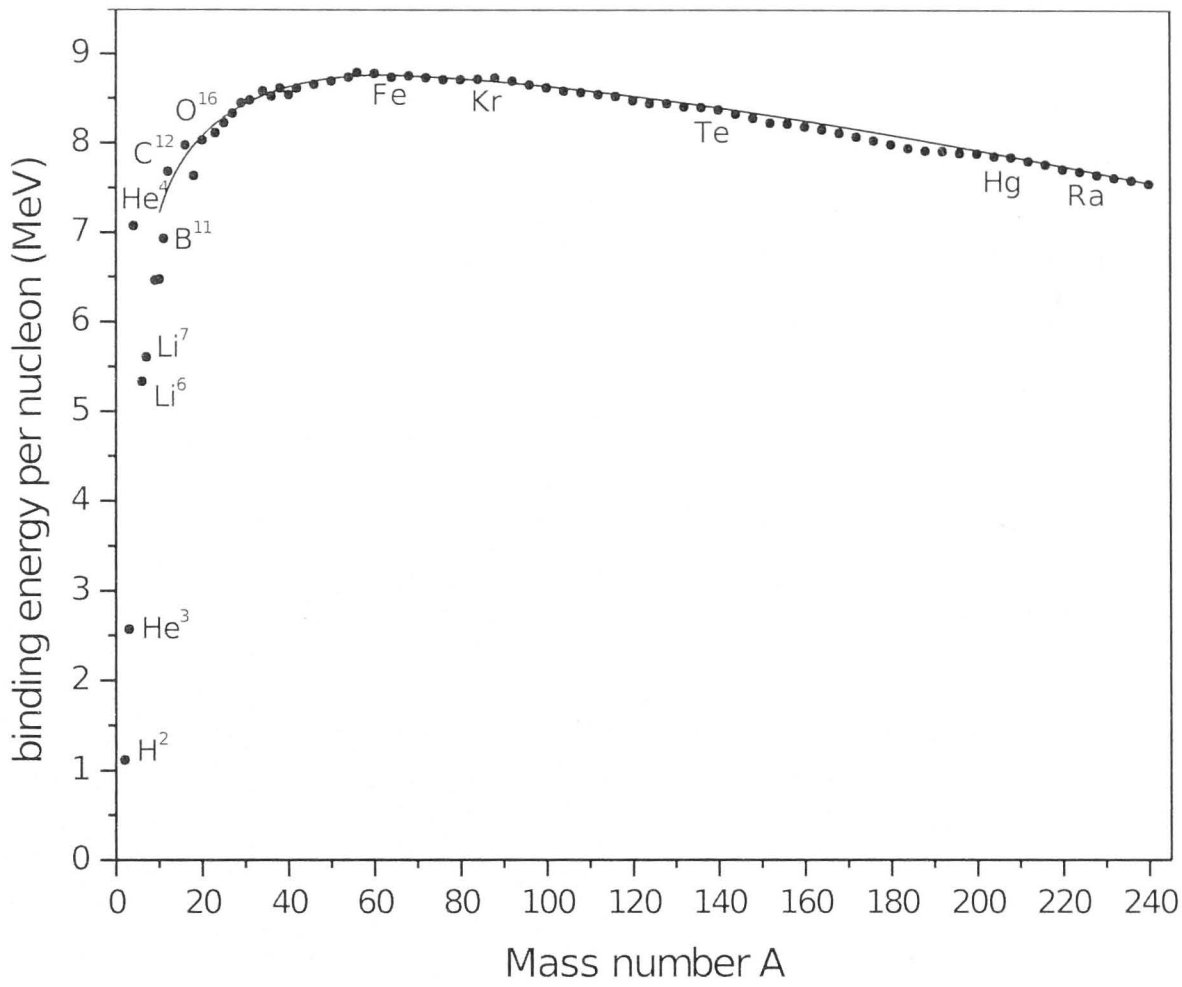

Figure 2.1: Binding energy per nucleon as a function of mass number A. The dots correspond to experimentally measured binding energies. The solid curve is the calculation of the semi-empirical mass formula (equation 2.1). It reproduces the overall experimental trend very well.

2.3.2 The Shell Model

The shell model is used to explain properties such as the local deviations observed in the binding energy curve, the quantised nature of energy, angular momentum and the fine structure of nuclei. This approach employs various forms of a central potential to reproduce experimentally observed properties. The corresponding Hamiltonian is used to determine the eigenenergies of the potential and build up a spectrum of energy levels. The harmonic oscillator together with the centrifugal potential is one example of a central potential [63]:

$$V_{Harmonic-Oscillator}(r) = \frac{m\omega_0^2}{2}r^2 + \frac{\hbar^2}{2mr^2}l(l+1), \tag{2.9}$$

where m is the average nucleon mass.

The Woods-Saxon potential is more commonly used to describe nuclei. Based on experimental measurements of nuclear density, it is empirically determined to be:

$$V_{Woods-Saxon} = -\frac{V_0}{1+e^{\frac{r-R_0}{a}}} \tag{2.10}$$

The Woods-Saxon and Harmonic-Oscillator potential alone do not reproduce all of the observed shell gaps. A shell gap is a sharp drop in the nuclear binding energy that occurs at certain nucleon numbers. They correspond to closed shell configurations. The Nilsson potential [64] uses a modified form of the harmonic oscillator potential:

$$V_{Nilsson} = \frac{m\omega_0^2}{2} r^2 - 2\kappa\hbar\omega_0 \left[l.s - \mu \left(l^2 - \left\langle l^2 \right\rangle_N \right) \right] \tag{2.11}$$

The parameters κ and μ are experimentally determined. They are adjusted so that the energy levels generated by the Nilsson potential match experimentally observed ones [60]. Solutions to the Schrödinger equation, using this potential predict the observed shell gaps.

Deformation in the shell model is accounted for by introducing a deformation parameter ϵ into the potential. This is done by allowing the radial term to differ in strength along one axis. The Nilsson potential then becomes:

$$V_{Nilsson} = \frac{m}{2} \left[\omega_\perp^2 \left(x^2 + y^2 \right) + \omega_z^2 z^2 \right] - 2\kappa\hbar\omega_0 \left[l.s - \mu \left(l^2 - \left\langle l^2 \right\rangle_N \right) \right] \tag{2.12}$$

$$\omega_\perp = \omega_0 \left(1 + \frac{1}{3}\epsilon \right) \tag{2.13}$$

$$\omega_z = \omega_0 \left(1 - \frac{2}{3}\epsilon \right) \tag{2.14}$$

$$\epsilon = \frac{\omega_\perp - \omega_z}{\omega_0} \tag{2.15}$$

When $\epsilon > 0$ one axis is longer than the other two and the deformation is called prolate. Conversely when $\epsilon < 0$ one axis is shorter than the other two and the deformation is called oblate. In the Woods-Saxon potential β_2 is used to parameterise quadrupole deformation and is related to ϵ via

$$\beta_2 = \sqrt{\frac{\pi}{5}} \left(\frac{4}{3}\epsilon + \frac{4}{9}\epsilon^2 \right) \tag{2.16}$$

Introducing deformation removes the degeneracies usually associated with a spherical potential and there is now a preferential orientation. Also j_z, the component of the

angular momentum along the axis of symmetry is the conserved quantity, not total angular momentum J.

2.3.3 Refinements to Models

The core concepts of the Liquid Drop and Shell Models have been presented here. The point here is not to explain each of these in detail but to highlight the fact that several variants of these models exist [65, 66] and several refinements are made depending on the application.

One example is the Rotating Liquid Drop Model (RLDM) [25] which incorporates rotation in the LDM. Further to this, the work of Sierk [67] presents a macroscopic model for the energy of rotating nuclei with several refinements to the RLDM. Refinements made include the addition of finite-range effects in the nuclear surface energy, finite surface diffuseness effects in the Coulomb energy and in the rotational moments of inertia and an improved specification of nuclear shapes. Another example is seen in the work of Krappe [68] where the temperature dependence of the nuclear free energy was described using a finite-range mass formula. Subsequently Karpov et al [69] also used a generalized finite-range liquid-drop model (FRLDM) to describe the fission dynamics of hot rotating nuclei. The potential energy, level-density parameter and Helmholtz free energy are calculated using the generalized FRLDM. In the work of Zagrebaev et al [70, 71, 72] an extended version of the two-centre shell model is used to calculate the multidimensional adiabatic potential energy of a dinuclear system. This allows for a unified description of DIC, QF and FF.

Macroscopic models are used to generate a multidimensional potential energy surface (PES) that describes the energy landscape encountered by a dinuclear system. Dinuclear systems, formed via heavy-ion reactions, have significant excitation energy E* that is distributed into internal degrees of freedom that evolve dynamically. These include deformation, orientation, neck and shape degrees of freedom, among others. PES are coupled with fluctuation-dissipation calculations that account for the dynamic evolution of the system over the PES. This approach allows us to treat the various degrees of freedom dynamically. The Langevin approach [55, 56, 70, 71, 72] is one such example that has had considerable success in reproducing mass and energy distributions and predicting the timescales of heavy-ion reactions. This formalism has been used extensively to model

several reactions and make predictions for formation cross sections of SHE [73, 74].

In this work we do not focus on macroscopic approaches but instead use Time Dependent Hartree Fock (TDHF), a microscopic theory, to study the dynamics of a nuclear reactions and add to the wealth of existing theoretical knowledge. Chapter 6 presents a comparison between this microscopic model and experimental results. To the author's knowledge this is the first time a microscopic model has been used in an extensive way that mimics the macroscopic approaches described above.

2.3.4 Time Dependent Hartree Fock Formalism

A complete and rigorous explanation is covered in [75, 76]. The following is only a summary of the important points.

For the low energies studied here, we assume a non-relativistic regime and that we can ignore the internal structure of nucleons; i.e assume that they behave as fundamental particles with no internal quark structure. In this non-relativistic regime, quantum systems obey the Schrodinger equation:

$$i\hbar\frac{d\Psi(t)}{dt} = \hat{H}\Psi(t) \tag{2.17}$$

This equation can be solved exactly for simple cases such as the Hydrogen atom. Increasing the number of particles quickly makes the problem intractable and to apply it more generally we need to make some approximations. The Pauli principle for fermions must be satisfied. Due to this principle, most collisions are forbidden in the nuclear medium; an effect known as Pauli blocking. It increases the mean free path of a nucleon to the order of the size of the nucleus. Pauli blocking is the main justification for independent particle approaches such as TDHF, in nuclear physics. Starting from the Schrodinger Equation, applying it within the framework of the Skyrme interaction and assuming that the system is described by an independent particle state gives the TDHF equation, which in its Liouville form reads

$$i\hbar\frac{\partial\rho}{\partial t} = [h[\rho], \rho] \tag{2.18}$$

where ρ is the one-body density matrix of the system and $h[\rho]$ is the self-consistent

Hartree-Fock single particle Hamiltonian.

The TDHF equation was derived by Dirac in 1930 [77]. It describes the evolution of the one-body density of the system and provides a self-consistent mean-field evolution where the interaction between the particles is replaced by a one-body mean-field potential generated by all the particles. It is then assumed that each particle evolves independently in this potential. The system is assumed to be always described by an asymmetrised independent particle wave function (Slater determinant). This is to satisfy the Pauli principle during the time evolution of the system. The independent particle picture is valid in low energy nuclear reactions because in this case, the Pauli principle prevents nucleon nucleon collisions. The one-body density matrix ρ can be used to compute the expectation values of any one-body observable. It also describes the time evolution of the observable within the TDHF framework and therefore accounts for one-body dissipation mechanisms. These one-body dissipation mechanisms are believed to play a dominant role [75] in the reaction mechanisms of low energy nuclear reactions investigated here.

The one-body density matrix of an independent particle system can be written as:

$$\rho\left(\mathbf{r}sq,\mathbf{r}'s'q'\right)=\sum_{i=1}^{A_1+A_2}\psi_i^*\left(\mathbf{r}'s'q'\right)\psi_i\left(\mathbf{r}sq\right) \tag{2.19}$$

where ψ_i are single particle wave functions, A_1 and A_2 are the number of nucleons in each nucleus and $\mathbf{r}$, s and q denote the position, spin and isospin of the nucleons, respectively. The single particle HF Hamiltonian is self consistent and can be written as:

$$h\left[\rho\right]\left(\mathbf{r}sq,\mathbf{r}'s'q'\right)=\frac{\delta E\left[\rho\right]}{\delta\rho\left(\mathbf{r}'s'q'\right),\mathbf{r}sq)} \tag{2.20}$$

where E[ρ] is the Skyrme energy density functional (EDF) which describes the interaction between the nucleons. This has been adjusted to fit a few nuclear structure properties as reported in [78, 79] and is the only phenomenological input in TDHF.

The success of the Skryme EDF extends not only to spherical nuclei but also to deformed nuclei. Hartree-Fock calculations for spherical nuclei using Skyrme's density-dependent effective nucleon-nucleon interaction gave a very good description of ground-state properties of spherical nuclei [80]. In particular remarkable fits to binding energies, nuclear radii, and elastic electron scattering cross sections were obtained. In subsequent work [81] the

same set of values for the Skyrme interaction were found to give a satisfactory description of axially deformed nuclei and nuclear deformations.

Chapter 3

Experimental Methods and Instrumentation

This chapter details the experimental tools and techniques utilized in making fission fragment measurements around the Coulomb barrier. A pair of position sensitive, gas filled, MWPCs were used to make these measurements. This chapter details the production of heavy-ion beams from the 14UD tandem accelerator, experimental setup and supercomputing facilities used for theoretical work.

All experiments were conducted at the 14UD Heavy Ion Accelerator Facility at the Australian National University (ANU). All beams were provided by the 14UD tandem accelerator and one was further boosted by the superconducting LINAC. Concerted efforts were made to obtain high statistics and precise data for all measurements. The analysis procedure is described in Chapter 4 and the experimental results are presented in Chapter 5.

3.1 The 14UD Accelerator

All beams were produced at the Australian National University Heavy Ion Accelerator Facility using the 14UD Tandem Van de Graaff accelerator [82, 83]. The 14UD is a National Electrostatics Corporation (NEC) Pelletron accelerator [83, 84], which is currently capable of maintaining terminal voltages up to 15.5 million volts [82]. The layout of the 14UD accelerator and experimental area for these measurements is shown in Figure 3.1 and briefly described in the following sections. A detailed description of its operating principles

is covered in Refs.[86, 87]. The projectile ions undergo the following processes in the accelerator: negative-ion production, pulsing, acceleration in the tandem, post acceleration in the LINAC and transportation, after which they are directed onto a target foil where the nuclear reaction takes place. The basic operational principle of the 14UD involves subjecting negatively charged particles to a large electrostatic potential thus accelerating them.

3.1.1 Beam Production

The ion source located at the top of the 14UD tower is an NEC SNICS - Source of Negative Ions produced by Caesium Sputtering shown schematically in Figure 3.2. It produces negative ions by sputtering Caesium (Cs) onto a cathode and extracting them via a electrostatic potential difference.

A reservoir of Caesium heated to 100-120 °C produces Cs vapour. This vapour is transported, by a delivery tube typically maintained at 200 °C, from the reservoir to the enclosed region between the cathode and the ionizer. The cathode, housing a cylinder containing the source material, is cooled to 20°C. Some of the Cs vapour condenses onto the cool surface of the cathode, forming a neutral layer of caesium atoms, while some of the Cs comes in contact with the surface of the ioniser. The ioniser is usually a surface made of Tungsten (W) or Molybdenum (Mo) heated to a temperature of 1000 °C. Caesium vapour that comes in contact with the ioniser deposits an electron due to the higher electron affinity of W and Mo relative to Cs. The positively charged Cs ions that emerge from the ioniser are accelerated towards the cathode, sputtering source material from the cathode upon impact. The sputtered atom can pick up an electron while passing through the neutral caesium layer and forms a beam of negatively charged ions. The negative ions are drawn out of the SNICS by a 5 kV potential difference between the cathode and the positively biased extractor electrode.

Negative ions are extracted either as atomic ions or as molecular ions depending on the electron affinity of the source material. For beams of Carbon, Oxygen, Silicon and Sulfur, atomic ions were extracted owing to their relatively high electron affinities. Calcium and Magnesium, owing to their low electron affinity, are extracted as hydride ions, formed by introducing ammonia (NH_3) into the volume around the cathode.

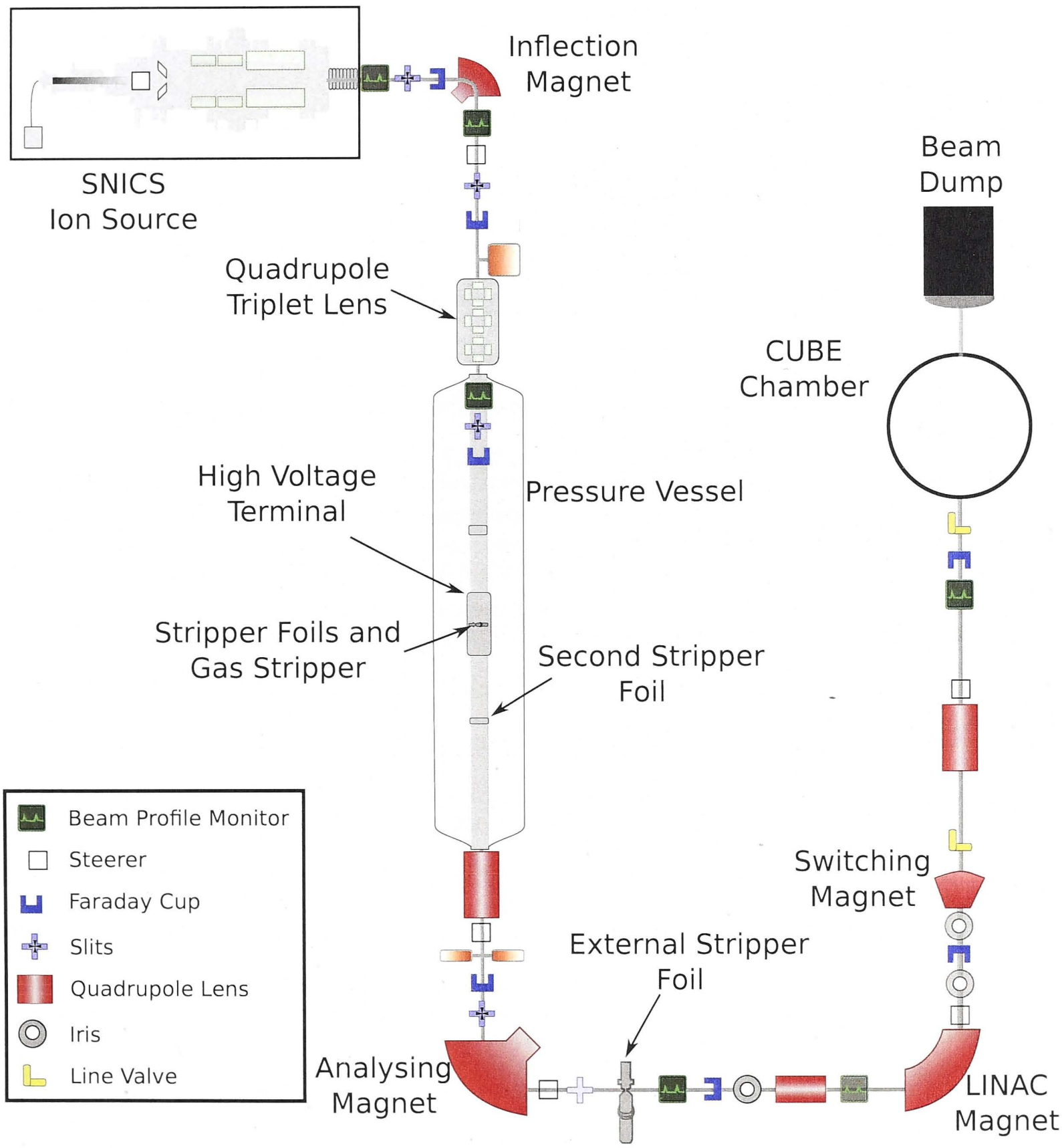

Figure 3.1: Schematic layout of the 14UD accelerator. Negative ions produced by the SNICS are injected into the accelerator after being deflected by the mass selection magnet. The singly charged ions are accelerated toward the positive terminal, where they pass through the stripper foil. Here electrons are stripped and the ions acquire a positive charge. The ions are accelerated a second time, away from the positive terminal, towards the ground potential, after which they are deflected by the analysing magnet which selects a specific charge state and defines the beam energy. If post acceleration using the LINAC is required, the LINAC magnet is set to degauss mode and the beam injected into the LINAC. The ions are finally guided via magnetic steerers and quadrupoles to the target chamber.

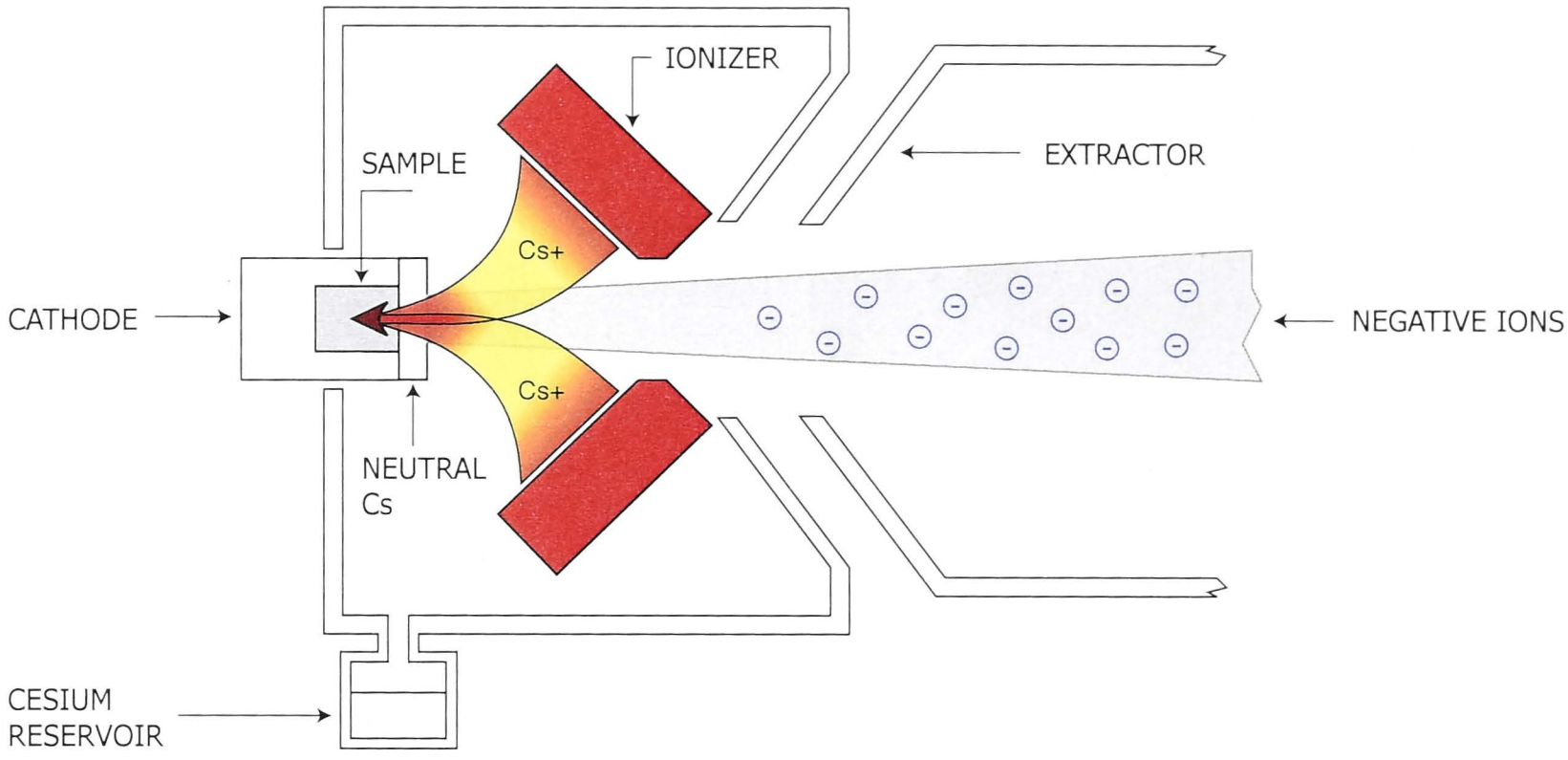

Figure 3.2: Schematic layout of SNICS. Positively charged caesium ions are focussed onto the cathode, sputtering the sample material on impact. The sputtered atoms pick up an electron while passing through the caesium deposited on the surface of the cathode, forming negatively charged ions. The ions are then extracted as a beam by a high voltage potential difference between the cathode and extractor.

3.1.2 Acceleration and Transportation

The negative ions produced by the ion source are accelerated across a 150 kV potential difference prior to being separated by mass using the 90° inflection magnet. The ions then enter the mass selection magnet where the magnetic field exerts a force, called the Lorentz force, on the moving ions. The resultant centripetal acceleration causes the ions to move in a uniform circle with radius r. As all ions have the same energy E and charge state q, the inflection magnet acts as a mass separator by bending ions of different masses through different radii. By adjusting the field strength, we can select the mass m of ions that are injected into the 14UD. The field setting B for the inflection magnet is given by:

$$B = \frac{\sqrt{2mE}}{rq} \tag{3.1}$$

Following injection, the ions undergo two stages of acceleration in the 14UD. The first stage of acceleration is from ground potential to the positively charged terminal at a voltage V_T (MV), during which the ions gain an energy equal to eV_T , where e the electronic charge of the ion is 1. Thus after the first stage of acceleration, for a given potential V_T at the terminal, the negative ions have an energy given by:

$$E = V_T + 0.150MeV \tag{3.2}$$

This static potential is provided by the Pelletron charging system consisting of three charging chains [84]. The charging chains are made of cylindrical metal pellets connected by insulating nylon links. At the base of the accelerator tube, the inductive charging system provides the pellets with a positive charge. The chains are then pulled towards the terminal by a pulley and motor system, and as each pellet leaves the terminal it provides a net positive charge, itself carrying away a negative charge. To prevent electrostatic discharge caused by the high potential and relatively small distance to the edge of the pressure vessel, the entire pressure vessel containing the terminal and charging system is filled with the insulating inorganic gas Sulphur Hexafluoride (SF_6) at a pressure exceeding 700 kPa or 6 bar. Biased corona discharge needles are utilized to modulate the charge on the terminal, and thus maintain precise terminal voltage.

Upon reaching the terminal, the negative ions pass through either a 4 μgcm^{-2} ^{nat}C stripper foil, or a gas filled stripper. Collisions with the stripper atoms remove electrons from the ions, resulting in a distribution of positively charged ions [88]. The charge state $\bar{q}$ is given by the semi-empirical formula for particles passing through solids [89, 90]:

$$\bar{q} = Z\left[1 + Z^{0.75}\left(3.86\frac{E}{A}\right)^{-1.67}\right]^{-0.6} \tag{3.3}$$

The beam then undergoes the second stage of acceleration from the positively charged terminal to ground potential. For charge state q_1 the energy gained by the ions during this phase of acceleration is $q_1 V_T$, with the beam having energy given by:

$$E = q_1 V_T + V_T + 0.150MeV \tag{3.4}$$

There exists a second ^{nat}C stripper foil assembly, a third of the distance between the terminal and the base of the pressure vessel, that can be used to attain a higher charge state distribution and thus a higher energy. Assuming a charge state of q_2 after this stripper, the energy is given by:

$$E = \frac{1}{3}q_1 V_T + \frac{2}{3}q_2 V_T + V_T + 0.150 \tag{3.5}$$

As the beam leaves the pressure vessel, a 90° analyzing magnet selects a specific charge state and hence the desired beam energy. The magnetic field of the analyzing magnet is measured using a sensitive nuclear magnetic resonance (NMR) probe. Setting the NMR frequency to a precise value allows selection of the correct beam rigidity. The relativistic relationship between the energy of the analyzed beam and the magnetic field is given by [91]:

$$E = KB^2 \left(\frac{q^2}{m}\right) \left(1 + \frac{E}{2mc^2}\right) \tag{3.6}$$

where K is the magnet constant. The latest calibration of the magnet constant was carried in 2008, using the ^{12}C(p,α)^{9}B resonance at 14.23 MeV, as described in Ref. [92]. The energy of the beam can be defined to better than 0.05 %. Thus for beam energies in the order of 100 MeV, the absolute beam energy is defined to ±50 keV.

The beam was transported in the beam lines using a system of beam optics that includes magnetic and quadrupole lenses, dipole magnets, magnetic steerers, slits and irises. Beam profile monitors (BPM) were used to check the shape of the beam, and Faraday cups to measure the beam currents. All of these were used to optimise and control beam intensity at the target. The beam energies and target combination are shown in the following section. The entire 14UD facility, including production, acceleration and transportation, is remotely controlled via a computer control system [93] and operated by the research staff and students.

3.1.3 The Superconducting LINAC

The LINAC increases the energy of heavy ion beams injected from the 14UD. It comprises 12 Split Loop Resonators (SLRs) housed in 4 separate cryostats. Figure 3.3 shows the layout of the facility. The LINAC magnet is common with the 14UD and is set to degauss mode to inject the beam from the 14UD into the LINAC. First, the superbuncher employs a Quarter Wave Resonator (QWR) to bunch the beam to 100ps FWHM. The beam is then deflected through 90 degrees by an achromat comprising a symmetric arrangement of 2 magnetic quadrupole triplets, 2 dipoles and a quadrupole singlet at the midpoint [94].

The 4 cryostats each house 3 lead plated SLRs manufactured by Applied Superconductivity Incorporated (ASI). They operate at or above a potential gradient of 2 MV/m

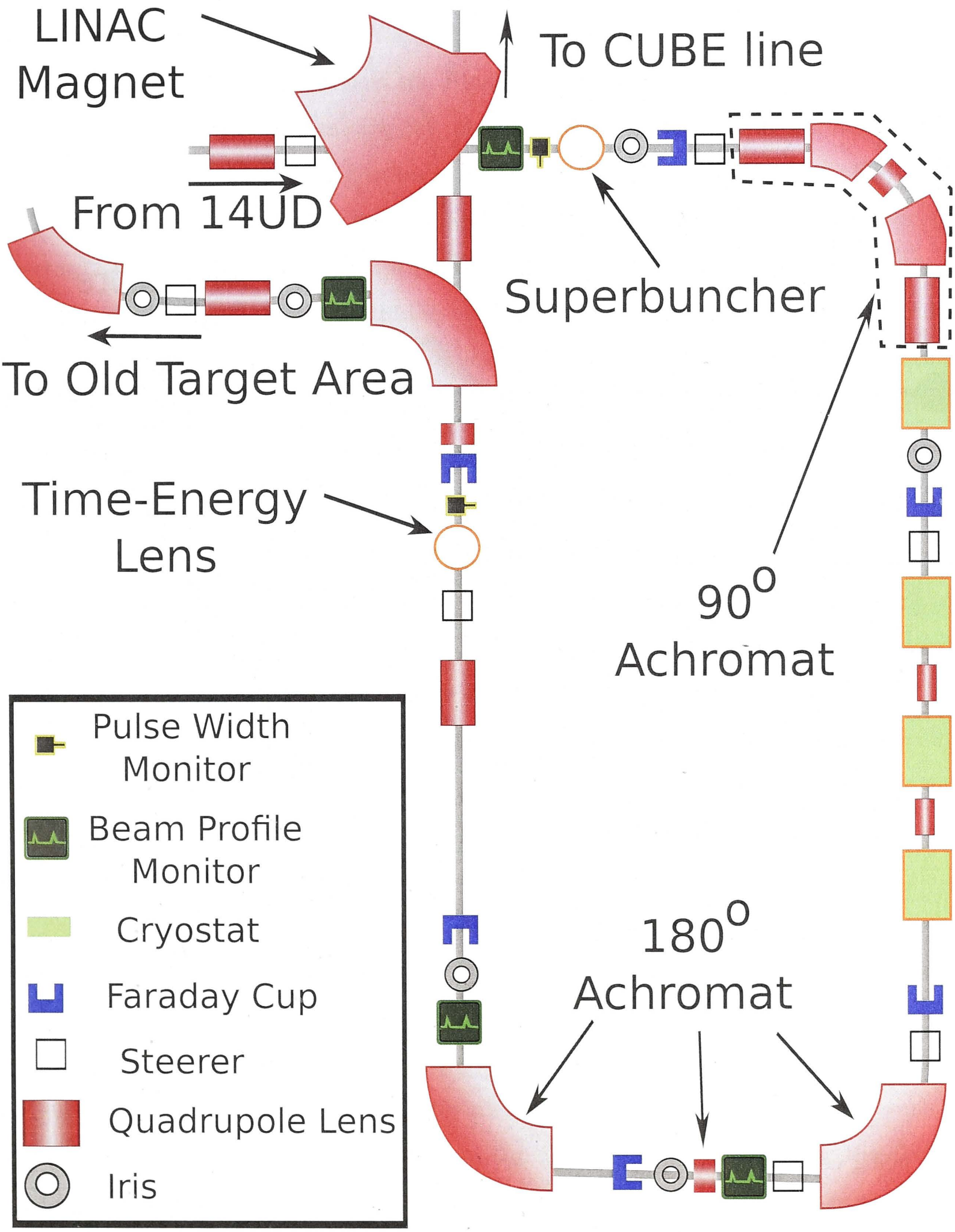

Figure 3.3: Schematic layout of the superconducting LINAC. Beams accelerated by the 14UD are injected into the LINAC, where they are rebunched by the superbuncher, boosted by superconducting SLRs and bunched again by the Time-Energy Lens before being directed to the target chamber.

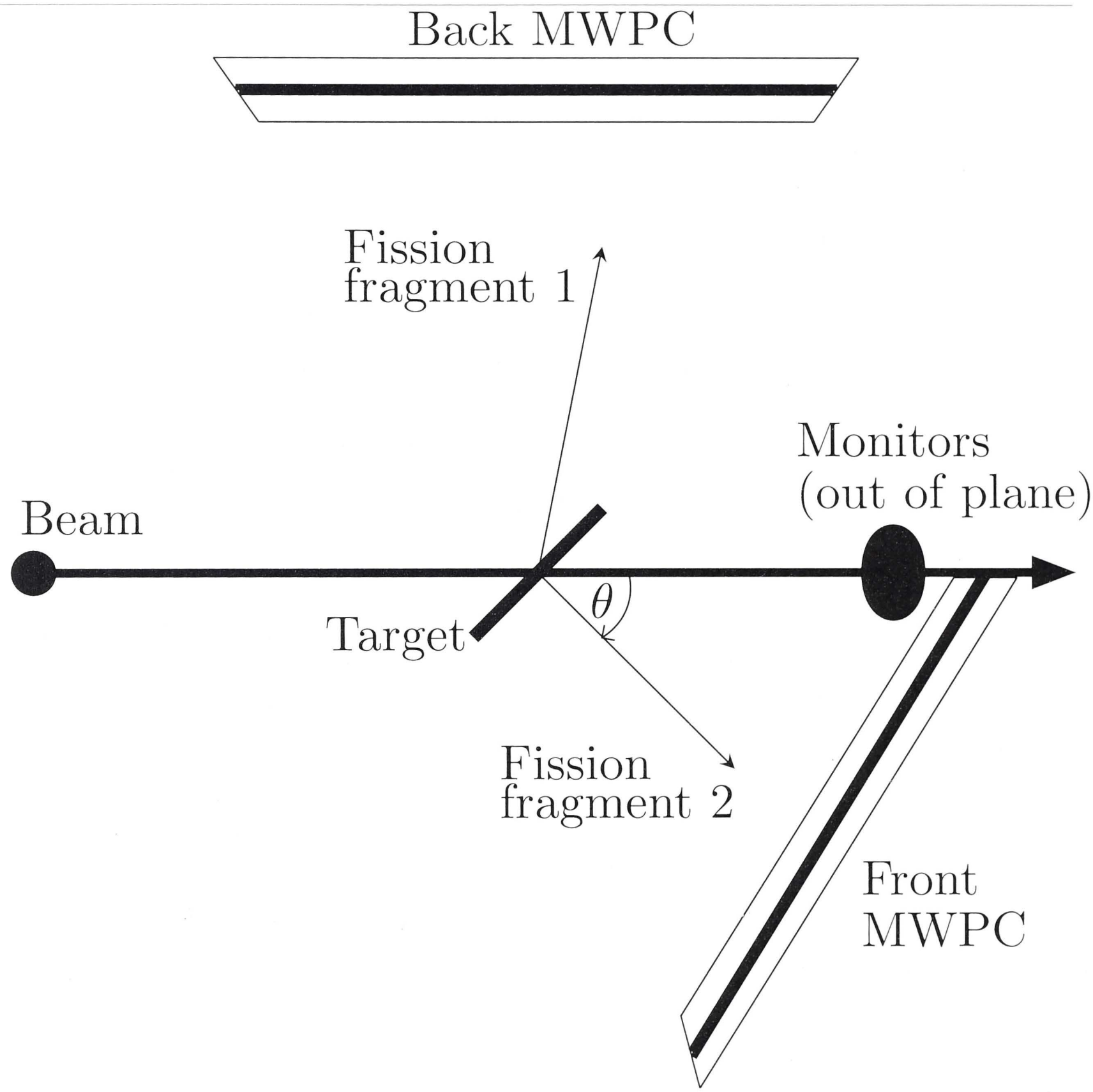

Figure 3.4: Typical configuration of the MWPCs used in the experiments.

after being conditioned in house at the ANU. The energy gain from these 4 modules is about 6 MeV/q, where q is the charge state of the injected heavy-ion. There is room for an additional two cryostats for future expansion. The LINAC accelerated beam is then deflected by a 180 degree achromat and directed back towards the beam line with the CUBE chamber displayed in Figure 3.1. The final beamline in the LINAC loop houses the Time-Energy Lens [95], a superconducting QWR. It rebunches the beam to provide good time resolution of the post-LINAC beam.

3.2 The Detector System: CUBE

All experiments were carried out in the CUBE scattering chamber. This is a multi-purpose vacuum chamber, which also houses the Breakup Array, a Si detector array, utilised for measurements of break-up fragments [96]. During operation the chamber is maintained at a vacuum of $2*10^{-5}$ Torr using a turbo pump at the base of the chamber. At the centre of the chamber sits a target ladder which can hold up to 7 targets and a 2 mm diameter aperture. The aperture is used to optimise the beam shape and position at the center of the target. It is placed in the path of the beam and the current on a suppressed Faraday cup, downstream from the chamber, is optimised by adjusting the steering and focusing units on the beam line. The target is flanked by two large-area (28.4 X 35.7 cm^2) position sensitive multi-wire proportional counters (MWPCs). Fission fragments were detected using these detectors, typically arranged as depicted in Figure 3.4.

The principle of operation of a MWPC is based on the interaction of charged particles with gases. As a charged particle enters the gaseous inter-electrode space of a MWPC, it loses a small fraction of its energy and ionises the gas. The degree of ionisation depends on the atomic number, mass and energy of the charged particle and the density and ionisation potential of the gas. In the absence of an electric field, the free electron-ion pairs that are produced rapidly lose their energy in collisions with gas molecules and assume a Maxwellian velocity distribution. The electrons and ions taking part in this random thermal motion diffuse away from the high ionization density region created along the path of the incident charged particle. Subsequently, the positive ions may neutralize through recombination of the electron-ion pair or by charge transfer in collisions with neutral gas molecules, while the free electrons form negative ions by interacting with the neutral gas molecules. Such events suppress the ionization process and information about the incident charged particle is lost. Applying a voltage between the electrodes results in a net drift motion of the ions and electrons. The electrons are accelerated by the electric field to a high velocity, causing a localised cascade of ionisation. This is collected on the wires and results in an electric current proportional to the energy loss of the incident particle.

Each MWPC consists of two planes of gold coated tungsten wires that provide position sensitivity. The X and Y planes are made up of 284 vertical and 357 horizontal wires, respectively. The wires are 20 μm in diameter and are spaced at 1 mm intervals. The two

planes are each 3 mm from the center foil. Each wire of the X and Y planes is connected to a 1 ns tap of a 10-tap passive delay chip, and all chips are connected in series. This delay line system provides a position resolution of 1mm. The center foil (cathode) of each MWPC provides the timing and energy-loss (ΔE) signals. The cathode is made of a 0.9 μm sheet of Mylar, coated on both sides with 40 μgcm^{-2} Au. In order to reduce the capacitance of the center foil it is divided into 4 quadrants. The centre electrode is biased with a voltage of typically 500 V. The volume of each MWPC was filled with propane to a pressure of 4 Torr and the purity of the gas is maintained by a gas flow system. The entrance window for each detector consisted of a 0.9 μm copper coated Mylar foil. The coating reduces the diffusion of gas from the detector and the build up of charge on the window. A grid of three horizontal and four vertical stainless steel wires of 0.45 mm diameter reduces the bowing of the window towards the target due to the 4 Torr pressure differential.

By design, the MWPCs can be mounted vertically in the CUBE chamber in 3 different positions such that the detectors are centered at one of three angles $\theta = 45°, 90°$ or $135°$ in the laboratory frame. The mount points were designed such that each MWPCs timing foil was 18.0 cm from the target centre. In principle we can mount 4 MWPCs, 2 at forward angles and 2 at backward angles. However, in practice we only use one forward and one backward MWPC. Each detector provided a coverage of 75° in scattering angle θ.

Measurements of all reactions used the detector configuration shown in Figure 3.4, with the front MWPC centered at $(\theta, \phi) = (45°,0°)$ and the rear MWPC centered at $(\theta, \phi) = (90°,180°)$. There was only a subtle difference in the positioning of the rear MWPC for some experiments. The detection area of the MWPCs is not symmetric in X (corresponding to θ). As a result, the back detector had an angular coverage of $\theta = 50°$ to $125°$ (labelled a in Table 3.1) for some experiments and $\theta = 55°$ to $130°$ (labelled b) for others.

A pair of silicon surface barrier detectors (monitors), placed at $\theta = 22.5°$ $\phi = 90°, 270°$, were used to measure the elastically scattered beam particles for elastic normalization and absolute cross-section determination. An electronic scheme of the system is included in Appendix B.

3.2.1 Position and Time Calibration

The raw position and timing information obtained from the MWPC detectors is used to calculate the velocity vectors of the fission fragments. The position and time calibration is described below while the determination of the velocity vectors using the Kinematic Coincidence method is described in the next chapter.

Position Calibration

To calibrate the position data, full coverage of the front and back MWPCs was recorded separately by collecting data in singles mode. This allows us to relate the raw channel numbers (figure 3.5) with the corresponding physical edges of the detectors and thus determine the (x, y) positions. The physical dimensions of the detectors and the position of the mid-points are known from the mount points in the CUBE chamber. These are used to convert the (x, y) positions to (θ, ϕ). The angular calibrations are checked by comparing measured elastic folding angles and (θ, ϕ) distributions with their calculated (and expected) values. Note that the angle calibration runs were recorded in singles but for the actual measurements there was a coincidence requirement.

Time Calibration

In Chapter 4 we describe the determination of the absolute time-of-flight (ToF). Before this can be done we need to calibrate the output of the timing electronics. Specifically, we require a calibration coefficient to convert the raw output, in channels, to a time, in nano seconds. The calibration of the TAC was done using an Ortec 462 time calibrator to produce pulses separated by 10 ns. This results in a time spectrum that consists of discrete peaks with a temporal separation of 10ns. The position of each peak in channels was used to calculate a scaling factor between the raw channels and time in nano seconds.

3.2.2 Timing Glitch Correction

During some of the measurements (^{34}S,^{28}Si,^{24}Mg and ^{40}Ca induced reactions) the TACs associated with the MWPC time signals behaved erratically. The output gain fluctuated randomly during data acquisition and due to this the timing information from the detectors needed to be corrected. The shifting gain is seen as abrupt changes in the response of

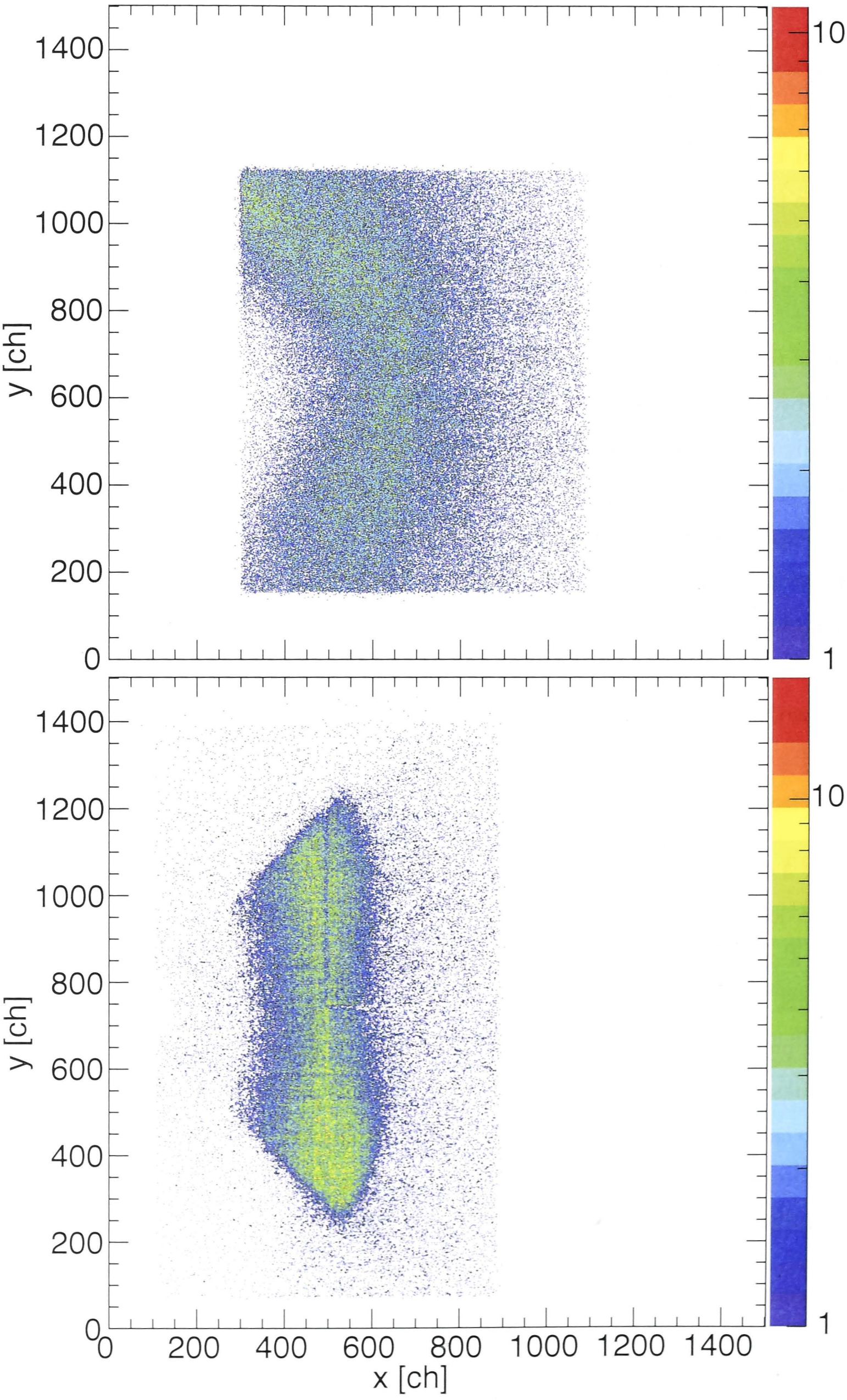

Figure 3.5: A spectrum of the raw position signals from the Back MWPC(top panel) and Front MWPC(bottom panel) showing the detector edges.

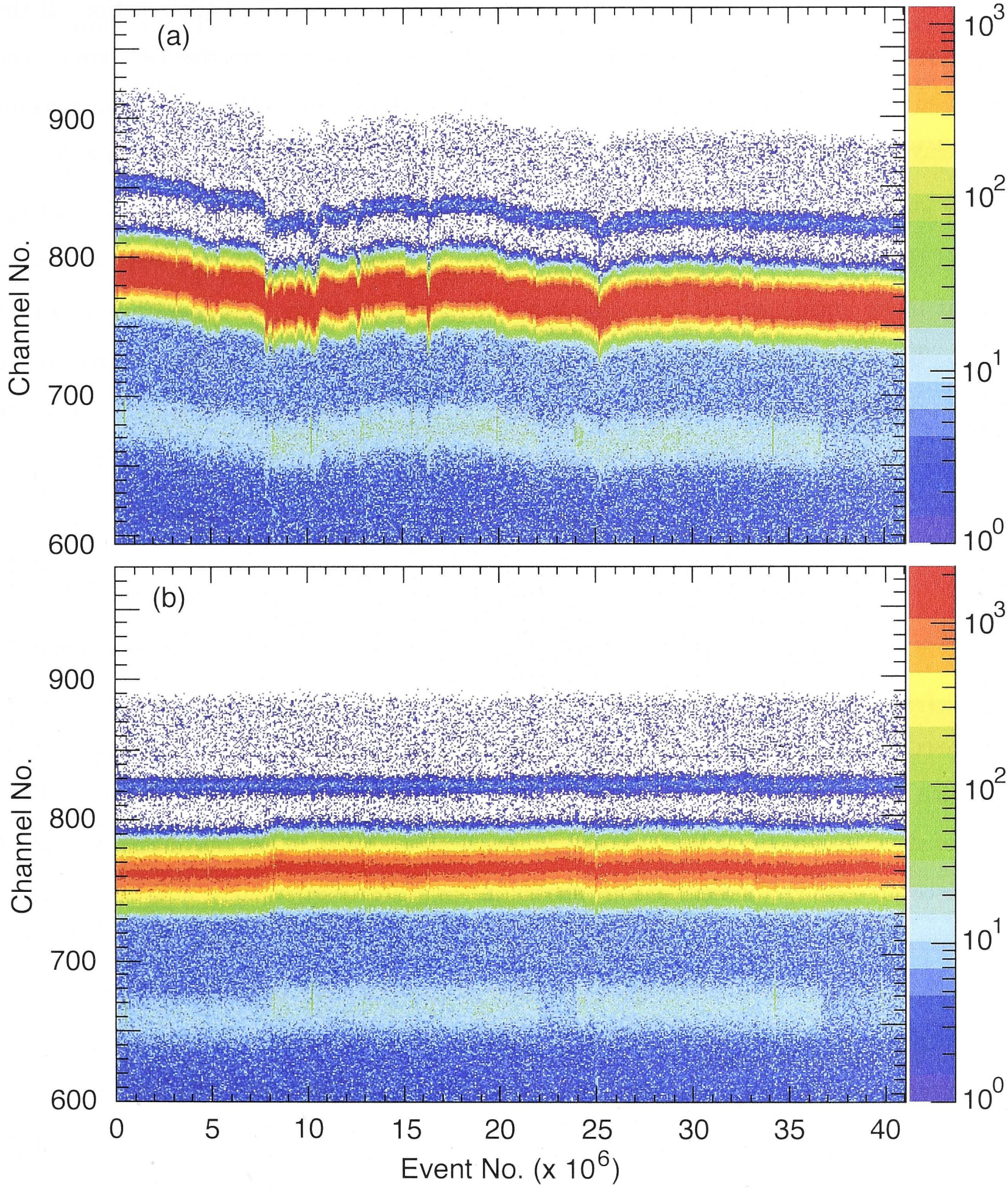

Figure 3.6: (a) A spectrum of the raw timing signal from the Back MWPC as a function of event number. (b) The time spectrum from the Back MWPC as a function of event number after accounting for the TAC gain drift.

the detectors as a function of event number as seen in Figure 3.6(a). The intense group seen below channel 800 corresponds to elastically scattered beam particles. The narrower distinct group around channel 850 is the pulser.

To correct for the drifting gain, we exploited the fact that the position of the pulser

in the time spectrum is expected to be constant and independent of the reaction. If the pulser position shifts then we assume that there has been a shift in the TAC gain. The expected value of the pulser was fixed by examining runs close to the calibration runs for the delay line readouts of the MWPCs. In the example shown this was channel 825.

For a given block of events we average over the pulser counts. If the average is within a fixed threshold (typically 2-3 channels) of the expected value then we leave all events in that block unchanged. If it is outside the fixed threshold we shift every event in that block. The magnitude of the shift is not constant. It is scaled linearly, relative to the pulser position, such that events below the pulser have a smaller scaling than those above it. The shift for a given block of events can be written as:

$$\Delta t_{MWPC} = \frac{pulser_{deviation}}{pulser_{expected}} * t_{MWPC} \tag{3.7}$$

where $pulser_{expected}$ is the expected value of the pulser, $pulser_{deviation}$ is the deviation of the pulser from the expected value and t is the channel number of the event being processed. Figure 3.6(b) corresponds to the same measurement shown in Figure 3.6(a) but with the shifting gain now corrected for. The pulser peak is stable. The shift in the time of the detected particles is caused by small phase shifts in the beam arrival time at the detector, caused, for example, by sparks in the 14UD.

3.2.3 The Experiments

In total we measured 8 reactions, with several calibration runs using targets of ^{208}Pb and ^{197}Au done during the measurements. In total 7 unique beams were accelerated, 6 using only the 14UD, and 1 using the 14UD in conjunction with the superconducting LINAC. Energies ranged from sub-barrier to above the barrier, as presented in Table 3.1. The barrier $V_{B,c.m.}$ referred to here is the average Coulomb barrier determined using the systematics of Swiatecki in [97]:

$$V_b = 0.85247z + 0.001361z^2 - 0.00000223z^3 MeV \tag{3.8}$$

where z is the Coulomb parameter:

Table 3.1: The range of beam energies for the reactions of interest. The columns correspond to the reaction, scaled Coulomb barrier (in the centre-of-mass frame - see text), range of energies measured (in the centre-of-mass frame) and detector geometry.

Reaction	$V_{B,c.m.}$ (MeV)	Energy (MeV)	geometry
$^{12}C + ^{238}U$	60.59	57.9 - 74.8	b
$^{18}O + ^{232}Th$	77.97	73.1 - 87.5	b
$^{24}Mg + ^{238}U$	119.74	110.8 - 142.6	a
$^{30}Si + ^{232}Th$	135.71	129.2 - 147.8	b
$^{28}Si + ^{238}U$	139.34	127.9 - 156.6	a
$^{34}S + ^{232}Th$	154.79	143.9 - 167.0	a
$^{40}Ca + ^{232}Th$	193.77	185.9 - 224.6	a
$^{40}Ca + ^{238}U$	197.3	186.6 - 225.4	a

$$z = \frac{Z_1 Z_2}{\left(A_1^{\frac{1}{3}} + A_2^{\frac{1}{3}}\right)} \tag{3.9}$$

Targets of 200 μgcm^{-2} ^{238}U, 80 μgcm^{-2} ^{232}Th and 80 μgcm^{-2} ^{208}Pb were evaporated onto 15-20 μgcm^{-2} ^{nat}C backings, while the 250 μgcm^{-2} ^{197}Au targets were self-supporting. The gold and thorium targets were made up of elemental material. For the lead targets, sulphide was used due to the higher melting point compared to elemental Pb (1114°C for PbS versus 327°C for Pb), allowing them to better withstand exposure to the incident beam without degradation. For the uranium targets, fluorides (UF_4) of ^{238}U were used. The targets were oriented with their normal at 60° with respect to the beam axis, with their backing facing downstream to minimise energy loss of the fission fragments detected in the rear MWPC.

Apart from sulphur, fluorine and the carbon backing, other light impurities may also be present in the targets. Reactions with these light impurities are above-barrier for all the measured beam energies, resulting in fusion evaporation residues travelling in the forward direction, thus giving little or no contribution to coincidence fragments at backward angles. Any small contribution is removed from the final results using the gates described in Chapter 4.

General Measurement Practice

During all experiments a few general protocols were followed to ensure consistency between measurements:

- Before each run the MWPCs were properly mounted in the CUBE chamber mount points, to ensure they were positioned and aligned as described above.

- The vacuum in the CUBE chamber was maintained at a pressure of 10^{-7} Torr during operation.

- A pulser was sent through to the MWPCs, triggered by signals from one of the monitor detectors, to monitor the system dead time. It also served a useful purpose in allowing us to correct for the unexpected TAC gain drift.

- Events were only recorded when events in the front counter came in coincidence with a trigger signal from the back counter. The trigger condition on the back counter was to limit counting rates. The front MWPC, being at angles close to the beam, was exposed to elastically scattered beam particles and thus triggering on this would result in a high count rate, in excess of the capacity of the data acquisition system. Fission fragment measurements were done with a hardware based multiplicity-2 requirement. Only calibration measurements were carried out in singles mode (no multiplicity requirement).

- For most of the experimental runs the count rate was limited to below 2000 Hz, by adjusting the beam intensity using irises.

- The elastic counts from the monitor detectors, were pre-scaled by a factor of 10 to 100 to limit the count rate. The pulser was triggered by the pre-scaled monitor events.

3.3 Supercomputing Facilities used

During the theoretical and computational work done in this thesis, two supercomputers were used to run the TDHF3D [98] code.

3.3.1 Vayu

One of the systems used was a high-density integrated cluster called VAYU, based on a Sun Microsystems Sun Constellation System. It is hosted at the National Computational Infrastructure National Facility (NCI-NF), located at the Australian National University in Canberra, Australian Capital Territory. As of November 2012 it was ranked 24th in world and the best in Australia. A summary of its specifications follows [99]:

The system comprises 11,936 Intel Xeon 2.93 GHz - Nehalem series CPUs in 1492 nodes in Sun X6275 blades. These provide a peak performance of 140 TFlops, a sustained performance of 250K Standard Performance Evaluation Corporation floating point (SPECfp) rate and total user resources of 110M hours per annum. The memory system consist of 24GB DDR3-1333 memory, 24GB Flash DIMM for swap and job scratch space. The system has a total of 36.9TB of RAM on computing nodes and 835 TBytes of user storage. Power consumption of the full 11936 CPU system is 605 kW, all from green energy sources [99, 100].

3.3.2 Mercure

The other system used was an SX-8 supercomputer called MERCURE hosted at the Centre de Calcul Recherche et Technologie (CCRT) at Commissariat *à* l'énergie atomique et aux énergies alternatives (CEA) in Saclay, France [101]. The SX-8 is a supercomputer built by Nippon Electric Company (NEC Corporation). The system comprises 4,096 Intel Xeon X5570 2.93 GHz CPUs in 512 nodes. It has a peak performance of 65 TFlops and the system has a total of 35.6TB of RAM on computing nodes and 400 TBytes of user storage.

Chapter 4

Mass-Angle Distributions (MADs)

4.1 Mass Angle Distributions and Nuclear Reactions

Mass Angle Distributions are a useful tool for studying and understanding heavy ion reactions. To understand what they are and how they arise we need to first visualise how a nuclear reaction between two heavy ions proceeds. Figure 4.1 (left panel) illustrates the evolution of the dinuclear system in a classical physics interpretation. The nuclei are drawn to be spherical liquid drops with no diffuseness or other quantum properties.

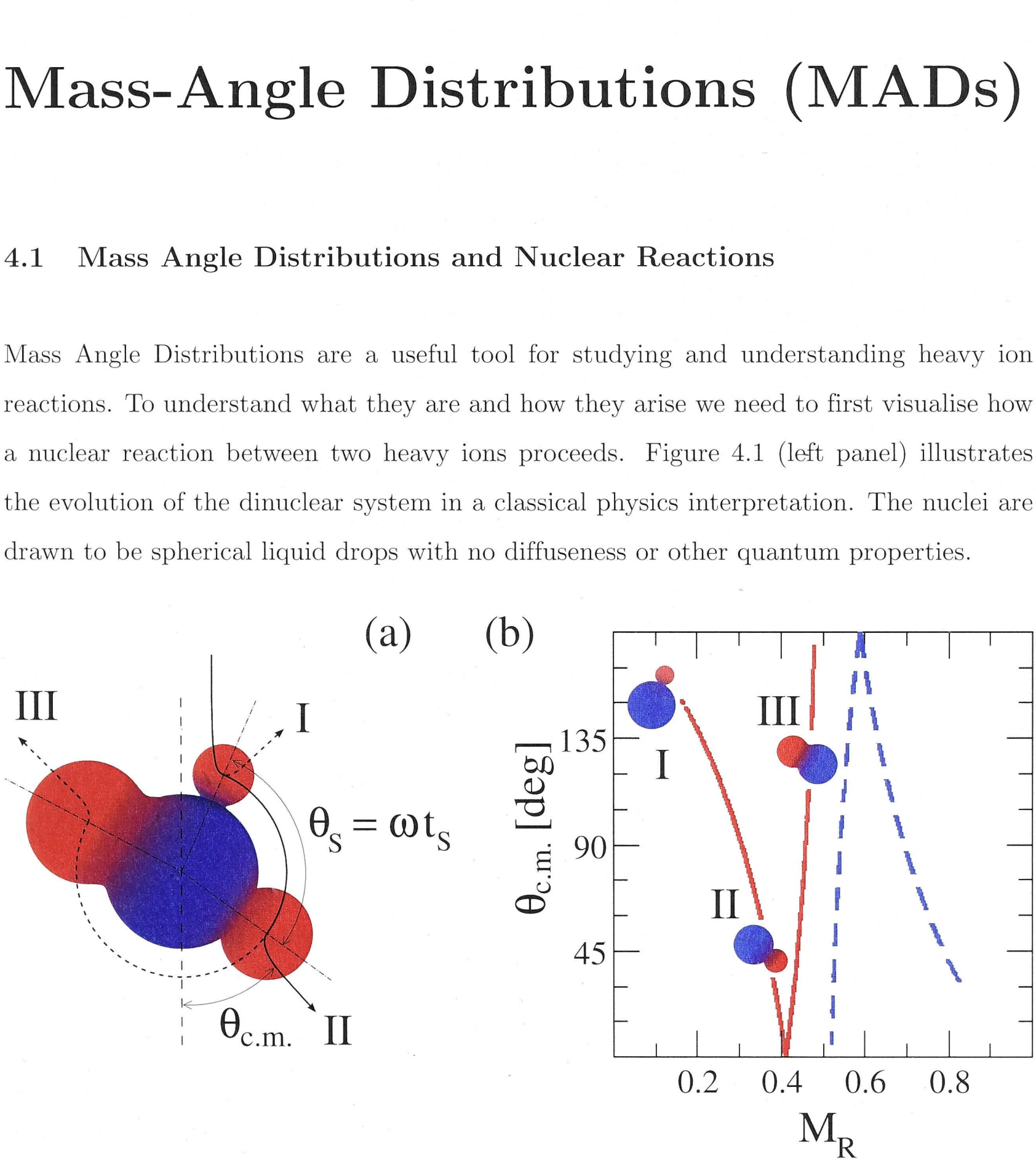

Figure 4.1: Schematic illustration of the evolution of a di-nuclear system. a) Three different quasi-fission outcomes (I to III) depending on reaction lifetime (τ) and rotation speed (ω). b) Corresponding expected MAD illustrating the correlation between emission angle ($\theta_{c.m.}$) and mass ratios (M_R).

The projectile nucleus (red) is incident from above and after contact with the target nucleus (blue) forms a dinuclear system. For non-central collisions this system will begin rotating due to the angular momentum conservation. As the system rotates the two nuclei exchange mass and on average, mass flow occurs from the heavy to the light fragment. The system is taken to approach mass-symmetry ($M_R = 0.5$) asymptotically with a characteristic time dependence proportional to $1 - exp(-t/\tau)$ [16, 26]; where τ is the characteristic mass-equilibration time constant.

After a time t the angle it rotates through is θ_S, as indicated in figure 4.1. If scission occurs soon after initial contact (label I) the system rotates through a small angle θ_S. Little mass is exchanged and the projectile-like fragment is ejected at backward angles ($\theta_{c.m.} > 90°$) with the corresponding target-like fragment ejected at forward angles ($\theta_{c.m.} < 90°$). If the dinuclear system stays intact for a bit longer before scission, it rotates through a larger angle and more mass is exchanged. Points II and III depict this.

The expected MAD for this di-nuclear evolution is shown in the right panel of figure 4.1. The three distinct cases explained above (I to III) have been placed at their corresponding mass ratios (M_R) and angles ($\theta_{c.m.}$). A long lifetime, where the system completes more than one rotation will destroy the correlation between mass and angle, resulting on average in symmetric mass splits independent of angle. The corresponding points in the MAD will have a uniform and narrow mass distribution about $M_R = 0.5$, for all angles.

MADs allow us to distinguish between reactions labelled I, II and III very clearly because of the significant differences in M_R and $\theta_{c.m.}$. However if scission takes place at time scales longer than those corresponding to III this distinction can no longer be made. Thus we see that the MAD technique is extremely sensitive to the shortest reaction time scales and insensitive to longer reaction timescales.

Quasifission in reactions forming heavy elements occurs on short timescales, $\leq 10^{-20}$ s [16, 35], fusion fission or CN fission, occurs on timescales $> 10^{-20}$ s to 10^{-16} s [35, 45]. Thus we see that the MAD technique is extremely sensitive to mass asymmetric quasifission (point I). It is also sensitive to more mass symmetric quasifission which shows up as a characteristic correlation between mass and angle (point II). Fusion fission is also observable in MADs but we cannot distinguish between different timescales for this process due to the uniform distribution in $\theta_{c.m.}$ (point III onwards). Elastic scattering, by its nature of having a well defined mass with a small width, shows up as a distinct group

at extreme mass ratios. Deep inelastic scattering will slightly broaden this group.

From this description it is clear that we can differentiate between several different reaction outcomes by accurately measuring the mass and angle of reaction fragments.

4.2 Determination of M_R

The determination of the angles θ and ϕ is explained in Chapter 3. Determining the mass ratios M_R of the fission fragments is a more involved process that requires an accurate determination of the fragment velocity vectors. The laboratory frame fragment velocity vectors are determined using the position information together with the ToF measured with respect to the pulsed beam. The analysis procedure described only works under the assumption of binary kinematics and this assumption is satisfied by selecting binary events via very specific gates. This section describes all of these steps of the analysis procedure.

4.2.1 Kinematic Coincidence Method

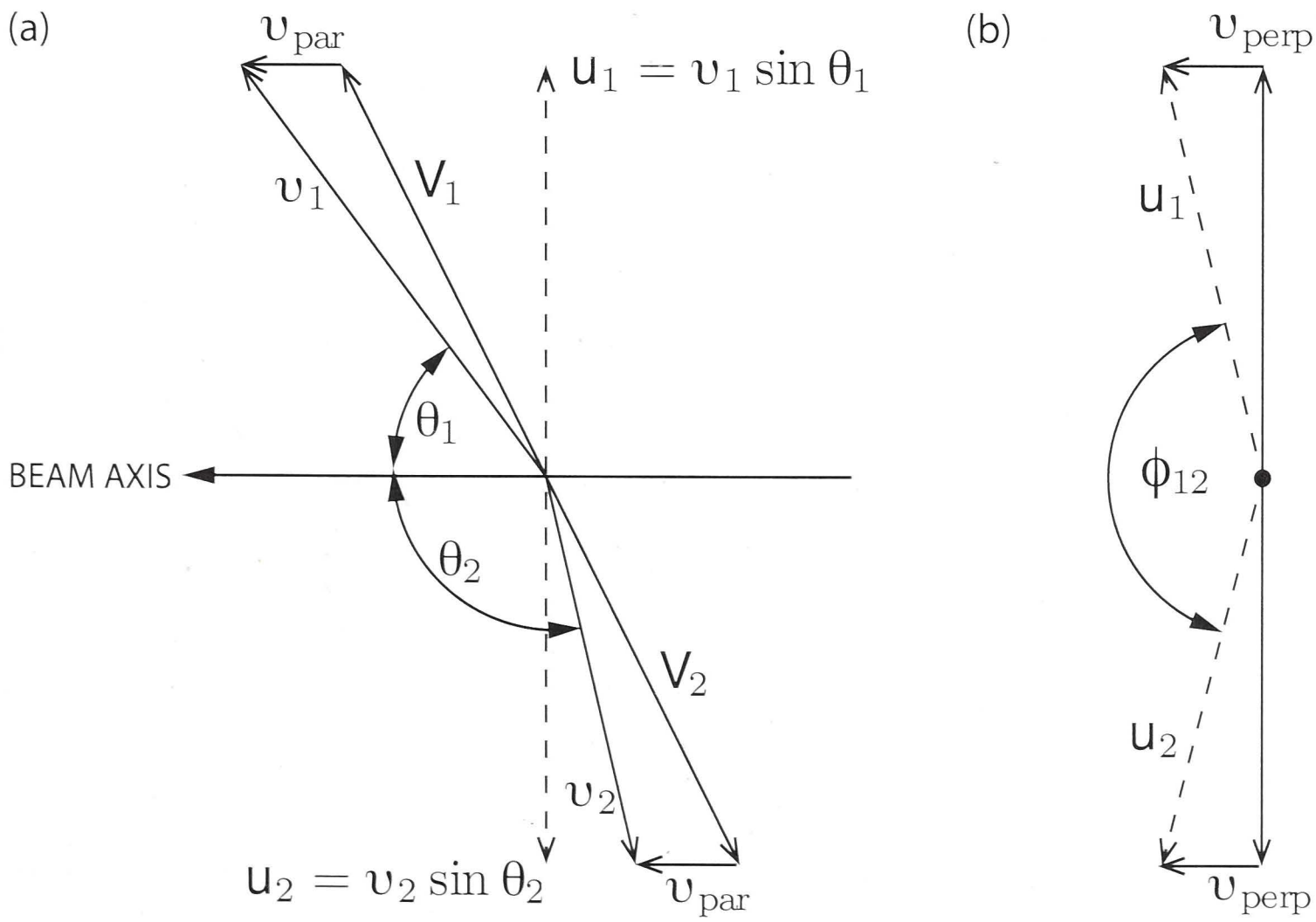

Figure 4.2: Diagram of the geometry used to describe the fission fragment velocities. a) View of the plane parallel to the beam axis and b) perpendicular to the beam axis.

The analysis procedure employed to determine M_R is called the Kinematic Coincidence

Method. Figure 4.2 depicts the geometric convention [36] used in this analysis. The coordinate origin is defined as being at the centre of the target. The scattering angles θ_i are measured with respect to the beam direction and the azimuthal angles ϕ_i are measured with respect to the forward detector. Note that we define velocity vectors and their components in two distinct planes, one parallel to the beam axis and one perpendicular to the beam axis. The centre-of-mass components are only relevant in the plane parallel to the beam. The components in the plane perpendicular to the beam are identical in the laboratory frame and center-of-mass frame since the beam has no momentum component in this plane.

The laboratory frame velocity vectors of the two fragments v_i are defined in spherical polar coordinates. The parallel and perpendicular components of v_i with respect to the beam axis are labeled v_{par} and v_{perp} respectively. The velocities of the fragments in the centre of mass frame (within the plane parallel to the beam axis) are labelled V_i. In the centre of mass frame the two fission fragments are emitted back to back, as shown in figure 4.2(a). Within the plane parallel to the beam axis (figure 4.2(a)) the measured velocity vectors v_i are decomposed into their parallel and perpendicular components with respect to the beam axis as follows:

$$w_i = v_{||,i} = v_i cos\theta_i \tag{4.1}$$

$$u_i = v_{\perp,i} = v_i sin\theta_i \tag{4.2}$$

Full momentum transfer fission (FMT) refers to when the projectile is completely captured by the target and followed by fission. For such events we assume that the velocity vectors of the two fission fragments are coplanar with the beam axis. This assumption of a well defined reaction plane is equivalent to assuming $v_{perp} = 0$. The component perpendicular to the scission plane (depicted in figure 4.2 part (b)) is determined from u_i and the azimuthal folding angle ϕ_{12} via:

$$v_{perp} = \frac{u_1 u_2 sin\phi_{12}}{\sqrt{u_1^2 + u_2^2 - 2u_1 u_2 cos\phi_{12}}} \tag{4.3}$$

This value deviates only slightly from zero for light particle emission. In the reactions

measured we expect only light particles such as neutrons, protons and α to be evaporated from the nuclei either before fission or from the fission fragments. These cause only a slight broadening of the velocity distributions. Thus the assumption of planar kinematics is sound for FMT events. The only events that cause a significant deviation from $v_{perp} = 0$ are transfer (or sequential) fission. In this case the assumption of binary kinematics and planar geometry break down but, as will be seen, we exclude these events via gates.

The fragments will be emitted in opposite directions in the centre of mass frame. If we neglect the small effects of pre-scission particle evaporation the ratios of their velocity components will remain constant:

$$\frac{u_1}{w_1 - v_{par}} = -\frac{u_2}{w_2 - v_{par}} \tag{4.4}$$

The minus sign arises from the fact that u can only be positive, unlike w which can be positive (for $\theta_i < 90°$) and negative (for $\theta_i > 90°$). Rearranging for v_{par} gives:

$$v_{par} = \frac{u_1 w_2 + u_2 w_1}{u_1 + u_2} = \frac{v_1 v_2 sin(\theta_1 + \theta_2)}{v_1 sin\theta_1 + v_2 sin\theta_2} \tag{4.5}$$

which for FMT events at near-barrier energies will be equal to the calculated centre of mass velocity v_{cn} for CN fission. This value is determined from momentum conservation:

$$v_{CN} = 1.389\sqrt{\frac{E_{lab}}{A_P}}\frac{A_P}{A_P + A_T} cm/ns. \tag{4.6}$$

Using these velocities we can now determine the mass ratio of the fission fragments. The mass ratio M_R is defined as the mass of fragment 2 with respect to the total mass of the system:

$$M_R = \frac{A_2}{A_1 + A_2} \tag{4.7}$$

Historically M_R has often been determined from momentum conservation in the plane perpendicular to the beam:

$$A_1 u_1 = A_2 u_2 \tag{4.8}$$

Combining equation 4.7 and 4.8 gives:

$$M_R = \frac{\frac{A_1 u_1}{u_2}}{A_1 + \frac{A_1 u_1}{u_2}} \tag{4.9}$$

which simplifies to:

$$M_R = \frac{u_1}{u_1 + u_2} \tag{4.10}$$

However, light particle emission (α, beta and neutron) perturbs the fission fragment vectors and results in a spread of v_{par} values. At values of θ_i around 90° this spread in velocity is small compared to the perpendicular velocities $v_{\perp,i}$ (u_i). This spread becomes more significant as the values of θ_i approach 0° and 180° and can severely affect the deduced mass ratio. To avoid this problem we instead use momentum conservation in the centre of mass frame [36]:

$$A_1 V_1 = A_2 V_2 \tag{4.11}$$

giving:

$$M_R = \frac{V_1}{V_1 + V_2} \tag{4.12}$$

This dictates the need for an accurate determination of the fragment velocity vectors of both fission fragments.

The instrumental resolution of the detector system, in terms of M_R is typically 0.018 which is equivalent to a mass of 4-6 amu. That is, the FWHM of the smallest resolvable peak is $M_R = 0.018$.

4.2.2 Determining Fragment Velocities

The fragment velocity vectors are determined using geometrical position information and the calibrated time-of-flight (ToF) measured with respect to a pulsed beam. The velocity vectors of the two fragments can be determined if the flight path and the absolute ToF between the target and the detectors are known. The RF reference signal used to pulse

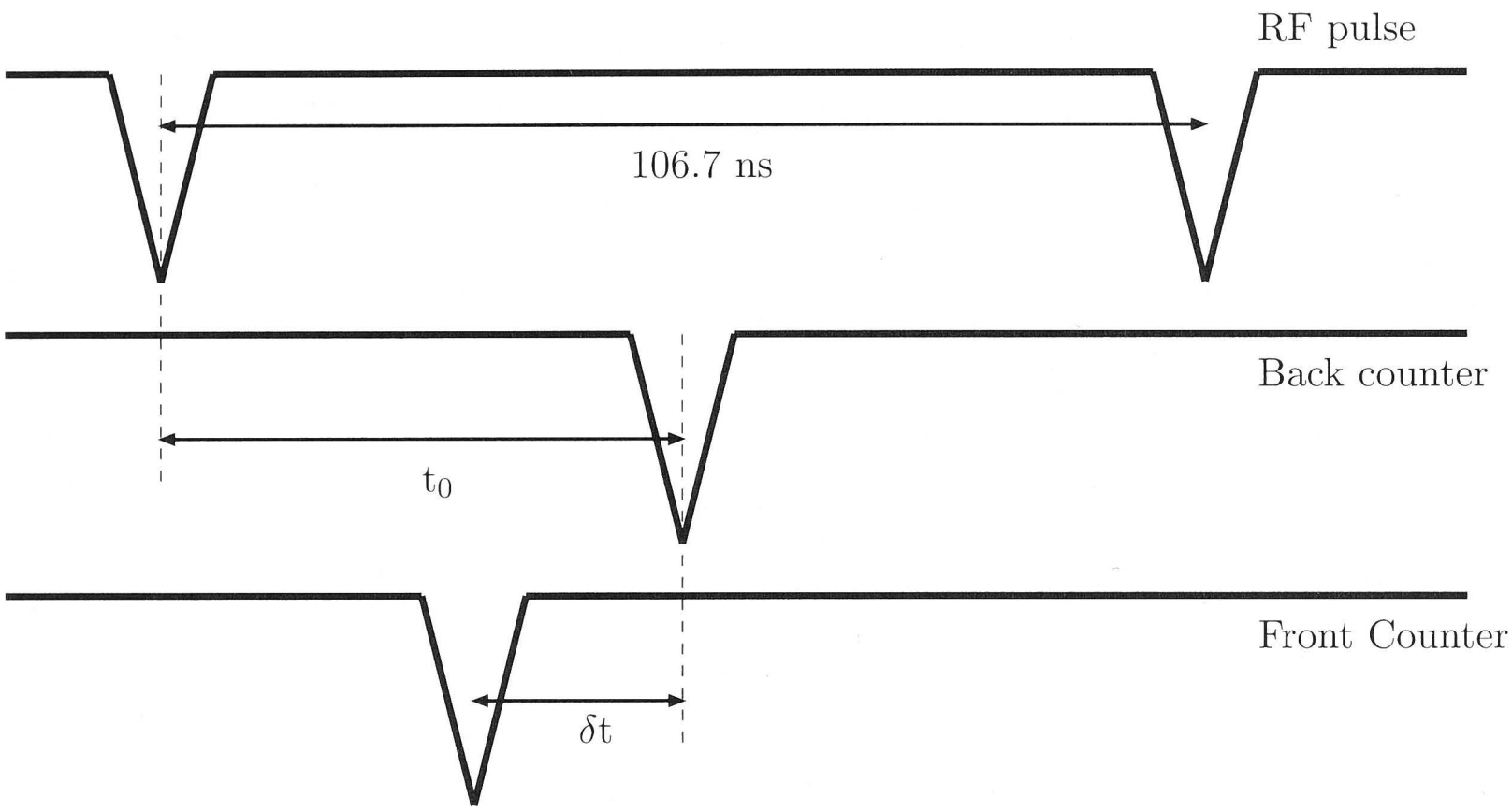

Figure 4.3: Illustration of the various signals associated with the RF pulsing and time-of-flight (ToF) system. The RF signal generated by the 14UD electronics has a spacing of 106.7ns. The ToF is measured with respect to the RF signal. t_0 is the time delay between the RF pulse being generated and the trigger signal from the rear MWPC. δt is the electronic time difference between the two MWPCs.

the beam was therefore also supplied to the data acquisition system to allow for a time measurement. Calibrating the TOF requires the optimisation of two parameters t_0 and δt.

Figure 4.3 is a diagram of the ToF system and associated time intervals. The RF signals are generated at intervals of 106.7ns. After a finite time the beam pulse arrives at the target and a fragment detected in the rear MWPC triggers the acquisition system. t_0 characterises the time between the RF reference signal being generated and the beam pulse arriving at the target. t_0 is dependent on the transmission time of the beam through the accelerator and the beam lines. Therefore it will be dependent on the beam species and energy.

At energies near the barrier we can neglect pre-equilibrium particle emission and the parallel velocity of the fragments v_{par} is expected to match the calculated centre-of-mass velocity for FMT events v_{CN}, as defined in equation 4.6 of section 4.2.1. t_0 was optimised based on this condition.

δt is a constant electronic delay between the two MWPCs and it is independent of beam energy. It arises due to differences in cable lengths and transmission times of the electronic signals of the two MWPCs. δt is optimised by requiring that the mass ratio distribution of binary fission fragments be symmetric about $M_R = 0.5$ at $\theta_{c.m.} = 90°$.

We do not expect δt to vary significantly between runs. We expect a minor variation as the temperature of the associated electronic systems varies but this will be a slow and gradual drift. A major variation was observed in some experimental runs due to an electronic glitch in the timing units of the acquisition system. After correcting for this glitch as described in section 3.2.2 the value of δt_0 varied only slightly (less than 0.2 ns) within any given experiment.

4.2.3 Event Selection

The Kinematic Coincidence Method described in section 4.2.1 is only applicable to binary events. A deviation from binary events violates the assumption of planar kinematics and any such events need to be eliminated from the data to produce reliable mass distributions. We employ a specific set of gates to eliminate any events that violate this assumption and select out only binary events.

Velocity Gates

Reactions with fissile targets such as ^{238}U and ^{232}Th produce a significant flux of transfer fission or three body fission events. These events generally have a non-zero v_{perp} component. The target like nucleus undergoes fission after a transfer reaction. Thus the fission fragments arising from the target like nucleus will generally not be emitted in the initial reaction plane.

The mass ratio of such events can no longer be accurately determined using the Kinematic coincidence method since the assumption of binary kinematics and planar geometry breaks down. Therefore these events are removed from the data by setting an appropriate gate on the fragment velocity vectors. Their elimination is an important step in the analysis procedure because their MAD will interfere with the MADs for reactions of interest (see figure 4.9 where the overlap with the region of interest is very apparent).

Figure 4.4 shows the velocity distributions for the ^{34}S + ^{232}Th reaction at the highest

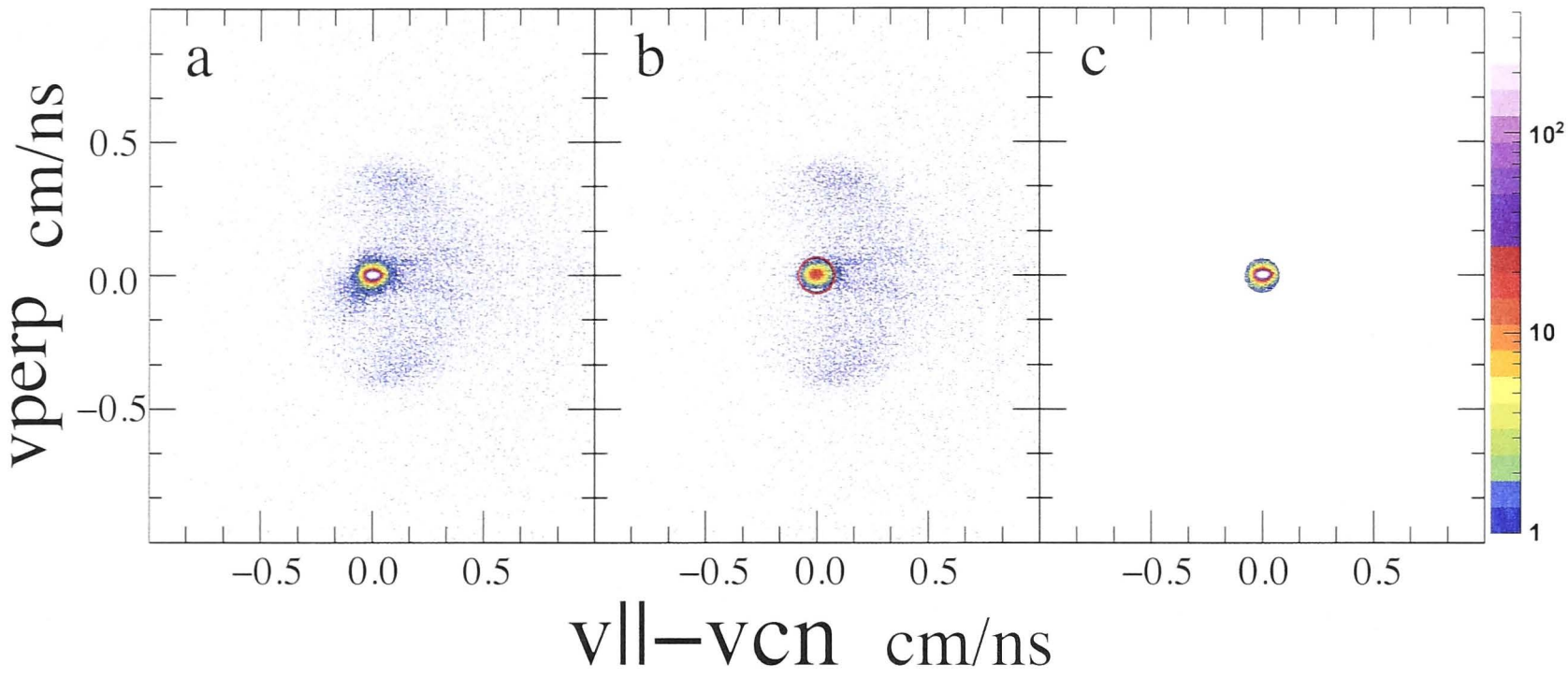

Figure 4.4: Velocity distributions for the highest energy measured in the ^{34}S + ^{232}Th reaction. The three panels correspond to a) Raw, ungated distribution b) the distribution between M_R=0.15 and 0.85; and c) Final, with velocity gate.

energy measured. Each panel corresponds to different gating conditions. Panel (a) shows the raw, ungated distribution. Panel (b) shows the distribution for events between 0.15 $< M_R <$ 0.85 (this removes the elastic scattering events). The intense group of events at $v_{perp} = 0$ and $v_{par} - v_{cn.} = 0$ are FMT events. In both panels (a)-and (b) the three body events can clearly be seen as a 'disc' like structure for $v_{perp} \neq 0$ and $v_{par} - v_{cn} > 0$. To eliminate them we apply an elliptical gate on the velocities centered at ($v_{par} - v_{cn}$,v_{perp}) = (0,0) cm/ns with radius ($v_{par} - v_{cn}$,v_{perp}) = (0.08,0.07) cm/ns. This is drawn in red in panel (b). Panel (c) shows the velocity distribution produced by applying this elliptical velocity gate. Note that this distribution is for events between $0 < M_R < 1$.

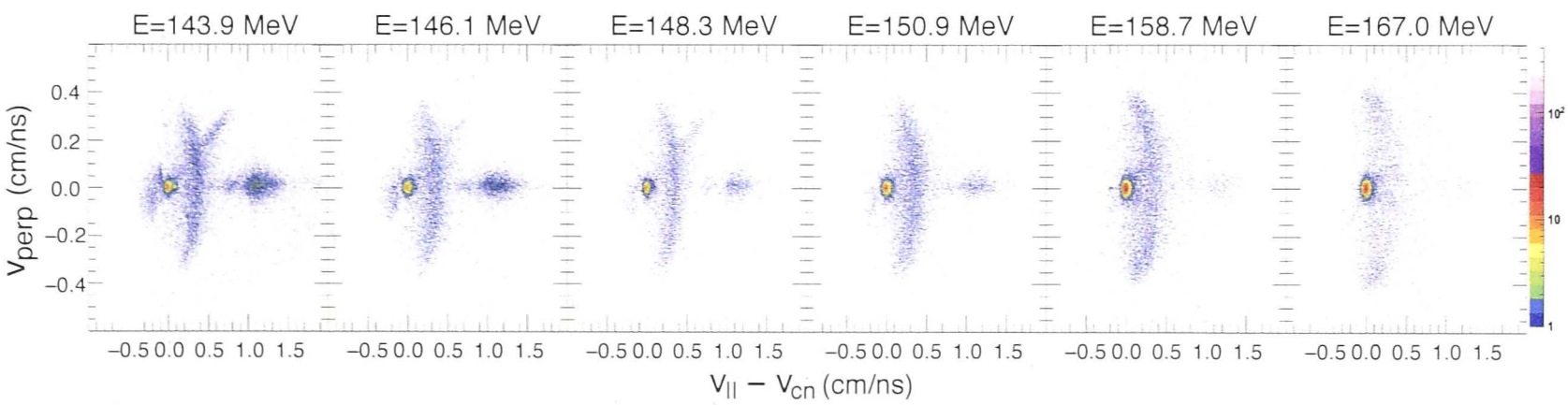

Figure 4.5: Velocity distributions at all energies measured for the ^{34}S + ^{232}Th reaction. v_{perp} is plotted relative to the calculated centre-of-mass velocity as $v_{par} - v_{cn}$. FMT fission events lie at v_{perp},$v_{par} - v_{cn} = 0$. The three body events can be clearly seen in the region $v_{perp}, v_{par} - v_{cn} \neq 0$.

Figure 4.5 shows the velocity distributions for the ^{34}S + ^{232}Th reaction for all measured energies. These are the raw ungated velocity distributions. The events forming a diagonal at $v_{perp} > 0.02$ and $v_{par} - v_{cn} > 0.02$ are correlated with a high counting rate and are

eliminated with the gate on $(v_{par} - v_{cn}), v_{perp}$. Note that figure 4.5 has a larger range for both axes when compared to figure 4.4. This is to show the events at $v_{perp} > 0.5$ cm/ns, which are due to reactions with the ^{12}C backing.

Total Kinetic Energy Gates

Figure 4.6 (top panel) shows the Relative Total Kinetic Energy (RTKE) (TKE normalised to the Viola systematics: $TKE = 0.1189 Z_{CN}^2 / A_{CN}^{\frac{1}{3}} + 7.3\ MeV$ [102]) distribution as a function of mass ratio prior to any gating. The plot shown here corresponds to the highest energy measured (like the distributions in figure 4.4 and the right most panel in figure 4.5). The elastics form an intense group around $M_R \approx 0.15$ and the fissions form a clear group centred just above $\frac{TKE}{TKE_{Viola}} = 1$. The group of events at $\frac{TKE}{TKE_{Viola}} > 2$ and $0.2 < M_R < 0.8$ are the three body events

Figure 4.6 (bottom panel) shows the RTKE distribution after the application of the elliptical velocity gate. This gate eliminates the majority of the three body events but a few are still present at $\frac{TKE}{TKE_{Viola}} > 2$. These three body events get past the velocity gate due to the fragments having a small but non zero probability of being emitted at $v_{par} - v_{cn} = 0$. This is evident from the trend seen at the highest energies in figure 4.5. As the beam energy increases the value of $v_{par} - v_{cn}$, for three body events, approaches 0. These events are eliminated via the RTKE gate shown in figure 4.6 (bottom panel). This gate on RTKE also serves to eliminate any tail of the elastic events that extends to low RTKE values. At lower beam energies these events can extend into the QF mass region in the MADs.

4.2.4 Angular Coverage

Figure 4.7 shows the typical angular coverage, in θ and ϕ, of the backward MWPC. This serves to highlight the fact that the coverage is uniform in ϕ. Note that the data were collected in coincidence mode.

4.3 Three Body Event Separation

For collisions with ^{238}U and ^{232}Th targets, three body events originate from the fission of an excited target or target-like nucleus. They correspond to collisions where a few

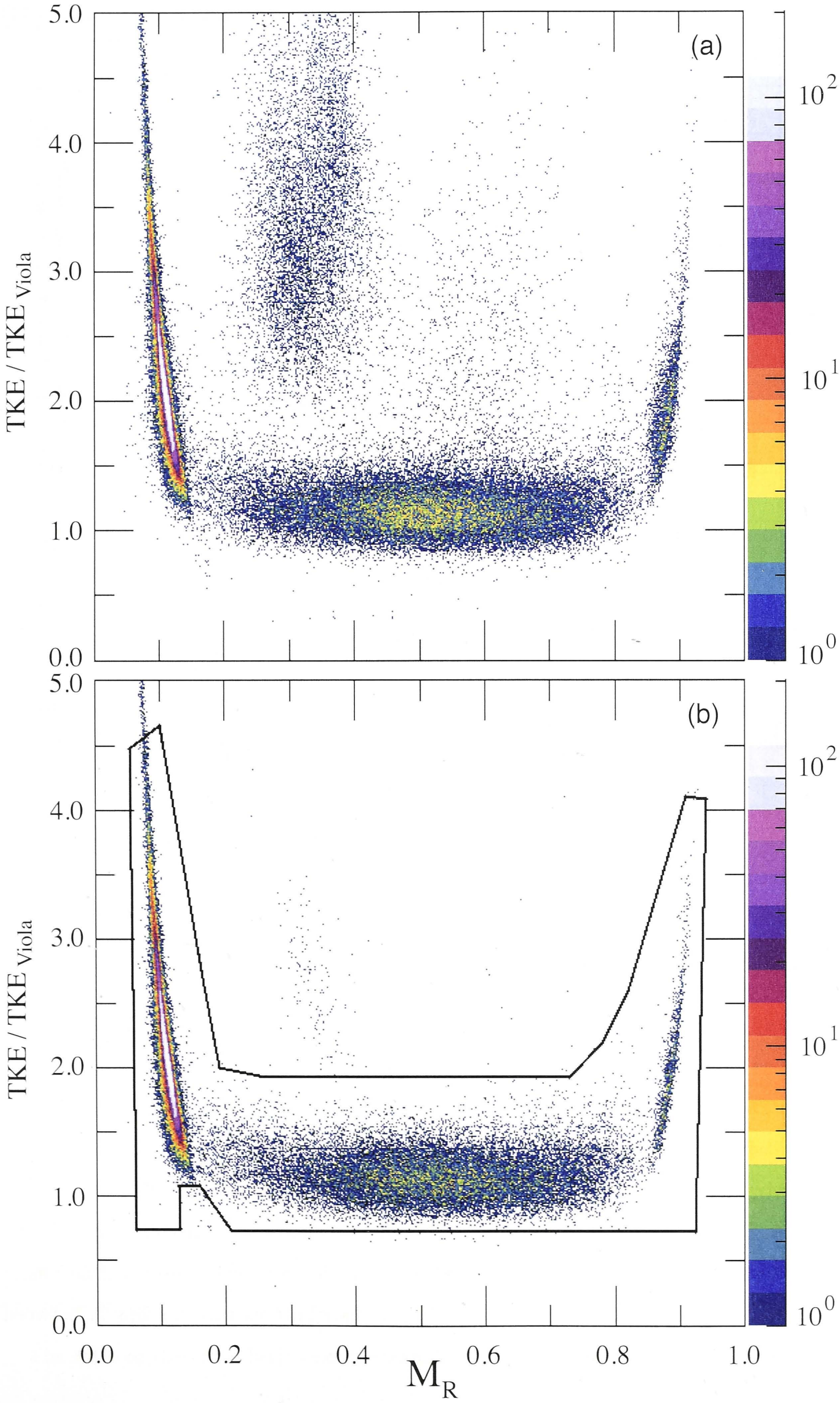

Figure 4.6: Relative Total Kinetic Energy ($\frac{TKE}{TKE_{Viola}}$) vs. M_R distribution for the ^{34}S + ^{232}Th reaction. The top panel shows the raw, ungated plot. The bottom

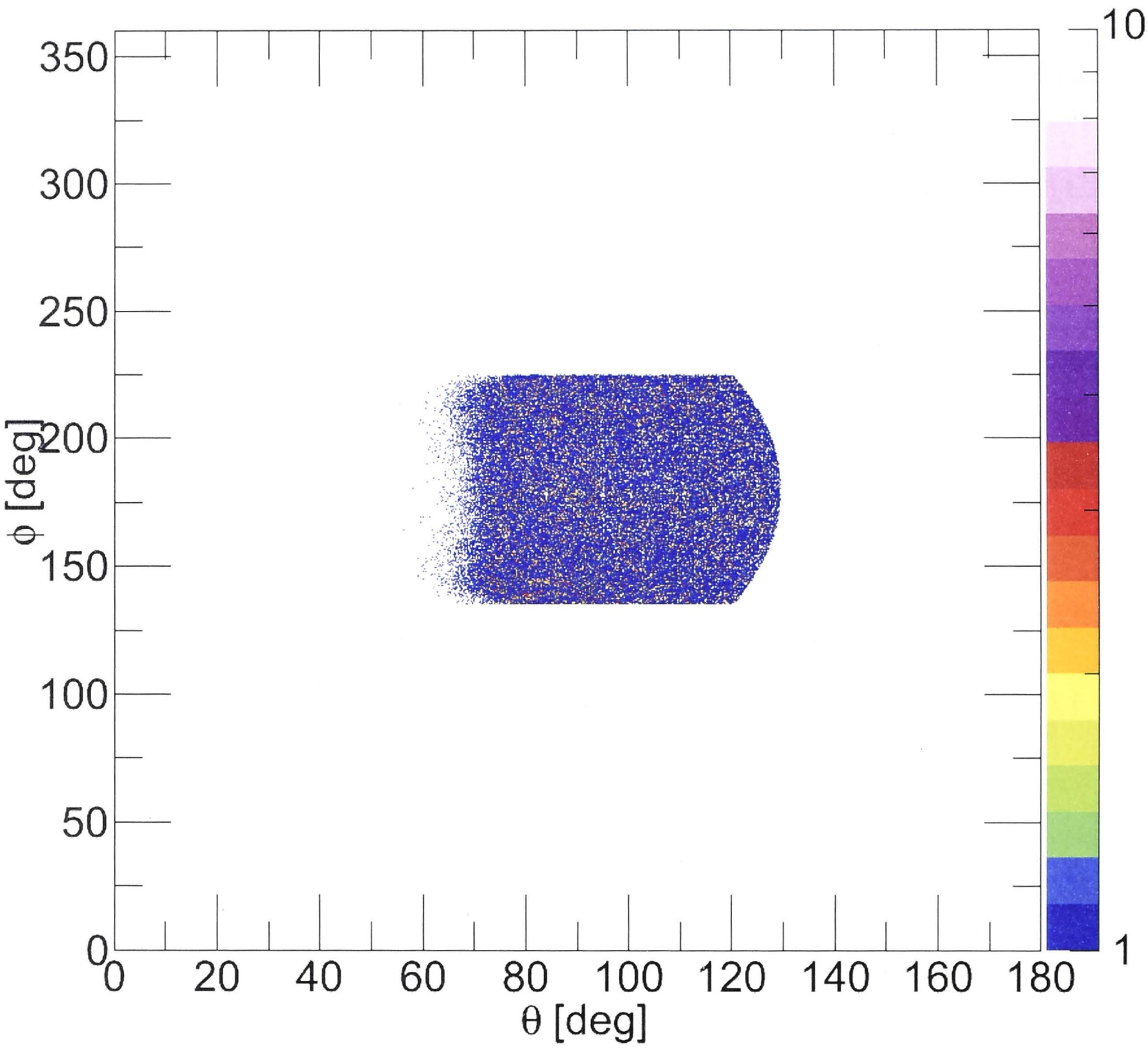

Figure 4.7: Angular coverage of the backward MWPC in coincidence mode.

nucleons are transferred to the projectile from the target. The heavy (^{238}U-like or ^{232}Th-like) nuclei, being in the actinide region, have a small fission barrier. In these partly of fully energy damped collisions, the energy deposited is enough to cause the target-like fragment to undergo fission. This fission of the heavy fragment, prior to detection by the MWPCs, leads to the three body flux. These events lie in the mass region between the mass-asymmetric quasifission peak at $M_R \approx 0.75$ (see figure 5.21) and the elastic peak at $M_R \approx 0.86$. If a large fraction of the three body events arise from events that correspond to mass-asymmetric quasifission, then the valleys seen around $M_R \approx = 0.2$ and 0.8 could very easily be filled and the distinct mass-asymmetric peak will no longer be evident. We would instead see 'U' shaped mass distributions with no dips in between the mass-asymmetric QF peaks and elastic peaks.

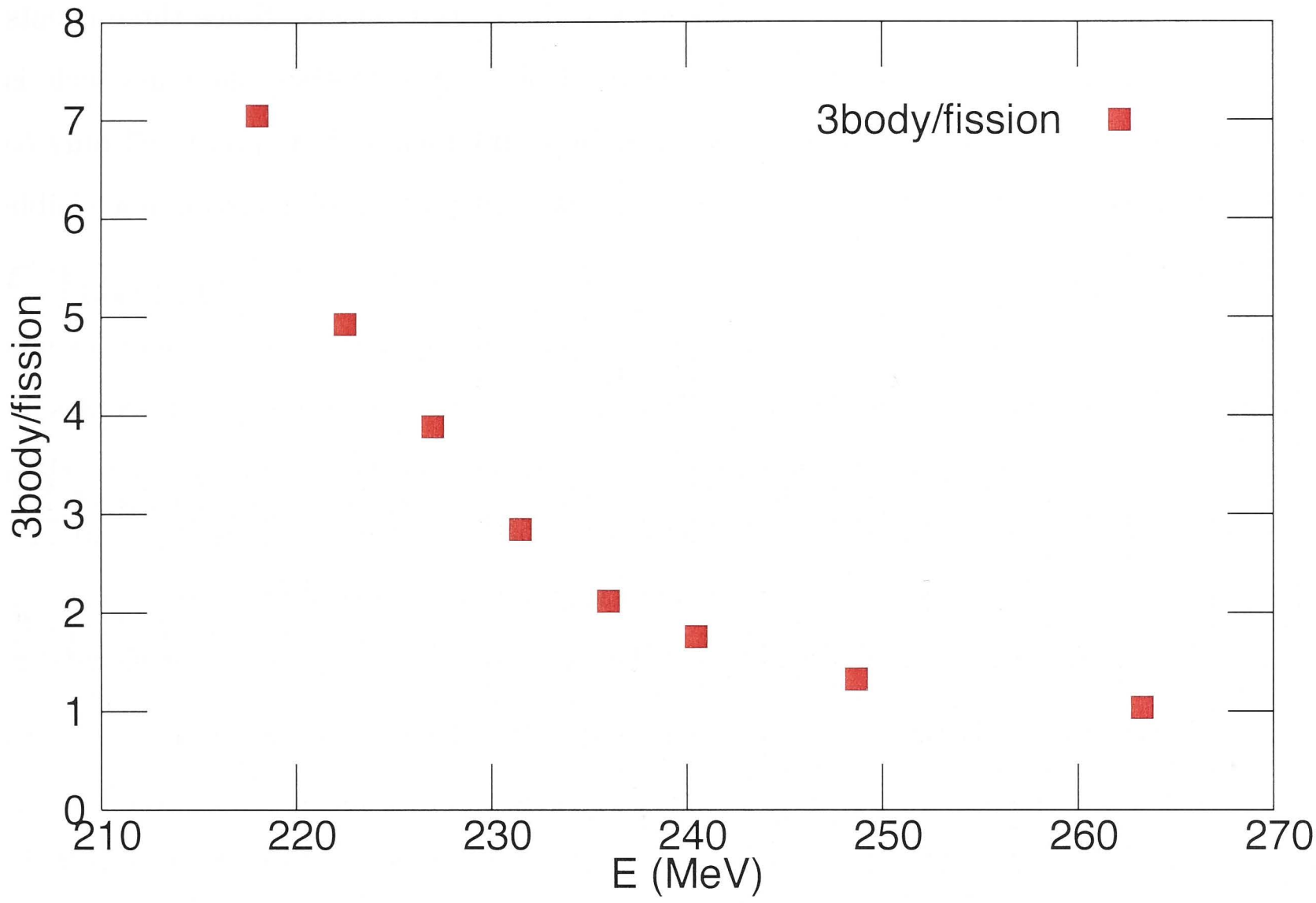

Figure 4.8: Three body flux normalised to fission counts as a function of Energy for the ^{40}Ca + ^{238}U reaction.

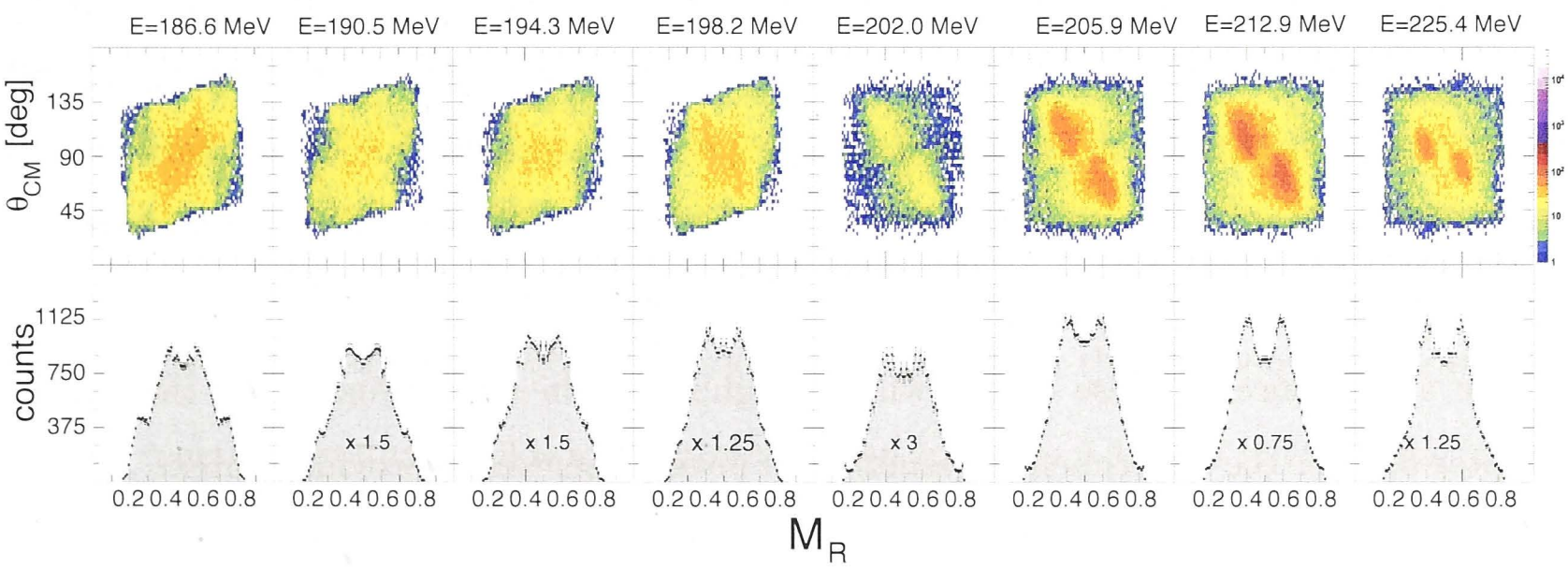

Figure 4.9: MAD for 3 body events in the ^{40}Ca + ^{238}U reaction. Like all other MADs the ones shown here have been mirrored around $M_R = 0.5$ and $\theta_{c.m.} = 90°$

To investigate this, three body events were isolated by gating out the elastic peaks and using the anti-gate of the elliptical velocity gate gate discussed in section 4.2.3. This was the gate previously used to eliminate the three body events. In this section we only focus on the ^{40}Ca + ^{238}U reactions. Other reactions with targets of ^{232}Th and ^{238}U exhibit very similar behaviour.

The ratio of the three body counts to that of the FMT events is plotted in figure 4.8.

Figure 4.9 shows the corresponding MADs for the three body events. Since these events cannot be correctly analysed using the Kinematic Coincidence Method the mass scale is not indicative of the actual masses of the three body fragments. It is presented only to allow a comparison with figure 5.2, to illustrate that this pattern of events is not visible in the FMT MADs.

From figure 4.8 we see that at the highest energy the number of three body events is roughly the same as the number of FMT events. This ratio increases with decreasing energy and at the lowest energies the number of three body events is 7 times greater than the FMT events. This straightaway highlights the importance of good gating requirements. The point is further strengthened when we consider that the three body events in figure 4.9 populate the same region of the MAD as the QF and FF events, as seen in figure 4.1.

The three body flux was reconstructed in Ref. [16] using a Monte Carlo model, to predict the flux of these events and where the corresponding mass splits would lie in the mass distribution. The cited work concluded that a negligible three body flux that populates the gap between elastic scattering peak and mass-asymmetric quasifission peak. Similarly, in the work of Nishio *et al.* [57], the three body events were eliminated via software gates and the flux considered negligible. In our work, we see that the three body flux (Figure 4.8) is at least as large as the two body flux, at the highest energies, and up to seven times higher, at the lowest energies; which depending on the primary masses populated that lead to sequential fission (three body events) could fill the valleys around $M_R \approx 0.2$ and 0.8.

The significance of these events will be highlighted in the discussion at the end of Chapter 5, after the experimental results have been presented to provide context.

Chapter 5

Results and Interpretation of MADs

In figure 5.1 the upper panels show three different mass-angle distributions (MADs), each with a different dominant reaction outcome. The lower panels show the corresponding mass projections. The MADs display the centre-of-mass angle (θ_{CM}) of the fission fragments versus their mass-ratio (M_R). The colours indicate the number of counts per bin in the MADs. Since we collect data in coincidence and record information for both the fission fragments, each point in the MADs has a corresponding point at a centre-of mass angle of 180°-θ_{cm} and at a mass ratio of 1-M_R. All the MADs shown in this work are presented in this way. This also makes visual identification of any mass angle correlations easier. Note that unless otherwise mentioned, all energies are reported in the centre-of-mass frame.

The reaction products following capture, shown in figure 5.1 from left to right, range from mass asymmetric quasifission (QF), to mass symmetric quasifission (MSQF), to compound nucleus fission also termed fusion-fission (FF).

In the first two panels, the intense groups seen at very high and very low mass ratios ($M_R \approx 0.15$ and $M_R \approx 0.85$) are elastically scattered beam particles and the corresponding target recoils. These are not seen in the third panel due to the low mass of the projectile, resulting in elastically scattered projectile nuclei, and the corresponding target recoils, being below the detector electronics thresholds.

The left panel (a) shows a typical example of mass asymmetric quasifission. In the MAD we see a group of events that is strongly focused at forward and backward angles and

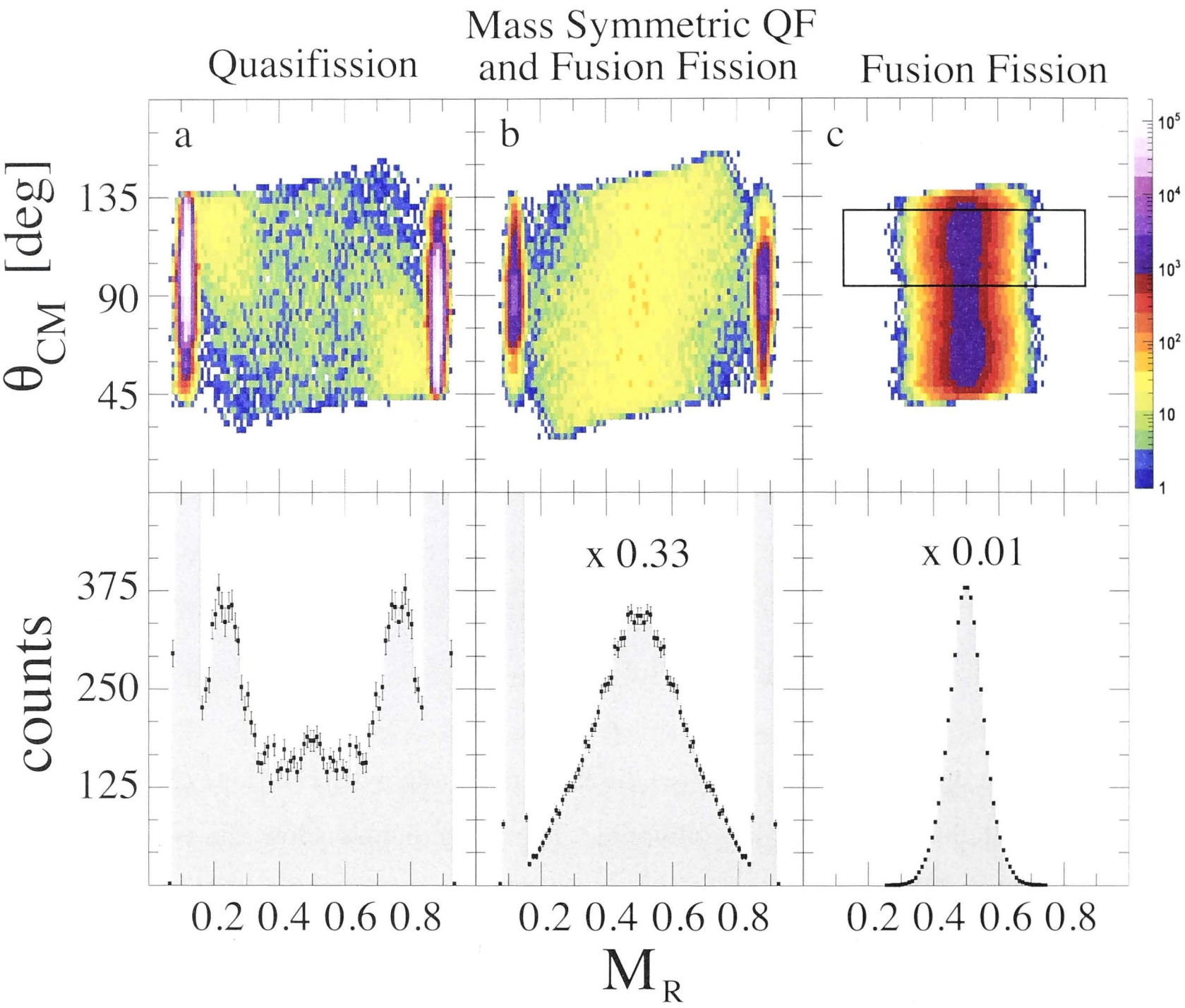

Figure 5.1: A sample of MADs corresponding to three distinct reaction outcomes. Left to right, the reaction channels shown range from predominantly mass asymmetric quasifission (panel a), to mass symmetric quasifission (panel b), to pure fusion fission (panel c). The upper panels show the mirrored MADs and the lower panels show the corresponding mass projections. The colours indicate the number of counts per bin in the MADs. The reactions shown are a)^{34}S + ^{232}Th at E_{cm} = 143.9 MeV, b)^{34}S + ^{232}Th at E_{cm} = 167 MeV and c)^{12}C + ^{208}Pb at E_{cm} = 71.9 MeV.

the corresponding mass distribution shows that these events have very asymmetric masses. These groups correspond to the target-like and projectile-like fragments, respectively. That is, for asymmetric quasifission the light peak is seen at backward angles and the heavy peak is seen at forward angles. We also see a few events around mass symmetry ($M_R = 0.5$), which may correspond to fusion fission or to mass symmetric quasifission. The presence of MSQF events is inferred based on the width σ_{M_R} of the mass-symmetric peak. A width $\sigma_{M_R} \leq 0.07$ is consistent with FF [35]; a width significantly higher than this indicates the presence of MSQF as well. Since the observable characteristics of FF and MSQF overlap significantly we cannot separate the two types of events. However, in this MAD, since mass-asymmetric QF forms a separate component altogether we can separate it from the

symmetrically peaked FF and MSQF components.

This is not the case in the middle panel (b). Here fission-like events furthest from symmetry are found at forward and backward angles. This is a clear example of mass-symmetric quasifission (MSQF). In the MAD there is a correlation between the mass ratio and the centre-of-mass angle, seen as a characteristic 'tilt', or anisotropic distribution, for $M_R \neq 0.5$. This is due to MSQF events, that are found at forward and backward angles for light and heavy splits furthest from M_R=0.5, respectively. Previous work [35] has shown that these events are quasifission taking place at time scales significantly longer than 10^{-21}s, with more mass being exchanged prior to reseparation. Events close to mass symmetry ($M_R = 0.5$) may correspond to fusion fission. Since the two components have significant overlap in their mass and angle [34, 35], the corresponding mass distribution is wide (σ_{M_R}=0.14) and peaked at M_R=0.5. Here we clearly see that MSQF events and FF events do not form two separate components in the MADs.

The contrast between this and the previous panel highlights the extreme sensitivity of the MAD technique to the shortest (few 10^{-21}s) QF reactions, and reduced sensitivity to longer reactions. QF reactions taking place at longer timescales (longer than 10^{-20}s) overlap with FF in the MADs, even though they themselves might have very different relative timescales (10^{-20}s for MSQF vs. 10^{-18}s to 10^{-16}s for FF [35]).

The right panel (c) is an example of pure fusion fission. The MAD exhibits an angular distribution symmetric around $\theta_{cm} = 90°$. The corresponding mass distribution is narrow ($\sigma_{M_R} = 0.056$) and symmetric about M_R=0.5. This is due to the CN splitting into two symmetric fragments after a relatively long contact time (10^{-18}s to 10^{-16}s [35]); and since all degrees of freedom have equilibrated, the fragments are emitted isotropically in θ. This example does not show the influence of shell structures generating mass-asymmetric fusion-fission. At lower excitation energies we may see an angular distribution symmetric around $\theta_{cm} = 90°$ but a corresponding mass distribution that has a mass-asymmetric component. This is not seen in our data for this particular reaction, but examples of this will be shown subsequently for other reactions.

To avoid any bias in characterisation of the mass distributions due to the geometrical acceptance of the detector system, a rectangular gate was applied when extracting mass ratio distributions. An example of such a gate is shown in the third panel of figure 5.1. Such a gate was applied to all systems, at all energies, to obtain mass ratio distributions

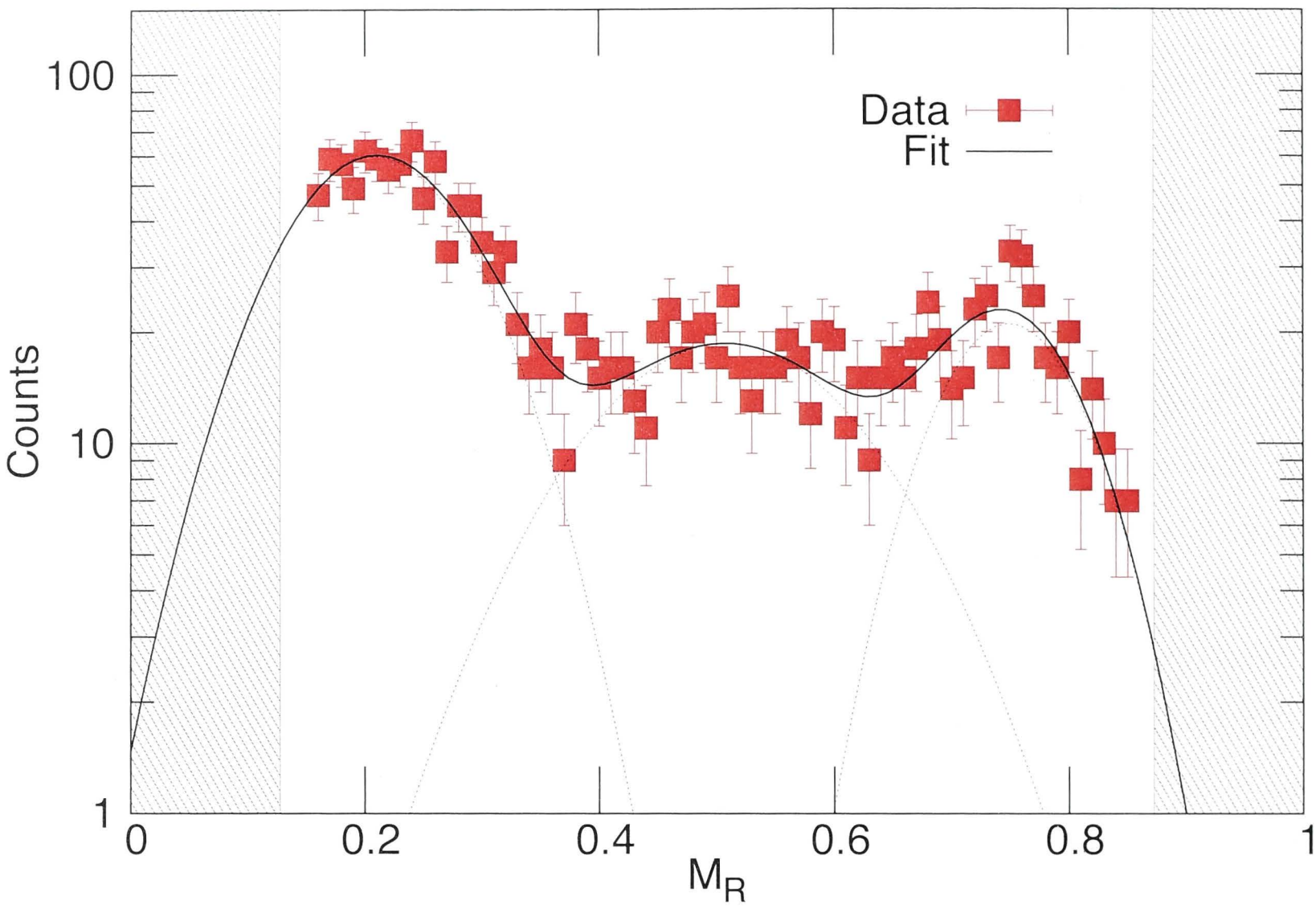

Figure 5.2: An example of a fit to the mass distributions. The dotted lines correspond to individual Gaussian functions while the solid line is the overall fit. The shaded area corresponds to the mass regions below and above elastic scattering.

unbiased by detector edge effects. Note that the gate shown here is only an indicative example. The angular width of the gate used for each reaction was not always as pictured. The gate was varied such that it only covered the region of full geometrical acceptance.

We extracted information from the unmirrored MADs (θ_{cm} from $\sim 90^\circ$ to $\sim 135^\circ$) primarily by fitting the mass distributions. That is, only the unsymmetrised mass distributions were used in the fitting protocol described below.

To quantify the differences between the reactions, the mass ratio distributions for all data sets were fitted with up to three overlapping Gaussian functions in the mass range between the elastic peaks (different for each reaction, typically $M_R \approx 0.15$ to 0.85). Figure 5.2 shows a typical fit of three overlapping Gaussian functions to a mass projection. Not all peaks were expected to be Gaussian. The use of Gaussians here is justified by the need to systematically quantify the peaks and extract centroids, widths and areas. The centroid allows us to calculate the corresponding average mass and estimate the charge of the fragments. The area allows us to estimate the flux in a certain reaction channel. When calculating the area under a certain peak, we restricted integration to the region

Table 5.1: Table of all reactions measured. The columns correspond to the entrance channel charge product, mass of composite system, scaled Coulomb barrier (in the centre-of-mass frame), Q value for fusion, reaction type and detector geometry. Except for the ^{40}Ca induced reactions, all other reactions comprise pairs that form the same compound nucleus.

Reaction	Z_pZ_t	A_{CN}	$V_{b,c.m.}$ (MeV)	Q (MeV)	type	geometry
^{12}C + ^{208}Pb	492	220	55.46	-32.02	calibration	b
^{18}O + ^{208}Pb	656	226	72.45	-45.73	calibration	b
^{30}Si + ^{197}Au	1106	227	122.28	-88.14	calibration	b
^{30}Si + ^{208}Pb	1148	238	125.76	-95.58	calibration	b
^{12}C + ^{238}U	552	250	60.59	-23.86	interest	b
^{18}O + ^{232}Th	720	250	77.97	-36.51	interest	b
^{24}Mg + ^{238}U	1104	262	119.74	-69.02	interest	a
^{30}Si + ^{232}Th	1260	262	135.71	-95.58	interest	b
^{28}Si + ^{238}U	1288	266	139.34	-87.89	interest	a
^{34}S + ^{232}Th	1440	266	154.79	-108.19	interest	a
^{40}Ca + ^{232}Th	1800	272	193.77	-135.69	interest	a
^{40}Ca + ^{238}U	1840	278	197.3	-140.21	interest	a

between the elastic peaks (unshaded region in figure 5.2). This avoids integration over unphysical masses, and masses not populated in the reactions. The width of the central, symmetric, peak gives some discrimination between MSQF and FF. Typically, the widths and centroids of the Gaussians were not constrained. Any exceptions to this general characterisation protocol will be explicitly described in the relevant section.

In the first section of this chapter we present the calibration reactions with targets of ^{208}Pb and ^{197}Au. The expectation of mass symmetric fission is exploited to determine δt and calibrate the time of flight (Details in Chapter 4). The second section presents reactions with ^{238}U and ^{232}Th targets, which were the reactions of interest. Table 5.1 lists all the reactions presented in this work.

The experiments were all done in the same scattering chamber under near-identical conditions. The changes made were minor and only slightly affected the geometry as detailed below. The back detector had an angular coverage of $\theta_{lab} = 50°$ to $125°$ (labelled a in Table 5.1) for some experiments and $\theta_{lab} = 55°$ to $130°$ (labelled b) for others. Reactions with ^{208}Pb and ^{197}Au were interleaved with reactions of ^{238}U and ^{232}Th, where

possible. In the cases where due to time constraints this was not possible, a minimum of two calibration runs were performed, one towards the beginning of the experiment and one towards the end.

5.1 Time Of Flight Calibration using Reactions with ^{208}Pb and ^{197}Au

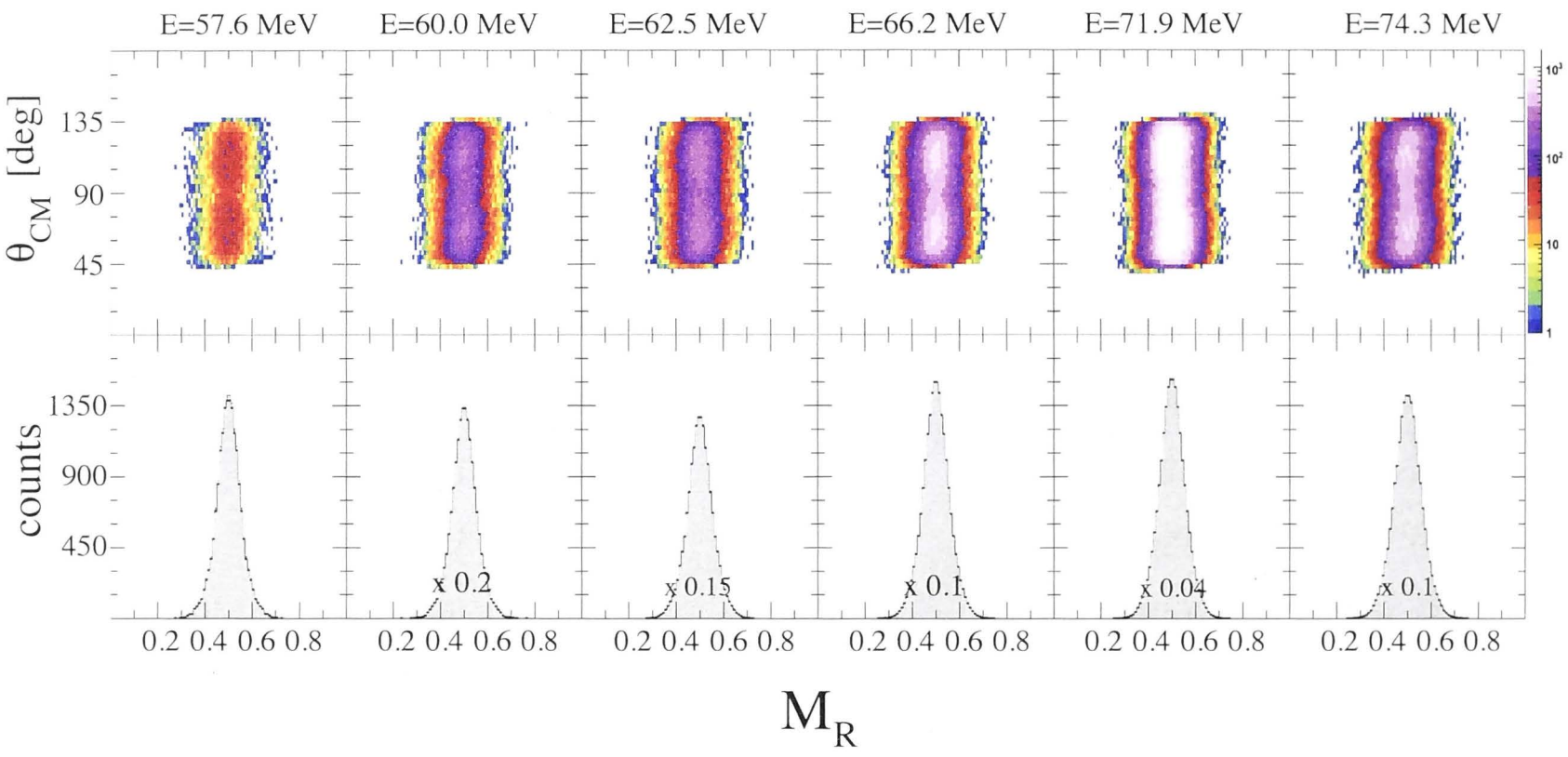

Figure 5.3: Mass angle distributions for FMT events in the reaction ^{12}C + ^{208}Pb ($V_{b,cm} = 55.46$ MeV). The lower frames show the corresponding projected mass-ratio distributions.

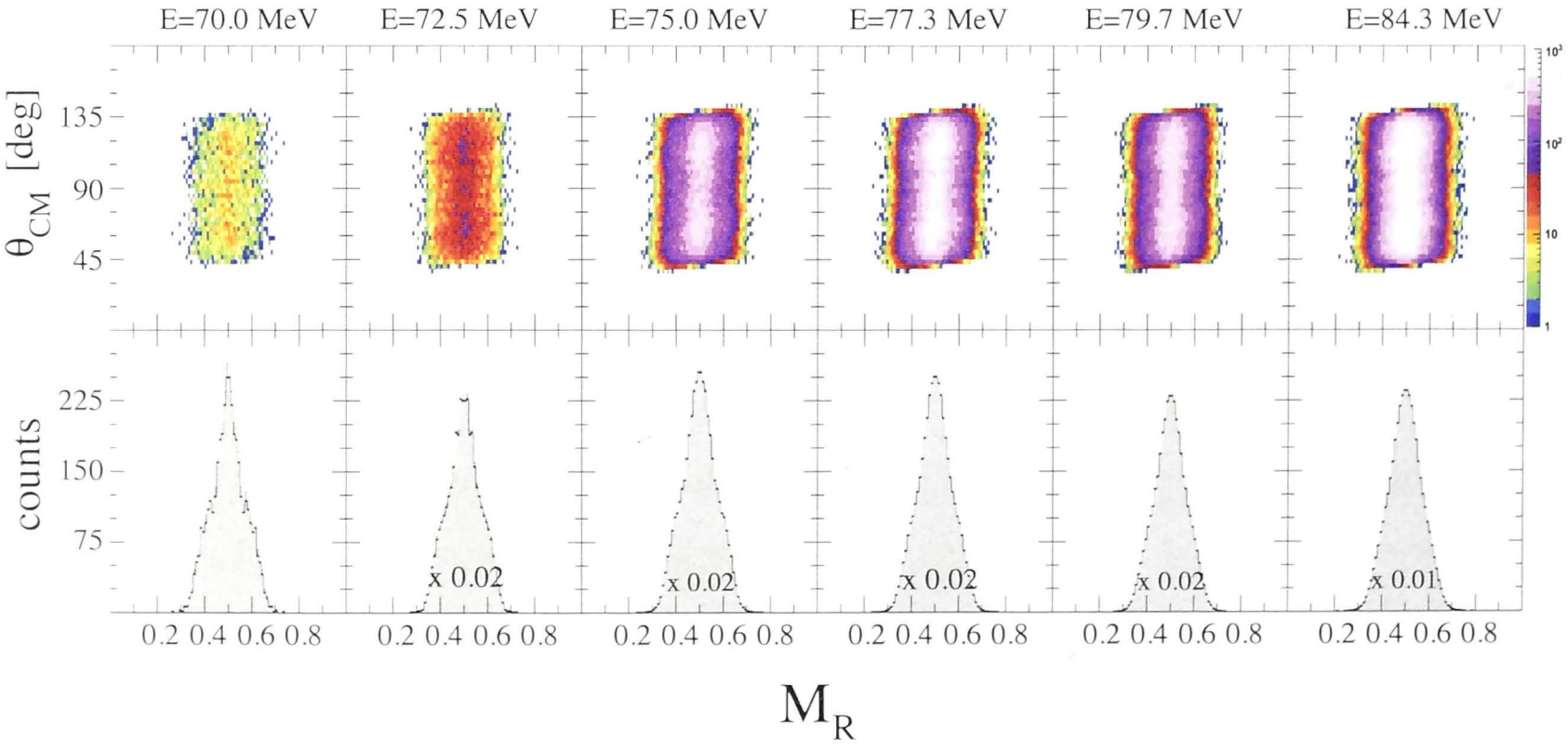

Figure 5.4: Mass angle distributions for FMT events in the reaction ^{18}O + ^{208}Pb ($V_{b,cm} = 72.45$ MeV). The lower frames show the corresponding projected mass-ratio distributions.

The reactions with ^{208}Pb and ^{197}Au presented in this section are not the focus of this

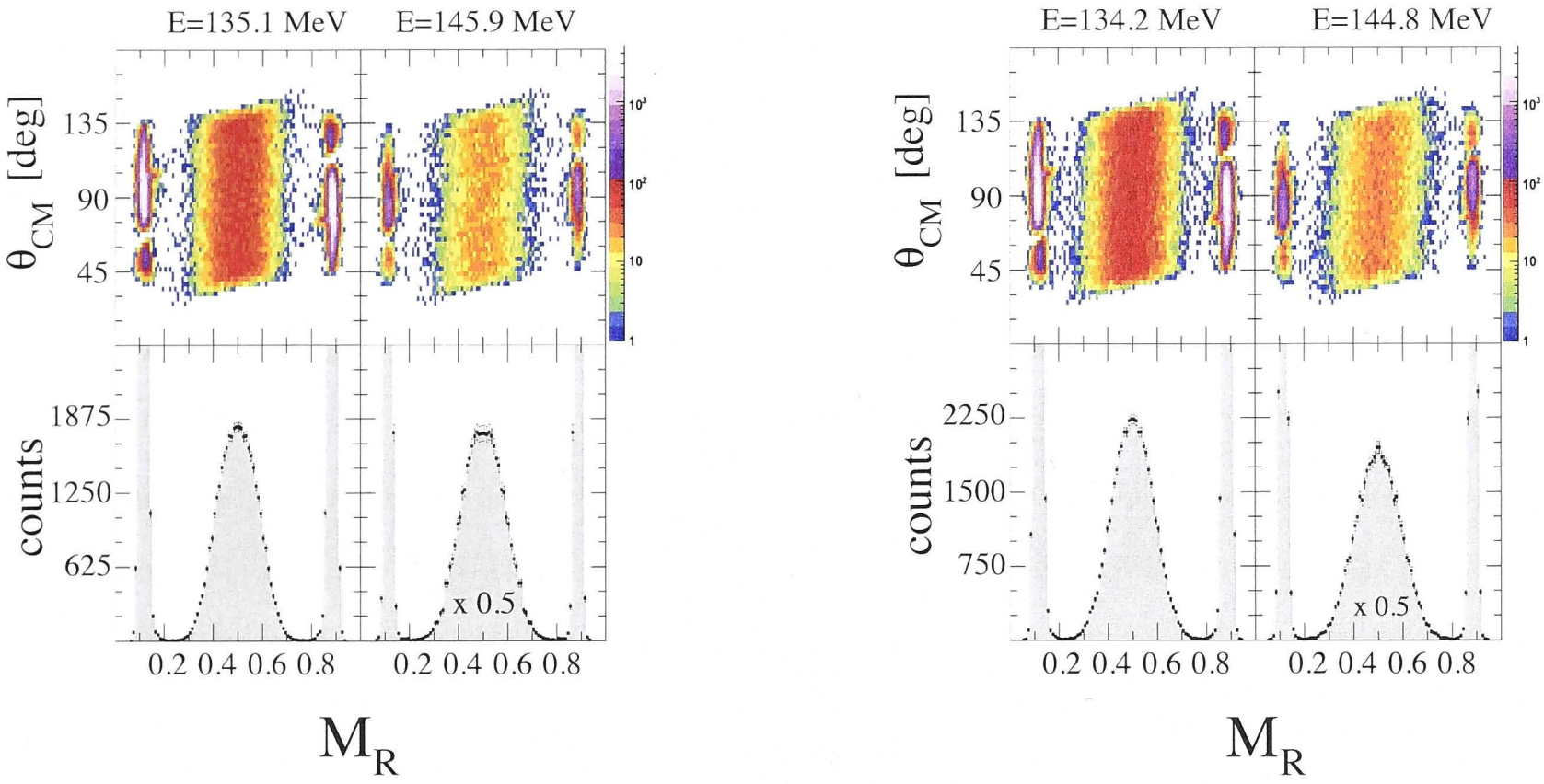

Figure 5.5: Mass angle distributions for FMT events in the reaction ^{30}Si + ^{208}Pb ($V_{b,cm}$ = 125.76 MeV) and ^{30}Si + ^{197}Au ($V_{b,cm}$ = 122.28 MeV), respectively. The lower frames show the corresponding projected mass-ratio distributions.

work and hence we do no go into a detailed investigation into the features seen here. We only need these reactions for the absolute calibration of the time-of-flight information (described in Chapter 4). To do this reliably we need reactions where the fission mass distribution is peaked at $M_R = 0.5$. Specifically, all we require is an unmirrored mass distribution that is peaked at $M_R = 0.5$, at $\theta_{c.m.} = 90°$.

Figures 5.3, 5.4 and 5.5 show the MADs of reactions with ^{208}Pb and ^{197}Au targets. The MADs for ^{12}C and ^{18}O induced reactions show no mass-angle correlation. The mass ratio distributions for the ^{12}C induced reactions are peaked at M_R=0.5, with no discrete asymmetric component. The same reaction was studied by I. V. Pokrovsky *et al.* in Ref.[103] at energies ranging from E_{cm} = 53.9 to 85.1 MeV. At the lowest energies, below the range measured in this work, an asymmetric fission mode was observed in addition to symmetric fission. At higher energies, matching the range measured in this work, the symmetric splits were dominant, in agreement with the results seen here.

The mass ratio distributions for the ^{18}O + ^{208}Pb reaction are peaked at $M_R = 0.5$ but also have a discrete mass-asymmetric component, clearly visible at the lowest energies. The same reaction was studied by I. V. Pokrovsky *et al.* in Ref.[104] at E_{cm} = 71.8 MeV, very close to the lowest energy studied in this work. The cited work observed a mass distribution with a symmetric and asymmetric component consistent with the mass distribution seen here.

The ^{30}Si + ^{208}Pb and ^{30}Si + ^{197}Au reactions exhibit a slight mass-angle correlation. The corresponding mass ratio distributions are peaked at M_R=0.5, with no discrete asymmetric component. The mass projections for the ^{30}Si + ^{208}Pb,^{197}Au reactions are broad compared to the ^{12}C + ^{208}Pb and ^{18}O + ^{208}Pb reactions.

From the MADs and mass projections it is clear that none of the reactions have a component that is consistent with mass-asymmetric quasifission. All reactions have a strong mass-symmetric component and thus were ideal for the absolute calibration of the time-of-flight information. The agreement with previous work in Refs.[103, 104] confirms that there was no experimental error or inconsistency during these measurements.

All reactions with ^{208}Pb and ^{197}Au have the added advantage that target-like nuclei have a large fission barrier and thus do not undergo transfer fission for the energies studied here. Thus we do not have to apply any special gates to eliminate transfer fission events, making the determination of δt a simpler process.

5.2 Reactions with ^{238}U and ^{232}Th

We now present the reactions of interest. These are reactions induced by various projectiles, ranging from ^{12}C to ^{40}Ca, with targets of ^{238}U and ^{232}Th. In total we present 8 reactions, 6 of which are in pairs forming the same compound nucleus. The discussion of the results is broken up into two parts. The MADs and mass projections are presented in this section, along with a discussion relevant to each reaction pair. The subsequent section ties all of these reactions together in a general discussion, including an analysis of the mass widths which are used to infer the presence of mass symmetric quasifission.

5.2.1 Reactions forming ^{250}Cf

Figures 5.6 and 5.7 show the mass angle distributions for all the measured energies for the ^{18}O and ^{12}C induced reactions respectively. Both reactions form the compound nucleus ^{250}Cf.

From the MADs it is clear that for both systems there is no significant dependence of mass ratio on the centre-of-mass angle, at any of the energies studied. The corresponding mass ratio distributions (shown for θ_{cm} from $\sim 90^\circ$ to $\sim 135^\circ$) do not have a component that is consistent with mass asymmetric quasifission. The mass projections have two mass

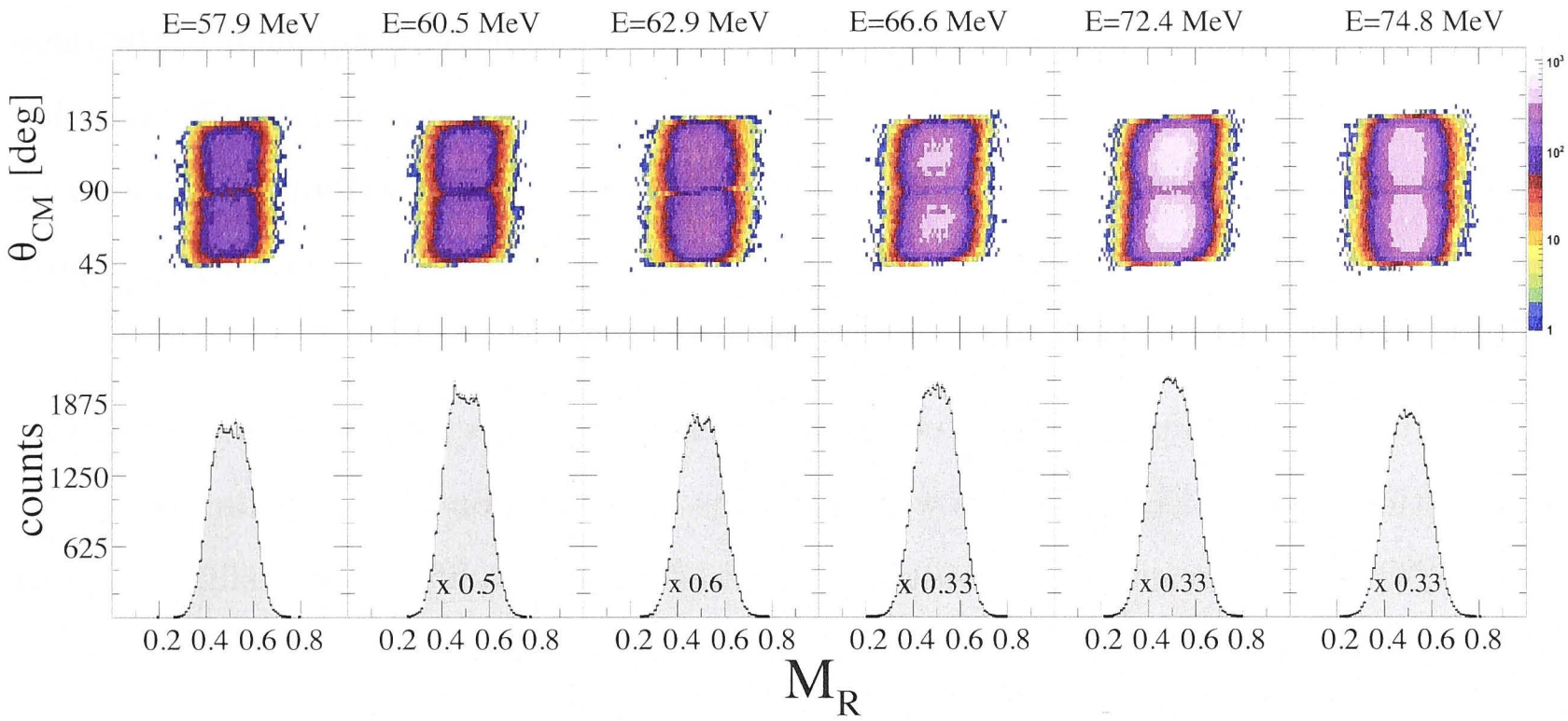

Figure 5.6: Mass angle distributions for FMT events in the reaction $^{12}C + ^{238}U$ ($V_{b,cm} = 60.59$ MeV). The gap seen at $\theta_{c.m.} \approx 90°$ in the MADs is due to the small forward focussing of fission fragments from this reaction and where the detector geometry gave no coverage. The resultant mirrored MAD has a drop in counts, seen as a gap. The lower frames show the projected mass-ratio distributions for the unsymmetrised MADs i.e. θ_{cm} from $\sim 90°$ to $\sim 135°$.

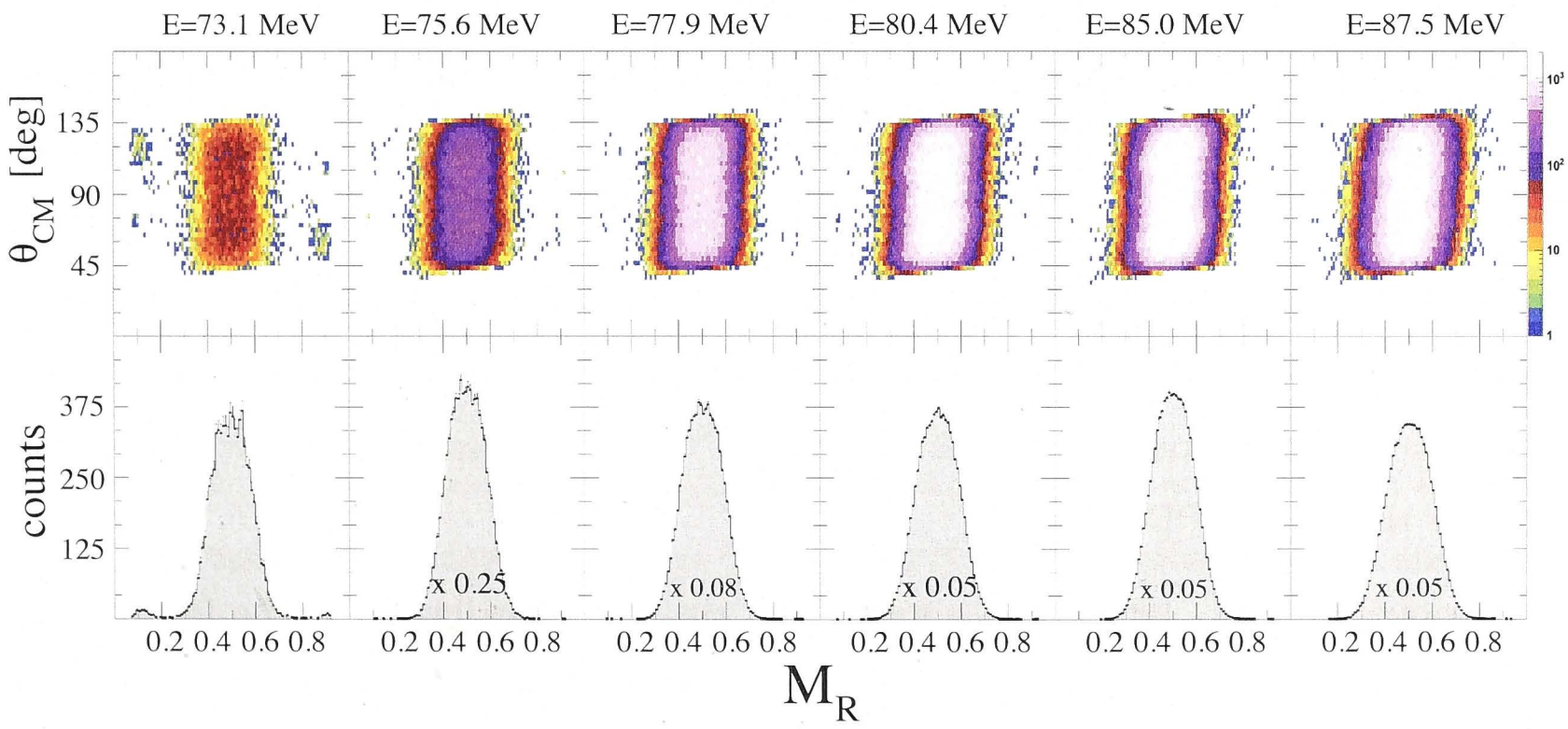

Figure 5.7: Mass angle distributions for FMT events in the reaction $^{18}O + ^{232}Th$ ($V_{b,cm} = 77.97$ MeV). The lower frames show the projected mass-ratio distributions for the unsymmetrised MADs i.e. θ_{cm} from $\sim 90°$ to $\sim 135°$.

asymmetric peaks close to M_R =0.5 at the lowest energies, tending to one broad peak at M_R =0.5 for the highest energies.

We used two separate fitting protocols to characterise the mass distributions, the first using a single Gaussian for all energies, and the second using two overlapping Gaussian for all energies. The single Gaussian fits were used to compare this work with that of Yadav et al. [105] where the same reactions were studied and single Gaussian fits were used.

The double Gaussian fits were used because we see an asymmetric component in the mass distributions in this work. Figure 5.8 shows a comparison of a single and double Gaussian fit to the same, unmirrored (i.e. θ_{cm} from $\sim 90°$ to $\sim 135°$) mass distribution. Comparing the single Gaussian fit ($\chi^2 = 50.905$) with the double Gaussian fit ($\chi^2 = 1.949$) we clearly see that a double Gaussian fit is more appropriate here.

Using the single Gaussian fits we compare the fragment mass ratio widths as a function of excitation energy. Figure 5.9 shows the widths as a function of excitation energy E*. For the $^{18}O + ^{232}Th$ reaction, the widths of the single Gaussian fits are only slightly higher for almost all energies.

In the work of Yadav et al. [105] the mass distributions were fitted using a single Gaussian and the $^{18}O + ^{232}Th$ reaction was found to have a wider mass width compared to the $^{12}C + ^{238}U$ reaction. The widths were scaled for T and $< l^2 >$ and the cited work concluded that the $^{18}O + ^{232}Th$ reaction shows signs of incomplete mass equilibration and therefore mass symmetric quasifission.

In [105] the measured mass distributions did not show as clearly, the asymmetric mass splits seen in this work at the lowest energies. Figure 5.10 depicts the mass of the two asymmetric peaks as a function of energy, from the double Gaussian fits. The mass splits show that, for both reactions, the heavy fragment lies close to A=140 and the light fragment lies close to A=110. The median mass number of the heavy fragment is, on average, a constant around A=139 $\pm$ 4u for the $^{18}O + ^{232}Th$ reaction and around A=139 $\pm$ 2u for the $^{12}C + ^{238}U$ reaction.

Previous work [21, 106, 107] has found that the mass distribution of the fission fragments, arising from the low-energy fission of actinide nuclei, were asymmetric. Several actinide nuclei ranging from ^{227}Th to ^{249}Cf were studied, summarised in [106], and the median mass of the heavy fragments was found to be a constant A=139, whereas the median mass of the light fragments varied to account for the total mass of the fissioning system (A=89 for the fissile system ^{227}Th and A=106 for the fissile system ^{249}Cf). It was concluded that the constancy of the mass number of the heavy fragment was related to the pronounced stability of the closed proton (Z=50) and closed neutron (N=82) shell structures found in this mass region. The constancy of the mass of the heavy fragment seen in this work, illustrated in figure 5.10, is consistent with the empirical systematics reported in [106].

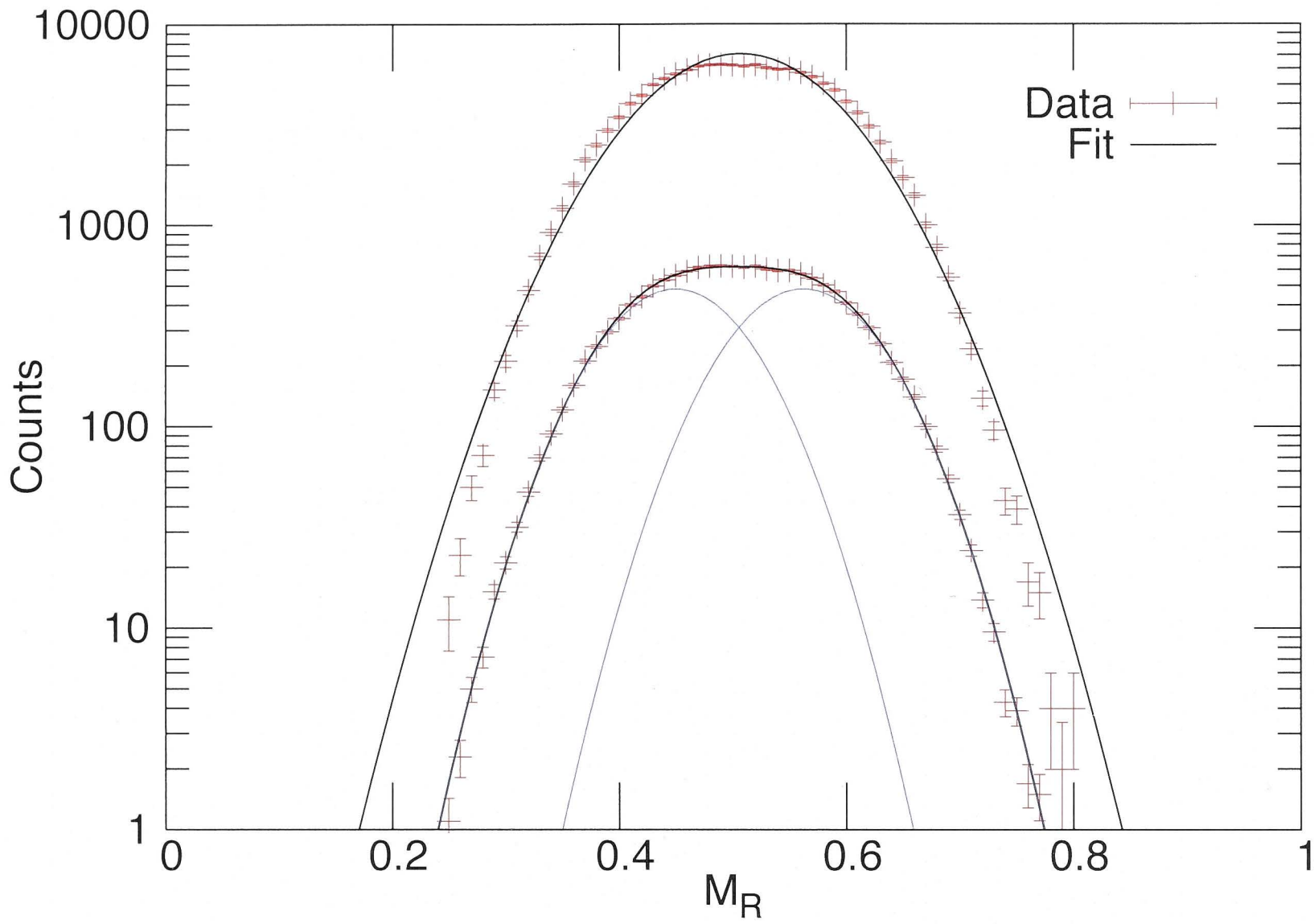

Figure 5.8: A comparison of single Gaussian and double Gaussian fits to the same, unmirrored mass distribution. The upper curve shows a single Gaussian fit to data. The lower curve is the same mass distribution, scaled down by a factor of 10 for the sake of comparison, with a fit using two overlapping Gaussians. The thin blue lines correspond to individual Gaussian functions while the thick black line is the overall fit.

We see increasing evidence for a symmetric fission component at the highest energies, where the mass distributions no longer have a flat top. This component is due to an increasing contribution from symmetric fusion fission as the excitation energy increases. The symmetric fission arises due to the disappearance of shell effects on the nuclear level density with increasing excitation energy [106, 107]. However, the asymmetric component is clearly still present and data from these energies can still be described with two overlapping Gaussian peaks.

We conclude that both these reactions lead predominantly to CN formation and its subsequent fission into two mass asymmetric fragments. This is the only explanation for what we see in this work: no mass-angle correlation and asymmetric mass distributions, characterised by **two** overlapping Gaussian peaks. The lack of a quasifission component is consistent with the large entrance channel mass asymmetry, or low charge product Z_pZ_t (see Table 5.1) of these reactions. In our work, we see no evidence for mass symmetric

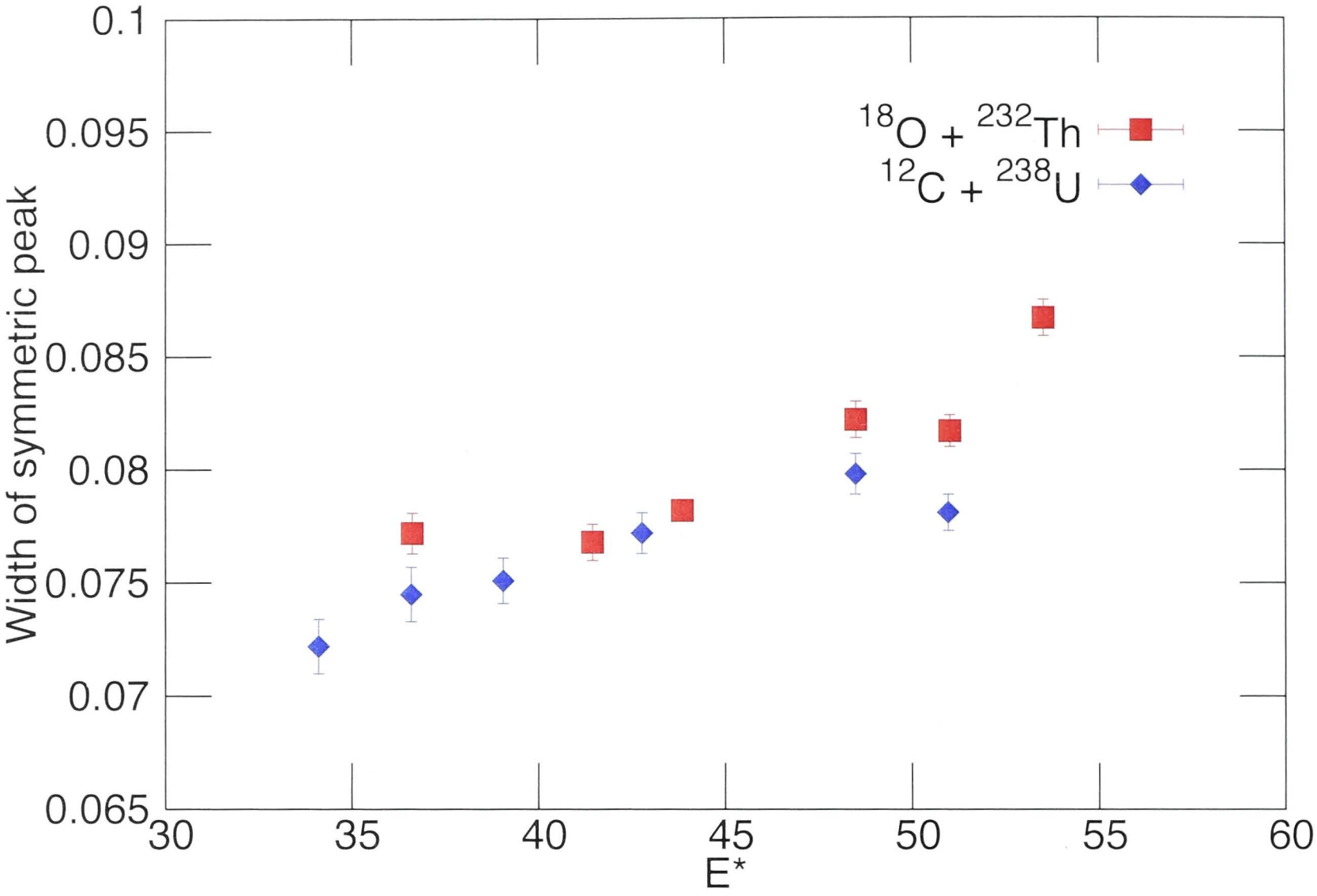

Figure 5.9: Fragment mass ratio widths for the ^{12}C and ^{18}O induced reactions as a function Excitation Energy E*. Both reactions form the ^{250}Cf compound nucleus.

quasifission. This would have been seen as a distinct correlation in mass and angle, as seen in Figure 5.1 panel (b). The corresponding mass distribution would be characterised by a **single** Gaussian, peaked at $M_R = 0.5$, with a width σ_{M_R} exceeding 0.07.

This conflict between our results and those of Yadav et al. may be due to the significantly higher statistics in this work. The larger angular coverage of our detector system aided in collecting high statistics data without extremely long run times. The detector setup in the cited work had an angular coverage, at backward angles, of $\theta_{c.m.} = 95°$ to 123° degrees. In this work we had an angular coverage, at backward angles, of $\theta_{c.m.} =$ 90° to 135° degrees. The statistics in the current work exceed that of the cited work by a factor of three for the lowest energies and a factor of ten for the highest energies.

5.2.2 Reactions forming ^{262}Rf

Figures 5.11 and 5.12 show the mass angle distributions for all the measured energies (E_{cm}) for the ^{24}Mg and ^{30}Si induced reactions, respectively. Both reactions form the ^{262}Rf compound nucleus.

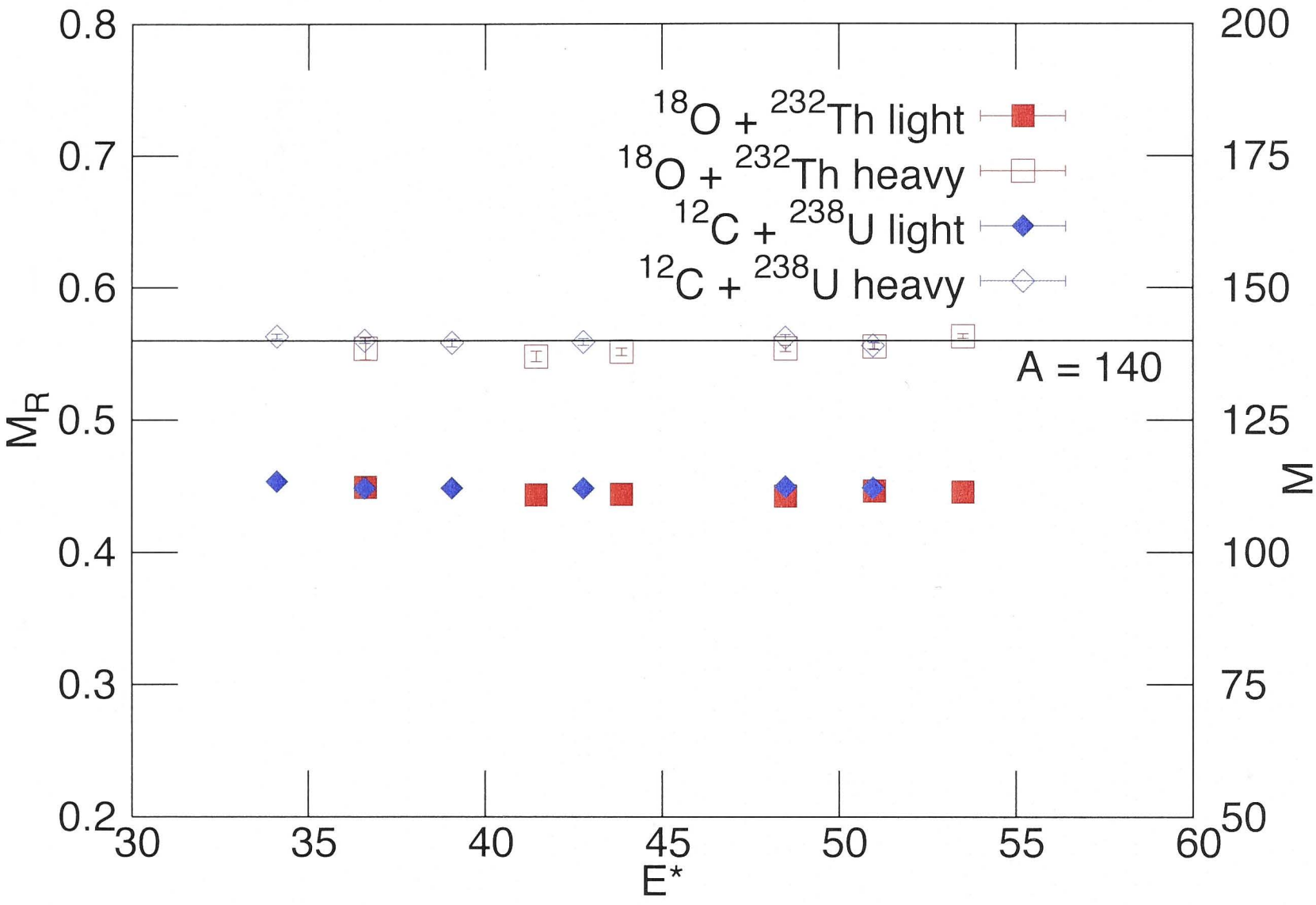

Figure 5.10: Masses of the light and heavy fragments for both reactions as a function of Excitation Energy E*. The solid line marks A=140.

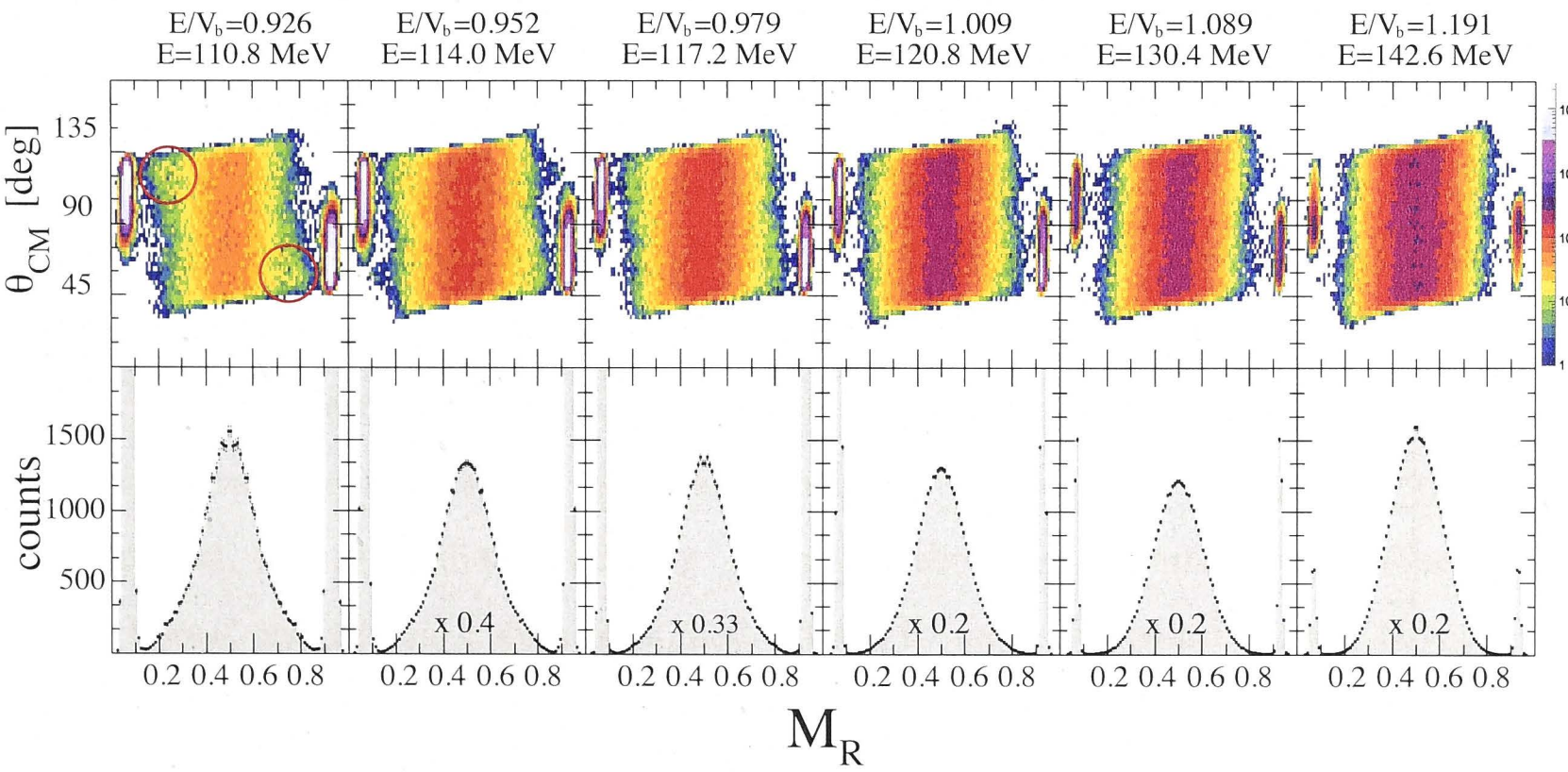

Figure 5.11: Mass angle distributions for FMT events in the reaction ^{24}Mg + ^{238}U ($V_{b,cm}$ = 119.74 MeV). The lower frames show the corresponding projected mass-ratio distributions. The circles on the MAD for E_{cm} = 110.8 MeV serve to highlight the weak mass-asymmetric component.

From the MADs for the ^{24}Mg induced reactions (figure 5.11) it is clear that there is no discrete mass-asymmetric component for most of the energies studied. The corresponding

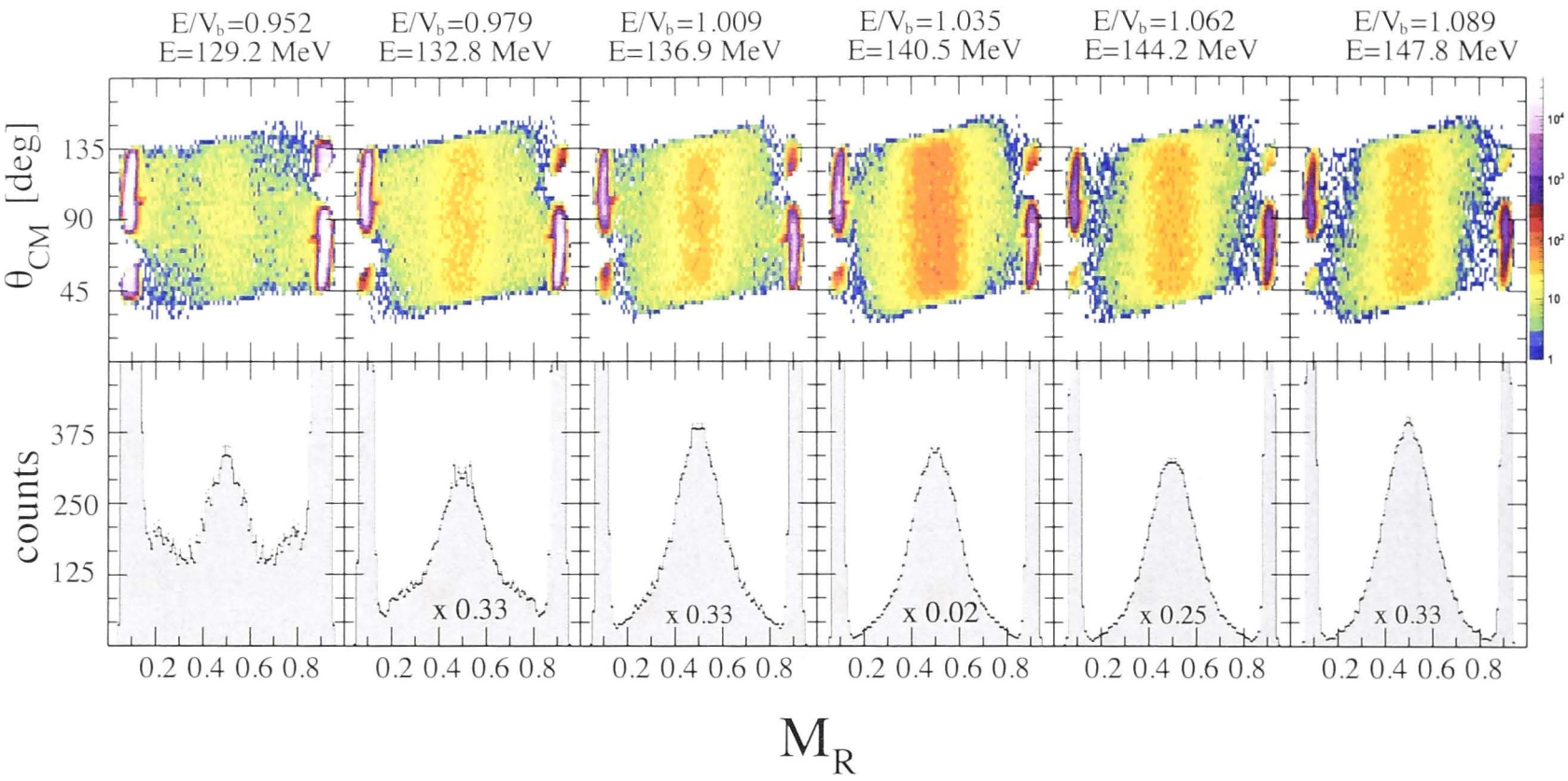

Figure 5.12: Mass angle distributions for FMT events in the reaction ^{30}Si + ^{232}Th ($V_{b,cm} = 135.71$ MeV). The lower frames show the corresponding projected mass-ratio distributions.

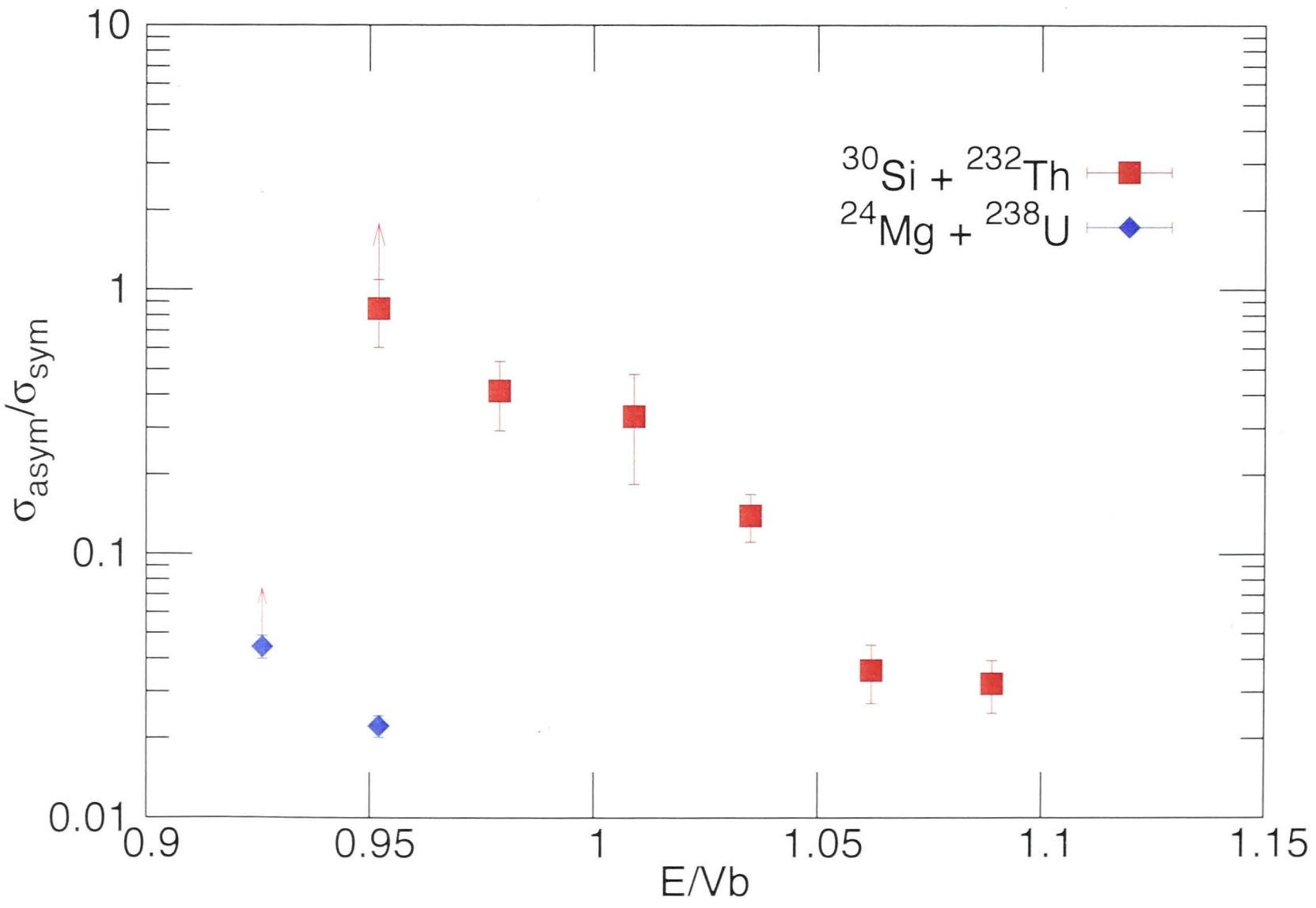

Figure 5.13: Relative yield of the asymmetric and symmetric mass components for ^{30}Si and ^{24}Mg reactions with respect to E/V_b. The arrows on the lowest energies indicate that the yield represents a lower bound to the mass-asymmetric quasifission flux.

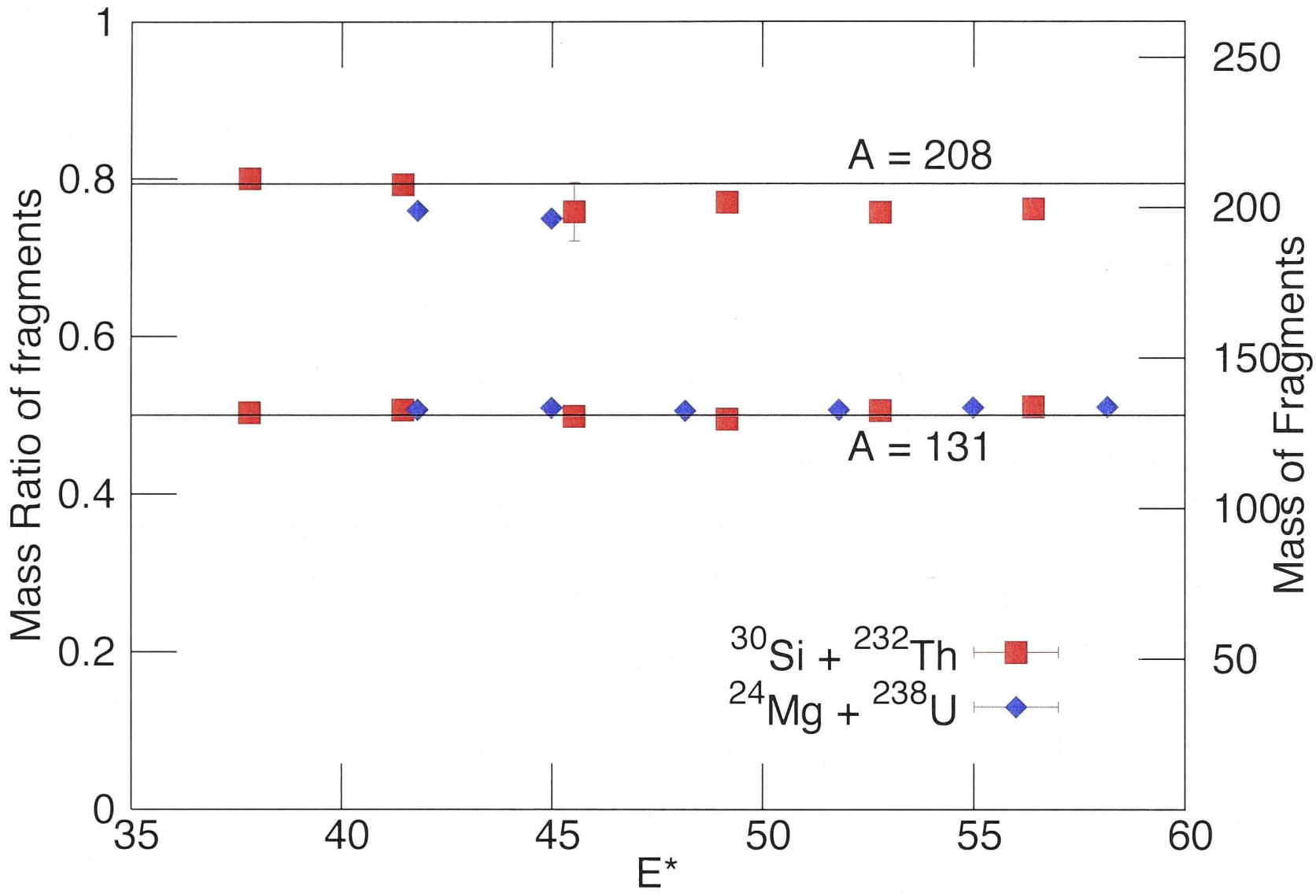

Figure 5.14: Masses of the heavy and symmetric fragments for ^{30}Si and ^{24}Mg reactions as a function of Excitation Energy E*. The two solid lines mark A=131 (symmetric fission) and A=208.

mass ratio distributions are symmetric and generally do not have a component that is consistent with mass asymmetric quasifission. The only exceptions are the two lowest energies where we see a small number of counts for the most asymmetric splits, at forward and backward angles. The projectile-like light fragments are seen at the most backward angles, whereas the target-like heavy fragments are seen at the most forward angles. The mass-asymmetric component is weak and therefore not visually apparent in the mass distributions. It is quantified via fitting. Note that the mass-asymmetric component seen at the lowest energies in Figure 5.11 may extend to more backward angles, beyond the acceptance of the detector geometry here, and could be considerably stronger. Thus the fitted yields represent a lower bound to the mass-asymmetric quasifission flux at the lowest energies (indicated by the arrows in Figure 5.11).

For the ^{30}Si induced reactions (figure 5.12), the lowest energies exhibit two distinct components in the MADs and mass projections; a mass-asymmetric component focused at forward and backward angles and a mass-symmetric component for all θ_{cm}. As energy decreases, we see a gradual increase in counts for asymmetric splits between the elastic

and mass symmetric peaks (between $M_R = 0.2$ and 0.4 at backward angles and between $M_R = 0.6$ and 0.8 at forward angles). At the lowest energy this asymmetric component is clearly visible in the mass ratio distribution as well. At the highest energies we only see the mass-symmetric component. The MADs at the highest energies show no dependence of mass ratio on the centre-of-mass angle. In the mass projections there is a clear increase in counts in the symmetric component, relative to the asymmetric component, with increasing energy.

The various mass components in these reactions are quantified by fitting the mass distributions. The mass distributions at the highest energies required a single Gaussian fit. For the lower energies, the presence of an asymmetric mass component called for a fit using three overlapping Gaussians.

The relative strengths of the asymmetric and symmetric components are quantified in figure 5.13. We see that for both reactions there is a mass asymmetric quasifission component at sub barrier energies that is strongest at the lowest energies and becomes weaker with increasing energy. For the ^{24}Mg induced reactions only the two lowest energies have a visible mass asymmetric component. For the ^{30}Si induced reactions, the mass asymmetric component peak is present at all energies. The mass asymmetric quasifission yield varies significantly between the two reactions. The ^{30}Si induced reaction has a much stronger mass asymmetric quasifission component as compared to the ^{24}Mg induced reaction. (Note that this is seen for other pairs of reactions forming the same CN as well and therefore will be discussed in the next section.)

Figure 5.14 shows the masses of the asymmetric (heavy) and symmetric peaks vs. energy for both reactions. It is sufficient to look at only the heavy and symmetric peaks since the light peak corresponds to the complementary projectile-like fragment and reveals no additional information. The two solid lines indicate A=131 (symmetric fission for this system) and A=208.

The mass splits seen in figure 5.14 show that the target-like fragment for both reactions lies close to A=208 and does not move significantly towards mass symmetry with increasing energy. Averaging over energies where a mass-asymmetric component is observed gives a light-heavy fragment mass of 62-199 $\pm$ 12u for the ^{30}Si induced reactions and 62-199 $\pm$ 2u for the ^{24}Mg induced reactions. Note that the uncertainties presented here (and for subsequent reactions) indicate the uncertainty in the average. The counts in

the asymmetric QF peaks are not enough for a detailed investigation. A detailed investigation is presented for subsequent reactions, where a stronger mass asymmetric quasifission component is observed.

5.2.3 Reactions forming ^{266}Sg

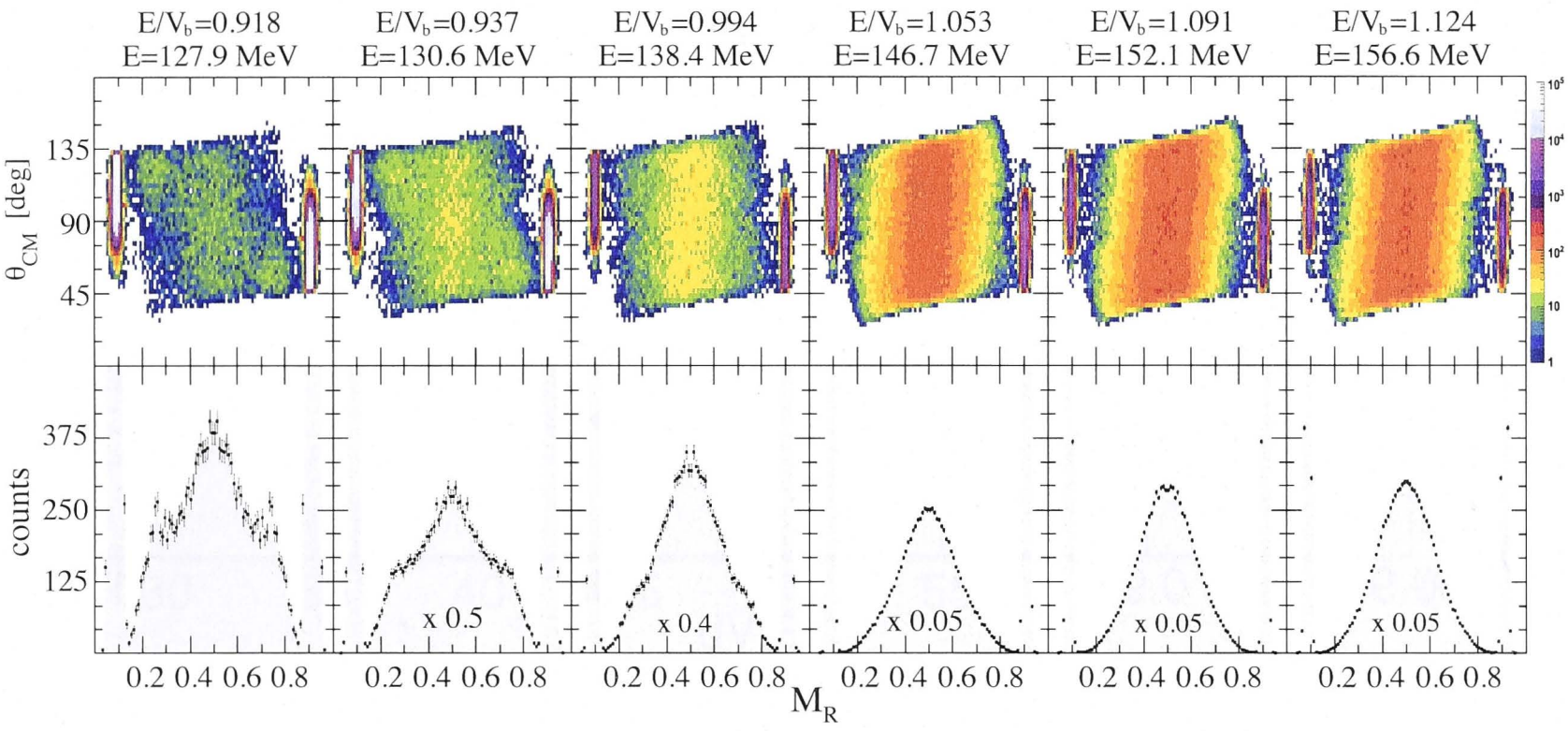

Figure 5.15: Mass angle distributions for FMT events in the reaction ^{28}Si + ^{238}U ($V_{b,cm}$ = 139.34 MeV). The lower frames show the corresponding projected mass-ratio distributions.

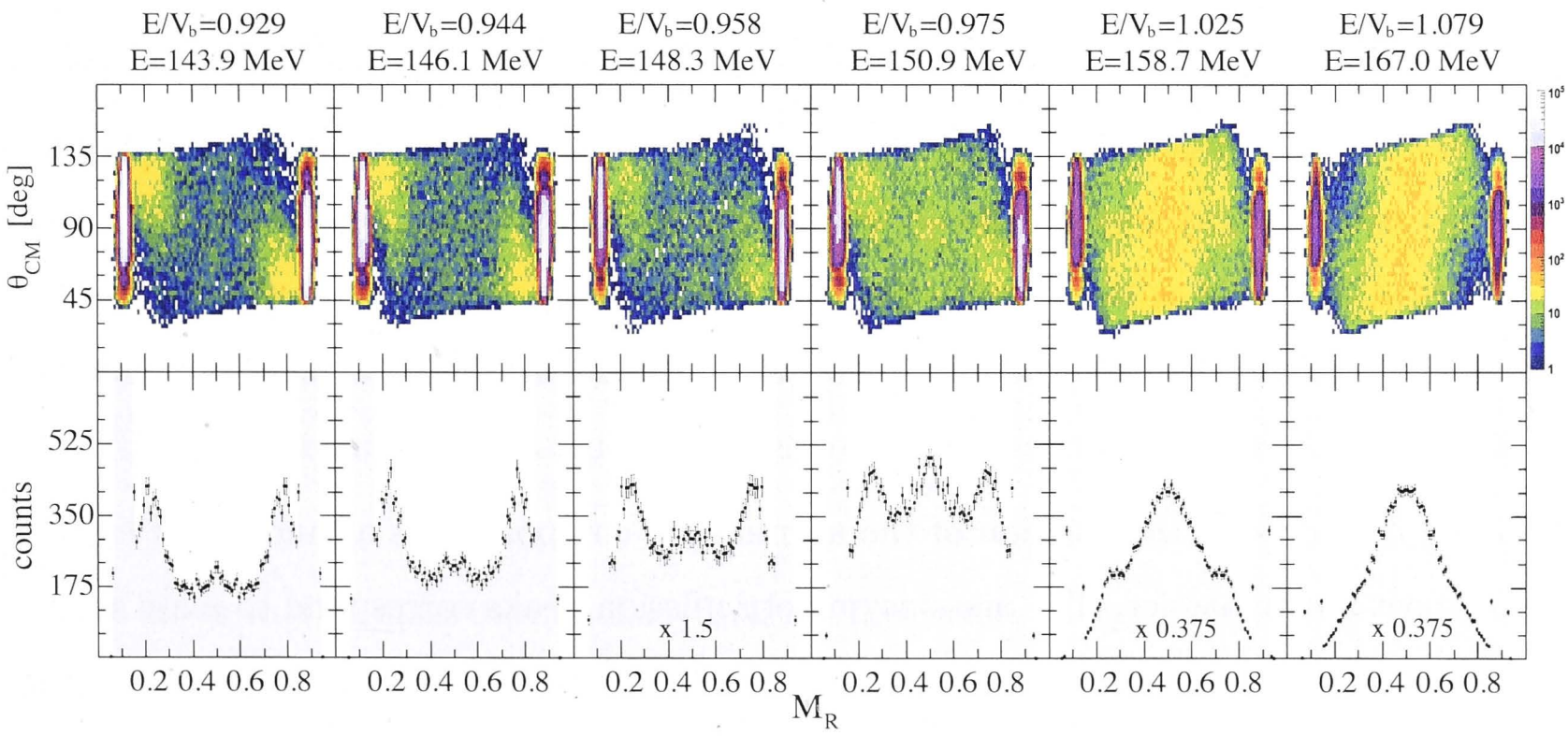

Figure 5.16: Mass angle distributions for FMT events in the reaction ^{34}S + ^{232}Th ($V_{b,cm}$ = 154.79 MeV). The lower frames show the corresponding projected mass-ratio distributions.

Figures 5.15 and 5.16 show the mass angle distributions for all the measured energies (E_{cm}) for the ^{28}Si and ^{34}S induced reactions respectively. Two distinct components are

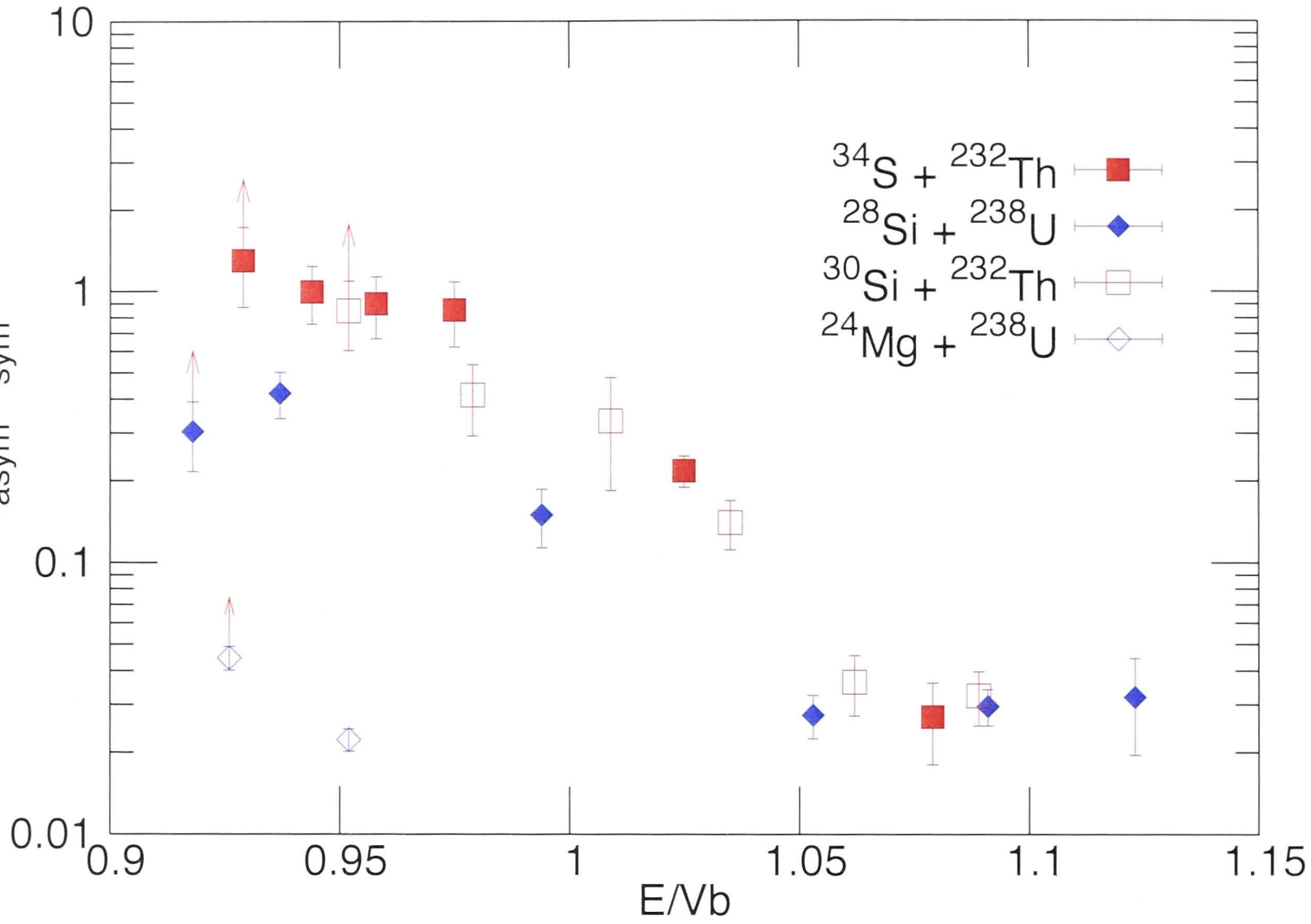

Figure 5.17: Relative yield of the asymmetric and symmetric mass components, for the four heaviest reactions presented so far, with respect to E/V_b. The arrows on the lowest energies indicate that the yield represents a lower bound to the mass-asymmetric quasifission flux.

evident in the MADs and the mass projections. At energies below the barrier we see a mass asymmetric component that is strongly focused at forward (heavy fragment) and backward angles (light fragment). At energies above the barrier we see a more mass-symmetric component with no particular angular focusing. In the mass projections for both reactions there is a clear increase counts in the symmetric component with increasing energy.

Figure 5.17 depicts the fraction of the asymmetric component as a function of energy with respect to the barrier. The mass-asymmetric fission peaks correspond to mass asymmetric quasifission while the symmetric fission peaks correspond to either fusion-fission or mass-symmetric quasifission.

From figures 5.16, 5.15 and 5.17 we see that for both reactions there is a strong mass asymmetric quasifission component at sub barrier energies. Both reactions also have a small mass asymmetric component at energies above the barrier. In addition to this, at the highest energies the MADs for both reactions measured show a correlation between

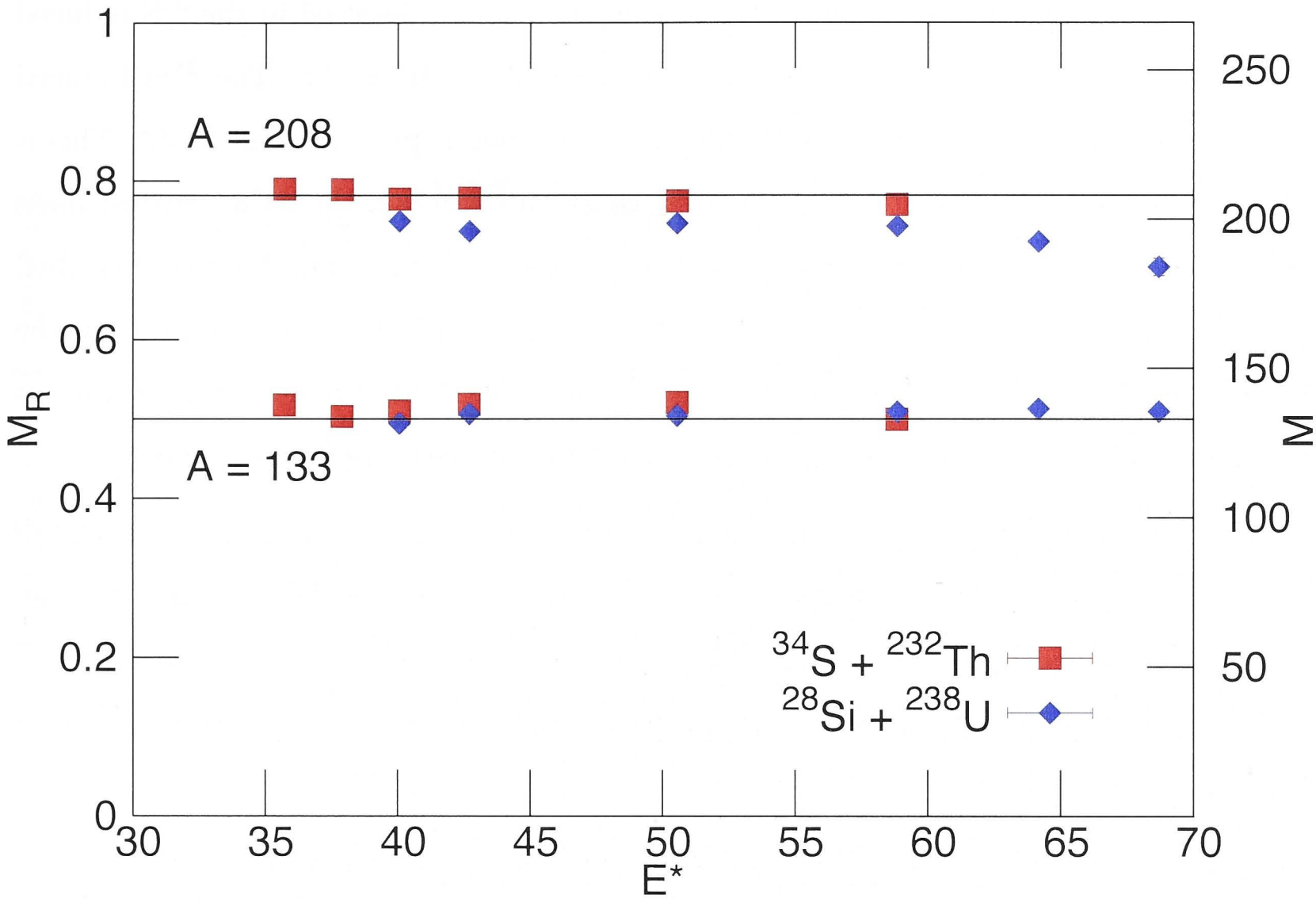

Figure 5.18: Masses of the heavy and symmetric fragments for both reactions as a function of Excitation Energy E*. The two solid lines mark A=133 (symmetric fission) and A=208. The error bars are smaller than the size of the point markers.

the mass ratio and the centre-of-mass angle. There is a significant overlap between mass symmetric and mass asymmetric fission at these energies. This might be due to the presence of FF, mass asymmetric quasifission (QF) and mass symmetric quasifission (MSQF) events. Nonetheless, the quasifission component is visible even at the highest energies. The mass asymmetric quasifission yield varies significantly between the two reactions. The ^{34}S induced reaction has a much stronger component as compared to the ^{28}Si induced reaction.

The drop in the mass-asymmetric flux, as the beam energy passes over the fusion barrier, seen in figure 5.17 may be due to the role of deformation alignment in the entrance channel as observed in ref. [36]. In ref. [36] it was found that collisions at low beam energies, where only contact with the tips of the target nuclei are possible, result in quasifission. Collisions above the fusion barrier, where all orientations of the target nuclei result in contact, lead to a mix of quasifission and fusion-fission events.

Figure 5.18 shows the masses of the asymmetric (heavy) and symmetric peaks vs.

energy for both reactions. On average the asymmetric splits observed in the ^{34}S induced reactions correspond to a light-heavy fragment mass of 62-204 $\pm$ 4u. The ^{28}Si induced reaction has a more symmetrised light-heavy fragment mass split of 71-195 $\pm$ 4u. This is partially due to the fact that the highest energies for this reaction show the greatest mass equilibration. If we average over energies below E*=60 MeV (matching the range studied for the ^{34}S induced reactions) the average is 88-198 $\pm$ 3u, still more symmetric than the ^{34}S induced reactions. The mass splits indicate that the doubly magic shell closure at ^{208}Pb might be playing a role in the outcome of the asymmetric reaction channel.

The more symmetric splits seen at the two highest excitation energies are not MSQF events but QF events. The increased mass symmetry of the splits might be due to shell effects being washed out as excitation energy increases. This damping of shell effects is apparent only at very high excitation energies, perhaps due to the large shell correction energy of ^{208}Pb.

The ^{34}S induced reactions were studied in further detail because of the large asymmetric quasifission component at low energies and better statistics as compared to the ^{28}Si induced reactions. For the ^{34}S induced reaction the lowest 3 energies were summed to boost statistics and 5° cuts in centre-of-mass scattering angle were made. For each angular cut the mass projections were fitted with up to three overlapping Gaussians. Figure 5.19 shows the mass ratio of the heavy and symmetric peaks vs. scattering angle obtained from these fits. Note that the bars correspond the widths (σ_M) of the respective peaks and do not overlap. The uncertainties on the centroid positions are on average as big as the point markers.

Following contact (for non-central collisions) the dinuclear system begins rotating and the angle it rotates through is directly proportional to the reaction time. Thus we can relate the outgoing angle of fragments (the measured angle) to the reaction time scale. For the heavy fragment a forward outgoing angle corresponds to short reaction times. Similarly for the light fragment a backward outgoing angle corresponds to short reaction times. If the dinuclear system separates after a slightly longer contact time, the outgoing angle of the heavy fragment will be more backward, while that of the light fragment will be more forward. This is explained in detail in Chapter 4 and Refs. [16, 35].

In figure 5.19, at the most forward angles the fragments correspond to the nucleus ^{208}Pb (assuming N/Z equilibration takes place early on in the collision [110]) which is

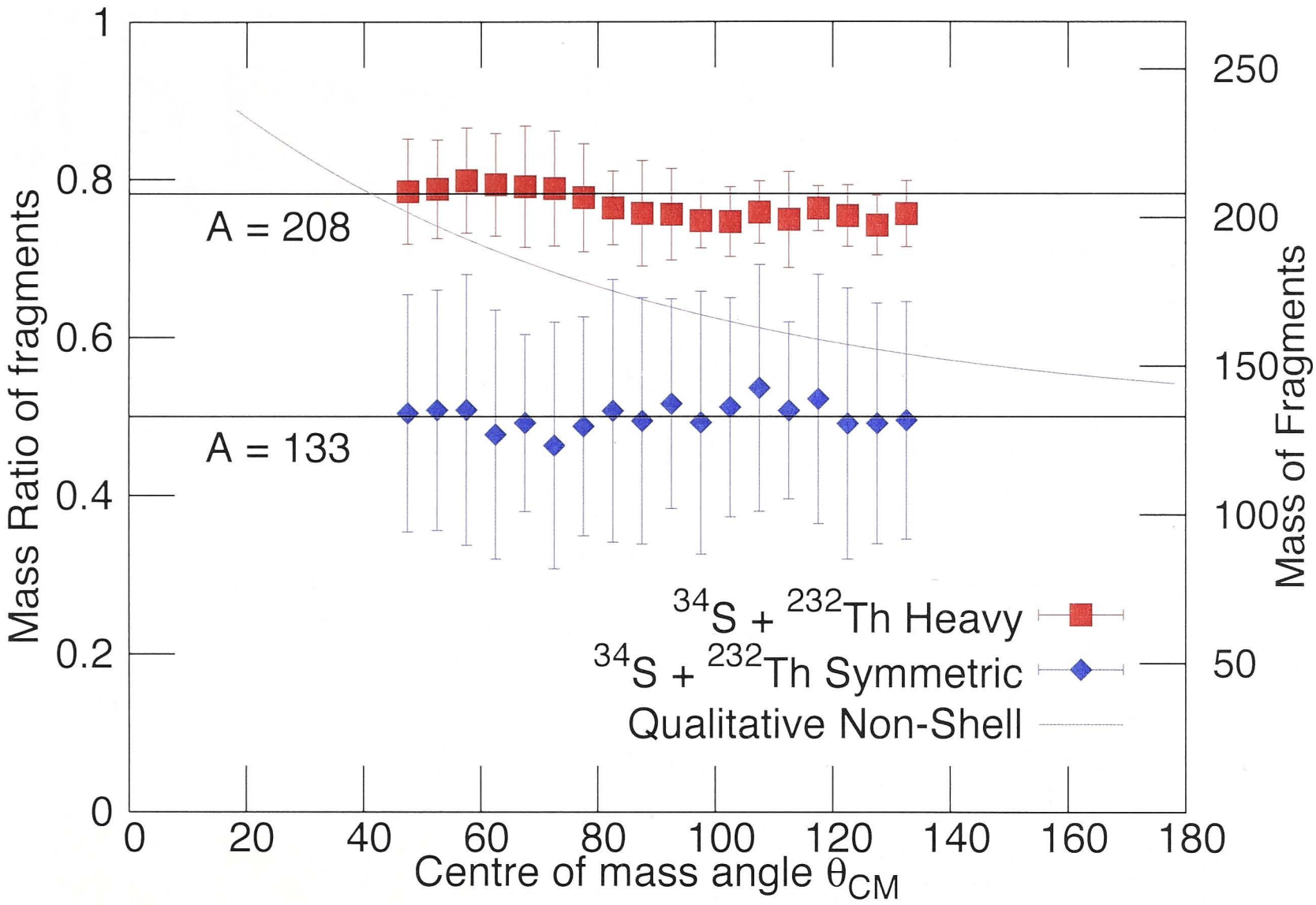

Figure 5.19: Masses of the heavy and symmetric fragments measured for the ^{34}S + ^{232}Th reaction vs. centre of mass scattering angle. Note that the bars shown here correspond to the widths (σ) of the respective peaks and that the uncertainties on the centroids are on average as big as the point markers. The two solid lines mark A=133 (symmetric fission) and A=208. The curved line depicts the expected qualitative mass evolution of the heavy peak in the absence of any shell effects.

the complementary light partner of ^{58}Cr. At the most backward angles the fragments correspond to ^{197}Au and ^{69}Co. The mass drift, of the heavy fragment, from $A = 208$ to $A = 197$ varies only slightly with respect to scattering angle. Thus the system exhibits a very strong tendency of splitting into two fragments with the heavier being in the $A = 208$ region. Since the outgoing angle is directly correlated with the interaction time of the dinuclear system this implies that once the dinucleus reaches the ^{208}Pb-^{58}Cr configuration the mass drift is slowed. In the absence of a shell closure we expect a smooth evolution of the (light fragment) mass from asymmetric splits at the most backward angles to more symmetric splits at forward angles. Therefore, the only explanation for the behaviour we see is that the doubly magic shell closure at ^{208}Pb strongly influences the evolution of the dinuclear system.

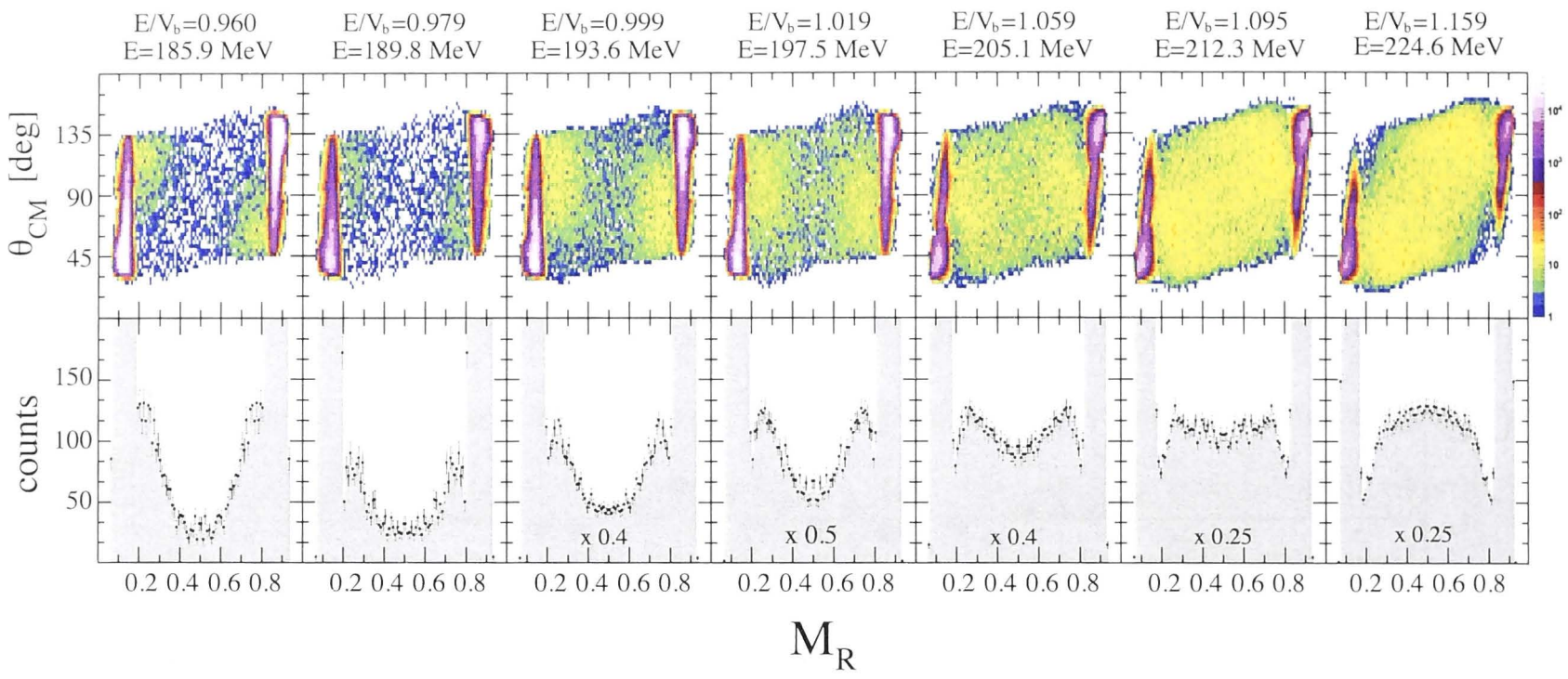

Figure 5.20: Mass angle distributions for FMT events in the reaction ^{40}Ca + ^{232}Th ($V_{b,cm}$ = 193.77 MeV). The lower frames show the corresponding projected mass-ratio distributions.

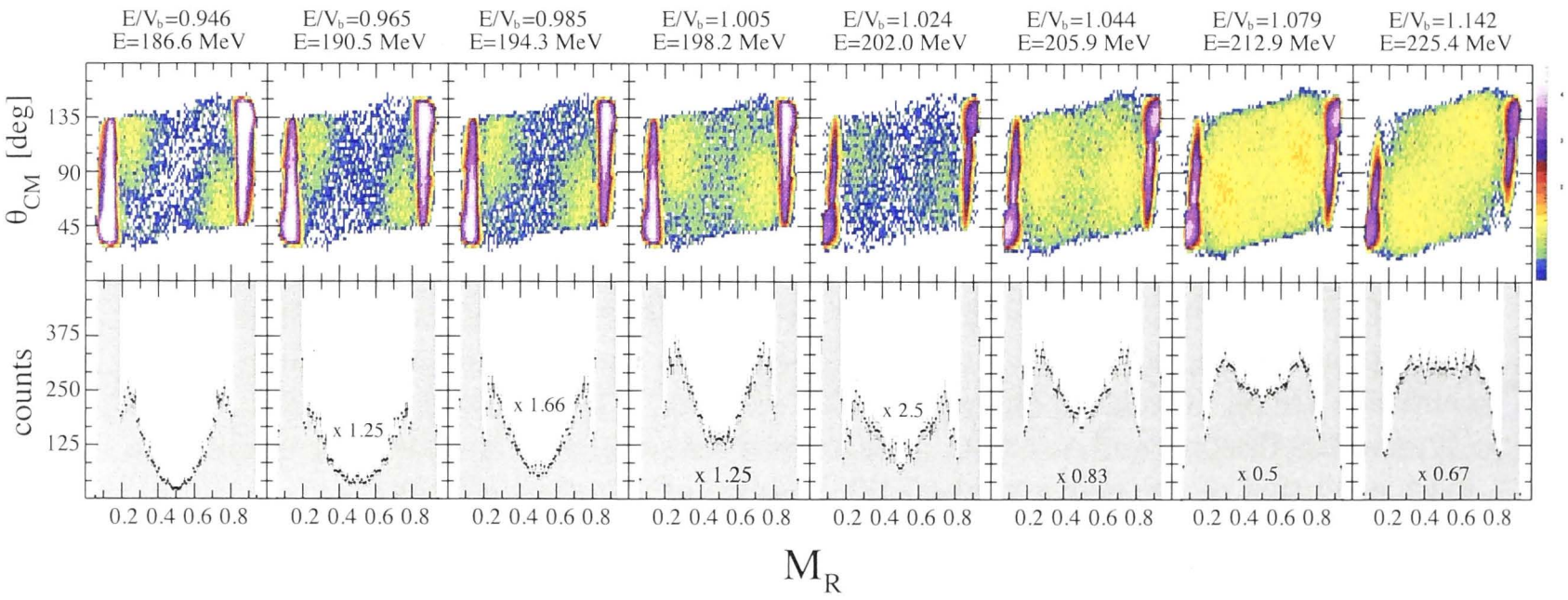

Figure 5.21: Mass angle distributions for FMT events in the reaction ^{40}Ca + ^{238}U ($V_{b,cm}$ = 197.3 MeV). The lower frames show the corresponding projected mass-ratio distributions.

5.2.4 ^{40}Ca Reactions forming ^{272}Ds and ^{278}Cp

Figures 5.20 and 5.21 show the mass angle distributions for all measured energies (E_{cm}) for the ^{40}Ca induced reactions.

The MADs for both reactions have a strong mass asymmetric component at all energies studied. The mass symmetric yield is only significant at the highest energies. Here the asymmetric component is still apparent in the MADs and the mass distributions. There is significant overlap between the symmetric and asymmetric channels at the highest energies. From the mass distributions at the three highest energies we see that the reaction with ^{238}U has a stronger asymmetric component, relative to the symmetric component, as compared

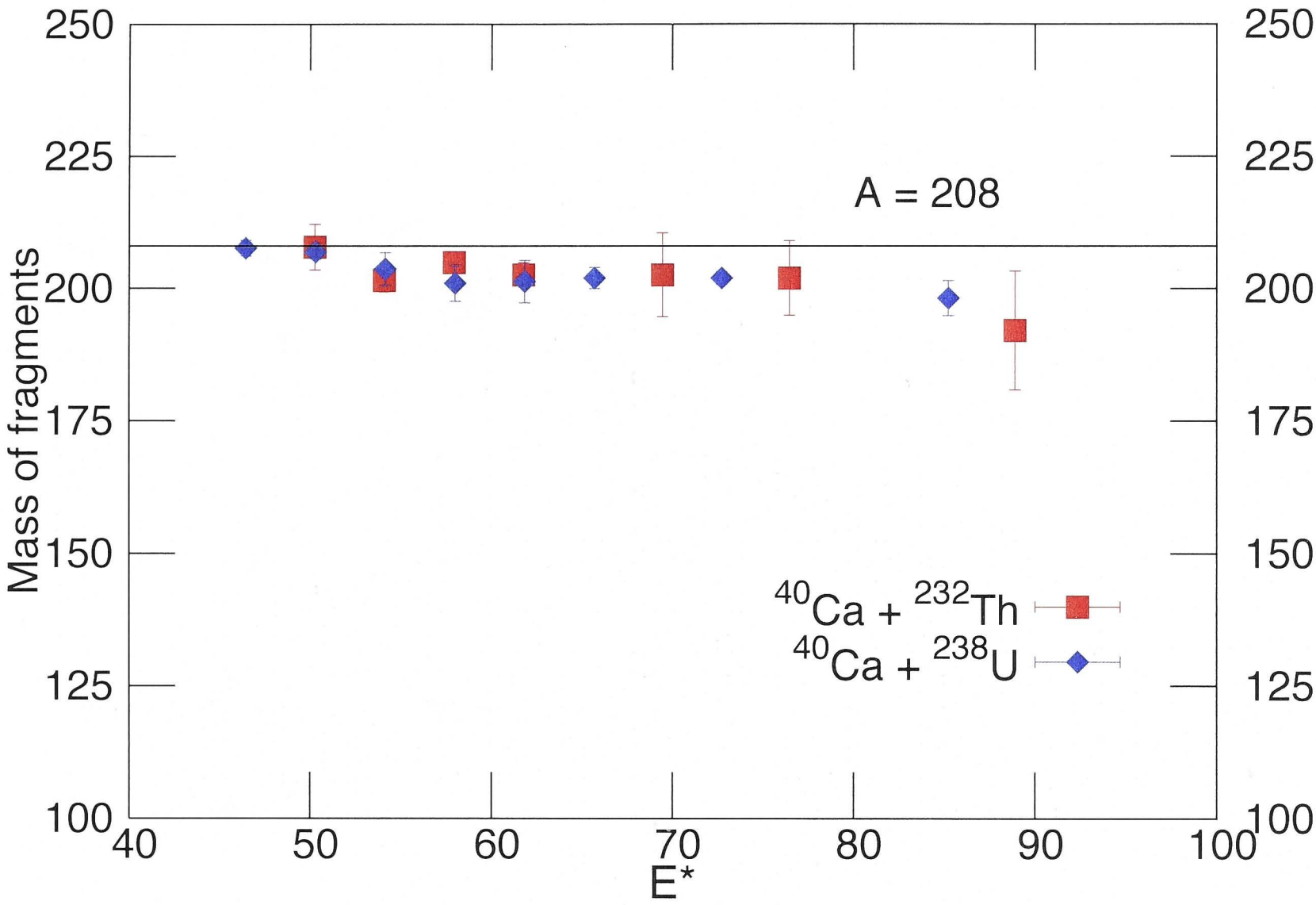

Figure 5.22: Masses of the heavy fragments for both reactions as a function of Excitation Energy E*. The solid line marks A=208.

to the reaction with ^{232}Th.

For the ^{40}Ca induced reactions quantifying the peak positions in a systematic manner was not straightforward. At the lowest energies the mass asymmetric peaks lie very close to the elastic peaks and therefore do not have a profile consistent with a Gaussian function. Moreover, a symmetric peak is not visible at these energies. Hence fitting the mass distribution with overlapping Gaussians was not possible. At higher energies there is a significant overlap with symmetric splits that have a very wide distribution. A fit of overlapping Gaussian was not possible in this case either.

To systematically quantify the mean mass splits at all energies we had to constrain the mass range for some of the fits, in contrast to the fitting protocol employed for previous reactions. For the lowest energies, where we do not see any contribution from the mass symmetric channel, we restricted the fitting from $M_R = 0.5$ to 0.8. For energies where we observe counts around mass symmetry as well, we fit the full range between the elastic peaks ($M_R = 0.2$ to 0.8) with up to two Gaussians, with the centroid of the mass symmetric peak constrained to $M_R = 0.5$.

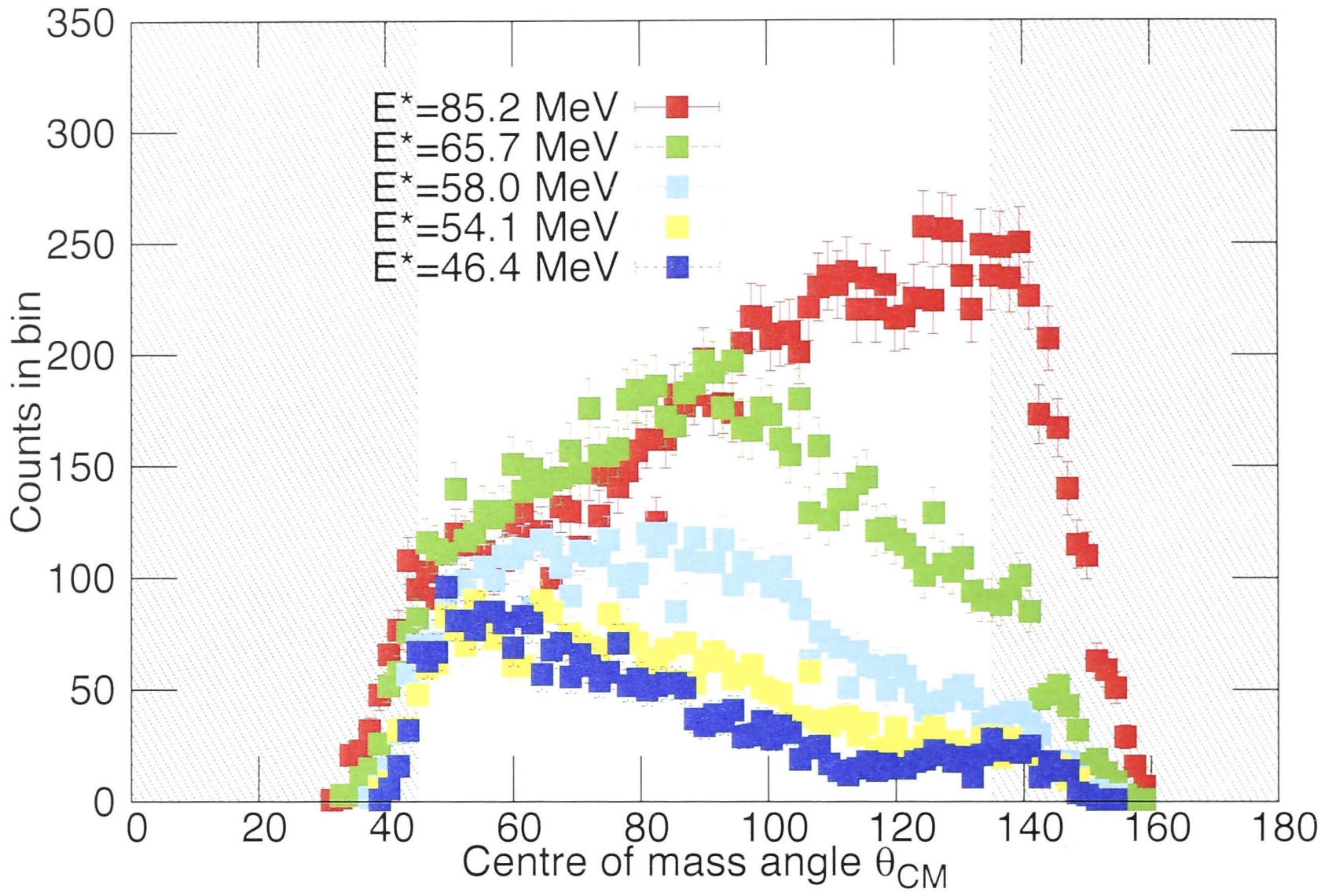

Figure 5.23: Angular distributions for M_R between 0.6 and 0.8 for the ^{40}Ca + ^{238}U reaction. Note that a subset of all the energies measured is shown. The region between the shaded area corresponds to full angular coverage.

Figure 5.22 depicts the mass of the heavy peak in these reactions as a function of excitation energy E*. Averaging over all energies studied, the asymmetric splits observed in ^{40}Ca reactions with ^{238}U and ^{232}Th correspond to a light-heavy fragment mass of 74-204 $\pm$ 8u and 70-202 $\pm$ 16u respectively.

To further investigate this tendency to split in the A=200 region we look at the evolution of the mass splits as a function of angle. We cannot follow the ^{34}S example here because of the relatively larger energy step between the lowest three energies and low statistics. Instead we look at the angular distribution of the asymmetric peak as a function of energy.

Figures 5.23 and 5.24 depict the angular distributions (full y-projections) between M_R= 0.5 and 0.8, for the reactions with ^{238}U and ^{232}Th respectively. Note that only a subset of all the energies measured are shown here. To avoid any bias due to a finite geometrical acceptance we only focus on the region between the shaded area that corresponds to full angular coverage. In this unshaded region we see that the angular distribution evolves in angle from being forward focused to more backward focused with increasing energy. We have already seen, from figure 5.22, that the mass splits corresponding to the asymmetric

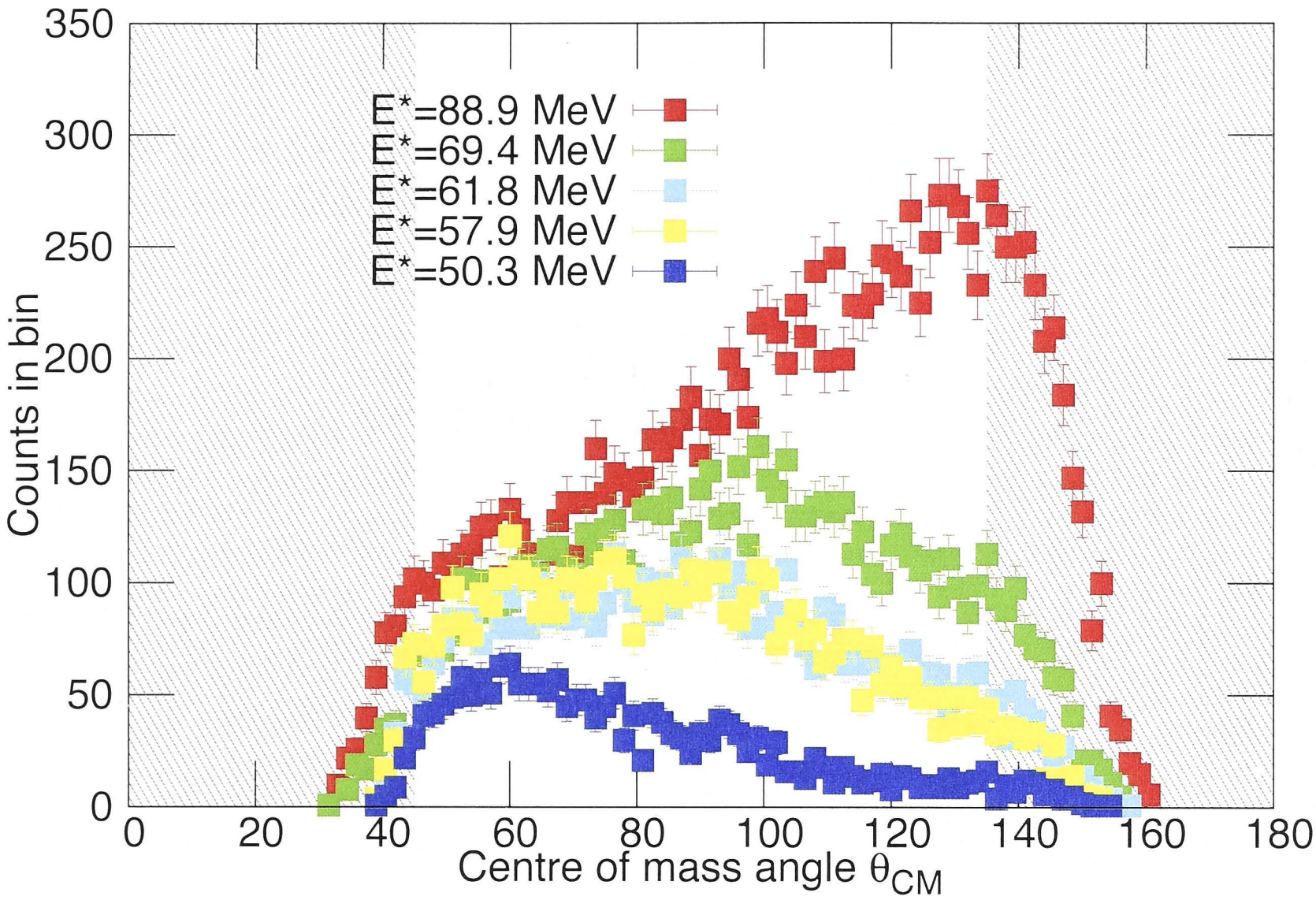

Figure 5.24: Angular distributions for M_R between 0.6 and 0.8 for the ^{40}Ca + ^{232}Th reaction. Note that a subset of all the energies measured is shown. The region between the shaded area corresponds to full angular coverage.

QF channel remain consistent around $A = 204$ for the ^{238}U target and around $A = 202$ for the ^{232}Th target.

The mass drift (from $A \approx 208$ to $A \approx 194$) varies only slightly with respect to the change in angular focusing from forward to backward angles. Thus the system exhibits a very strong tendency of splitting into two fragments with the heavier being in the $A = 208$ region. Since the outgoing angle is directly correlated with the interaction time of the dinuclear system, this implies that once the dinucleus reaches the configuration where the target like nucleus has $A \approx 208$, the mass drift is slowed. From the slow evolutions of the mass splits, as a function of energy and angle, it is clear that the doubly magic shell closure at ^{208}Pb influences the outcome of the asymmetric reaction channel for both reactions.

We will return to the ^{40}Ca + ^{238}U reaction in the next chapter, where a theoretical investigation is presented.

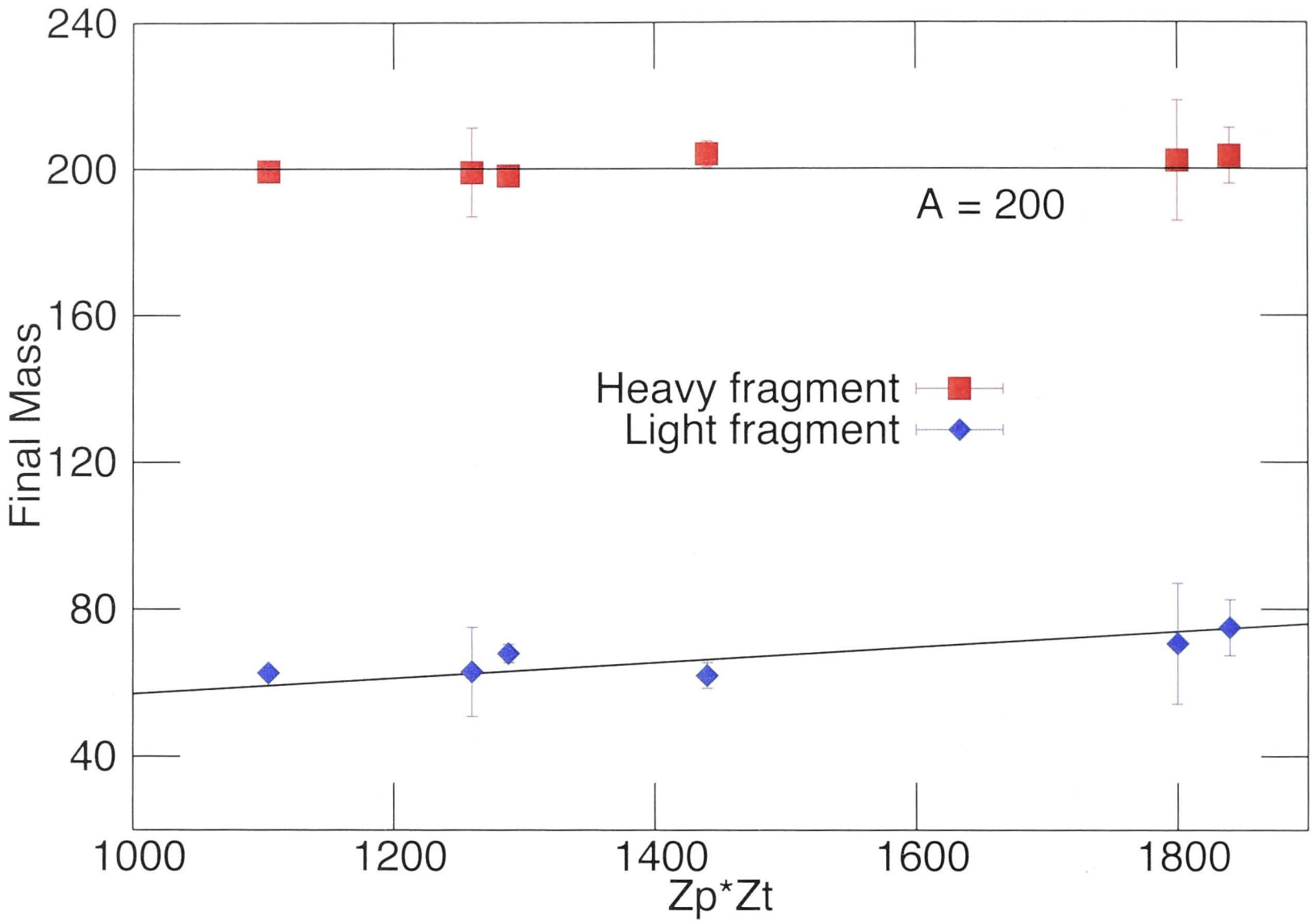

Figure 5.25: Average masses of the heavy and light fragments as a function of Z_pZ_t for reactions where mass asymmetric quasifission was observed. The numbers are listed in table 5.2

5.3 Discussion of all Reactions

In the previous section the reactions studied were presented in pairs, in increasing mass of the composite nucleus. Here we discuss attributes shared by the reactions and some global features that emerge from looking at all of the reactions.

5.3.1 Shell Effects

In Chapter 4 we discussed the importance of eliminating three body events because of their large flux and overlap, in MADs, with binary fission events. The nature of events has important implications on the shell effects seen in this work since the three body flux can greatly perturb the binary fission mass distribution. Any conclusions based on the mass distributions are therefore only relevant to the binary fission flux. However the reaction time scales inferred by the MAD technique remain unaffected.

Figures 5.25 shows the variation of the average mass split as a function of entrance

channel charge produce Z_pZ_t for the reactions of interest. The mass number of the heavy group is approximately a constant around A=200, whereas that of the light group varies to account for the total mass of the system. The nearly constant position of the heavy group is observed for all systems where mass asymmetric quasifission is observed. The pronounced stability of this position is an indication of the influence of the closed proton (Z=82) and closed neutron (N=126) shells found in this mass region.

Table 5.2: Table of reactions of interest. The columns correspond to the entrance channel charge product, average mass of the heavy peak determined from the mass distributions and calculated mass of the heavy fragment (see text). Except for the ^{40}Ca induced reactions, all other reactions comprise pairs that form the same compound nucleus.

Reaction	Z_pZ_t	A_{CN}	M_H	M_H^{Shell}
^{40}Ca + ^{238}U	1840	278	204±8	204
^{40}Ca + ^{232}Th	1800	272	202±16	201
^{34}S + ^{232}Th	1440	266	204±4	198
^{28}Si + ^{238}U	1288	266	198±3	198
^{30}Si + ^{232}Th	1260	262	199±12	196
^{24}Mg + ^{238}U	1104	262	199±2	196
^{18}O + ^{232}Th	720	250	139±4	190
^{12}C + ^{238}U	552	250	139±2	190

Table 5.2 lists the average mass of the heavy peak, determined from the mass distributions, for each reaction where an asymmetric peak was observed. This summarises the outcomes of the various reactions studied. The heaviest reactions have an asymmetric split corresponding to mass-asymmetric QF whereas the lightest two reactions have mass-asymmetric splits corresponding to CN fission.

Also listed is the predicted mass of the heavy peak M_H^{Shell} for each reaction based on the following basic assumptions/calculation [108]. The Z=82, N=126 (doubly magic ^{208}Pb) shell closure strongly influences the asymmetric quasifission reaction channel (seen in the current work and in refs [71, 108, 109]). So far we have not focused on shell effects in the light fragment. It may be the case that closed shells at Z=28, N=50 affect the mass drift in the dinuclear system. This could lead to a shift of the mass-asymmetric quasifission peak. We used these shell closures to calculate the masses of the corresponding heavy fragments. We assumed that the heavy quasifission fragment was influenced by the Z=82,

N=126 shell closure giving a calculated heavy fragment mass of 208u, while the light quasifission fragment was influenced by the Z=28, N=50 shell closure giving a calculated heavy fragment mass of A_{CN}-78u. Averaging over 208u and A_{CN}-78u gives M_H^{Shell} in Table 5.2.

The values calculated from these basic assumptions agree well with the experimentally determined ones. This confirms that, averaged over all energies, the mass-asymmetric QF yield is influenced by a mixture of the Z=82, N=126 and Z=28, N=50 shell closures. Since the lightest two reactions proceed via CN fission, the comparison with M_H^{Shell} is not applicable. Here the system forms a compact shape prior to fission and therefore the outgoing fragments are not sensitive to the shell effects around ^{208}Pb. On the other hand for the six heaviest reactions of interest, the quasifission flux arises from the scission of an elongated dinuclear system which is sensitive to shell effects around ^{208}Pb during its shape and mass evolution. The same calculations were employed in [108] and a similar agreement with experiment was observed for reactions of projectiles ranging from ^{26}Mg to ^{64}Ni with targets of ^{234}Cm and ^{238}U.

We now compare our experimental results with a macroscopic-microscopic model by looking at an adiabatic Potential Energy Surface (PES). Figure 5.26 shows a two dimensional (PES) for the ^{266}Sg system generated using the macroscopic-microscopic model of Y. Aritomo [55, 56]. The distance parameter z characterises the radial distance between the centres of the two interacting nuclei R, scaled to the radius of the compound nucleus R_{CN} i.e. $z = \frac{R}{R_{CN}}$. We see a wide valley corresponding to ^{208}Pb at a mas ratio of $M_R = 0.78$ and $z \approx 1.25$. Such a PES is typical for the six heaviest reactions studied in this work. The prediction of a wide local minimum around ^{208}Pb is consistent with the experimental results presented in this chapter.

5.3.2 Evidence for MSQF and Quasifission Thresholds

Figure 5.27 shows the RMS of the mass distributions between M_R= 0.2 and 0.8 as a function of excitation energy. For all reactions, except for those induced by ^{18}O and ^{12}C, we see an decrease in RMS value of the mass distribution with increasing energy. The decreasing RMS value reflects the decrease in the mass-asymmetric channel as energy increases.

Figure 5.28 shows the widths of the mass-symmetric peak, extracted from the fits, as

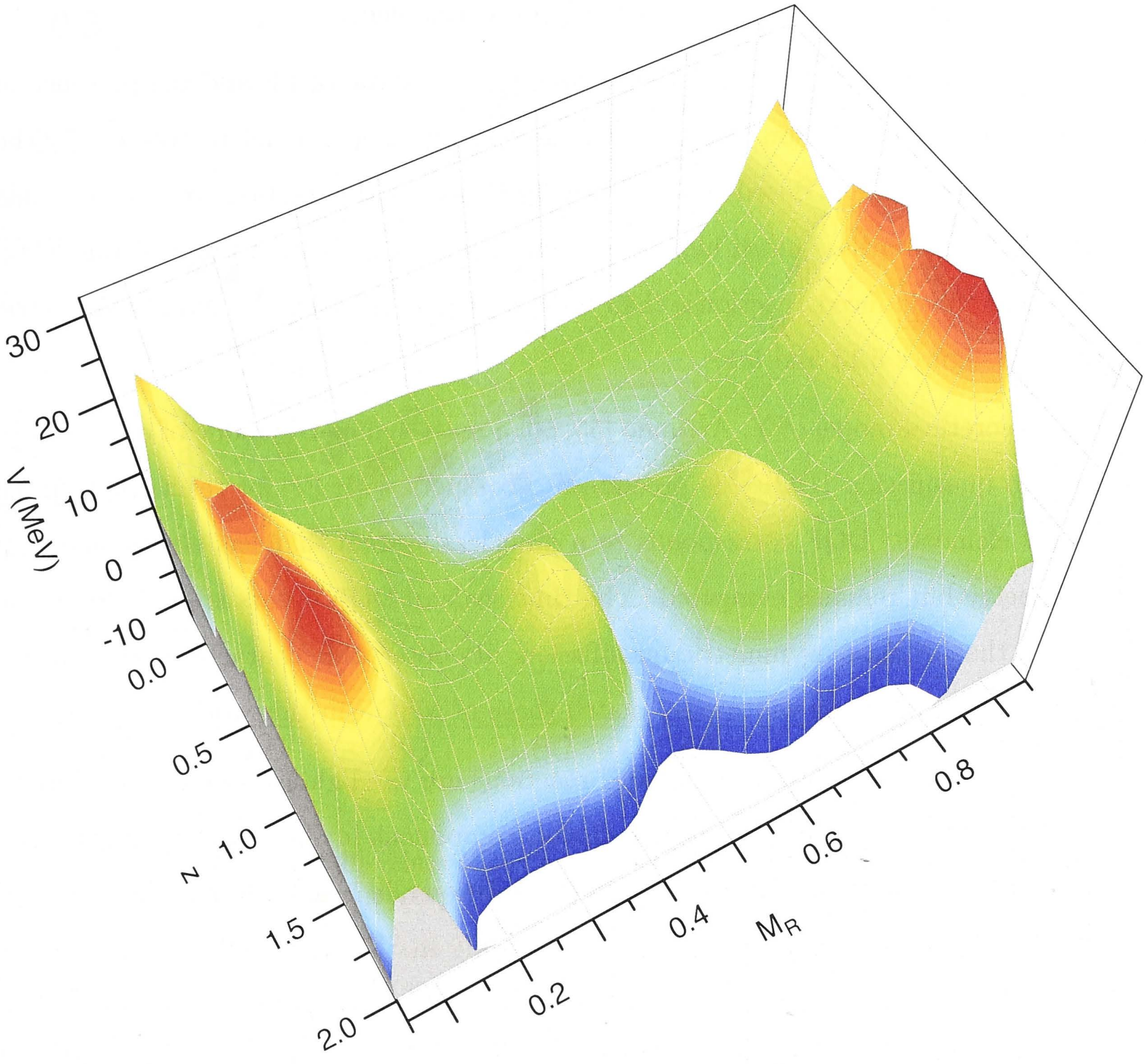

Figure 5.26: Potential Energy Surface for reactions forming the ^{266}Sg composite system. The axes correspond to the distance parameter z (see text), mass ratio M_R and potential energy V.

a function of excitation energy. The ^{40}Ca induced reactions did not have a systematic mass-symmetric peak and hence are not shown. We recall that reactions with a mass-symmetric peak with σ_{M_R} exceeding 0.07 [35] are thought to have a significant MSQF flux. The global trend for all reactions is a decrease in the width of the mass-symmetric peak with increasing energy. The width of the mass-symmetric peak increases with the mass of the composite system as well. This implies that the MSQF flux increases with the mass of the composite system and decreases as excitation energy increases. We conclude that all reactions, except for those induced by ^{18}O and ^{12}C, have a significant MSQF flux. The mass-symmetric peaks for the ^{18}O and ^{12}C induced reactions are not characterised by a **single** Gaussian, as discussed in Section 5.2, and hence do not correspond to MSQF.

The data from these reactions are plotted only for consistency.

The observable characteristics of MSQF overlap with those of FF and the presence of MSQF implies that the fusion fission flux is not simply proportional to the flux in the mass-symmetric channel. Based on the data presented in this section we can conclude that quasifission comprises much higher fraction of the total reaction flux, for the ^{24}Mg, ^{30}Si, ^{28}Si and ^{34}S induced reactions, than what is represented by the mass-asymmetric flux shown in figures 5.13 and 5.17.

In the theoretical model of Y. Aritomo [55, 56] a mass-symmetric mode of quasifission, termed deep quasifission (DQF), is predicted to compete with FF for reactions forming superheavy elements. DQF corresponds to a dinuclear system that has almost achieved mass-symmetry but remains elongated. The time scale of DQF events is predicted to be longer than that of mass-asymmetric quasifission. Its observable characteristics of mass-symmetry and a wide mass width σ_{M_R} match those of MSQF in this work.

In this work, the ^{24}Mg and ^{30}Si induced reactions are the lightest studied that have a MSQF component. The lack of any quasifission component in the reactions induced by the ^{18}O and ^{12}C projectiles suggests that these reactions lie below the threshold for QF and MSQF. Mass-asymmetric QF is only seen weakly in ^{24}Mg induced reactions and is much stronger in ^{30}Si reactions. This suggests that, for reactions with ^{238}U and ^{232}Th, the transitions from mass-asymmetric QF to MSQF to FF, lie around this combination of projectile and target. We infer that the transition from mass-asymmetric QF to MSQF occurs for Z_pZ_t below 1104, for reactions with ^{238}U and ^{232}Th. The transition from MSQF to FF lies between the reactions forming ^{250}Cf and ^{262}Rf, i.e. between $Z_pZ_t = 720$ and 1104, for reactions with ^{238}U and ^{232}Th.

The projectiles studied here do not include Fluorine, Neon and Sodium, lying between ^{18}O and ^{24}Mg. The corresponding jump in Z_pZ_t values is significant. It may be the case that the actual thresholds lie somewhere between these values; a point to be considered in future work.

5.3.3 Variation between Targets

From figures 5.13, 5.17 and 5.28, we consistently see that for reactions forming the same CN, reactions with ^{232}Th have a significantly higher QF and MSQF flux than those with

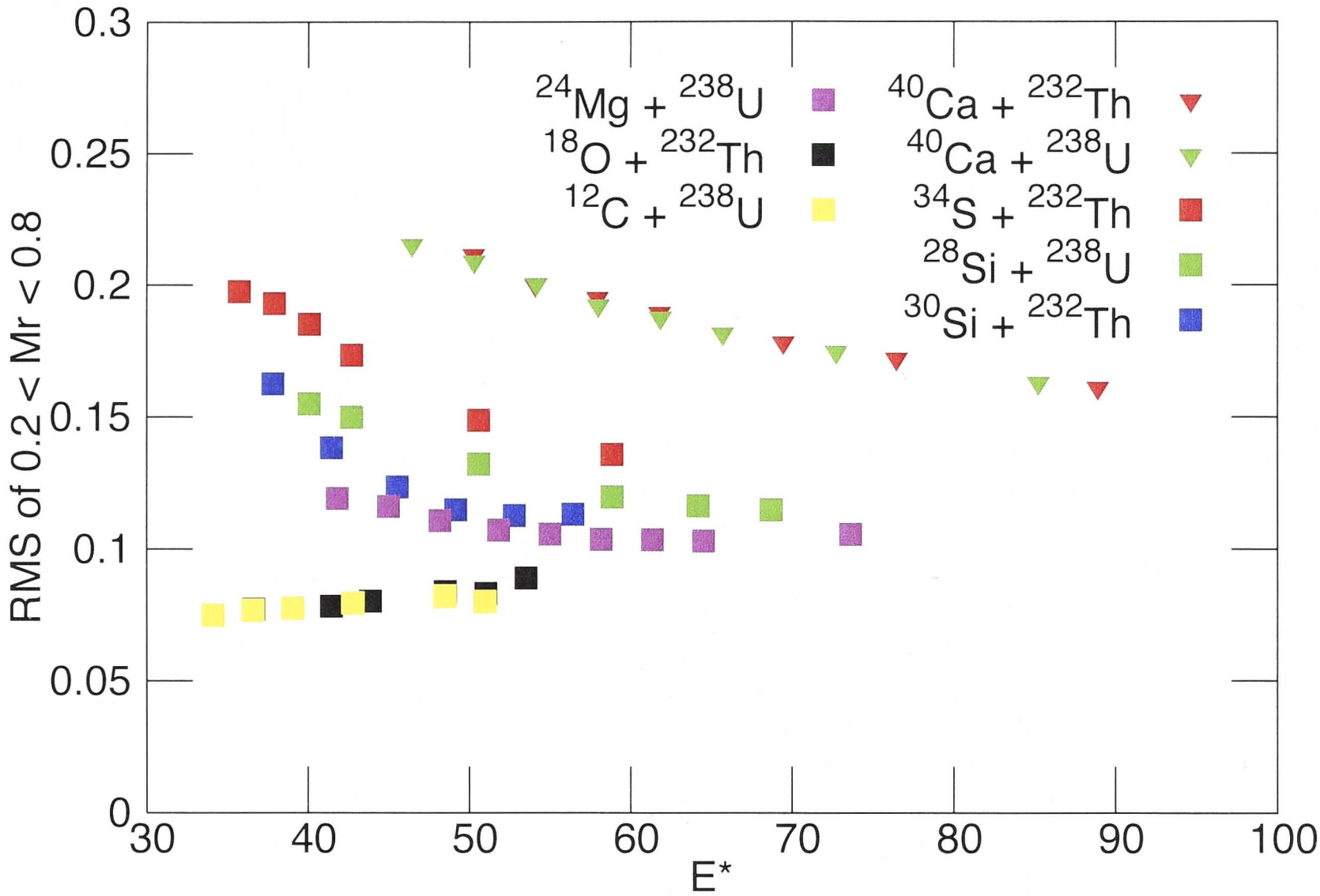

Figure 5.27: The RMS values of the mass distribution between M_R= 0.2 and 0.8, as a function of excitation energy E* for all reactions.

^{238}U. Secondly, we see that for a given target, as the projectile mass increases, the quasifission flux increases. These observations are explained by the dependence of quasifission on the entrance channel mass-asymmetry; a well studied phenomenon [17, 108, 111]. For reactions forming heavy systems, the quasifission flux increases with decreasing entrance channel mass-asymmetry.

5.4 Summary and Outlook

Mass-angle distributions were studied for reactions of ^{18}O, ^{30}Si, ^{34}S and ^{40}Ca projectiles with targets of ^{232}Th and ^{12}C, ^{24}Mg, ^{28}Si and ^{40}Ca projectiles with targets of ^{238}U, at energies below and above the Coulomb barrier. The target and projectile combinations were chosen such that, except for the ^{40}Ca induced reactions, all other reactions comprise pairs that form three unique compound nuclei. The compound nuclei produced ranged from ^{250}Cf to ^{278}Cp.

A detailed analysis of the MADs, mass ratio distributions and angular distributions indicated that the doubly magic ^{208}Pb shell closure strongly influences the evolution of

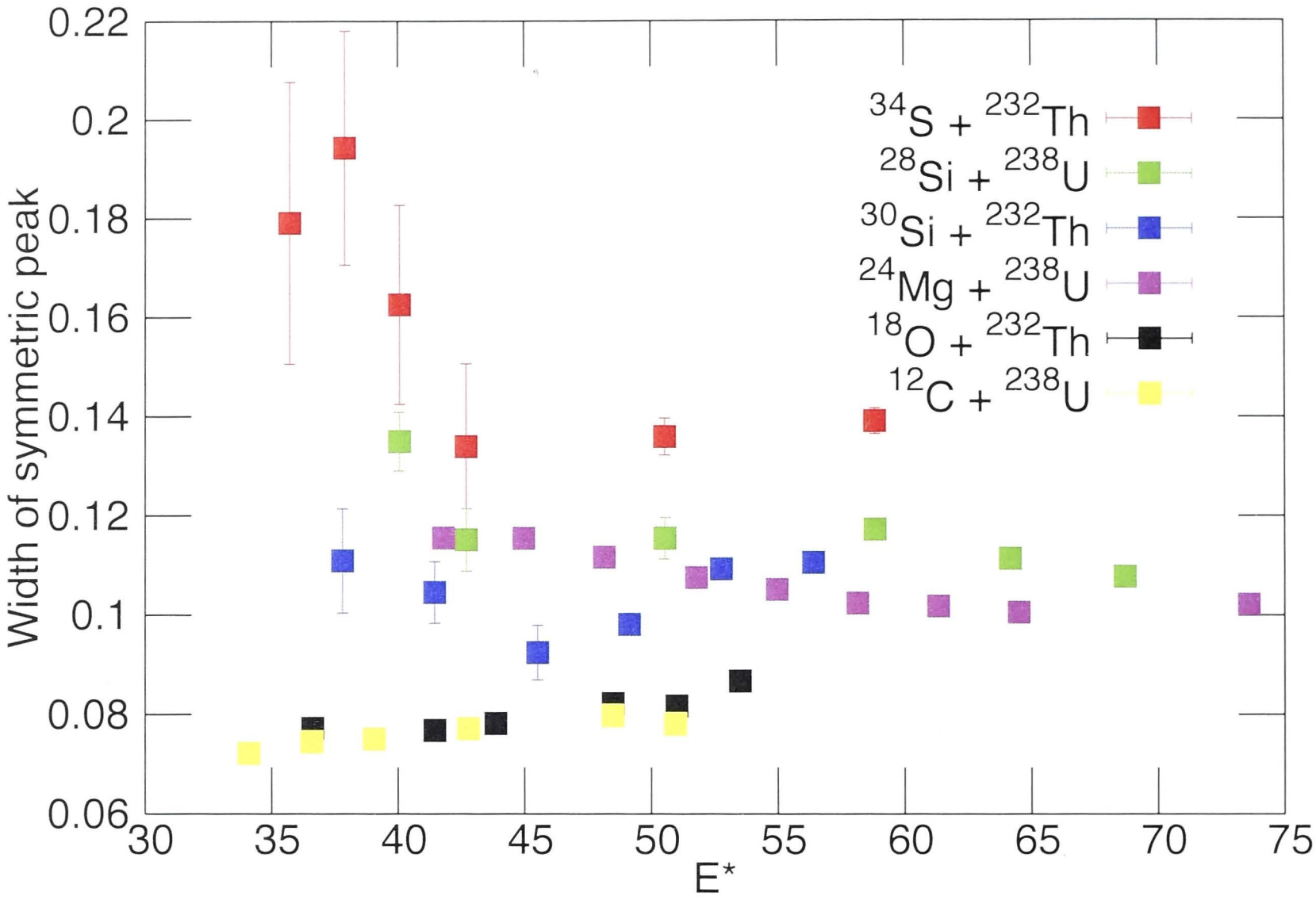

Figure 5.28: The width of the mass symmetric peak for Gaussian fits, as a function of excitation energy E*.

the dinuclear system. The presence of this shell effect was confirmed by exploiting the fact that we can relate the outgoing angle of fragments (the measured angle) to the reaction time scale. We found that the light-heavy mass split for the mass-asymmetric quasifission fragments did not vary in a smooth continuous fashion with the reaction time scale. Instead, the flow of mass between the target-like fragment and projectile-like fragment is slowed as the system passes through the configuration where the heavy fragment has A $\approx$ 208u. For example, in the ^{34}S + ^{232}Th reaction (*cf.* figure 5.19) we saw that the heavy fragment evolves in mass, from A=204 at the most forward angles (and correspondingly shortest quasifission times), to A=195 at the most backward angles (and correspondingly longer quasifission times). This effect was seen clearly in a range of reactions, including ^{34}S + ^{232}Th, ^{40}Ca + ^{232}Th and ^{40}Ca + ^{238}U. Evidence for this shell effect was seen in the ^{30}Si + ^{232}Th and ^{28}Si + ^{238}U reactions as well.

Based on the widths σ_{M_R} of the mass-symmetric splits, evidence for a strong component from mass-symmetric quasifission was also seen, for all but the two lightest reactions. The latter two reactions (^{18}O + ^{232}Th and ^{12}C + ^{238}U) were found to proceed via CN fission;

perhaps influenced by the Z=50 and N=82 shells. However it is very likely that deformed shell gaps are playing a role as well. In the work of Böckstiegel et al. [22] it was observed that fragment mass distributions arising from the fission of neutron deficient actinide nuclei had mass-asymmetric components. They were described by multiple modes of fission and it was concluded that the fragment splits were influenced by deformed shell closures around Z = 53 and N = 88. Similarly in the work of Itkis et al. [112], it was found that the weights of the fission channels are principally determined by an interplay of the neutron shells at N = 82 and N = 88 with the liquid-drop potential. Thus it is plausible that the mass splits seen for the ^{18}O + ^{232}Th and ^{12}C + ^{238}U reactions (A=139) may well be due to these deformed shells. A detailed study of the Total Kinetic Energies may shed more light on the origin of the fragment mass distributions for the reactions studied here. This is not the focus of the current work and is left for future research.

Finally, the large range of reactions studied allowed for a rough deduction of thresholds in Z_pZ_t, for reactions with ^{232}Th and ^{238}U, between mass-asymmetric quasifission, mass-symmetric quasifission and fusion fission.

These conclusions were possible only due to the detailed and comprehensive experimental measurements carried out in this work. The large area detectors that covered a wide angular range, combined with the versatility of the 14UD in delivering high quality beams was crucial. The work here adds to the existing body of experimental work that investigates the properties of quasifission, providing a rich testing ground for theories and dynamical models that attempt to predict the synthesis of superheavy elements. Such work will help understand and form a complete picture of the nuclear reaction process

Outlook

Some interesting questions were raised during the course of this work that lead the way for future experimental efforts:

- It would be worth studying the three body events in further detail. The author proposes experiments using MWPCs in conjunction with the double-sided silicon strip detectors (DSSD) [96] used in breakup measurements. Placing the DSSDs at forward angles would facilitate detection of transfer-fission events. This would allow a kinematic reconstruction of these events, independent of any assumptions or model calculations.

- To better define thresholds between mass-asymmetric QF, MSQF and FF, reactions with projectiles intermediate to the ones used here could be studied. These would include reactions of projectiles F, Ne, Na, Al, P, Cl, Ar and K with targets of ^{232}Th and ^{238}U. The author is confident that these reactions, studied using the large angular coverage of the CUBE detector system, would cover the range of reaction outcomes observed here and better define thresholds between them.

Chapter 6

Time-Dependent Hartree-Fock Calculations

The tenets of a good physical model are twofold: to make correct predictions and no (or few) incorrect ones; and as a secondary objective, to have a certain economy and elegance. It is judged by the extent to which its predictions agree with experimental observations and on its ability to make new predictions which can be verified by observations. It is further judged by its beauty in simplicity, a notion sometimes called "Ockham's razor" in which the simpler of two theories that describe the same system just as well is preferred. An important aspect of this elegance is a connection to reality. As physicists, we are interested in the development of models driven by real, testable properties of systems we describe.

The time-dependent Hartree-Fock (TDHF) [113] theory is one that shows promise in satisfying these criteria. The Time-Dependent Hartree-Fock theory provides a self-consistent mean-field description of the dynamics of quantum many-body systems. Proposed by P. A. M Dirac, it is applied in a Nuclear Physics context to model nuclear properties and reactions.

Studies of nuclear reaction dynamics have been performed using several theoretical models. For example, some macroscopic approaches [72] use multidimensional Langevin equations to determine the outcome of the reaction by calculating its trajectory over a multidimensional Potential Energy surface. Microscopic models like TDHF use the same formalism to describe both the structure and reaction mechanisms of nuclei. With only

a few input parameters, TDHF is elegant and has excellent predictive powers [114, 115, 116, 117].

Previous work [115, 116, 117] on TDHF predicts and describes several qualitative and quantitative features of nuclear reactions. Early work [115] on TDHF approximated nuclear collisions as the collisions of two slabs of spin and isospin symmetric nuclear matter. This relatively simplistic model predicted a wide variety phenomena, such as fusion, dissipation, strongly damped collisions, shock wave propagation, and fragmentation. Subsequent work [116], relaxed these approximations and modeled the collisions of ^{16}O with ^{16}O. In this work, the fusion excitation functions predicted by TDHF are in good agreement with experiment. In a review article [117], calculations based on TDHF and extensions addressed heavy-ion collisions, fusion and strongly damped collisions. The salient features of forward transmission, fusion, and deep-inelastic scattering were predicted, consistent with experimental results [117].

In this work, we use TDHF to model the quasifission process in reactions of ^{40,48}Ca with ^{238}U. The first part of this chapter describes briefly the TDHF systematics and the numerical investigation protocol. The results are presented and discussed in the subsequent section. To the authors knowledge, this particular work is the first detailed study of the quasifission process within the TDHF framework. This complements experiments (as described in previous chapters) on the same reactions using the Mass and Angle distribution (MAD) technique. The experiments and theoretical calculations were performed independent of each other and no attempt was made to adjust the parameters of the model to match experimental results.

6.1 Numerical Application with the TDHF3D code

6.1.1 Introduction to the TDHF3D Code

The HF and TDHF calculations were both performed with the SLy4d Skyrme energy density functional [98, 118] allowing for a fully consistent treatment of nuclear structure and reaction dynamics.

HF is a variational principle that provides the energy minimum in the sub-space of independent particles. The nuclei were assumed to be initially in their Hartree-Fock (HF) ground state. The HF ground states are generated using the imaginary time method [119]

by solving the stationary version of the TDHF equation.

The single-particle wave functions are spatially discretised on a regular, three dimensional Cartesian grid. In the calculations to be discussed below, the mesh size is equal to 0.8 fm [98]. The mesh unit must be small enough to give an accurate representation of nuclei. On the other hand, computing speed and storage considerations favour a large mesh size. This number was chosen as a compromise between these two considerations, as in the work in [76, 98, 113].

Each single-particle wavefunction ψ_i is defined in a rectangular bounding box. This bounding box was made large enough such that the tails of the HF wave functions are not significantly affected by the hard box boundary condition. The coordinate axes (shown graphically in Figure 6.1) are defined as follows: the x-axis is parallel to the horizontal direction, the y-axis to the vertical direction and the z-axis perpendicular to both of these, out of the plane of the paper. The HF box had dimensions of 14 mesh units of Δx from the coordinate origin with the centre of the nucleus being at the origin. This corresponds to a cubic box with side length of 22.4 fm. The HF calculations for all nuclei were converged using a $28^3\Delta x^3$ box with 3 planes of symmetry at $x = 0$, $y = 0$ and $z = 0$.

The dynamical (TDHF) calculations are performed in a half-box where only the z=0 plane of symmetry is kept. The dynamical calculations for central collisions are performed in a half-box with $N_x = 70$, $N_y = 28$ and $N_z = 28$ mesh points. For non-central collisions the box size is increased along the y and x axes such that we have $N_x = 84$ and $N_y = 70$ mesh points. This is to allow for full re-separation of the fragments and avoid spurious reflections off the hard box boundaries, before the fragments have fully separated.

The initial velocity vectors of the nuclei are determined assuming a Rutherford trajectory prior to the start of the calculation. That is, the Rutherford trajectory is accounted for prior to any nuclear interaction. To give the nuclei an initial translation energy they are given the appropriate Galilean boost by applying a translation in momentum space [120].

The TDHF equations are then solved iteratively using a real time propagation algorithm that ensures energy conservation [115, 121]. The TDHF3D [98] code employed in this work used a time step of $1.5*10^{-24}$s. The final TDHF result is a many body wavefunction of the system at the last time step. It contains all the information about the system and from it we can extract the expectation values of one body operators.

The aforementioned parameters, used in this work, are applicable to a broad range of reactions and they were adopted from the latest work in the existing literature. Within the existing literature there is little variation in these values.

6.1.2 Systems Studied

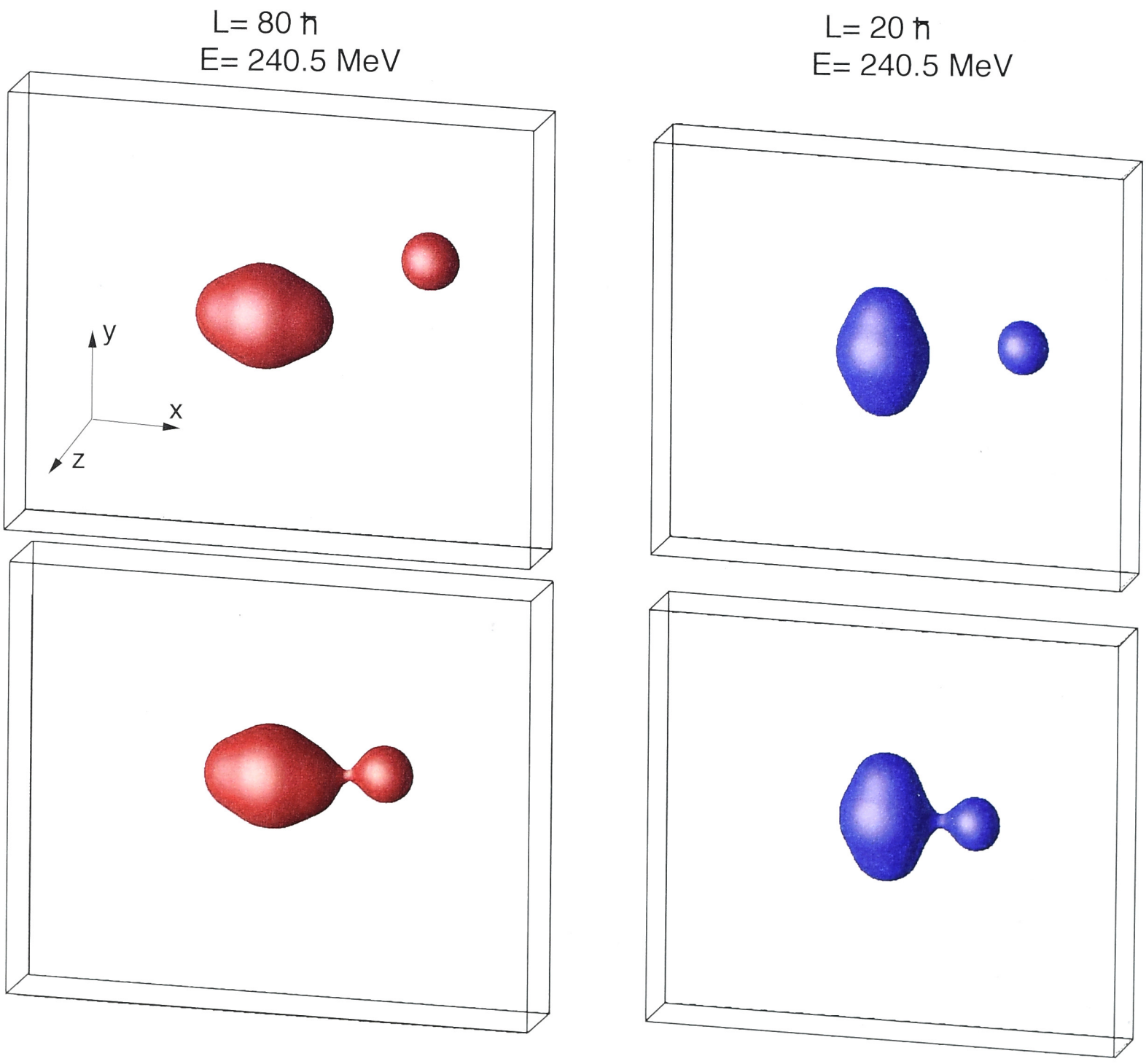

Figure 6.1: Density plots showing the two extreme orientations studied. The left panels depict the axis orientation and the right panels depict the equator orientation. The top and bottom panels depict relative positions of the nuclei at initial separation and just after contact, respectively. The initial conditions were set such that for every case investigated the nuclei always made contact at the extreme orientations shown here.

In this work we studied the ^{40,48}Ca + ^{238}U reactions, primarily focusing on the ^{40}Ca + ^{238}U reaction. The ^{48}Ca was studied as well, in less detail, to check for consistency between isotopes. In principle we expect no drastic variation in reaction outcome between the two isotopes.

In Chapter 5 the ^{40}Ca + ^{238}U reaction was studied using the MAD technique and high statistics experimental data have been presented. We saw almost exclusively mass-asymmetric quasifission for sub barrier energies ($\frac{E}{V_b}$= 0.95) and a strong quasifission component even at the highest energies ($\frac{E}{V_b}$= 1.14).

For each TDHF calculation we need to set parameters that describe the entrance channel of the reactions of interest. These independent variables are interaction energy E, initial angular momentum L, relative initial orientation of the deformed ^{238}U nucleus and the relative initial positions of the two colliding nuclei. The number of time steps, another independent variable, determines the interaction time of the calculations.

Interaction Energy

The reactions were studied at energies ranging from $\frac{E}{V_b} = 0.88$ to 1.26, similar to the range studied experimentally in Chapter 5. As previously V_b is the average barrier determined using the systematics of Swiatecki in [97] (equation 3.8). The energy was varied in steps of $\Delta\frac{E}{V_b} > 0.05$.

A few specific energies were also studied in detail by varying the impact parameter. The energies chosen for this were a subset of those measured using the MAD technique. We chose three energies, one below the average Coulomb barrier where asymmetric quasifission is the strongest, one just above it where we still see asymmetric quasifission and fusion fission/mass symmetric fission as well and one well above the average barrier where quasifission is no longer the dominant exit channel and has significant overlap with fusion fission/mass symmetric fission. The choice of energies was limited by computational time constraints and a choice of energies where we had good statistics in the experimental MADs.

Initial Angular Momentum

In reality only a small fraction of collisions will be central ($L = 0$) and the vast majority will occur at non zero impact parameters, with a finite angular momentum $L\hbar$ being introduced to the dinuclear system. The system subsequently rotates while exchanging mass. Therefore we also studied non central collisions ($L > 0$) for three specific energies. A range of L values were studied from $L = 0$ to $L = 150$. This was done to ensure that

all reaction outcomes from fusion (expected at low L) to elastic scattering (expected at high L) were covered. By making this extensive series of calculations, MADs could be interpreted using TDHF calculations. To the author's knowledge this has not been done previously.

The computationally intensive nature of TDHF calculations makes a very detailed investigation extremely time consuming. As a compromise between computing time and adequate resolution in L, the step size was $\Delta L \geq 5$.

Initial Orientation of ^{238}U

The ^{238}U exhibits a strong prolate deformation and in the initial stages of the interaction can take all possible orientations. In these calculations, due to computational considerations, we studied two out of three extreme orientations, labelled "axis" and "equator". They are defined according to how the elongated axis of deformation was oriented with respect to the coordinate axes.

The axis (aligned) case corresponds to the deformation axis of ^{238}U being parallel to the x-axis, while the equator (anti-aligned) case corresponds to it being perpendicular to the x-axis and parallel to the y-axis. These initial orientations are shown in the figure 6.1 top left and top right panels, respectively. The third extreme orientation corresponds to the deformation axis being perpendicular to the x-axis and parallel to the z-axis. To prevent clutter the labels axis (axial collisions) and equator (equatorial collisions) will be used henceforth.

In axial collisions, contact first occurs between the elongated tip of the ^{238}U nucleus and the spherical ^{40,48}Ca nuclei (figure 6.1 bottom left panel). Conversely in equatorial collisions, contact first occurs between the shortened side of the ^{238}U nucleus and the ^{40,48}Ca nuclei (figure 6.1 bottom right panel).

Note that for collisions with the ^{238}U nucleus initially in the axis orientation, there is less distance between the nuclear surfaces of the interacting nuclei. Thus contact between it and the Calcium nucleus occurs at larger distances than in the equator orientation. At energies below the average barrier, only the axis configuration will lead to contact. The equator orientation will lead to contact only at energies above the average barrier.

Relative Initial Positions of Nuclei

For all cases studied the initial separation of the nuclei is > 22.4 fm. This minimum was set to give the nuclei enough time in the approach phase to allow Coulomb excitation/polarisation to take place prior to contact.

For central collisions ($L = 0$) the axis along which collisions take place is parallel to the x-axis. For non central collisions ($L > 0$) this is not the case and the collision axis is angled with respect to the x-axis. The initial positions of the nuclei were set such that collisions with the axis/equator took place at the Rutherford distance of closest approach. This ensured that every case, at $L > 0$, corresponded to either an axial or equatorial collision. Thus we maintained uniformity and consistency in the point of first contact. This point of initial contact is shown in figure 6.1, bottom panels. In the bottom right panel of figure 6.1 we see that the neck begins to form prior to the nuclei reaching the Rutherford distance of closest approach. However, at the distance of closest approach the relative positions of the nuclei were consistent with the axial orientation.

Interaction Time

The calculations in this work were set for a minimum simulation time (TDHF time) of $2.3*10^{-20}$ s, unless the system reseparated prior to this. This duration was sufficient for contact followed by a long interaction time in all cases studied. Only a few cases were studied for longer times (up to $5.4*10^{-20}$ s). These will be identified on a case by case basis in subsequent sections.

On average, to calculate 10^{-20} s in TDHF we require 100 hours on a machine equivalent to the NCI facility of Australia. The calculations were done on the NCI facility at the ANU and on the Mercure system at CCRT in CEA (described in Chapter 3). The comprehensive nature of the work done here required a total computing time exceeding 13,000 hours, corresponding to 1.6 years of CPU time.

6.2 Results: The ^{48,40}Ca + ^{238}U case

To compare experimental results with TDHF results we need to choose a set of parameters that are experimentally accessible and simultaneously predicted by the model. In the MAD technique we accurately measure the mass and angle of each fragment. Based on

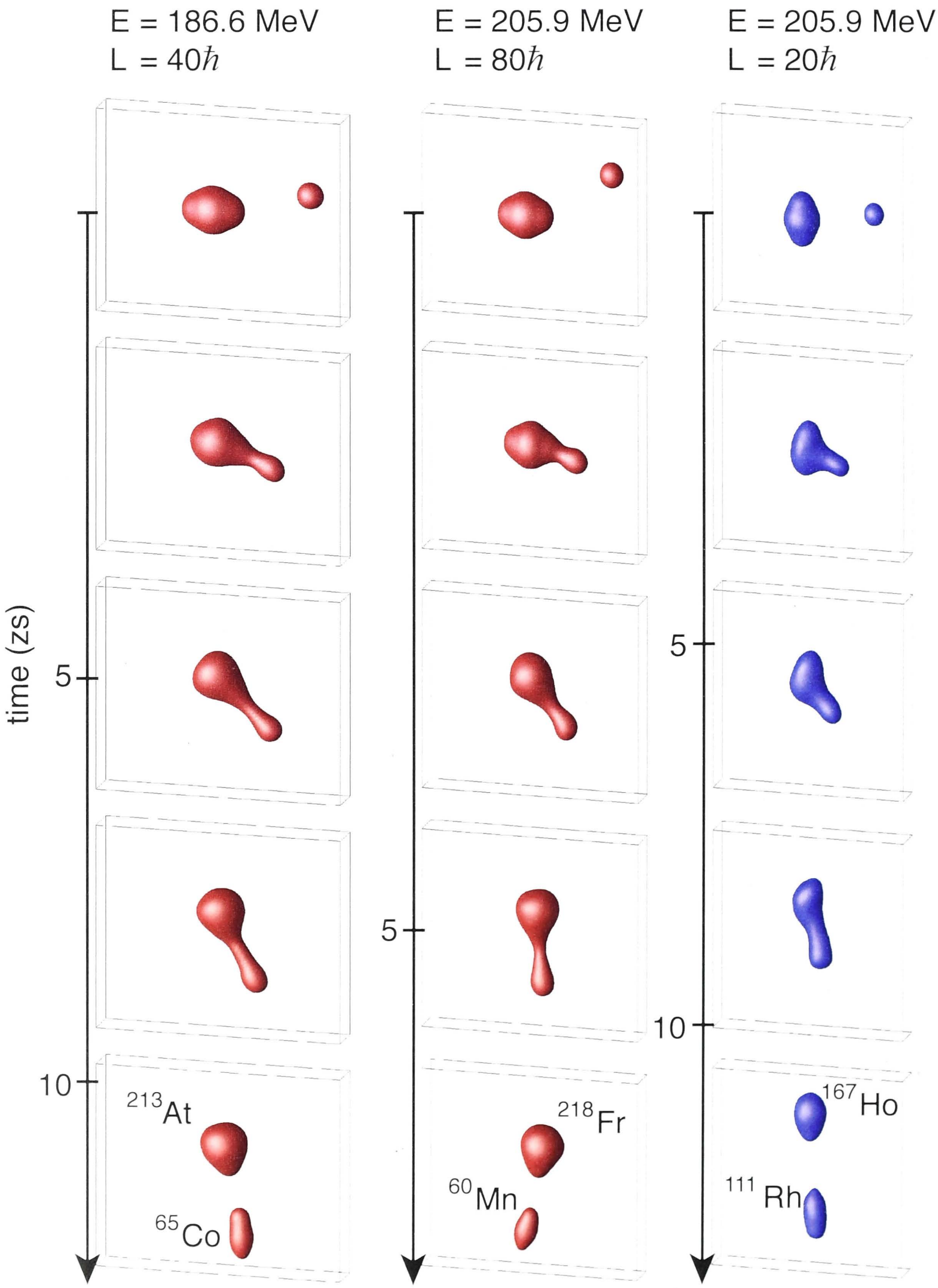

Figure 6.2: Isodensities at half the saturation density, i.e., $\frac{\rho_0}{2} = 0.08$ fm^{-3}, in ^{40}Ca + ^{238}U collisions. Evolutions associated to the two initial configurations, axis and equator, are plotted for non central collisions at energies below and above the average barrier energy. Snapshots are given at times ranging from t=0 to reseparation, from top to bottom.

the model presented in Chapter 4 we can differentiate between reaction timescales in the range 10^{-20}-10^{-21}s.

The TDHF outputs give an average (expectation) value for the mass, proton and neutron numbers of each fragment. In these calculations, nucleons are counted by integrating wave functions at the final time step over a regime where the nuclear density exceeds 0.001 fm^{-3}. The time scale is explicitly known since this is an independent variable. Based on the initial and final momentum vectors we can also determine the incoming and outgoing angles. This allows us to calculate the centre of mass angle. Thus the number of outputs provided by TDHF exceeds the number that we have measured with the MAD technique. We compare the mass and angle outputs with experimental MADs. We also use the neutron and proton numbers predicted by TDHF to gain additional insights into the ^{40}Ca + ^{238}U reaction.

The next two sections deal with a brief investigation of the dependence of net mass transfer and contact time, on interaction energy. In this preliminary investigation only the interaction energy was varied for central collisions ($L = 0$). The behaviour of contact time and net mass transferred are discussed separately before examining their interdependence. The third section deals with a detailed study of three energies for which the impact parameter was varied. Here we look at net mass transferred, interaction time, neutron, proton numbers and outgoing angles. We end with a TDHF based interpretation of MADs for these three energies.

6.2.1 Contact time

Contact time was defined as the duration between contact and re-separation of the two interacting nuclei, or the time spent as a dinucleus. A dinuclear configuration is defined by the formation of a neck with a minimum critical density, defined arbitrarily, of 0.08 fm^{-3} (half the nuclear saturation density). Thus initial contact was defined as the point in time when the neck density exceeded 0.08 fm^{-3} and re-separation was defined as the time when the neck density dropped below 0.08 fm^{-3}.

Figure 6.3 shows the contact time as a function of energy for central collisions ($L = 0$) for each initial relative orientation. The arrows on points lying above a contact duration of $\approx 2*10^{-20}$ s correspond to cases where the dinuclear system did not re-separate within the maximum calculation time. Assuming these configurations stay in contact for long enough

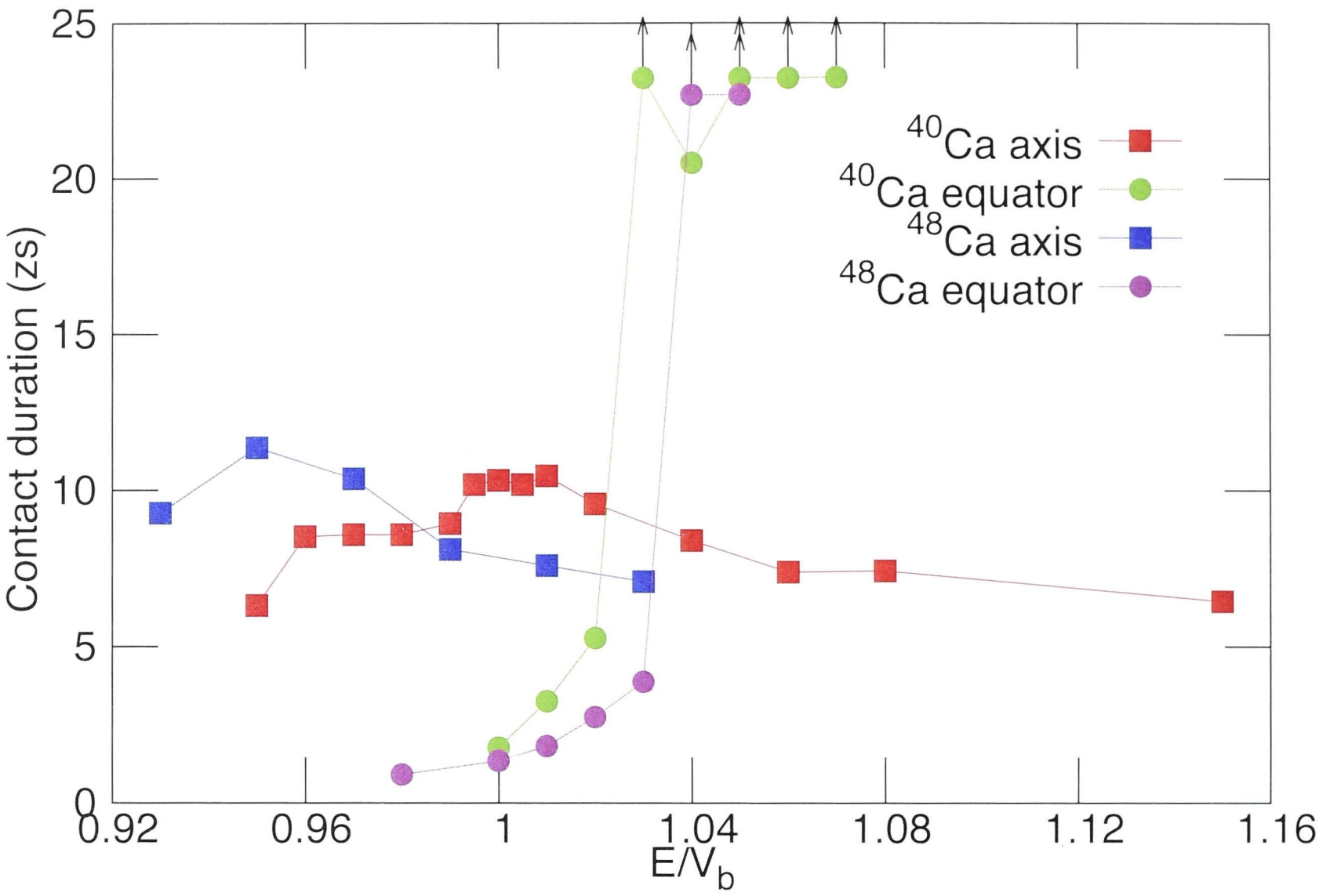

Figure 6.3: Contact time for $L = 0$ as a function of beam energy. Points with arrows correspond to calculations where the dinuclear system did not reseparate within the time limit.

to form a CN, subsequent decay would occur by fission or, the less likely, evaporation residue formation. However, we were interested in the quasifission reaction process which takes place on timescales of $\approx 10^{-20}$ s and hence the calculations for the aforementioned cases were not extended beyond $2.3{*}10^{-20}$s.

For ^{40}Ca induced reactions with ^{238}U in the axial orientation, the contact time shows a slight peak at energies around the average barrier and the system reseparates at all of the energies studied, even at $E/V_b = 1.15$. A similar trend is seen for the axis orientation of the ^{48}Ca induced reactions with contact time peaking slightly below the average barrier and the system reseparating for all energies, even above the average barrier.

For equatorial collisions with ^{40}Ca, contact time increases rapidly as a function of energy and exceeds the calculation time limit ($2.3{*}10^{-20}$ s) for all but one of the energies above $E/V_b = 1.02$. At these energies the two nuclei are assumed to fuse within the time scales studied in this work. This conclusion was made by examining the isodensity of the neck and the elongation of the dinucleus at $2.3{*}10^{-20}$ s. We assumed that a compact

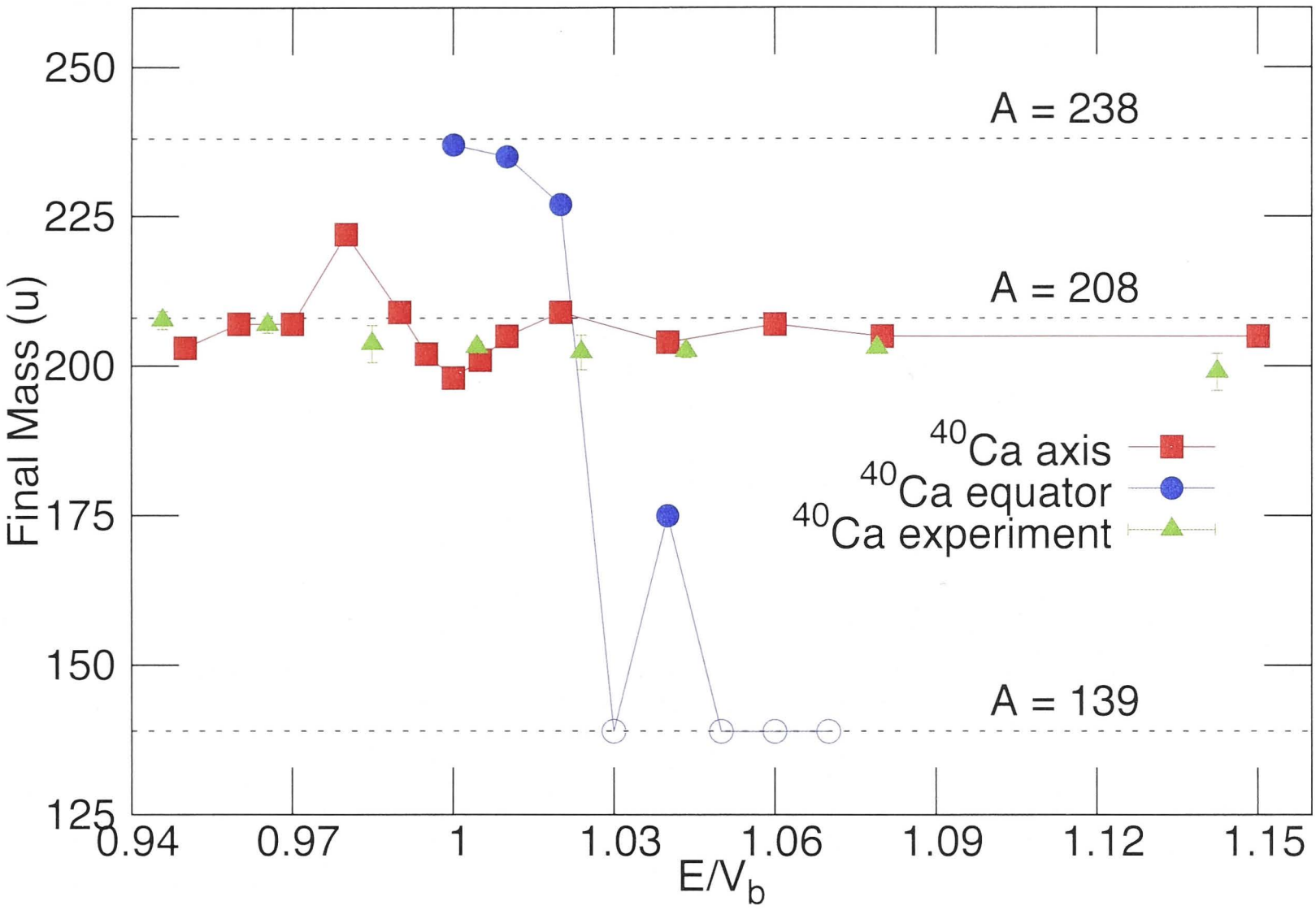

Figure 6.4: Mass of the heavy fragment, for $L = 0$, as a function of beam energy for ^{40}Ca + ^{238}U. The dotted lines correspond to A = 238, 208 and 139. The points at A = 139 (open symbols) correspond to cases where the nuclei do not separate within the calculation time and were assumed to have formed a CN that subsequently decayed via symmetric fission. The mass splits from experimental measurements are also presented.

shape and a neck density well above 0.08 fm^{-3} suggested that the nuclei were not about to reseparate soon after this time limit. In fact, there was no neck at all. The ^{48}Ca reactions exhibit a similar trend, not reseparating for $E/V_b > 1.05$ for equatorial collisions. For the equator configuration all of the reactions at lower energies re-separate within $5*10^{-21}$ s of contact. The time scales on which the systems reseparate are consistent with quasifission [16, 26, 35], confirmed in the next section based on the masses of the outgoing fragments.

6.2.2 Net Mass Transferred

Figures 6.4 and 6.5 show the mass of the heavy fragment as a function of energy for central collisions ($L = 0$). The dotted lines represent the masses $A = 208$ and $A = 238$, corresponding to ^{208}Pb and the target mass in the entrance channel, respectively. The dotted lines at $A = 139$ and 143 correspond to $\frac{A_{CN}}{2}$. The trend lines are shown to guide

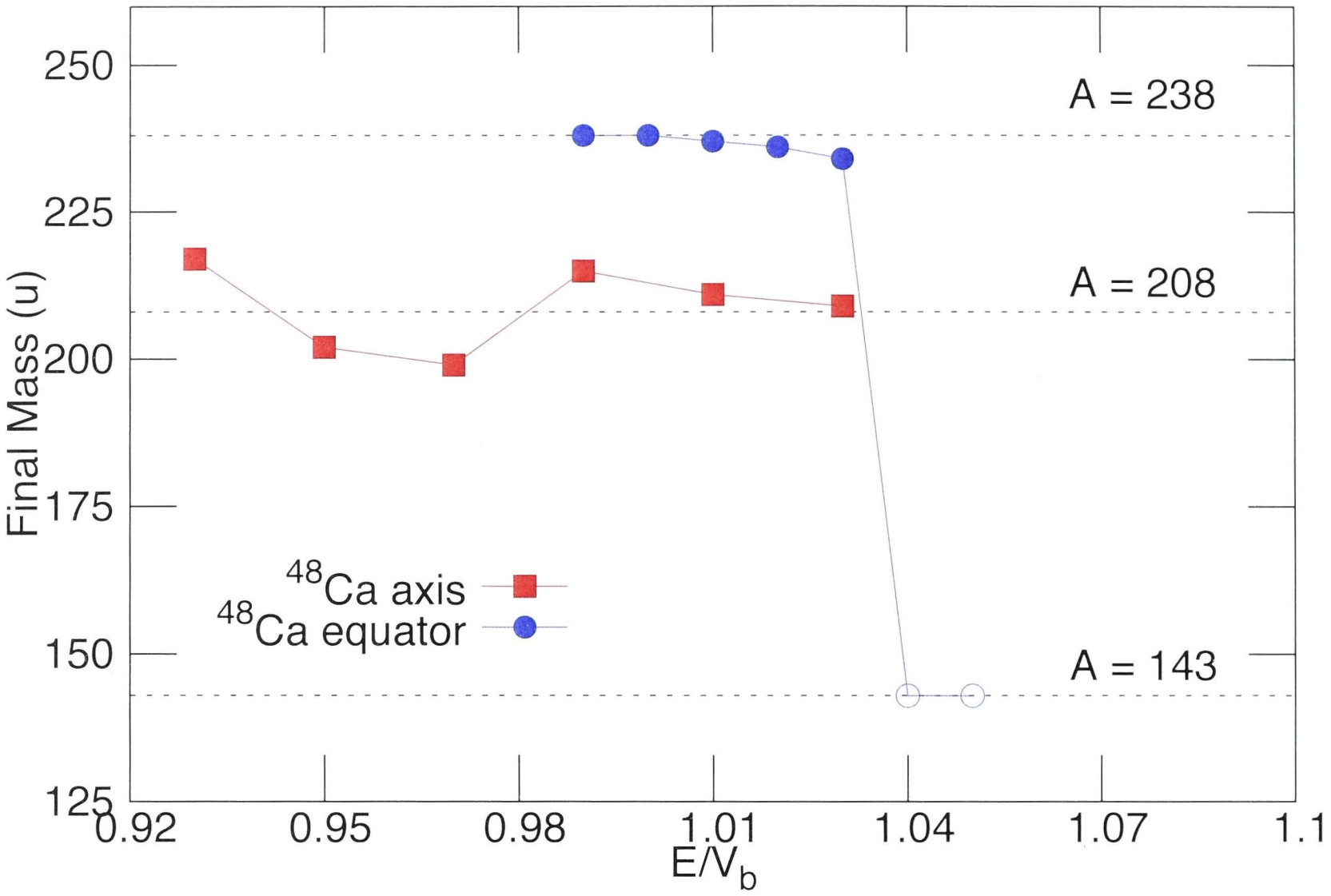

Figure 6.5: Mass of the heavy fragment, for $L = 0$, as a function of beam energy for ^{48}Ca + ^{238}U. The dotted lines correspond to A = 238, 208 and 143. The points at A = 143 (open symbols) correspond to cases where the nuclei do not separate within the calculation time and were assumed to have formed a CN that subsequently decayed via symmetric fission.

the eye. For a few of the higher energies there are open symbols at $A = 139$ and 143, indicating that the system did not re-separate within the calculation time. For these cases we assumed that the system forms a CN which subsequently undergoes symmetric fission.

Events corresponding to asymmetric quasifission are expected to lie between A $\approx$ 140 to 238 for the heavy fragment. Quasi-elastic and deep inelastic scattering events are expected to lie near the entrance channel at A = 238. There are three distinct groups of events in figures 6.4 and 6.5, one around A $\approx$ 140 (CN fission or fusion-fission), a second around A $\approx$ 200 (asymmetric quasifission) and a third group around A $\approx$ 238 (quasi-elastic and deep inelastic collision).

For both Calcium isotopes the net mass flow, from the heavy to the light fragment, for axial collisions shows very little change with increasing energy. The total number of nucleons transferred is maximum at energies around the average barrier. The system re-separates for all energies studied and the resulting heavy fragment masses are scattered

on average around A = 207. This partial mass symmetrisation prior to re-separation is consistent with quasifission. The average mass of the heavy fragment suggests that it is driven by the doubly magic shell closure around ^{208}Pb.

For both Ca isotopes, the behaviour of the equator configuration at low energies is very different to that at high energies. Focusing on the low energy region ($E/V_b < 1.03$ for ^{40}Ca, $E/V_b < 1.04$ for ^{48}Ca) we see little to no net mass transfer prior to re-separation. At higher energies the system does not re-separate within the maximum calculation time. Thus for the equator configuration there is a rapid transition from collisions where the system reseparates, to the system does not reseparate. Note that some of these cases may reseparate if the calculation time is extended, so this rapid transition does not necessarily represent the onset of true fission. The important point here is the significant difference in reaction outcomes, at various energies, between the axis and equator configurations.

Note that all the mass splits seen here correspond only to the expected average of the fragment mass distributions for a given initial orientation of the ^{238}U nucleus. In reality, the nuclei can take on any orientation in the entrance channel and this will result in a distribution about each point studied. Particle number fluctuations in the fragments would also contribute to this distribution [123]. These will be the subject of future studies.

Discussion of Net Mass Transfer and Contact Time

So far we have only looked at the contact time and net mass transferred separately. The following is an overall discussion, of the preliminary TDHF calculations with central collisions.

Firstly, both Calcium isotopes exhibit very similar behaviour and we see no clear isotopic dependence on the gross features. There is no change in the quasifission component with respect to isotope. The only difference between the two isotopes is the barrier or "fusion" threshold: the threshold, in terms of E/V_b, between the systems reseparating and not reseparating. In Ref. [110] where we studied reactions of ^{48,40}Ca + ^{208}Pb, TDHF calculations predicted fast equilibration of N/Z in the two fragments early in the collision. This transfer of nucleons was predicted to break the shell effect and cause the reaction with ^{40}Ca to behave more like a non-magic one, showing strong evidence for quasi-fission, though both nuclei are doubly magic. The reaction with ^{48}Ca did not exhibit this behaviour, suggesting that ^{48}C retains its magicity in a reaction.

Table 6.1: Table comparing barriers determined by various methods. The columns correspond to the reaction, scaled barrier using Swiateckis systematics [97], barrier determined by HF frozen calculations and barrier determined from TDHF calculations.

Reaction	Swiatecki	HF Frozen	TDHF
^{40}Ca + ^{238}U	197.3	Axis: 183.78	no fusion
		Equator: 199.13	202.22
^{48}Ca + ^{238}U	192.59	Axis: 181.27	no fusion
		Equator: 196.14	203.12

In the current work, reactions with ^{48}Ca have a higher "fusion" threshold compared to ^{40}Ca. Table 6.1 shows the barriers for the two reactions as determined by the systematics of Swiatecki [97], by HF Frozen calculations [114] and by TDHF calculations. Note that the HF Frozen calculations allow us to take into account the orientation of the deformed nucleus. Thus we get two barriers, one for the axial and one for the equatorial configuration. We see that the barriers or "thresholds" as predicted by Swiatecki's systematics and HF Frozen are lower for the ^{48}Ca case.

The point of distinction is the shift in barrier, i.e. the difference in "fusion" threshold between the dynamical TDHF calculations and the static model calculations, for the ^{40}Ca case as compared to the ^{48}Ca case. Compared to HF Frozen we see that the shift is higher for the ^{48}Ca case (6.98 MeV) than for the ^{40}Ca case (3.09 MeV).

This relatively larger shift for the ^{48}Ca case may be due to the fact that ^{48}Ca preserves its magicity and is more inert than ^{40}Ca. As a result a higher interaction energy is required to initiate nucleon transfer with ^{48}Ca.

Indeed this is the behaviour seen at sub-barrier energies. At $E/V_b = 0.9$ the exit channel for the ^{40}Ca ($\frac{N}{Z} = 1$) and ^{238}U ($\frac{N}{Z} = 1.5869$) case shows signs of N/Z equilibration initiating nucleon transfer. The outgoing fragments, on average, are ^{42}K ($\frac{N}{Z} = 1.2105$) and ^{236}Np ($\frac{N}{Z} = 1.5376$) thereby deviating from the magic configuration of the entrance channel. In contrast to this, at the same energy the ^{48}Ca ($\frac{N}{Z} = 1.4$) case does not transfer nucleons and the outgoing fragments, on average, are ^{48}Ca and ^{238}U. Nucleon transfer for the ^{48}Ca case is only observed above $E/V_b = 0.92$. This difference between the two isotopes is consistent with the behaviour seen in [110], where N/Z equilibration was responsible for breaking entrance channel magicity early on in collisions of ^{40}Ca and ^{238}U.

Secondly, the axis configuration always reseparates and has very short contact times, even for energies well above the average barrier. This is due to a rapid increase in nuclear density at the contact point for axial collisions. The neck density saturates rapidly, reaching an average value above 0.154 fm^{-3} typically within $6*10^{-22}$ s after initial contact, thereby developing a repulsive core in the dinucleus and helping the system to re-separate.

The outcomes of axial collision are consistent with the experimentally measured asymmetric mass splits reported in Chapter 5. This preliminary investigation shows good agreement with experimental results (Figure 6.4). Note that the asymmetric channel is largely populated by axial collisions. The contact times of cases that result in mass splits consistent with mass-asymmetric quasifission are all between 5 to 20 zs, in agreement with the expected time scales for mass-asymmetric quasifission [35].

For collisions of ^{40}Ca with ^{238}U in the equator configuration, the point at $E/V_b = 1.04$ deviates from the trend seen at high energies and re-separates in less than $2.3*10^{-20}$ s. The points at $E/V_b = 1.03$ and $E/V_b = 1.05$ do not. This apparent deviation can be attributed to strong dynamical fluctuations of the internal density, causing a deviation from standard transfer where nucleon exchange takes place with a smooth change of the shape of the fragments. Instead, the breaking point of the nuclear system may be modified as described in Ref. [113].

Finally, we see a correlation between net mass transfer and contact time in this preliminary investigation. The peak in mass transferred correlates with peak in contact time around $E/V_b \approx 1$ for ^{40}Ca and around $E/V_b \approx 0.95$ for ^{48}Ca. Recalling from Chapter 4, as a dinuclear system evolves, the two nuclei exchange mass and on average, mass flow occurs from the heavy to the light fragment. The system approaches mass-symmetry ($M_R = 0.5$) asymptotically with a characteristic time dependence proportional to $1 - exp(t/\tau)$ [16, 26]; where τ is the characteristic mass-equilibration time constant. Thus the net number of nucleons transferred from the heavy nucleus to the light nucleus is expected to be proportional to the time spent by the fragments in a dinuclear configuration [124]. The initial orientations of the colliding nuclei are also expected to play a role here, as previous work [113] has shown. This correlation between net mass transfer and contact time is quantified subsequently in this chapter.

This general investigation of the dependence of reaction outcome on interaction energy suggests that the ^{208}Pb shell closure influences the quasifission exit channel, particularly

for collisions with ^{238}U initially in the axis configuration. To investigate this further we now look at non central collisions for three specific energies.

6.2.3 TDHF and Non-central collisions for ^{40}Ca + ^{238}U

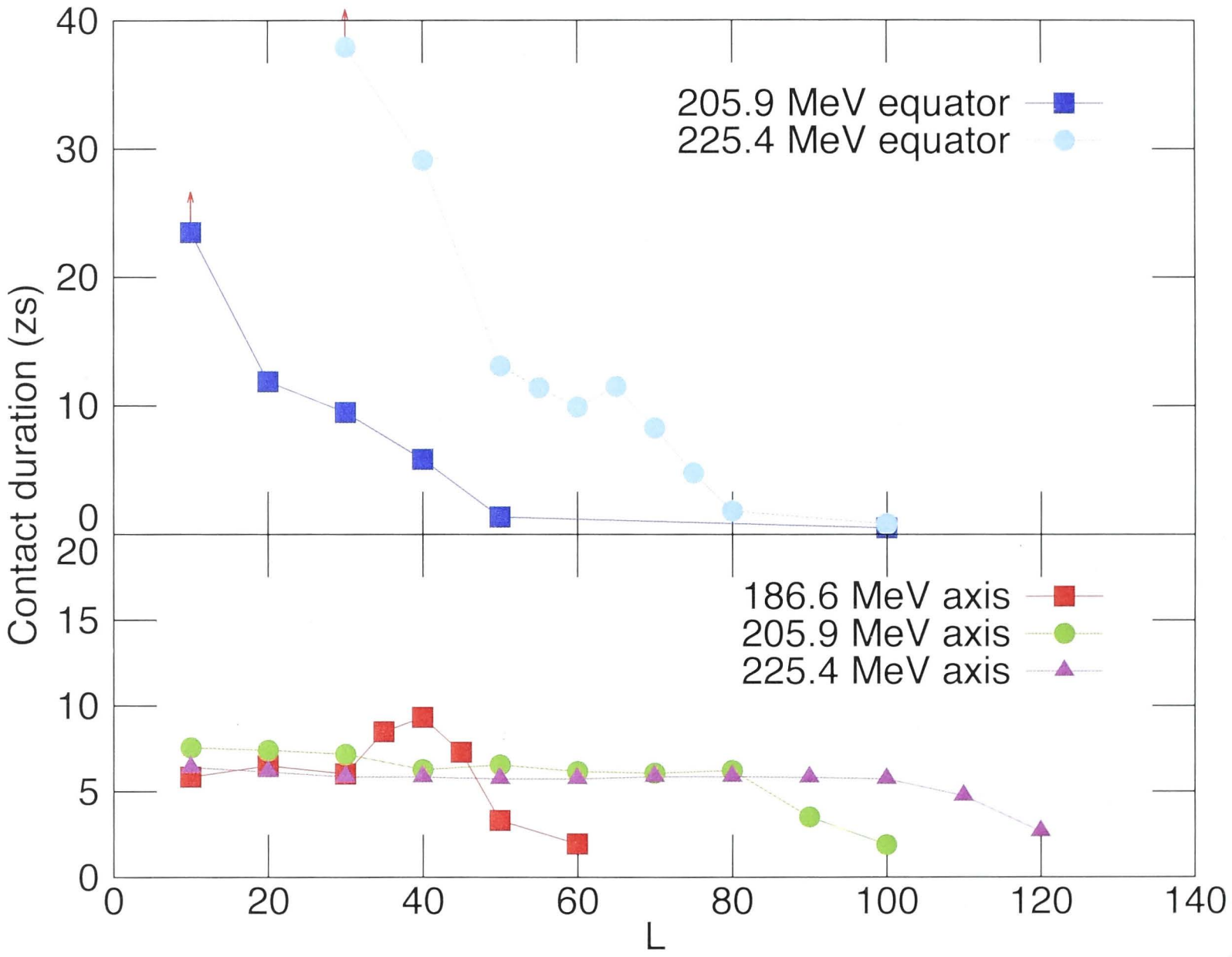

Figure 6.6: Contact time as a function of angular momentum L for energies corresponding to experimentally measured MADs. The points with the arrows correspond to cases where the system did not reseparate within the total time of the calculation.

Increasing the impact parameter is expected to reduce the contact duration and the number of nucleons transferred due to centrifugal repulsion. We now investigate the role of the initial angular momentum L by looking at the contact time, net mass transferred, neutron and proton numbers and outgoing angles of the fragments in the exit channel. The final mass and angle should allow us to compare these results with MADs from Chapter 5. The final neutron and proton numbers should provide additional insights into the role of the ^{208}Pb shell closure.

Figures 6.6 and 6.7 show the contact time and the mass of the heavy fragment as a function of L, respectively. In figure 6.7 the dotted lines represent the masses $A = 208$ and

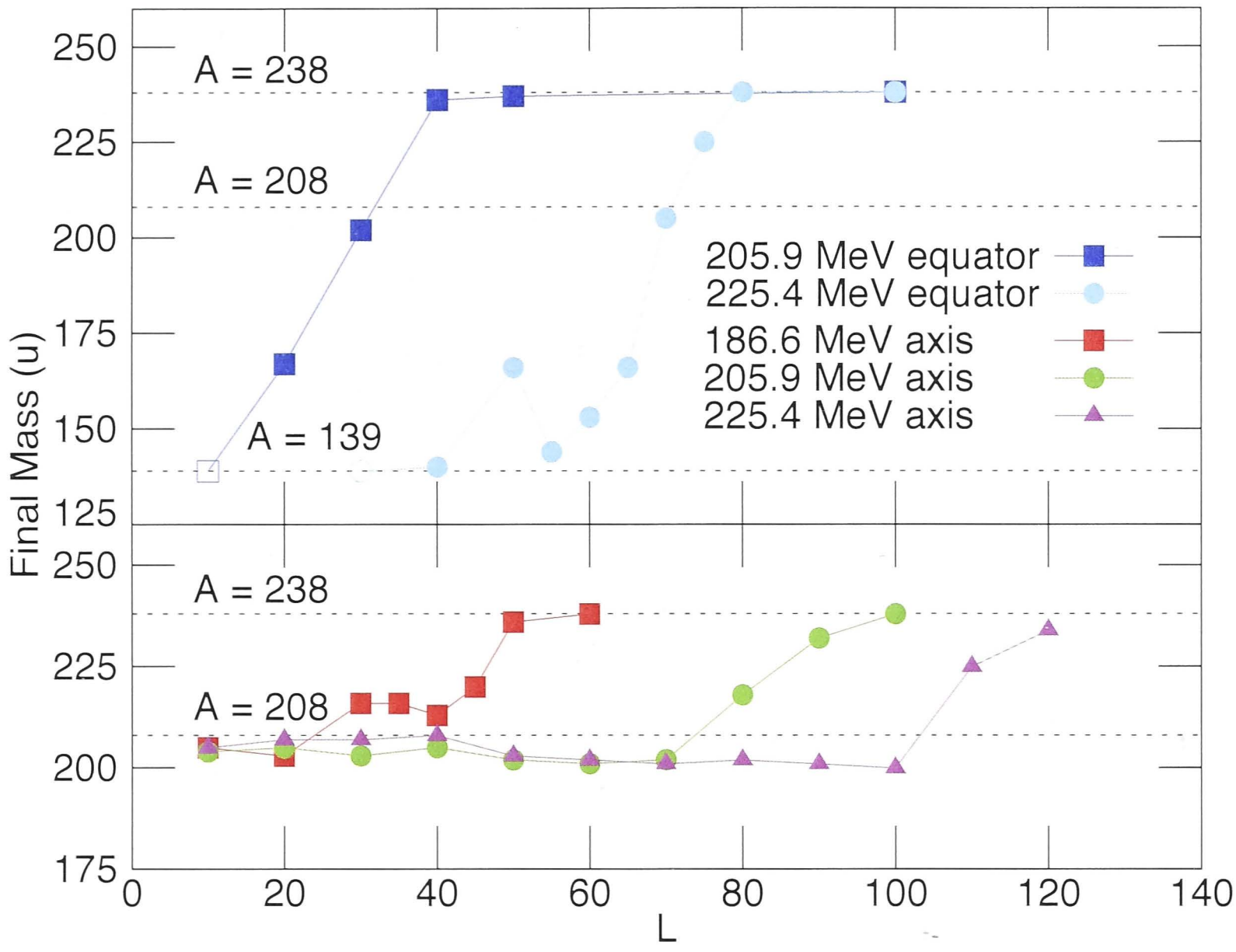

Figure 6.7: Final masses of the heavy fragment as a function of angular momentum L for energies corresponding to experimentally measured MADs. The dotted lines correspond to A = 238, 208 and 139. The open symbols correspond to cases where the nuclei are assumed to fuse and subsequently undergo symmetric fission.

$A = 238$, corresponding to ^{208}Pb and the target mass in the entrance channel, respectively. The dotted line at $A = 139$ corresponds to $\frac{A_{CN}}{2}$. Overall, the total number of nucleons transferred and contact time are strongly dependent on the orientation of the ^{238}U nucleus, as seen earlier in section 6.2.2.

For the axis orientation at 225.4 MeV there is only a slight, gradual decrease in contact time with increasing L. Above $L = 100$ the contact time drops off quickly. The total number of nucleons transferred remains relatively constant as a function of L till $L = 100$ after which it drops off as well. For $L < 110$ the average light/heavy split was $A_L/A_H = 74/204$, consistent with mass asymmetric quasifission. Above $L = 100$ the mass splits transition to quasi-elastic and deep inelastic scattering.

The same behaviour was seen for the axis orientation at 205.9 MeV. In this case the threshold between mass asymmetric quasifission and quasi-elastic/deep inelastic scattering

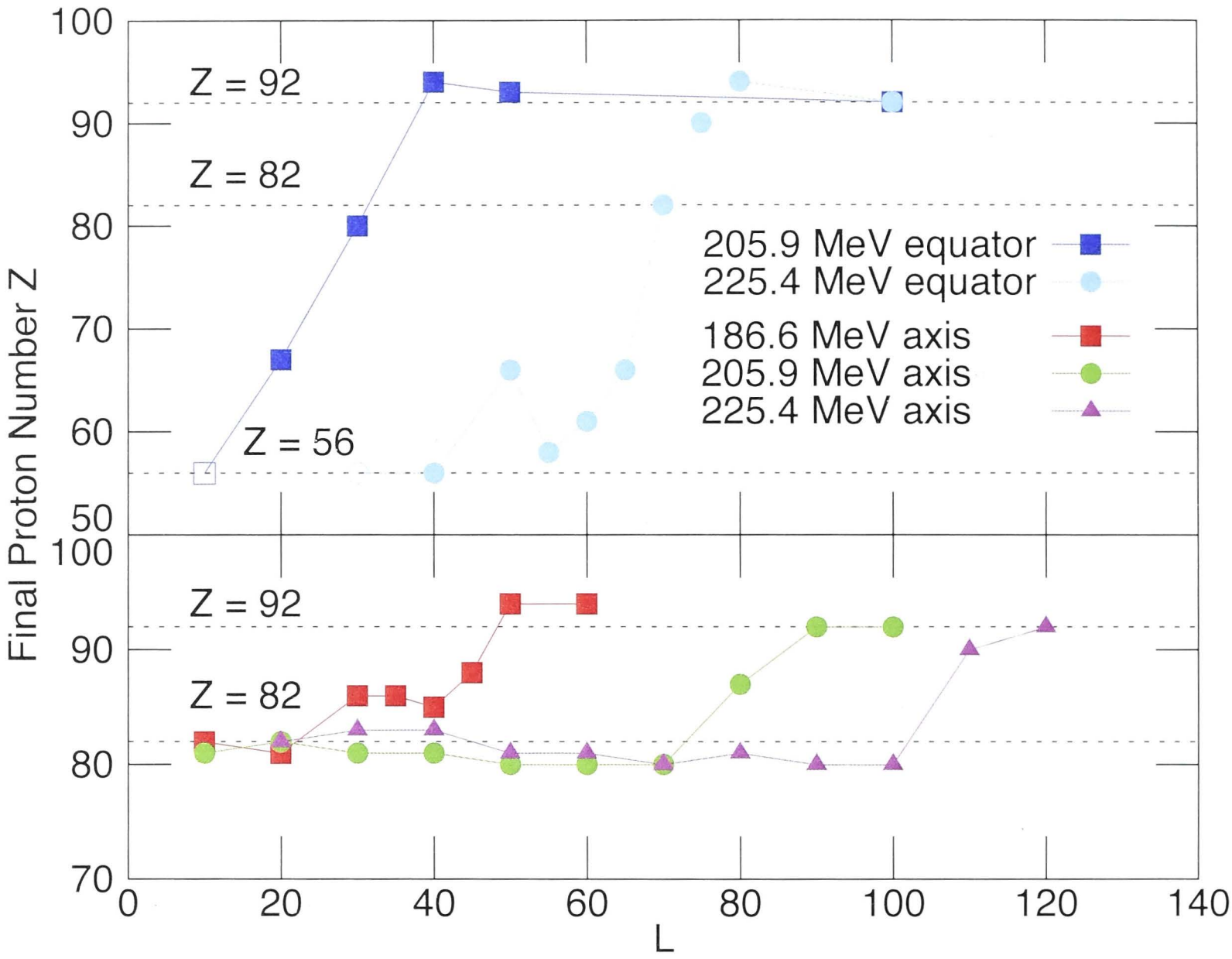

Figure 6.8: Final Proton number (Z) of the heavy fragment as a function of angular momentum L for energies corresponding to experimentally measured MADs. The dotted lines correspond to Z = 92, for ^{238}U and Z = 82, for ^{208}Pb and Z = 56. The open symbols correspond to cases where the nuclei are assumed to fuse and subsequently undergo symmetric fission.

is $L = 80$. For $L < 80$ the average light/heavy split remains consistent around $A_L/A_H = 75/203$, consistent with mass asymmetric quasifission.

The behaviour for axial collisions at 186.6 MeV only showed a slight variation from this behaviour. The contact time remains relatively constant with a slight increase (30%) between $L = 30$ and $L = 45$. Contact time drops off quickly above $L = 45$. The mass transferred remains relatively constant here as well, despite the slight increase in contact time. This is one exception seen, in this work, of the limitation to the direct proportionality observed between contact time and net mass transfer. For $L < 45$ the average light/heavy split remains consistent around $A_L/A_H = 67/211$, consistent with mass asymmetric quasifission. Although this is higher than $A_L/A_H = 70/208$, in the subsequent section we see that the average proton and neutron numbers for these splits ($Z = 84$ and $N = 127$, respectively) are still in the ^{208}Pb region.

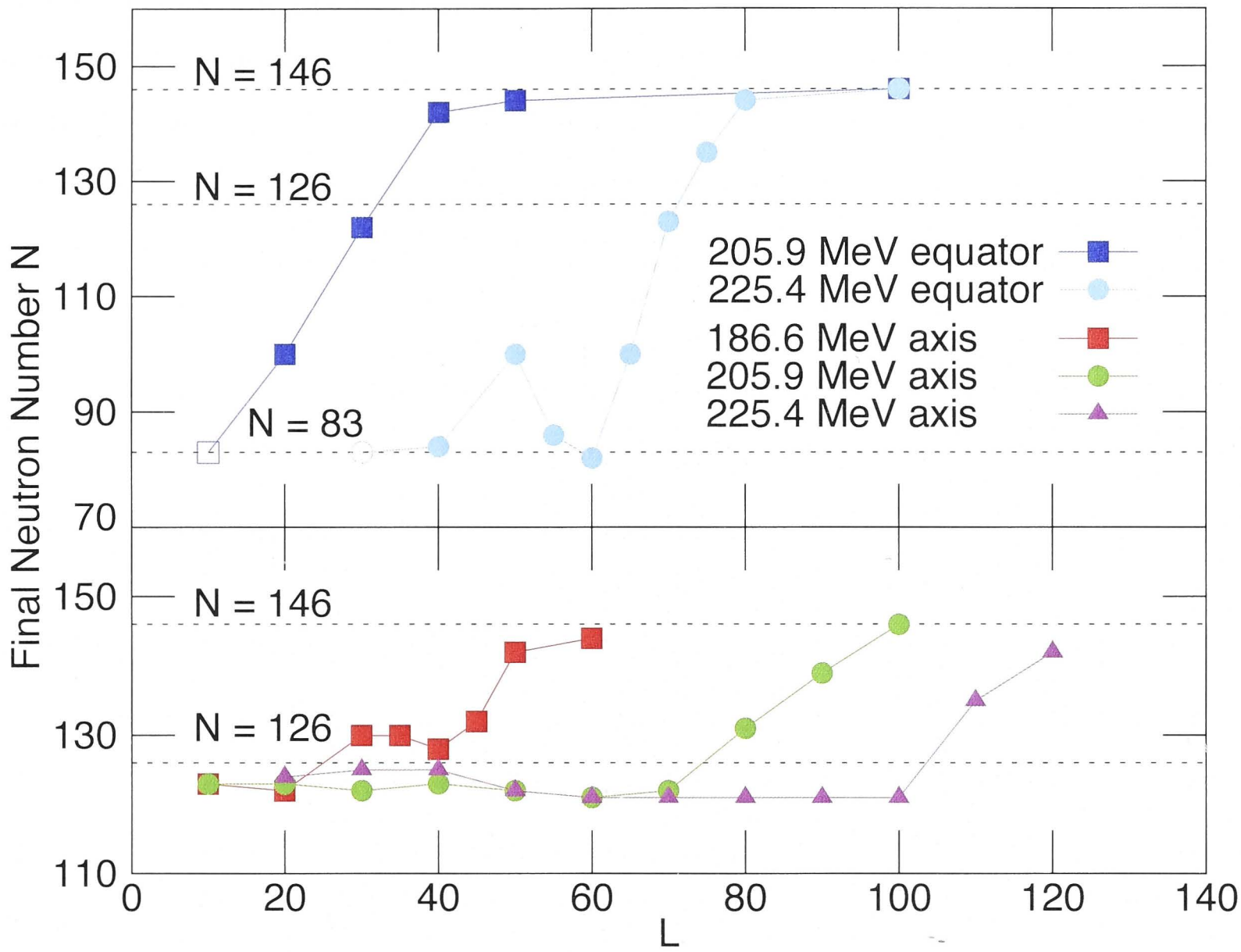

Figure 6.9: Final Neutron number (N) of the heavy fragment as a function of angular momentum L for energies corresponding to experimentally measured MADs. The dotted lines correspond to N = 146, for ^{238}U and N = 126, for ^{208}Pb and N = 83. The open symbols correspond to cases where the nuclei are assumed to fuse and subsequently undergo symmetric fission.

The equator orientation exhibits very different behaviour. For the equator orientation at 225.4 MeV, contact time drops off sharply above $L = 30$. Below this the dinuclear system does not re-separate within the calculation time and we assume that the system forms a CN. The total number of nucleons transferred drops off with increasing angular momentum and decreasing contact time. The same behaviour was seen for the equator orientation at 205.9 MeV with the exception that contact time drops off sharply above $L = 10$ and below this the dinuclear system does not re-separate within the calculation time.

The 205.9 MeV L=0 and 225.4 MeV L=30,40 calculations were extended beyond the normal $2.3*10^{-20}$s limit to $5.4*10^{-20}$, $2.9*10^{-20}$ and $3.8*10^{-20}$s respectively. This was done because the isodensity of the neck at $2.3*10^{-20}$ s suggested that the nuclei were about to reseparate soon after this limit.

In figure 6.7 the points at 225.4 MeV, $L = 70$ and at 205.9 MeV, $L = 40$ are the only two consistent with mass asymmetric quasifission. We also see a few mass splits around $A = 110$ and $A = 170$ (225.4 MeV, $L = 50, 65$; and 205.9 MeV, $L = 20$) that are consistent with more mass symmetric quasifission, also known as deep quasi fission (DQF) [55, 56]. The respective timescales ($> 10^{-20}$ s) of these points in figure 6.6 are consistent with DQF.

Neutron and Proton Numbers

The dependence of the proton and neutron numbers in the outgoing heavy fragment (^{238}U like), as a function of initial angular momentum, is plotted in Figures 6.8 and 6.9, respectively. The dotted lines at $Z, N = 92, 146$ and $Z, N = 82, 126$ represent the nucleon values of the target nucleus in the entrance channel and ^{208}Pb, respectively. The dotted lines at $Z, N = 56, 83$ corresponds to $\frac{Z_{CN}}{2}$ and $\frac{N_{CN}}{2}$.

The equator orientations for 205.9 MeV and 225.4 MeV show two distinct groups, one towards mass symmetry at $Z < 70$ and $N < 100$ and one around elastic scattering at $Z = 92$ and $N = 146$. There is a rapid transition between symmetric splits and elastic scattering. Only one point for each energy (L=30 for 205.9 MeV and L=70 for 225.4 MeV) is consistent with mass asymmetric quasi fission around $Z = 82$ and $N = 126$. Contrary to this, the axis orientations for 205.9 MeV and 225.4 MeV show a remarkable consistency around $Z = 82$ and $N = 126$, with only the lowest energy (186.6 MeV) exhibiting slightly more asymmetric splits.

Interpreting MADs

Figure 6.10 is a compilation of experimental MADs and masses and angles calculated by TDHF. The MADs correspond to the three energies studied in detail in TDHF. This representation provides a clear visual comparison between the points studied in TDHF and experimental data. The elliptical points indicate the mass and angle obtained for each TDHF calculation for a given energy and L value. The pink points correspond to the axis configuration and the blue points correspond to the equator configuration. The angles shown here have not been corrected for the Coulomb trajectory following re-separation of the dinuclear system. The correction was ignored due to this being a small effect, typically less than 2°-3°, and time constraints. Collisions in which the system did not reseparate are

not shown since we cannot extract mass and angle values for these cases. The points are labelled with the corresponding initial angular momentum. The labels for axial collisions are shown next to the projectile-like fragments while the labels for the equatorial collisions are shown next to the target-like fragments. This was done to avoid clutter.

For the lowest energy (186.6 MeV), only the axial orientation leads to contact. Hence the blue points, corresponding to equatorial collisions, are only shown for elastic scattering. The TDHF points (overlayed pink ellipses on the MAD) follow the same trend as the experimental data. For $L < 40$ we see points at extreme mass asymmetry, consistent with mass asymmetric quasifission. The TDHF points also show the same angular focusing as the experimental data. The experimental angular distribution, for the projectile like fragment, falls off at $\theta_{cm} = 60°$. For $L > 40$ the TDHF points depict little mass transfer and at $\theta_{cm} = 60°$ there is a transition to mass splits consistent with elastic scattering.

At the energy just above the average Coulomb barrier (205.9 MeV) both the axis and equator configurations lead to contact. For $L < 80$ the axis configuration leads to mass splits with only partial mass symmetrisation, consistent with the experimental data presented in the MAD. The drop off in the angular distribution takes place at $L = 80$ at angles beyond the coverage of the experimental setup. Hence we cannot make the same comparison here. The equator configuration populates more mass symmetric splits with only one point, at $L = 30$, consistent with mass asymmetric quasifission. The points below $L = 30$ are consistent with more mass symmetric quasifission (DQF). Above $L = 30$ there is a transition to mass splits consistent with elastic scattering.

At the highest energy (225.4 MeV) both the axis and equator configurations lead to contact. For $L < 100$ the axis configuration leads to mass splits consistent with mass asymmetric quasifission. Note that the point at $L = 100$, for axial collisions, is depicted by a dotted outline on the point marker and dotted line connecting the marker to higher L values. Here the dinuclear system undergoes more than half a rotation prior to reseparating. Here too, we see a few points beyond the coverage limitations of the experimental setup and cannot use these to compare between TDHF and data. Again, only the equator configuration populates more symmetric splits. Only one point, at $L = 70$ is consistent with mass asymmetric quasifission. The points below $L = 70$ are consistent with more mass symmetric quasifission (DQF) with two cases at the lowest L being very close to mass symmetry and having a reaction time scale consistent with DQF. Above $L = 70$

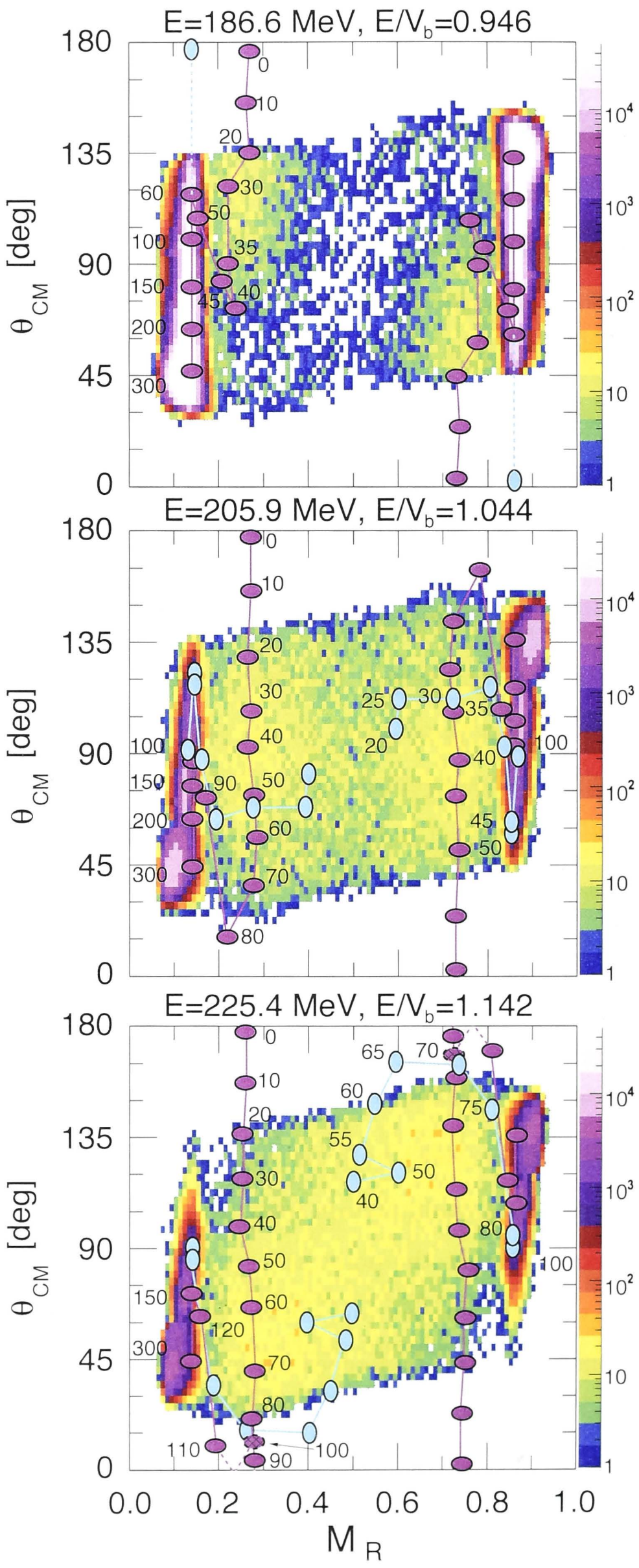

Figure 6.10: MADs for the energies studies in detail using TDHF. The elliptical points indicate the mass and angle obtained for each TDHF calculation for a given energy and L value. The pink points correspond to the axis configuration and the blue points correspond to the equator configuration.

there is a transition to mass splits consistent with elastic scattering.

An interesting observation, common to all energies, is the angle at which TDHF predicts a transition between collisions that lead to mass transfer and collisions that lead to (in)elastic scattering. The angle of onset of elastic scattering, as predicted by TDHF, matches well with the experimental measurements. We focus on the light mass region ($M_R \approx 0.150$) for the following discussion.

At 186.6 MeV TDHF predicts a transition to elastic scattering at $L \geq 60$ for axial collisions. The axial orientation populates elastic scattering for angles $\theta_{cm} < 120°$, consistent with the tail of the (in)elastics seen in the MAD. At 205.9 MeV the transition to elastic scattering is at $L \geq 100$ for axial collisions and at $L \geq 50$ for equatorial collisions. The axial orientation populates (in)elastic scattering for angles $\theta_{cm} < 90°$. Here the equatorial orientation populates elastic scattering for angles $\theta_{cm} < 135°$, consistent with the tail of the elastics seen in the MAD. Finally, at 225.4 MeV it predicts (in)elastic scattering at $L \geq 150$ for axial collisions and at $L \geq 80$ for equatorial collisions. The axial orientation populates (in)elastic scattering for angles $\theta_{cm} < 75°$. The equatorial orientation populates (in)elastic scattering for angles $\theta_{cm} < 90°$, also consistent with the tail of the (in)elastics.

Overall, the TDHF mass splits and angular distributions show excellent agreement with experimental data. The size of the blue and red points in figure 6.10 is not indicative of the width of the mass distributions. Reproducing experimental mass widths in TDHF is not a trivial process. However, it is likely that any such calculation will only bolster the level of agreement seen currently between TDHF and experiment.

6.2.4 Summary and Discussion

Figure 6.11 depicts the net number of nucleons transferred as a function of contact time. We see that for both configurations the net mass transferred is proportional to contact time and not very sensitive to minor variations in contact time. From figures 6.6 and 6.7, for axial collisions at 186.6 MeV we see a slight (30 percent) increase in contact time around $L \approx 40$, but the final mass splits remain relatively unaffected. Axial collisions at 205.9 MeV and 225.4 MeV show a gradual decrease in contact time with increasing L but no significant variation in net mass transfer during this decrease. Equatorial collisions at 205.9 MeV and 225.4 MeV also show a direct proportionality between contact time and net mass transfer. The only exception is at $L = 50$ for 225.4 MeV. This is attributed to

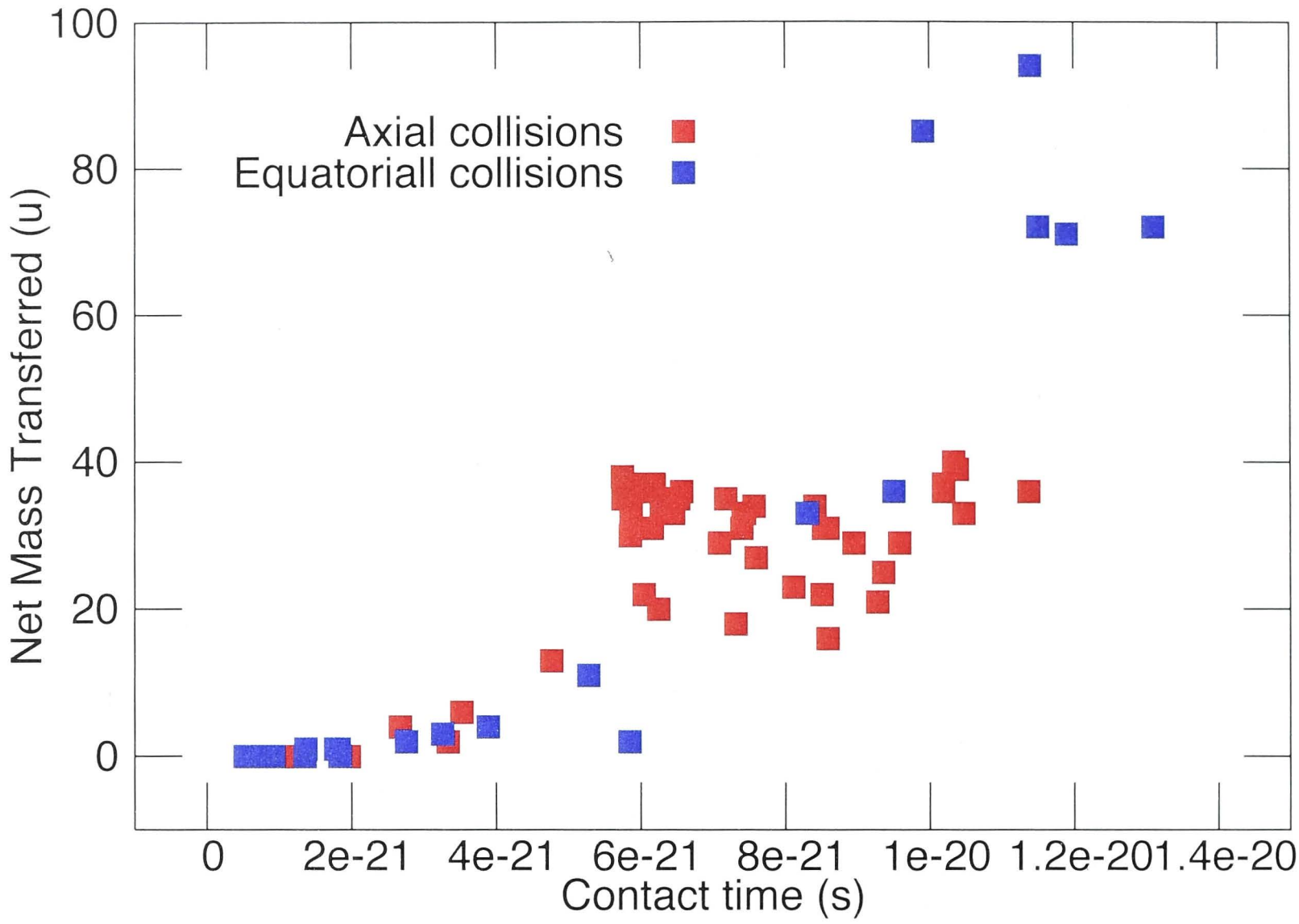

Figure 6.11: Net mass transferred, from the heavy to the light fragment, as a function of contact time. The points shown here correspond to central and non central collisions where the dinuclear system reseparates.

strong dynamical fluctuations of the internal density as seen in[113].

The mass splits in figures 6.4 and 6.7 show excellent agreement with the mass splits from experimental measurements of the ^{40}Ca + ^{238}U reaction. TDHF predicts quasifission to be the dominant reaction outcome at all energies, particularly for axial collisions. The added information of contact time in figures 6.3 and 6.6 is consistent with the timescales expected for quasifission [35] as well. For times ranging from $5.75*10^{-21}$s to $9.5*10^{-21}$s after contact, the final mass split of the system is close to $A_L/A_H \approx 70/208$. Thus we can infer that the dinuclear system tends to form a $A_L/A_H \approx 70/208$-like system early on in the reaction and stays that way for relatively long contact times, primarily in axial collisions.

The proton (fig 6.8) and neutron numbers (fig 6.9) of the fragments in the exit channel were found to be very consistent around $Z = 82$ and $N = 126$. The TDHF mass splits, whether as a function of energy or initial angular momentum, also suggest that the doubly magic ^{208}Pb shell closure influences the evolution of the system. Note that the average Z values are very close to 82, whereas the average N values are somewhat lower (122) than

126. This may be due to N/Z equilibration, which for $^{278}Cp_{112}$, the CN made here, would result in Z=82,N=122.

A few points also populate the mass region consistent with more mass symmetric quasi-fission, also known a deep quasi fission (DQF). Indeed the time scales for these cases are longer than 10^{-20}s, consistent with the expected timescale for DQF [55, 56]. We do not have enough points here to investigate this particular reaction channel in detail.

In Chapter 5 we saw that shell effects in the asymmetric quasifission channel become less apparent with increasing energy. From a physical point of view this is due to shell effects damping as the excitation energy increases. In TDHF the axis configuration is apparently more sensitive to shell effects around ^{208}Pb than the equator configuration, regardless of energy. Thus not only is the contribution to asymmetric quasifission primarily from axial collisions (there is a small contribution from equatorial collisions within a very narrow range of L values), it is also seemingly independent of energy. This can be interpreted by considering the relative cross sections of the various orientations as a function of energy.

At energies below the average barrier, only axial collisions lead to contact. At higher energies the equatorial collisions also lead to contact; and as energy increases the equatorial collisions will be favoured over axial collisions. Thus at the highest energies the apparent 'damping' of shell effects may be due to the equatorial collisions being increasingly selected over axial collisions, leading to less quasifission overall.

Systems formed via equatorial collisions are the only ones that do not reseparate within timescales studied in this work. This suggests that they are the only collisions that can lead to fusion and CN formation. This is important from the point of view of SHE formation. Current experiments aimed at SHE formation are conducted at energies close to the average barrier to ensure CN formation and ER survival. From our calculations we can conclude that fusion and CN formation at above barrier energies is mainly due to equatorial collisions (and possibly other similar configurations) and not axial collisions.

6.3 Conclusion

The TDHF model was used to study the ^{40,48}Ca + ^{238}U reactions. The role of entrance channel interaction energy, deformation, orientation and angular momentum was investigated and the output parameters of net mass transferred, contact time, neck density, N

and Z numbers and outgoing angle were used to interpret the results. TDHF results were compared with experimental measurements of the ^{40}Ca + ^{238}U reaction.

In all cases studied, whether as a function of energy or angular momentum a few global observations can be made:

- The axis configuration always reseparates after a short contact time and leads to asymmetric mass splits in the A=208 region. The quasifission process was found to be the primary component in axial collisions. The short contact times corresponding to these splits are also consistent with quasifission. A detailed analysis of the N and Z numbers confirms that this is due to the doubly magic ^{208}Pb shell closure.

- The equator configuration lead to fusion for high energies and low initial angular momenta L. This configuration leads to relatively longer contact times and much greater mass transfer compared to the axis case. Thus equatorial collisions are far more likely to lead to CN formation.

- The theoretical mass splits match the experimental mass splits very well. Outgoing angles extracted from TDHF accurately reproduce experimental MADs as well.

Overall, excellent agreement was seen between TDHF and the experiments discussed in Chapter 5. A few points can be investigated further in future work.

Outlook

There are two main avenues available for future work, at the TDHF level and beyond TDHF. At the TDHF level there are several options we plan to pursue in future work:

- The ^{40}Ca + ^{238}U system can be studied in more detail: In this work we only looked at the two extreme orientations where the deformation axis of ^{238}U was parallel to the x-axis (axial) and y-axis (equatorial). There is a third extreme orientation where the deformation axis is parallel to the z-axis that could be explored. We expect this orientation to behave more like the equator orientation for central collisions. For non central collisions the axis of rotation now passes through the deformation axis and thus the behaviour may lie intermediate to axial and equatorial collisions.

  An extension of this line of thought would be to investigate intermediate orientations where the deformation axis is not parallel to the coordinate axes, but angled with

respect to them. By populating the QF channel with orientations other than axis, we could gain additional insight into the dynamics of this QF process. In the current work, we also see hints of QF and DQF within a narrow range of L values for equatorial collisions. A detailed look into the interplay between all these processes might also be fruitful.

Furthermore, we could select only few energies and study them experimentally in much more detail. I.e. collect data for longer, such that we have extremely high statistics to compare fine structures in the MADs with TDHF results.

- We also propose investigating other, lighter reactions. The first would be ^{34}S + ^{232}Th, before moving on to other systems studied in this thesis. For the lightest systems we expect TDHF to consistently predict fusion at energies above the average barrier. The aim of this investigation would be to see where TDHF predicts the threshold between QF and FF to lie and how this compares with experimental results.

- Finally, beyond TDHF methods like Balian-Vénéroni [114] and particle number projection [123] can be used to predict mass widths. These methods are beyond the scope of this work, but are currently being investigated and may be promising candidates for future applications to quasifission. This would provide, by far, the most robust comparison with experimental MADs.

All these are steps towards testing TDHF as a reliable model of reaction dynamics. Guided by experimental results, we aim to investigate and uncover the interplay between reaction channels ranging from FF to DQF to QF using one model, with a limited and self consistent initial parameter space. TDHF and its extensions are promising candidates for this goal.

Chapter 7

Conclusion

Experimental and theoretical studies were carried to develop a quantitative understanding of the variables influencing quasifission.

Experimental measurements were carried out using the ANU 14UD accelerator. Reactions of projectiles ranging from ^{12}C to ^{40}Ca, with targets of ^{238}U and ^{232}Th were studied. In total eight reactions were studied, six of them in pairs forming the same composite nucleus, at a range of energies spanning the fusion barrier. The measurements utilized the large angular coverage of the CUBE fission spectrometer allowing wide ranging mass-angle spectra to be obtained for each reaction.

A systematic analysis, based on the mass and angle of binary fission fragments was carried out. Results indicate that the lightest two reactions, forming ^{250}Cf proceed via true compound nucleus fission, with the fission of the CN being mass-asymmetric due to shell effects. The remaining six reactions of interest, forming the ^{262}Rf, ^{266}Sg, ^{272}Ds and ^{278}Cp composite systems, all have a measurable quasifission flux. The quasifission flux observed had two modes, mass-asymmetric and mass-symmetric. The reactions forming ^{262}Rf had the weakest mass-asymmetric quasifission flux of all reactions studied. The reactions forming ^{266}Sg had a much stronger mass-asymmetric quasifission flux, visible at all energies studied. The ^{40}Ca induced reactions forming ^{272}Ds and ^{278}Cp were dominated by mass-asymmetric quasifission, with only a few of the highest energies studied leading to mass-symmetric splits.

The mass splits of these six reactions indicated that the mass-asymmetric quasifission flux is influenced by doubly magic shell closure at ^{208}Pb. A detailed analysis of the mass

of the outgoing fragments as a function of outgoing angle revealed conclusively that the ^{208}Pb shell closure slows the evolution of the dinuclear systems as the heavy fragment passes through this mass region. A simple calculation that accounted for the role of shell effects in the light fragment indicated that shell closures around Z=28, N=50 also influence the evolution of the dinuclear system.

Based on the fission mass widths we identified the presence of mass-symmetric quasifission. Its overlap with the observable characteristic of fusion-fission implied that a significant fraction of the mass-symmetric flux is due to non-equilibrium fission (quasifission). Thus CN formation is severely hindered by quasifission in these reactions. These measurements also revealed that the transition from quasifission to fusion-fission, for reactions with ^{238}U and ^{232}Th, occurs below $Z_pZ_t = 1104$.

We also saw evidence for the role of entrance channel on the quasifission flux. The quasifission flux increased with decreasing entrance channel mass-asymmetry, a well studied phenomenon in the literature.

The experimental work was complemented by a theoretical study of the heaviest reaction: ^{40}Ca + ^{238}U. The TDHF theory, applied numerically via the TDHF3D code was used to study central and non-central collisions for two different extreme orientations of the deformed ^{238}U nucleus, at a range of energies spanning the fusion barrier. Masses, angles, neutron (N) and proton (Z) numbers of the reaction products were extracted from the outputs and used to compare TDHF results with experimental results. For three specific energies where non-central collisions were studied, MADs were calculated using the TDHF results. As a check, central collisions were also studied for the ^{48}Ca + ^{238}U reaction.

The calculations for central collisions revealed that the mass splits predicted by TDHF, as a function of interaction energy, match well with the experimental results. The entrance channel magicity was found to to be weaker for ^{40}Ca induced reactions compared to ^{48}Ca induced reactions. N/Z equilibration was found to play a strong role in initiating nucleon transfer in the ^{40}Ca case, but not in the ^{48}Ca case.

The MADs calculated from non-central TDHF collisions agreed well with the experimental MADs. The global features of the experimental MADs, namely the position of the mass-asymmetric quasifission peaks, were reproduced well by TDHF. The timescales of reactions consistent with quasifission were found to be few 10^{-21}s, in agreement with

the experimentally inferred time scale of quasifission. The orientation of the deformed ^{238}U nucleus was found to play a major role in reaction outcome with the aligned case always leading to quasifission and the anti-aligned case being the only orientation leading to longer contact times, with a few cases not reseparating within the calculation time. Additionally, the angular threshold between mass-transfer collisions and (in)elastic collisions was also reproduced well by TDHF. An investigation into the N and Z numbers confirmed that the ^{208}Pb shell influences the mass-asymmetric quasifission splits for this reactions. The outgoing fragments were found to be consistent around $Z = 82$ and $N = 126$.

The measurements presented in this thesis are the most comprehensive data set of wide angular coverage mass-angle distributions for reactions with ^{238}U and ^{232}Th forming superheavy composite nuclei. The theoretical work presented in this thesis comprises the most comprehensive set of TDHF calculations for the ^{40}Ca + ^{238}U reaction forming the ^{278}Cp composite nucleus. The agreement with experimentally observed and inferred quantities demonstrates the predictive power of TDHF.

Any dynamical model aimed at predicting the synthesis of superheavy elements should be able to describe the presence of quasifission for such a wide range of systems and calculate the detailed and consistent structures seen in the experimental mass-angle distributions. The combination of experimental and theoretical work as presented in this thesis is a step towards this goal. Similarly detailed investigations of other reactions promise to shed light onto the nature of quasifission, eventually leading to a consistent picture of all observables and a full understanding of the variables controlling heavy element formation.

Bibliography

[1] Yu. Ts. Oganessian, V. K. Utyonkov, Yu. V. Lobanov, F. Sh. Abdullin, A. N. Polyakov, R. N. Sagaidak, I. V. Shirokovsky, Yu. S. Tsyganov, A. A. Voinov, G. G. Gulbekian, S. L. Bogomolov, B. N. Gikal, A. N. Mezentsev, S. Iliev, V. G. Subbotin, A. M. Sukhov, K. Subotic, V. I. Zagrebaev, G. K. Vostokin, M. G. Itkis, K. J. Moody, J. B. Patin, D. A. Shaughnessy, M. A. Stoyer, N. J. Stoyer, P. A. Wilk, J. M. Kenneally, J. H. Landrum, J. F. Wild and R. W. Lougheed, Phys. Rev. C **74**, 044602, 2006.

[2] S. Hofmann, D. Ackermann, S. Antalic, H. G. Burkhard, V. F. Comas, R. Dressler, Z. Gan, S. Heinz, J. A. Heredia, F. P. Heßberger, J. Khuyagbaatar, B. Kindler, I. Kojouharov, P. Kuusiniemi, M. Leino, B. Lommel, R. Mann, G. Münzenberg, K. Nishio, A. G. Popeko, S. Saro, H. J. Schött, B. Streicher, B. Sulignano, J. Uusitalo, M. Venhart and A. V. Yeremin, Eur. Phys. J. A **32**, 251, 2007.

[3] M. Morjean, D. Jacquet, J. L. Charvet, A. L'Hoir, M. Laget, M. Parlog, A. Chbihi, M. Chevallier, C. Cohen, D. Dauvergne, R. Dayras, A. Drouart, C. Escano-Rodriguez, J. D. Frankland, R. Kirsch, P. Lautesse, L. Nalpas, C. Ray, C. Schmitt, C. Stodel, L. Tassan-Got, E. Testa and C. Volant, Phys. Rev. Lett. **101**, 072701, 2008.

[4] A. Sobiczewski, F. A. Gareev and B. N. Kalinkin, Phys. Lett. **22**, 500, 1966.

[5] P. Armbruster, Comptes Rendus Physique **4**, 571, 2003.

[6] K. Morita, K. Morimoto, D. Kaji, T. Akiyama, S. Goto, H. Haba, E. Ideguchi, K. Katori, H. Koura, H. Kikunaga, H. Kudo, T. Ohnishi, A. Ozawa, N. Sato, T. Suda, K. Sueki, F. Tokanai, T. Yamaguchi, A. Yoneda and A. Yoshida, J. Phys. Soc. Jpn. **76**, 045001, 2007.

[7] Yu. Ts. Oganessian, A. V. Yeremin, A. G. Popeko, S. L. Bogomolov, G. V. Buklanov, M. L. Chelnokov, V. I. Chepigin, B. N. Gikal, V. A. Gorshkov, G. G. Gulbekian, M. G. Itkis, A. P. Kabachenko, A. Yu. Lavrentev, O. N. Malyshev, J. Rohac, R. N. Sagaidak, S. Hofmann, S. Saro, G. Giardina and K. Morita, Nature **400**, 242, 1999.

[8] Yu. Ts. Oganessian, V. K. Utyonkov, Yu. V. Lobanov, F. Sh. Abdullin, A. N. Polyakov, I. V. Shirokovsky, Yu. S. Tsyganov, G. G. Gulbekian, S. L. Bogomolov, B. N. Gikal, A. N. Mezentsev, S. Iliev, V. G. Subbotin, A. M. Sukhov, O. V. Ivanov, G. V. Buklanov, K. Subotic, M. G. Itkis, K. J. Moody, J. F. Wild, N. J. Stoyer, M. A. Stoyer, R. W. Lougheed, C. A. Laue, Ye. A. Karelin and A. N. Tatarinov, Phys. Rev. C **63**, 011301R, 2000.

[9] Yu. Ts. Oganessian, F. Sh. Abdullin, P. D. Bailey, D. E. Benker, M. E. Bennett, S. N.Dmitriev, J. G. Ezold, J. H. Hamilton, R. A. Henderson, M. G. Itkis, Yu. V. Lobanov, A. N. Mezentsev, K. J. Moody, S. L. Nelson, A. N. Polyakov, C. E. Porter, A. V. Ramayya, F. D. Riley, J. B. Roberto, M. A. Ryabinin, K. P. Rykaczewski, R. N. Sagaidak, D. A. Shaughnessy, I. V. Shirokovsky, M. A. Stoyer, V. G. Subbotin and R. Sudowe, Phys. Rev. Lett. **104**, 142502, 2010.

[10] W. J. Swiatecki, Phys. Scr. **24**, 113, 1981.

[11] S. Bjørnholm and W. J. Swiatecki, Nucl. Phys. A **391**, 471, 1982.

[12] J. P. Blocki, H. Feldmeier and W. J. Swiatecki. Nucl. Phys. A **459**, 145, 1986.

[13] P. Moller and A. J. Sierk, Nature **422**, 485, 2003.

[14] N. Bohr, Nature **37**, 344, 1936.

[15] W. U. Schroeder and J. R. Huizenga, Damped Nuclear Reactions Vol. **2**, 115, Plenum Press, New York, 1984.

[16] J. Tōke, R. Bock, G. X. Dai, A. Gobbi, S. Gralla, K. D. Hildenbrand, J. Kuzminski, W. F. J. Müller, A. Olmi, H. Stelzeret, B. B. Back and S. Bjørnholm, Nucl. Phys. A **440**, 327, 1985.

[17] B. B. Back, P. B. Fernandez, B. G. Glagola, D. Henderson, S. Kaufman, J. G. Keller, S. J. Sanders, F. Videbæk, T. F. Wang and B. D. Wilkins, Phys. Rev. C **53**, 1734, 1996.

[18] D. J. Hinde, A. C. Berriman, R. D. Butt, M. Dasgupta, I. I. Gontchar, C. R. Morton, A. Mukherjee and J. O. Newton, J. Nucl. Radiochem. Sci. **3**, 31, 2002.

[19] S. Mitsuoka, H. Ikezoe, K. Nishio, K. Satou and J. Lu, Phys. Rev. C **65**, 054608, 2002.

[20] G. N. Knyazheva, E. M. Kozulin, R. N. Sagaidak, A. Yu. Chizhov, M. G. Itkis, N. A. Kondratiev, V. M. Voskressensky, A. M. Stefanini, B. R. Behera, L. Corradi, E. Fioretto, A. Gadea, A. Latina, S. Szilner, M. Trotta, S. Beghini, G. Montagnoli, F. Scarlassara, F. Haas, N. Rowley, P. R. S. Gomes and A. Szanto de Toledo, Phys. Rev. C **75**, 064602, 2007.

[21] D. C. Hoffman, Acc. Chem. Res. **17**, 235, 1984.

[22] C. Böckstiegel, S. Steinhäuser, K.-H. Schmidt, H.-G. Clerc, A. Grewe, A. Heinz, M. de Jong, A. R. Junghans, J. Müller, B. Voss, Nucl. Phys. A **802**, 12, 2008.

[23] B. B. Back, J. Phys. Conf. Ser. **282**, 012003, 2011.

[24] B. Heusch, C. Volant, H. Freiesleben, R. P. Chestnut, K. D. Hildenbrand, F. Pühlhofer, W. F. W. Schneider, B. Kohlmeyer and W. Pfeffer, Z. Phys. A **288**, 391, 1978.

[25] S.Cohen, F.Plasil and W.J. Swiatecki, Ann. Phys. **82**, 557, 1974.

[26] W. Q. Shen, J. Albinski, A. Gobbi, S. Gralla, K. D. Hildenbrand, N. Herrmann, J. Kuzminski, W. F. J. Muller, H. Stelzer, J. Tōke, B. B. Back, S. Bjørnholm and S. P. Srensen, Phys. Rev. C **36**, 115, 1987.

[27] C. Lebrun, F. Hanappe, J.F. LeColley, F. Lefebvres, C. Ngô, J. Péter and B. Tamain, Nucl. Phys. A **321**, 207, 1979.

[28] B. Borderie, M. Berlanger, D. Gardés, F. Hanappe, L. Nowicki, J. Péter, B. Tamain, S. Agarwal, J. Girard, C. Grégoire, J. Matuszek and C. Ngô, Z. Phys. A **299**, 263, 1981.

[29] B. B. Back, R. R. Betts, K. Cassidy, B. G. Glagola, J. E. Gindler, L. E. Glendenin and B. D, Phys. Rev. Lett. **50**, 818, 1983.

[30] B. B. Back, R. R. Betts, J. E. Gindler, B. D. Wilkins, S. Saini, M. B. Tsang, C. K. Gelbke, W. G. Lynch, M. A. McMahan and P. A. Baisden, Phys. Rev. C **32**, 195, 1985.

[31] B.B.Back, H. -G. Clerc, R. R. Betts, B. G. Glagola and B. D. Wilkins, Phys. Rev. Lett. **46**, 1068, 1981.

[32] D.J. Hinde, R. du Rietz, M. Dasgupta, R. G. Thomas and L. R. Gasques, Phys. Rev. Lett. **101**, 202701, 2008.

[33] H.Q. Zhang, C. L. Zhang, C. J. Lin, Z. H. Liu, F. Yang, A. K. Nasirov, G. Mandaglio, M. Manganaro and G. Giardina, Phys. Rev. C **81**, 034611, 2010.

[34] D.J. Hinde, R. du Rietz, M. Dasgupta, R. G. Thomas and L. R. Gasques, Phys. Rev. Lett. **101**, 092701, 2008.

[35] R. du Rietz, D. J. Hinde, M. Dasgupta, R. G. Thomas, L. R. Gasques, M. Evers, N. Lobanov and A. Wakhle, Phys. Rev. Lett. **106**, 052701, 2011.

[36] D. J. Hinde, M. Dasgupta, J. R. Leigh, J. C. Mein, C. R. Morton, J. O. Newton and H. Timmers, Phys. Rev. C **53**, 1290, 1996.

[37] D. J. Hinde, M. Dasgupta, J. R. Leigh, J. P. Lestone, J. C. Mein, C. R. Morton, J. O. Newton and H. Timmers, Phys. Rev. Lett. **74**, 1295, 1995.

[38] R. G. Thomas, D. J. Hinde, D. Duniec, F. Zenke, M. Dasgupta, M. L. Brown, M. Evers, L. R. Gasques, M. D. Rodriguez and A. Diaz-Torres, Phys. Rev. C **77**, 034610, 2008.

[39] R. Bock, Y. T. Chu, M. Dakowski, A. Gobbi, E. Grosse, A. Olmi, H. Sann, D. Schwalm, U. Lynen, W. Muller, S. Bjørnholm, H. Esbensen, W. Wolfli and E. Morenzoni, Nucl. Phys. A **388**, 334, 1982.

[40] R. Rafiei, R. G. Thomas, D. J. Hinde, M. Dasgupta, C. R. Morton, L. R. Gasques, M. L. Brown and M. D. Rodriguez, Phys. Rev. C **77**, 024606, 2008.

[41] M.G. Itkis, J. Äystö, S. Beghini, A.A. Bogachev, L. Corradi, O. Dorvaux, A. Gadea, G. Giardina, F. Hanappe, I.M. Itkis, M. Jandel, J. Kliman, S.V. Khlebnikov, G.N. Kniajeva, N.A. Kondratiev, E.M. Kozulin, L. Krupa, A. Latina, T. Materna,

G. Montagnoli, Yu.Ts. Oganessian, I.V. Pokrovsky, E.V. Prokhorova, N. Rowley, V.A. Rubchenya, A.Ya. Rusanov, R.N. Sagaidak, F. Scarlassara, A.M. Stefanini, L. Stuttgé, S. Szilner, M. Trotta, W.H. Trzaska, D.N. Vakhtin, A.M. Vinodkumar, V.M. Voskressenski, V.I. Zagrebaev, Nucl. Phys. A **734**, 136, 2004.

[42] M.G. Itkis, A.A. Bogachev, I.M. Itkis, J. Kilman, G. N. Knyazheva, N. A. Kondratiev, E. M. Kozulin, L. Krupa, Yu. Ts. Oganessian, I. V. Pokrovsky, E. V. Prokhorova, A. Ya. Rusanov, Nucl. Phys. A **787**, 150c, 2007.

[43] M.G. Itkis, Yu. Ts. Oganessian, A. A. Bogatchev, I. M. Itkis, M. Jandel, J. Kliman, G. N. Kniajeva, N. A. Kondratiev, I. V. Korzyukov, E. M. Kozulin, L. Krupa, I. V. Pokrovski, E. V. Prokhorova, B. I. Pustylnik, A. Ya. Rusanov, V. M. Voskresenski, F. Hanappe, B. Benoit, T. Materna, N. Rowley, L. Stuttgé, G. Giardina and K. J. Moody, Fusion Dynamics At The Extremes, 93, 2001.

[44] E.M. Kozulin, G.N. Knyazheva, I.M. Itkis, M.G. Itkis, A.A. Bogachev, L. Krupa, T.A. Loktev, S.V. Smirnov, V.I. Zagrebaeva, J. ÕĄystÕê, W.H. Trzaska, V.A. Rubchenya, E. Vardaci, A.M. Stefanini, M. Cinausero, L. Corradi, E. Fioretto, P. Mason, G.F. Prete, R. Silvestri, S. Beghini, G. Montagnoli, F. Scarlassara, F. Hanappe, S.V. Khlebnikov, J. Kliman, A. Brondi, A. Di Nitto, R. Moro, N. Gelli, S. Szilner, Phys. Lett. B **686**, 227, 2010.

[45] D.J. Hinde, D. Hilscher, H. Rossner, B. Gebauer, M. Lehmann and M. Wilpert, Phys. Rev. C **45**, 1229, 1992.

[46] K. Siwek-Wilczyńska, J. Wilczynski, R. H. Siemssen, H. W. Wilschut, Nucl. Phys. A **583**, 141, 1995.

[47] M. F. Rivet, R. Alami, B. Borderie, H. Fuchs, D. Gardes and H. Gauvin, Z. Phys. A **330**, 295, 1988.

[48] J. C. Mein, D. J. Hinde, M. Dasgupta, J. R. Leigh, J. O. Newton and H. Timmers, Phys. Rev. C **55**, R995, 1997.

[49] J. P. Lestone, A. A. Sonzogni, M. P. Kelly and R. Vandenbosch, J. Phys. G **23**, 1349, 1997.

[50] K. Nishio, H. Ikezoe, Y. Nagame, M. Asai, K. Tsukada, S. Mitsuoka, K. Tsuruta, K. Satou, C. J. Lin and T. Ohsawa, Phys. Rev. Lett. **93**, 162701, 2004.

[51] S. Mitsuoka, H. Ikezoe, K. Nishio and J. Lu, Phys. Rev. C **62**, 054603, 2000.

[52] A. C. Berriman, D. J. Hinde, M. Dasgupta, C. R. Morton, R. D. Butt and J. O. Newton, Nature **413**, 144, 2001.

[53] A. Yu. Chizhov, M. G. Itkis, I. M. Itkis, G. N. Knyazheva, E. M. Kozulin, N. A. Kondratiev, I. V. Pokrovsky, R. N. Sagaidak, V. M. Voskressensky, A. V. Yeremin, L. Corradi, A. Gadea, A. Latina, A. M. Stefanini, S. Szilner, M. Trotta, A. M. Vinodkumar, S. Beghini, G. Montagnoli, F. Scarlassara, A. Ya. Rusanov, F. Hanappe, O. Dorvaux, N. Rowley and L. Stuttgé, Phys. Rev. C **67**, 011603(R), 2003.

[54] D. J. Hinde, M. Dasgupta and A. Mukherjee, Phys. Rev. Lett. **89**, 282701, 2002.

[55] Y. Aritomo, J. Nucl. Radiochem. Sci. **3**, 17, 2002.

[56] Y. Aritomo and M. Ohta, Phys. Atom. Nucl. **66**, 1105, 2003.

[57] K. Nishio, H. Ikezoe, I. Nishinaka, S. Mitsuoka, K. Hirose, T. Ohtsuki, Y. Watanabe, Y. Aritomo, and S. Hofmann, Phys. Rev. C **82**, 044604, 2010.

[58] Yu. Ts. Oganessian, V. K. Utyonkov, Yu. V. Lobanov, F. Sh. Abdullin, A. N. Polyakov, I. V. Shirokovsky, Yu. S. Tsyganov, G. G. Gulbekian, S. L. Bogomolov, B. N. Gikal, A. N. Mezentsev, S. Iliev, V. G. Subbotin, A. M. Sukhov, A. A. Voinov, G. V. Buklanov, K. Subotic, V. I. Zagrebaev, M. G. Itkis, J. B. Patin, K. J. Moody, J. F. Wild, M. A. Stoyer, N. J. Stoyer, D. A. Shaughnessy, J. M. Kenneally, P. A. Wilk, R. W. Lougheed, R. I. Il'kaev and S. P. Vesnovskii, Phys. Rev. C **70**, 064609, 2004.

[59] K. Krane, Introductory Nuclear Physics, John Wiley and Sons USA, 1988.

[60] S. Nilsson and I. Ragnarsson, Shapes and Shells in Nuclear Structure, Cambridge University Press, 1995.

[61] A. Bohr and B. R. Mottelson, Nuclear Structure, Volume 1, World Scientific, 1998.

[62] W. D. Myers and W. J. Swiatecki, Ann. Phys. **55**, 395, 1969.

[63] D. J. Griffiths, Introduction to Quantum Mechanics, Prentice-Hall USA, 1989.

[64] S. Nilsson, Mat. Fys. Medd. Dan Vid. Selsk **29**, 16, 1955.

[65] V. M. Strutinsky, Nucl. Phys. A **95**, 420, 1966.

[66] K. Pomorski and J. Dudek, Phys. Rev. C **67**, 044316, 2003.

[67] A. J. Sierk, Phys. Rev. C **33**, 2039, 1986.

[68] H. J. Krappe, Phys. Rev. C **59**, 2640, 1999.

[69] A. V. Karpov, P. N. Nadtochy, E. G. Ryabov and G. D. Adeev, J. Phys. G **29**, 2365, 2003.

[70] V. I. Zagrebaev and W. Greiner, J. Phys. G **31**, 825, 2005.

[71] V. I. Zagrebaev, Yu. Ts.Oganessian, M. G. Itkis and W. Greiner, Phys. Rev. C **73**, 031602, 2006.

[72] V. I. Zagrebaev and W. Greiner, Phys. Rev. Lett. **101**, 122701, 2008.

[73] V. I. Zagrebaev and Walter Greiner, Phys. Rev. C **83**, 044618, 2011.

[74] V. I. Zagrebaev, A. V. Karpov and Walter Greiner, Phys. Rev. C **85**, 014608, 2012.

[75] C. Simenel, Eur. Phys. J. A **48**, 152, 2012.

[76] D. J. Kedziora and C. Simenel, Phys. Rev. C **81**, 044613, 2010.

[77] P. A. M. Dirac, Proc. Camb. Philos. Soc. **26**, 376, 1930.

[78] E. Chabanat, P. Bonche, P. Haensel, J. Meyer and R. Schaeffer, Nucl. Phys. A4 **627**, 710, 1997.

[79] E. Chabanat, P. Bonche, P. Haensel, J. Meyer and R. Schaeffer, Nucl. Phys. A1 **635**, 231, 1998.

[80] D. Vautherin and D. M. Brink, Phys. Rev. C **5**, 626, 1972.

[81] D. Vautherin Phys. Rev. C **7**, 296, 1973.

[82] T. R. Ophel, J. S. Harrison, J. O. Newton, R. H. Spear, E. W. Titterton and D. C. Weisser, Nuclear Instruments and Methods **122**, 227, 1974.

[83] D. A. Bromley, Nuclear Instruments and Methods **122**, 1, 1974.

[84] R. G. Herb, Nuclear Instruments and Methods **122**, 267, 1974.

[85] N. R. Lobanov and D. C. Weisser, Symposium of North Eastern Accelerator Personnel, **255**, 1999.

[86] R. Middleton, Nuclear Instruments and Methods **122**, 35, 1974.

[87] R. Middleton, Nuclear Instruments and Methods **214**, 139, 1983.

[88] A. B. Wittkower and H. D. Betz, Atomic Data and Nuclear Data Tables **5**, 113, 1973.

[89] V. S. Nikolaev and I. S. Dmitriev, Phys. Lett. A **28**, 277, 1968.

[90] J. L. Yntema, Nuclear Instruments and Methods **122**, 45, 1974.

[91] R. H. Spear, D. C. Kean, M. T. Esat, A. M. R. Joye and M. P. Fewell, Nuclear Instruments and Methods **147**, 455, 1977.

[92] J. R. Leigh, M. Dasgupta, D. J. Hinde, J. C. Mein, C. R. Morton, R. C. Lemmon, J. P. Lestone, J. O. Newton, H. Timmers, J. X. Wei and N. Rowley, Phys. Rev. C **52**, 52, 1995.

[93] P. M. Davidson and G. S. Foote, Nuclear Instruments and Methods **382**, 178, 1996.

[94] B. A. Mackinnon, A. E. Stuchbery and D. C. Weisser, Nuclear Instruments and Methods Res. B **92**, 138, 1994.

[95] A. E. Stuchbery and D. C. Weisser, Nuclear Instruments and Methods Res. A **382**, 172, 1996.

[96] R. Rafiei, R. du Rietz, D. H. Luong, D. J. Hinde, M. Dasgupta, M. Evers and A. Diaz-Torres, Phys. Rev. C **81**, 024601, 2010.

[97] W. J. Swiatecki, K. Siwek-Wilczyńska and J. Wilczynski, Phys. Rev. C **71**, 014602, 2005.

[98] K.-H. Kim, T. Otsuka and P. Bonche, J. Phys. G **23**, 1267, 1997.

[99] http://nci.org.au/facilities-and-sevices/national-facility/current-peak-system/

[100] http://www.theage.com.au/technology/sci-tech/australias-new-supercomputer-outflops-the-lot-20091116-ihew.html

[101] http://www-ccrt.cea.fr/fr/moyen_de_calcul/mercure.htm

[102] V. E. Viola, K. Kwiatkowski and M. Walker, Phys. Rev. C **31**, 1550, 1985.

[103] I. V. Pokrovsky, L. Calabretta, M. G. Itkis, N. A. Kondratiev, E. M. Kozulin, C. Maiolino, E. V. Prokhorova, A. Ya. Rusanov and S. P. Tretyakova, Phys. Rev. C **60**, 041304, 1999.

[104] I. V. Pokrovsky, M. G. Itkis, J. M. Itkis, N. A. Kondratiev, E. M. Kozulin, E. V. Prokhorova, V. S. Salamatin, V. V. Pashkevich, S. I. Mulgin, A. Ya. Rusanov, S. V. Zhdanov, G. G. Chubarian, B. J. Hurst, R. P. Schmitt, C. Agodi, G. Bellia, L. Calabretta, K. Lukashin, C. Maiolino, A. Kelic, G. Rudolf, L. Stuttge and F. Hanappe, Phys. Rev. C **62**, 014615, 2000.

[105] C. Yadav, R. G. Thomas, R. K. Choudhury, P. Sugathan, A. Jhingan, S. Appannababu, K. S. Golda, D. Singh, Ish Mukul, J. Gehlot, E. Prasad and H. J. Wollersheim, Phys. Rev. C **86**, 034606, 2012.

[106] R. Vandenbosch and J. R. Huizenga, Nuclear Fission, Academic, New York, 1973.

[107] V. S. Ramamurthy, S. S. Kapoor and S. K. Kataria, Phys. Rev. Lett. **25**, 386, 1970.

[108] I. M. Itkis, E. M. Kozulin, M. G. Itkis, G. N. Knyazheva, A. A. Bogachev, E. V. Chernysheva, L. Krupa, Yu. Ts. Oganessian, V. I. Zagrebaev, A. Ya. Rusanov, F. Goennenwein, O. Dorvaux, L. Stuttgé, F. Hanappe, E. Vardaci, E. de Goés Brennand, Phys. Rev. C **83**, 064613, 2011.

[109] Z.-Q. Feng, G.-M. Jin and J.-Q. Li, Phys. Rev. C **80**, 067601, 2009.

[110] C. Simenel, D.J. Hinde, R. du Rietz, M. Dasgupta, M. Evers, C.J. Lin, D.H. Luong and A. Wakhle, Phys. Lett. B **710**, 607, 2012.

[111] M. Dasgupta and D.J. Hinde, Nucl. Phys. A **734**, 148, 2004.

[112] M. G. Itkis, V. N. Okolovich, A. Yu. Rusanov, G. N. Smirenkin, Sov. J. Part. Nucl. **19**, 301, 1988.

[113] C. Golabek and C. Simenel, Phys. Rev. Lett. **103**, 042701, 2009.

[114] C. Simenel, C. Golabek and D. J. Kedziora, Eur. Phys. J. **17**, 09002, 2011.

[115] P. Bonche, S. Koonin and J. W. Negele, Phys. Rev. C **13**, 1226, 1976.

[116] P. Bonche, B. Grammaticos and S. Koonin, Phys. Rev. C **17**, 170, 1978.

[117] J. W. Negele, Rev. Mod. Phys. **54**, 913, 1982.

[118] E. Chabanat, P. Bonche, P. Hansel, J. Meyer and R. Schaeffer, Phys. Scr. T **56**, 231, 1995.

[119] K. Davies, H. Flocard, S. Krieger and M. Weiss, Nucl. Phys. A **342**, 111, 1980.

[120] D. J. Thouless and J. G. Valatin, Nucl. Phys. **31**, 211, 1962.

[121] H. Flocard, S. E. Koonin and M. S. Weiss, Phys. Rev. C **17**, 1682, 1978.

[122] R. Bass, Nuclear Reactions with Heavy Ions, Chapter 7.4, 318, Springer-Verlag, New York, 1980.

[123] C. H. Dasso, T. Døssing and H. C. Pauli, Z. Phys. A **289**, 395, 1979.

[124] V. F. C. Lijachev, PhD Thesis, 2012.

Appendix A

Codes used for Data Analysis

A.1 Code used to Correct Gain Drift

```
// This neat little program will (hopefully) take input cube
// raw data file (e.g. SSITHU_RUN010.root) and shift the time spectrum
// based on the value of the pulser drift.
// Include standard stuff
#include <string>
#include <fstream>
#include <iostream>
#include <stdio.h>
#include <stdlib.h>
#include <sys/stat.h>
// Include ROOT stuff
#include <TCanvas.h>
#include <TCutG.h>
#include <TROOT.h>
#include <TH2.h>
#include <TH1.h>
#include <TGListBox.h>
#include <TFile.h>
#include <TEnv.h>
#include <TKey.h>
#include <TDirectory.h>
#include <TVector3.h>
#include <TMath.h>
#include <TTree.h>
#include <TGTab.h>
```

```
#include <TGProgressBar.h>
#include <TGFileDialog.h>
#include <TGTableLayout.h>
#include <TGTextEntry.h>
#include <TGComboBox.h>
#include <TPRegexp.h>
#include <TString.h>
//Type def for the cube tree branches
typedef unsigned short DCPElement;
//Structure of the Tree
typedef struct TAG_InterestingData{
  // Branch "Cube"
  DCPElement EBack;
  DCPElement EFront;
  DCPElement TBack;
  DCPElement TFront;
  DCPElement XBack;
  DCPElement YBack;
  DCPElement XFront;
  DCPElement YFront;
  // Branch "Monitors"
  DCPElement AlphaPulser;
  DCPElement Monitor1;
  DCPElement Monitor2;
  // Branch "Annular"
  DCPElement EAnnular;
  DCPElement TAnnular;
  // Branch "Front"
  DCPElement EAlphaFront;
  DCPElement TAlphaFront;
} TInterestingData;
//Structure of the Tree
typedef struct NEW_TAG_InterestingData{
  // Branch "Cube"
  DCPElement EBack;
  DCPElement EFront;
  DCPElement TBack;
  DCPElement TFront;
  DCPElement XBack;
  DCPElement YBack;
  DCPElement XFront;
```

```
  DCPElement YFront;
  // Branch "Monitors"
  DCPElement AlphaPulser;
  DCPElement Monitor1;
  DCPElement Monitor2;
  // Branch "Annular"
  DCPElement EAnnular;
  DCPElement TAnnular;
  // Branch "Front"
  DCPElement EAlphaFront;
  DCPElement TAlphaFront;
} TNEWInterestingData;

int timeshift(){
  // Set number of bins to divide file into
  // Set the desired position of TBack pulser and TFront pulser (in channels
     [continued] )
  // Set the tolerance on this (typically 2-5 channels)
  // Set names of file to process and file to write to
  // Set BShiftFlag and FShiftFlag to select either a constant shift (0);
  // or a linear shift (1) that scales with the position of  the pulser
  // Finally go to line 160 and set gates to accurately select the pulser
  int maxbins = 100;
  int TBPulser = 131.0;
  int TFPulser = 772.0;
  int Btolerance = 100.0;
  int Ftolerance = 2.0;
  int BShiftFlag = 0;
  int FShiftFlag = 1;
  TFile *runfile = new TFile("CAGEX.RUN018.root");
  TString outfileName = "CAGEXTS.RUN018.root";
  TFile *outfile;
  outfile = new TFile(outfileName,"RECREATE","ROOT file");
  outfile->SetCompressionLevel(1);
  // get tree and assign branches
  TTree *cubetree = (TTree *)runfile->Get("CubeTree");
  TInterestingData id;
  TNEWInterestingData idnew;
  //setting the branch addresses of the raw data tree.
  //This is the standard format with which the data
  //are converted to root format from the DCP format (courtsey Micheal Brown
     [continued] )
```

```
cubetree->SetBranchAddress("Cube", &id.EBack);
cubetree->SetBranchAddress("Monitors", &id.AlphaPulser);
cubetree->SetBranchAddress("Annular", &id.EAnnular);
cubetree->SetBranchAddress("Front", &id.EAlphaFront);
int nevent_tot = (int) cubetree->GetEntries();
int nevent = nevent_tot;
double shift[1026][3];
double TBTotal = 0;
double TFTotal = 0;
double TBavg=0;
double TFavg=0;
int bin=0;
int frac =1;
int count=0;
TTree *newTree = new TTree();
newTree = new TTree("CubeTree","ROOT tree filled with raw data");
newTree->SetAutoSave(1000000000);
newTree->Branch("Cube",&idnew.EBack,"EBack/s:EFront:TBack:TFront:XBack:
    [continued] YBack:XFront:YFront");
newTree->Branch("Monitor",&id.AlphaPulser,"AlpaPulser/s:Monitor1:Monitor2
    [continued] ");
newTree->Branch("EAnnular",&id.EAnnular,"EAnnular/s:TAnnular");
newTree->Branch("Front",&id.AlphaPulser,"EAlpaPulser/s:TAlphaPulser");
cout << "START EVENT LOOP ..." <<nevent<< endl;
// Loop to generate array of bins and corresponding time shifts
for (int evt = 00000; evt<nevent; evt++)
  { // get the old stuff
    cubetree->GetEvent(evt);
//select pulser via a very comprehensive gate
//then calculate values for a given bin
if (id.TBack>100 && id.TBack<170 && id.TFront>650 && id.TFront<850 &&
    [continued] id.YBack>1080 && id.YBack<1180 && id.XBack>1080 && id.
    [continued] XBack<1180 && id.EBack>300)
  {
    TBTotal = TBTotal + id.TBack;
    TFTotal = TFTotal + id.TFront;
    count++;
  }
//store values on a bin by bin basis
//depending on the valus of frac
if (evt%(nevent/maxbins)==0 || evt==nevent-1 )
```

```
//if (frac*evt%(nevent/maxbins)==0 || evt==nevent-1)
{
  if(count!=0)
    {
      TBavg=TBTotal/count;
      TFavg=TFTotal/count;
    }
  shift[bin][0]=evt;
  shift[bin][1]=TBavg;
  shift[bin][2]=TFavg;
  // print values for bins above maxbins-25 as a check
  if (bin>maxbins-25)
    cout<<bin<<" "<<evt<<" "<<TBavg<<" "<<TFavg<<" "<< count << endl
      [continued] ;
    if(bin==maxbins) bin--;
    bin++;
    //frac++;
    TBTotal=0;
    TFTotal=0;
    count=0;
    TBavg=0;
    TFavg=0;
    // cout<<" check"<< evt << endl;
   }
  // cout<<" check"<<endl;
 }
//Loop to write new tree with modified TBack and TFront
//TBack pulser should be @ ch TBPulser and TFront Pulser @ ch TFPulser
//Allow a tolerance of 5 or less channels on either side
double binstart=0;
double binend=0;
int flagf=0;
int flagb=0;
double DeltaTB=0;
double DeltaTF=0;
for (int nbin = 0; nbin<maxbins; nbin++)
  { // set flags to determine if we have to shift TBack
    // and TFront, only TBack, only TFront, or none
    if ((shift[nbin][1]<(TBPulser-Btolerance) || shift[nbin][1]>(TBPulser+
      [continued] Btolerance))&& shift[nbin][1]!=0)
      flagb=1;
```

```
else
  flagb=0;
if ((shift[nbin][2]<(TFPulser-Ftolerance) || shift[nbin][2]>(TFPulser+
  [continued] Ftolerance)) && shift[nbin][2]!=0)
  flagf=1;
else
  flagf=0;
// set start and end of event loop
// according to bins
if (nbin==0)
  {
    binstart=0;
    binend=shift[0][0];
  }
if (nbin>0)
  {
    binstart=shift[nbin-1][0]+1;
    binend=shift[nbin][0];
  }
// set delta TB and TF depending on flag status
if (flagb==0 && flagf==0)
  {
    DeltaTB=0;
    DeltaTF=0;
  }
if (flagb==1 && flagf==0)
  {
    DeltaTB=TBPulser-shift[nbin][1];
    DeltaTF=0;
  }
if (flagb==0 && flagf==1)
  {
    DeltaTB=0;
    DeltaTF=TFPulser-shift[nbin][2];
  }
if (flagb==1 && flagf==1)
  {
     DeltaTB=TBPulser-shift[nbin][1];
    DeltaTF=TFPulser-shift[nbin][2];
  }
for(int evt =binstart; evt<=binend; evt++)
```

```
{
  //get old values and set new values
  cubetree->GetEvent(evt);
  idnew.EBack = id.EBack;
  idnew.EFront = id.EFront;
  if(BShiftFlag==0)
    {
      idnew.TBack = DCPElement(id.TBack + DeltaTB);
    }
  if(BShiftFlag==1)
    {
      idnew.TBack = DCPElement( id.TBack + (DeltaTB/TBPulser)*id.
          [continued] TBack );
    }
  if(FShiftFlag==0)
    {
      idnew.TFront = DCPElement(id.TFront + DeltaTF);
    }
  if(FShiftFlag==1)
    {
      idnew.TFront = DCPElement( id.TFront + (DeltaTF/(TFPulser-
          [continued] DeltaTF))*id.TFront );
    }
  idnew.XBack = id.XBack;
  idnew.YBack = id.YBack;
  idnew.XFront = id.XFront;
  idnew.YFront = id.YFront;
  //write to new Tree
            newTree->Fill();
          }

      }
    newTree->Write();
    outfile->Write();
    return 1;
}
```

A.2 Code used to Plot Event vs. Run Time

```
// Include standard stuff
#include <string>
#include <fstream>
#include <iostream>
#include <stdio.h>
#include <stdlib.h>
#include <sys/stat.h>
// Include ROOT stuff
#include <TCanvas.h>
#include <TCutG.h>
#include <TROOT.h>
#include <TH2.h>
#include <TH1.h>
#include <TGListBox.h>
#include <TFile.h>
#include <TEnv.h>
#include <TKey.h>
#include <TDirectory.h>
#include <TVector3.h>
#include <TMath.h>
#include <TTree.h>
#include <TGTab.h>
#include <TGProgressBar.h>
#include <TGFileDialog.h>
#include <TGTableLayout.h>
#include <TGTextEntry.h>
#include <TGComboBox.h>
#include <TPRegexp.h>
#include <TString.h>
//Type def for the cube tree branches
typedef unsigned short DCPElement;
// define the tree structures
//Structure of the Tree
typedef struct TNEWInterestingData{
  // Branch "Cube"
  DCPElement EBack;
  DCPElement EFront;
  DCPElement TBack;
  DCPElement TFront;
  DCPElement XBack;
  DCPElement YBack;
```

```
DCPElement XFront;
DCPElement YFront;
// Branch "Monitors"
DCPElement AlphaPulser;
DCPElement Monitor1;
DCPElement Monitor2;
// Branch "Annular"
DCPElement EAnnular;
DCPElement TAnnular;
// Branch "Front"
DCPElement EAlphaFront;
DCPElement TAlphaFront;
  // Branch "EventInfo"
  DCPElement EventNo;
} TNEWInterestingData;
int plotter(){
  gROOT->Reset();
  // get the stuff from the tree
  //TFile *infile = new TFile("NEWSSITHU.RUN042.root");
  TFile *infile = new TFile("raw_CAGEX/CAGEXTS.RUN050.root");
  // TFile *infile = new TFile("tmprun044.root");
  TTree *cubetree = (TTree *)infile->Get("CubeTree");
  TNEWInterestingData idnew;
  cubetree->SetBranchAddress("Cube", &idnew.EBack);
  cubetree->SetBranchAddress("Monitors", &idnew.AlphaPulser);
  cubetree->SetBranchAddress("Annular", &idnew.EAnnular);
  cubetree->SetBranchAddress("Front", &idnew.EAlphaFront);
  int nevent_tot = (int) cubetree->GetEntries();
  int nevent = nevent_tot;
  int sort = nevent;
  TCanvas *c4 = new TCanvas();
  c4->ToggleEventStatus();
  //  c4->ToggleCrossHair();
  c4->Divide(1,2);
  c4->SetFillColor(0);
  c4->GetPad(1)->SetLogz();
  c4->GetPad(2)->SetLogz();
  TH2D *Plot = new TH2D("TBackvsEvent","Plot",1024,0,sort,1024,1,1024);
  TH2D *Plot1 = new TH2D("TFrontvsEvent","Plot1",1024,0,sort,1024,1,1024);
  TH2D *Plot2 = new TH2D("TdiffvsEvent","Plot2",1024,0,sort,2049,-1024,1024)
```

[continued] ;

```
for (Int_t i=0;i<sort;i++) {
  cubetree->GetEntry(i);
  // put back the old stuff
  idnew.EBack;
  idnew.EFront;
  idnew.TBack;
  idnew.TFront;
  idnew.XBack;
  idnew.YBack;
  idnew.XFront;
  idnew.YFront;
  Plot->Fill(i,idnew.TBack);
    Plot1->Fill(i,idnew.TFront);
  }
  c4->cd(1);
  Plot->Draw("colz");
  c4->cd(2);
  Plot1->Draw("colz");
  return 1;
}
kk
```

A.3 Code used to Merge Output ROOT Files

```
#include <iostream>
#include <fstream>
#include <stdio>
#include <stdlib>
#include <string>
#include <ctime>
#include <cstdlib>
#include <math.h>
void addhistosv2()
{
  TFile *runfile1 = new TFile("SICO.RUN023.PEG.root");
  TFile *runfile2 = new TFile("SICO.RUN024.PEG.root");
  TFile *runfile3 = new TFile("SICO.RUN025.PEG.root");
  TFile *outfile;
  outfile = new TFile("SUM023_024_025.PEG.root","RECREATE","ROOT file");
```

```
outfile->SetCompressionLevel(1);
TDirectory *mydir1 =(TDirectory *)runfile1->Get("Histo2D");
TDirectory *mydir2 =(TDirectory *)runfile2->Get("Histo2D");
TDirectory *mydir3 =(TDirectory *)runfile3->Get("Histo2D");
// read histos from mydir1 of runfile1 into h2f1[i]
TH2F *h2f1[100];
int histcount=0;
TKey *key = NULL;
TIter next(mydir1->GetListOfKeys());
while ((key = (TKey*) next()))
  {
    obj = key->ReadObj();
    if(obj->IsA() == TH2F::Class())
      {
        h2f1[histcount++] = (TH2F *) obj;
      }
  }
// read histos from mydir2 of runfile2 into h2f2[i]
TH2F *h2f2[100];
int histcount=0;
TKey *key = NULL;
TIter next(mydir2->GetListOfKeys());
while ((key = (TKey*) next()))
  {
    obj = key->ReadObj();
    if(obj->IsA() == TH2F::Class())
      {
        h2f2[histcount++] = (TH2F *) obj;
      }
  }
// read histos from mydir3 of runfile3 into h2f3[i]
TH2F *h2f3[100];
int histcount=0;
TKey *key = NULL;
TIter next(mydir3->GetListOfKeys());
while ((key = (TKey*) next()))
  {
    obj = key->ReadObj();
    if(obj->IsA() == TH2F::Class())
      {
        h2f3[histcount++] = (TH2F *) obj;
```

```
        }
    }
// add histos from h2f1[i] and h2f2[i] and h2f3[i] store in h2f3[i]
int histcount=0;
for(histcount=0;histcount<=58;histcount++)
  {
    h2f3[histcount]->Add (h2f1[histcount]);
    h2f3[histcount]->Add (h2f2[histcount]);
  }
// Write histograms to outfile
for(histcount=0;histcount<=58;histcount++)
    {
      h2f3[histcount]->Write();
    }
  outfile->Close();
}
```

Appendix B

CUBE Electronic Scheme

A schematic of the CUBE electonics is shown in figures B.1 and B.2. Figure B.1 depicts the electronics near the beam line and figure B.1 is a map of the ADC patch panel near the data acquisition system in the 14UD control room.

The three signals that we get from the MWPC's are Energy (ΔE), position and timing. Energy is derived by integrating over the centre foil signals using the modules highlighted in figure B.1 with boxes numbered 1. Timing is derived from the centre foil output as well using the modules highlighted in figure B.1 with boxes numbered 2. Position information is derived from the delay lines and processed using the modules highlighted in figure B.1 with boxes numbered 3.

The rf-sync pulse is used as a stop for the MWPC-B timing and for generating a fission pulser (drawn in blue in figure B.1).

The DAQ trigger is generated from one of three signals, monitor 1, monitor 2 (figure B.2 boxes 1 and 2) or one of the MWPCs (MWPC-B for this diagram). The ADC gate is generated from the centre foil signal of MWPC-B.

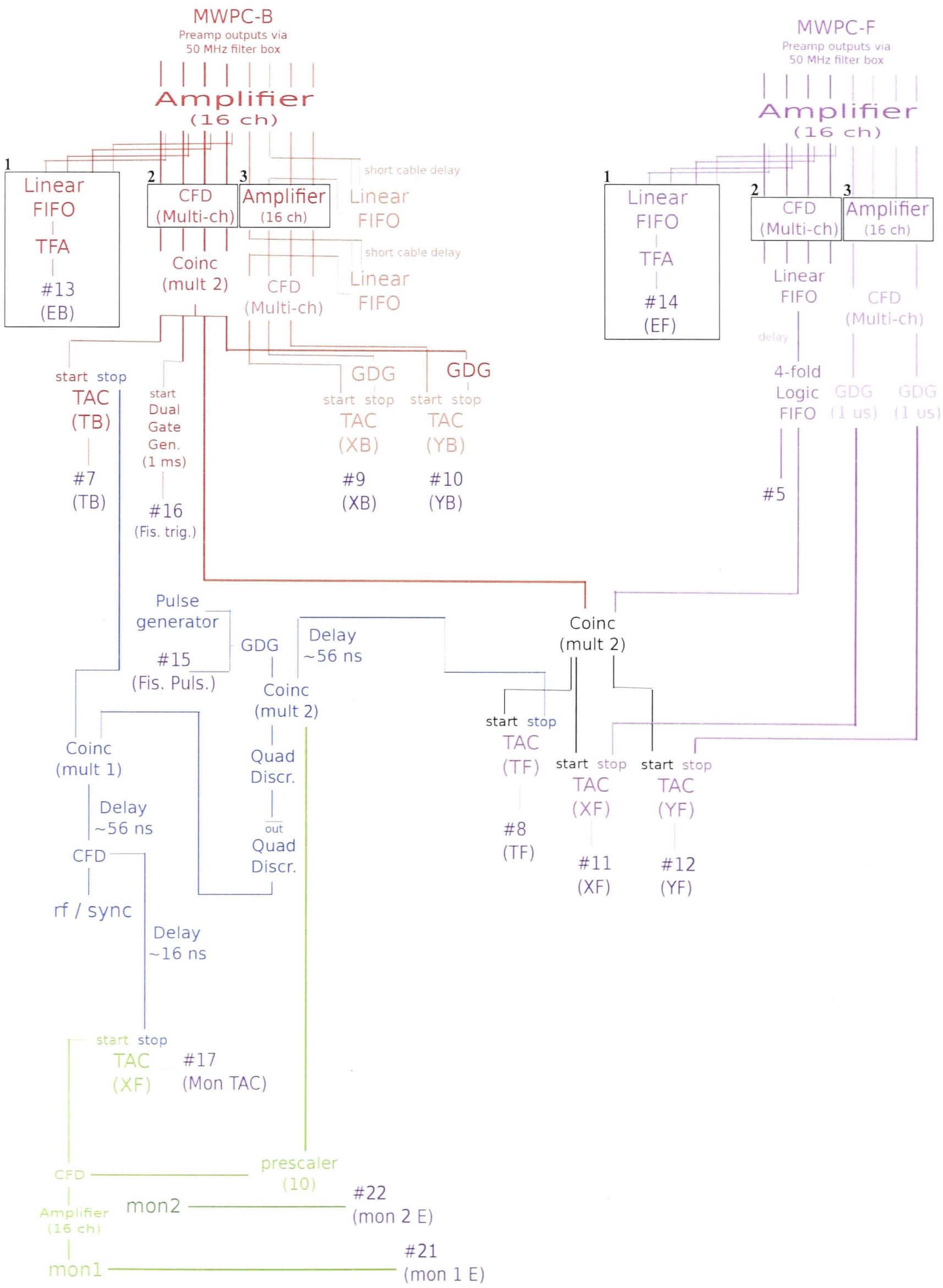

Figure B.1: CUBE Electronic Scheme for electronics near the beam line. Numbered outputs in purple correspond to CUBE patch panel labels.

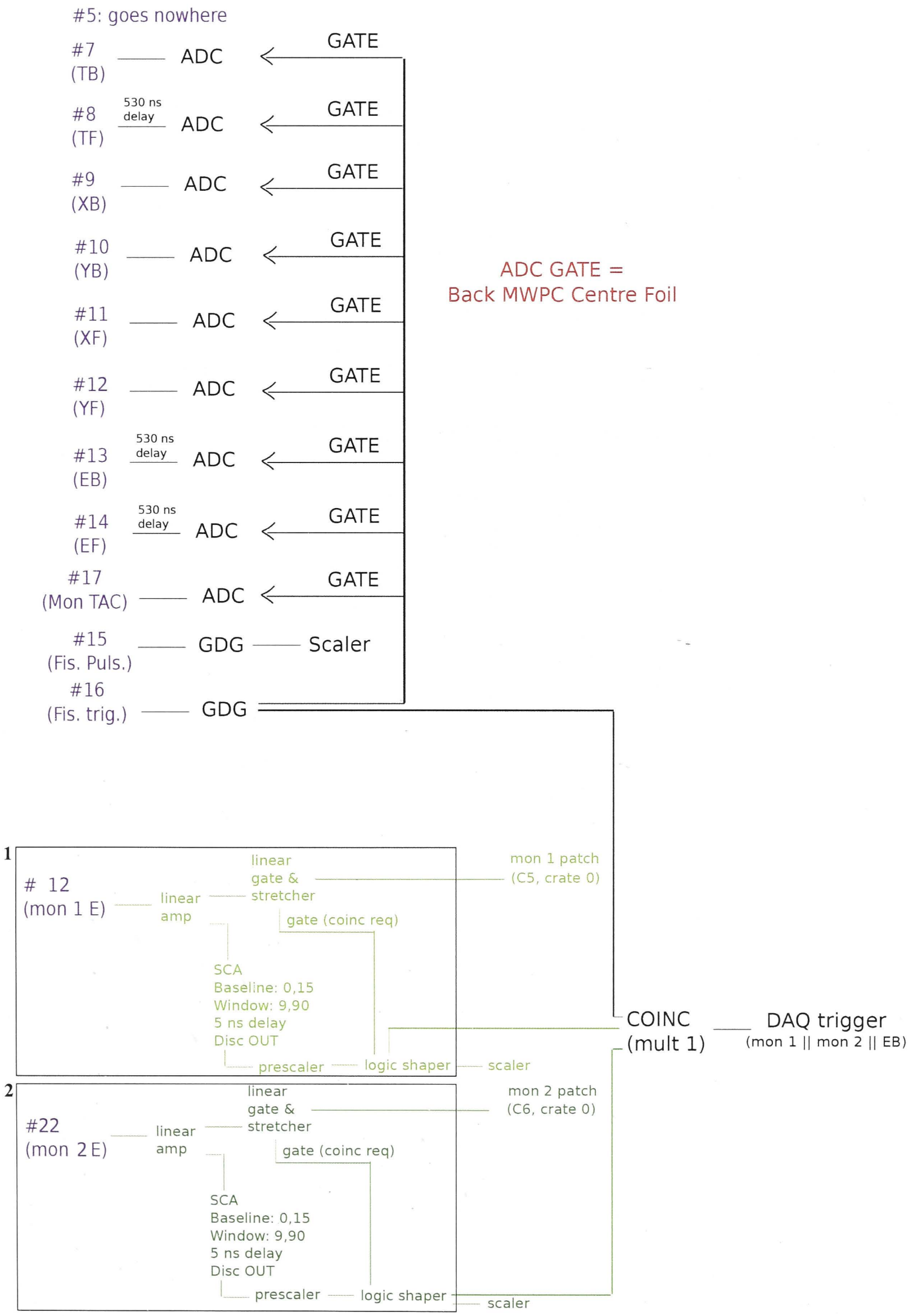

Figure B.2: Electronic Scheme for the patch panel in the 14UD control room.